ISBN 978-82-326-4292-2 (printed version)
ISBN 978-82-326-4293-9 (electronic version)
ISSN 1503-8181

Doctoral theses at NTNU, 2019:348

Karoline Hovde

Parieto-frontal architecture, connectivity and behavioral representations in rodents

NTNU
Norwegian University of
Science and Technology
Faculty of Medicine and Health Sciences
Kavli Institute for Systems Neuroscience/
Centre for Neural Computation

NTNU
Norwegian University of
Science and Technology

Doctoral Thesis

Karoline Hovde

Doctoral theses at NTNU, 2019:348

NTNU

NTNU
Norwegian University of
Science and Technology

Karoline Hovde

Parieto-frontal architecture, connectivity and behavioral representations in rodents

Thesis for the degree of Philosophiae Doctor

Trondheim, December 2019

Norwegian University of Science and Technology
Faculty of Medicine and Health Sciences
Kavli Institute for Systems Neuroscience/
Centre for Neural Computation

NTNU
Norwegian University of
Science and Technology

NTNU
Norwegian University of Science and Technology

Thesis for the degree of Philosophiae Doctor

Faculty of Medicine and Health Sciences
Kavli Institute for Systems Neuroscience/
Centre for Neural Computation

ISBN 978-82-326-4292-2 (printed version)
ISBN 978-82-326-4293-9 (electronic version)
ISSN 1503-8181

Doctoral theses at NTNU, 2019:348

Printed by Skipnes Kommunikasjon as

NORGES TEKNISK-NATURVITENSKAPELIGE UNIVERSITET

FAKULTET FOR MEDISIN OG HELSEVITENSKAP

Parietal-frontal arkitektur, forbindelser og representasjon av handlinger i gnagere

Posterior parietal korteks (PPC) og frontal-motoriske hjernebarkområder er viktige for en rekke kognitive prosesser, inkludert sensorimotorisk integrasjon, beslutningsprosesser, planlegging og utførelse av målrettede handlinger. I samtlige pattedyr er PPC og frontal-motoriske hjernebarkområder koblet sammen med sterke nevrale forbindelser som danner det parieto-frontale nettverket. Her er 'speilnevroner', som først ble oppdaget i primater, kanskje det mest kjente eksemplet på sensorimotorisk integrasjon. Gnagere har en stadig større rolle i studier av de cellulære mekanismene i kognitive prosesser i PPC og frontale kortikale områder. Denne avhandlingen tar sikte på å beskrive de anatomiske og funksjonelle egenskapene i dette nettverket i både mus og rotter. Den første studien i avhandlingen gir en anatomisk beskrivelse av PPC i forhold til nærliggende ekstrastriatale områder i musehjernen. Tidligere definisjoner av PPC i mus har vært upresise, noe som kompliserer tolkningen av funksjonelle studier. Min studie viser at PCC i mus er lik PPC i rotter og er delt inn i tre forskjellige anatomiske områder; medial, lateral og posterior PPC (henholdsvis mPPC, lPPC og PtP). Hvert av disse områdene overlapper delvis med anteriore aspekter i flere extrastriate områder.

I den andre studien undersøkte jeg om forbindelsene mellom PPC og frontale cortices langs midtlinjen i rottehjernen er topografisk organisert på samme måte som rapportert i primater. Denne studien viste at PPC har en sterk topografisk forbindelse til sekundær motorisk cortex (M2), hvor mPPC fortrinnsvis er koblet med den posteriore delen av M2, mens lPPC og PtP er forbundet med den mellomliggende anterior-posteriore delen. Forbindelser med orbitofrontal cortex hadde en tendens til å strekke seg fra medialt til lateralt, hvor mPPC fortrinnsvis er koblet til den mediale halvdelen, inkludert det mediale og det ventrale underområdet. lPPC og PtP, derimot, er fortrinnsvis forbundet med den mediale og sentrale delen av ventrolaterale orbitofrontal cortex. Funnene av topografisk organiserte forbindelser med M2 indikerer heterogenitet i både PPC og M2 i gnagere, noe som førte til den siste studien i avhandlingen. Her ble det undersøkt om nevroner i M2 og PPC i musehjernen koder for utførte så vel som observerte handlinger slik som de gjør i primater. Ved å bruke *in vivo* kalsiumavbildning fant vi at både M2 og PPC stabilt koder for en rekke naturalistiske atferder som musen utfører, men at slike responser ikke forekommer når den samme musen observerer lik atferd hos en annen mus.

Oppsummert har jeg (i) definert PPC anatomisk i mus og (ii) vist at underregioner av PPC i rotte er gjensidig forbundet med frontale hjernebarkområder lang midtlinjen av hjernen på en topografisk måte, likt som i primater. (iii) I mus koder nevroner i M2 og PPC pålitelig for utførte handlinger, men ikke observasjon av lik atferd i andre mus, noe som tyder på at det er begrensninger for den funksjonelle likheten mellom PPC og frontale hjernebarkområder i gnagere og primater.

Navn kandidat: Karoline Hovde
Institutt: Kavli Institute for Systems Neuroscience/Centre for Neural Computation/Egil and Pauline Braathen and Fred Kavli Centre for Cortical Microcircuits
Veiledere: Jonathan R. Whitlock og Menno P. Witter
Finansieringskilder: European Research Council, Det medisinske fakultet NTNU

Ovennevnte avhandling er funnet verdig til å forsvares offentlig
for graden PhD i medisin.
Disputas finner sted i Auditoriet MTA, Medisinsk teknisk forskningssenter
Torsdag 12. desember 2019, kl. 12:15

ABSTRACT

The posterior parietal cortex (PPC) and frontal motor cortices are important for a variety of cognitive processes including sensorimotor integration, decision-making, planning and execution goal-directed actions. Across mammals, PPC and frontal motor cortices are strongly connected and form the parieto-frontal network, where 'mirror' neurons, perhaps the most famous example of sensorimotor integration, were first discovered in primates. Since rodents are serving an ever-greater role in studying the cellular mechanisms of cognitive processes in PPC and frontal cortical areas, the work in this thesis aims to describe the anatomical and functional properties of this network in both mice and rats. The first study in the thesis provides an anatomical description of the mouse PPC relative to the neighboring extrastriate areas, since PPC in mice is poorly defined, which confounds the interpretation of functional studies. I show that, like in rats, the mouse PPC is divided into anatomically distinguishable medial, lateral and posterior subdivisions (mPPC, lPPC and PtP, respectively), and that each of these areas partly overlaps with anterior aspects of multiple extrastriate areas. Second, I investigate whether the connections of rat PPC with frontal midline cortices are topographically organized as reported in primates. The results reveal that PPC is strongly connected with secondary motor cortex (M2) in a topographical manner, such that mPPC is preferentially connected with the most posterior portion of M2, whereas lPPC and PtP connect with the intermediate anterior-posterior portion. Connections with orbitofrontal cortex showed a medial-to-lateral trend, where mPPC preferentially connects with the medial half, including the medial and ventrolateral subregions. lPPC and PtP are preferentially connected with the medial and central portion of the ventrolateral orbitofrontal cortex. The topographical organization of connections with M2 indicates heterogeneity in both PPC and M2 in rodents, which prompts the final study in the thesis probing whether neurons in mouse M2 and PPC encode performed as well as observed actions like in primates. Using *in vivo* calcium imaging, we show that both M2 and PPC stably encode a variety of naturalistic behaviors when performed, but that such responses do not occur when the same animals observed the same behaviors being performed by another animal. In summary, I have (i) defined PPC anatomically in the mouse and (ii) shown that the rat PPC subregions are reciprocally connected with frontal midline cortices in a topographical manner, like in primates. (iii) In mice, neurons in M2 and PPC reliably encode performed but not observed behaviors, suggesting that that there are limits to the functional similarity of PPC and frontal cortices in rodents and primates.

ACKNOWLEDGEMENTS

This thesis work was carried out at the Kavli Institute for Systems Neuroscience and Centre for Neural Computation at the Norwegian University of Science and Technology (NTNU), under the supervision of Associate Professor Jonathan R. Whitlock and Professor Menno P. Witter.

I am deeply grateful to Jonathan for offering me this opportunity, for his careful scientific advice and guidance. Thank you for always being so enthusiastic and supportive of both my work in the lab and the many extra-curricular scientific activities that I have attended or organized. To my PhD thesis co-supervisor and former master's supervisor Menno, thank you for being such a great mentor for the past years, and for sharing your passion and expertise in neuroanatomy. I am also grateful to members and alumni of the Whitlock lab for fruitful discussions and sharing of knowledge. I further would like to thank co-authors of the papers, in particular Benjamin Dunn, Tuce Tombaz, Bartul Mimica, Ryan Cubero, Pranav Mamidanna, Michele Gianatti and Grethe M. Olsen. Ben, your excellent ideas, computational knowledge and your genuine interest in teaching others made it a privilege to work with you on the third paper. It would not have been the same without you. Michele, thanks for amazing times in and outside the lab from the start, and for always being there for me. A special thanks to Grethe for all the things you have taught me in the lab and our collaboration on the second paper; it has been a pleasure working with you. Bruno Monterotti, thanks for your excellent technical help and the lovely conversations that brightened my days.

It has been an exciting and intense journey, and I am grateful for this experience that has allowed me to grow personally and scientifically. The scientific environment at the Kavli Institute is inspiring and I have also been privileged to attend outstanding courses and summer schools. To my CAJAL friends, I had the three most amazing weeks with you at the summer school in Lisbon, both scientifically and socially. Alex, thanks for keeping me grounded and always welcoming me in London. Stephanie, you have inspired me as a scientist and as a friend. To my office mate, Andrea, thanks for all the great moments together and your positive energy. Finally, I would like to thank all my friends and family for the love, support and for always believing in me. Especially Florence, your encouragement and support have been invaluable.

LIST OF PAPERS

Paper 1

Hovde, K., Gianatti, M., Witter, M.P., Whitlock, J.R.
Architecture and organization of mouse posterior parietal cortex relative to extrastriate areas

European Journal of Neuroscience, November 2018, doi: 10.1111/ejn.14280

Paper 2

Olsen, G.M.*, Hovde, K.*, Kondo, H., Sakshaug, T., Sømme, H.H., Whitlock, J.R., Witter, M.P.
Organization of posterior parietal-frontal cortical connections in the rat

Frontiers of Systems Neuroscience, August 2019, doi: 10.3389/fnsys.2019.00038

Paper 3

Tombaz, T.*, Dunn, B.A.*, Hovde, K.§, Cubero, R.J.§, Mimica, B.§, Mamidanna, P., Roudi, Y., Whitlock, J.R.
Action representation in the mouse parieto-frontal network

Manuscript, BioRxiv 2019, doi.org/10.1101/646414

ABBREVIATIONS

Cortical areas

- AGm, Medial agranular motor cortex
- Au, Auditory cortex
- Cg, Cingulate cortex
- cM2, Caudal secondary motor cortex
- EC, Entorhinal cortex
- FEF, Frontal eye fields
- iM2, Intermediate secondary motor cortex
- IPL, Inferior parietal lobule
- IPS, Inferior parietal sulcus
- lPPC, Lateral posterior parietal cortex
- M1, Primary motor cortex
- M2, Secondary motor cortex
- MO, Medial orbitofrontal cortex
- MOs, Secondary motor cortex
- mPPC, Medial posterior parietal cortex
- POR, Postrhinal cortex
- PPC, Posterior parietal cortex
- PtP, Posterior part of parietal cortex
- rM2, Rostral secondary motor cortex
- RSA, Agranular retrosplenial cortex
- RSC, Retrosplenial cortex
- RSG, Granular retrosplenial cortex
- S1, Primary somatosensory cortex
- S1B, Barrel fields of primary somatosensory cortex
- SPL, Superior parietal lobule
- STS, Superior temporal sulcus
- Te, Temporal association cortex
- V1, Primary visual cortex
- V2L, Lateral secondary visual cortex
- V2M, Medial secondary visual cortex
- VLO, Ventrolateral orbitofrontal cortex
- VO, Ventral orbitofrontal cortex

Extrastriate areas

- A, Anterior area
- AL, Anterolateral area
- AM, Anteromedial area
- LI, Laterointermediate area
- LM, Lateromedial area
- MM, Mediomedial area
- P, Posterior area
- PM, Posteriomedial area
- RL, Rostrolateral area

Subcortical areas

- DLG, Dorsal lateral geniculate nucleus
- LD, Laterodorsal nucleus
- LP, Lateral posterior nucleus
- LPlr, Lateral posterior nucleus, anterolateral part
- LPmr, Lateral posterior nucleus, anteromedial part
- Po, Posterior thalamic nuclear group
- SC, Superior colliculus
- VPM, Ventral posterior nucleus, medial part

Orientation

- A, Anterior
- C, Caudal
- D, Dorsal
- L, Lateral
- M, Medial
- P, Posterior
- R, Rostral
- V, Ventral

Visualized protein and tracers

- BDA, Biotinylated dextran amine 10KD
- FB, Fast Blue
- FG, Fluorogold
- PHA-L, *Phaseolus vulgaris* leucoagglutinin
- PV, Parvalbumin
- M2AChR, Muscarinic acetylcholine receptor type 2

CONTENTS

INTRODUCTION

How the brain generates voluntary movements in a seemingly effortless way in everyday life, like reaching for a cup of coffee, is one of the fundamental questions in neuroscience. To produce the complex series of motor actions necessary to grasp the cup, the brain first needs to integrate and combine multiple sensory information including visual, proprioceptive and somatosensory inputs. For example, information such as the position of the cup relative to the hand, the shape of the cup's handle, as well as the posture, motion and location of your hand compared to the cup are crucial to correctly execute the movement (Andersen and Buneo, 2002). These kinds of sensorimotor transformations are essential to our daily life, and some of the best-studied computations take place along the visuo-motor pathway, in the posterior parietal cortex (PPC) and frontal motor areas with which it is connected.

Early in the processing stream of human and primates, visual information diverges from primary visual cortex into dorsal and ventral visual processing pathways. The ventral stream, which projects towards higher visual and temporal areas, is thought of as the 'what' pathway and subserves recognition and discrimination of visual shapes and objects. The dorsal stream, which projects via higher visual areas towards PPC and motor regions was originally called the 'where' or 'action' pathway, and is important for integrating visual information into meaningful actions (Ungerleider et al., 1982; see Goodale, 2011 for review). This knowledge, like much of what is known about the human brain, came from lesion studies in patients who suffered from brain injury or stroke. Damage to the temporal lobe was found to produce deficits in the perception of objects, whereas damage to the parietal lobe often led to difficulties in guiding spatial movements. These and other symptoms following PPC lesions were summarized by the Austro-Hungarian neurologist Rezső Bálint, who proposed that the parietal lobe constructs a map of peripersonal space and the coordination of actions in it (Whitlock, 2017). One of the symptoms he described following damage to the parietal lobe was optic ataxia, the inability to reach for an object in front of oneself, which provided some of the earliest evidence that PPC is involved in visual-motor integration. Several decades later, Goodale and Milner (1992) hypothesized that the dorsal stream is a key cortical substrate supporting 'vision for action'. This was mostly based on the essential role played by the parietal lobe in extracting sensory information about one's own body and the external world in order to guide and plan movements, independently from or in parallel with perceptional processing of the input.

PPC, together with the ventral premotor, primary and supplementary motor cortices are crucial for planning and executing simple as well as more complex goal-directed actions (Andersen, 1997). It is in the same parieto-frontal system that 'mirror' neurons are also found (Gallese et al., 1996;Rizzolatti et

al., 1996), which are neurons that fire both when an animal perform an action and when it observes the same action performed by another. These neurons are thought to have the capacity to represent the actions of others internally through the convergence of numerous inputs from several high-level sensory and motor areas (Rizzolatti et al., 1996). Despite years of research, a simple biological model for the mirror mechanism and knowledge about the neural pathways necessary for mirror neuron properties to emerge, are still lacking, which could be easily addressed in another species like rodents.

In this thesis, I present studies on the anatomical connectivity and functional organization of the parieto-frontal system in rodents, and test whether sensorimotor integration in this system in mice generates mirror-like neurons as described in primates.

The location of the posterior parietal cortex in primates and rats

The parietal cortex derives its name from the overlying parietal bone and is commonly divided into a posterior part, PPC and an anterior part, the somatosensory cortex. While the latter mainly processes somatosensory and proprioceptive information from the peripheral nervous system, PPC combines information from virtually all sensory modalities, as well as from motor and frontal cortices, and is therefore considered an associative area (Whitlock et al., 2008). It supports a variety of cognitive functions, including linking sensory cues with motor actions (sensorimotor integration), decision-making, spatial navigation and early motor planning.

PPC has been described in many mammals including humans, monkeys and rats, and the comparative location and anatomical organization is presented in Figure 1 (Whitlock, 2017). In humans, PPC consists of four cytoarchitectonically defined regions surrounding the intraparietal sulcus (IPS); Brodmann areas 5 and 7 on the superior parietal lobule dorsal to IPS, and areas 39 and 40 on the inferior parietal lobule, ventrally (Brodmann, 1909). Brodmann also subdivided the macaque PPC into two subdivisions: an area 5 dorsal to, and an area 7 ventral to, the IPS (Figure 1, middle). Later, a homologue to monkey area 7 was found in the rat based on its location between somatosensory and visual cortices and its similarity in cyto- and myeloarchitecture (Krieg, 1946). The existence of PPC in rats was for a long time a matter of debate that led to diverse delineations of PPC. In particular, PPC's anterior-posterior and mediolateral extent greatly varied between studies, and the border with secondary visual cortex was particularly challenging to demarcate (see Whitlock et al., 2008).

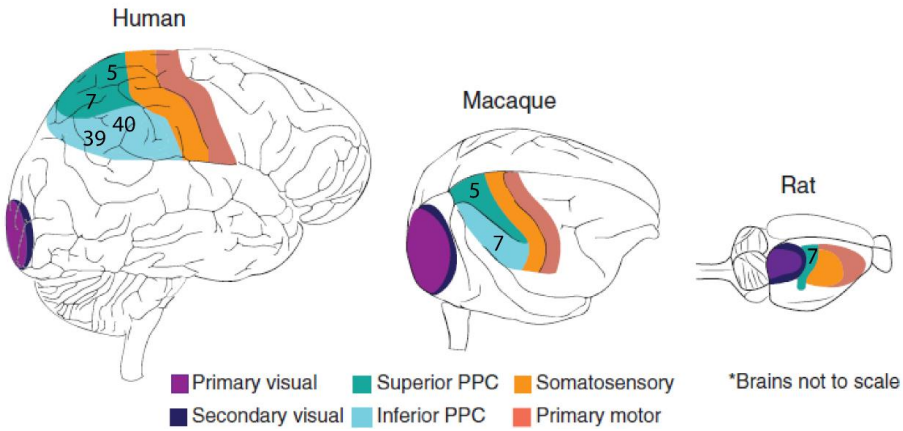

Figure 1. Illustration of the location of the posterior parietal cortex relative to neighboring areas in humans, macaques and rats. Modified from Whitlock, 2017.

Several factors contribute to this variability between PPC studies. First, the rodent cortex is smooth and lacks sulci and gyri, thus making it challenging to distinguish neighboring areas of cortex. Second, PPC is characterized by poor cytoarchitectonic laminar differences, which contrasts with the neighboring primary somatosensory (S1) and visual cortices. However, thalamocortical connectivity has proven an additional useful tool for distinguishing cortical regions (Lashley, 1941). In the rat, PPC has been shown to connect with the posterior complex (Po) and lateral posterior nucleus (LP) (Kolb and Walkey, 1987;Chandler et al., 1992;Reep et al., 1994;Kamishina et al., 2009;Wilber et al., 2015), which are considered homologue areas to the primate anterior and medial pulvinar complex, respectively, with which the primate PPC is strongly connected (Jones, 2007). To better characterize PPC, a comprehensive study by Olsen and Witter (2016) divided the rat PPC into three subregions – a medial (mPPC), a lateral (lPPC) and a posterolateral posterior parietal cortex (PtP) – and differentiated them from the neighboring cortical areas based on a combination of cyto- and chemoarchitecture and thalamic connectivity (Figure 2). This study showed subregional differences in thalamic connectivity pattern - mPPC is preferentially connected with Po and LP, whereas lPPC and PtP connect with Po, suggesting that the rat PPC is a heterogenous region like in primates. This claim was supported in another study by the same authors where they showed that the different subregions of PPC have different preferential connectivity with the parahippocampal regions (Olsen et al., 2017), a part of the brain important for spatial navigation (Moser et al., 2008). These connections have also been described previously and are overall sparse (Reep et al., 1994;Burwell and Amaral, 1998a;Agster and Burwell, 2009).

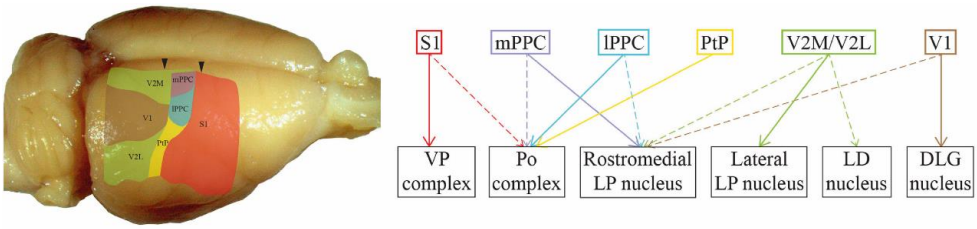

Figure 2. Location of PPC relative to neighboring areas in the rat (left) and the projections of PPC subregions and neighboring areas to the thalamus (right). For abbreviations, see list of abbreviations. Modified from Olsen and Witter (2016).

Location of PPC relative to extrastriate areas in mice

As with rats, the posterior parietal cortex in mice is located between the visual and somatosensory cortices. If the rodent visual streams resemble those of primates, PPC in mice should be at the 'end' of the dorsal stream. Researchers have indeed proposed analogs to the dorsal ('where'/ 'action') stream and ventral ('what'/ 'perception') visual streams in mice by mapping the connectivity of extrastriate areas (Wang et al., 2011;Wang et al., 2012). In rodents, the primary visual cortex (V1) has been estimated to be surrounded by as many as 10 extrastriate areas based on extrinsic V1 projections (Montero et al., 1973;Olavarria et al., 1982;Wang and Burkhalter, 2007), with each one processing different spatial and temporal information (Marshel et al., 2011). Extrastriate areas medial and/or anterior to V1 (PM, AM, A, RL and AL) are preferentially connected with parietal, motor and limbic cortices, resembling a dorsal stream of visual information flow (Wang et al., 2012). Laterally and posteriorly located areas (LM, LI, P and POR), in contrast, are strongly linked to temporal and parahippocampal areas, forming a ventral stream. Based on this, PPC should participate in the dorsal stream, however, the exact location of PPC relative to, and whether it overlaps with, extrastriate areas is not known in mice. This is also of particular interest since retinotopic mapping of extrastriate areas has been used to locate PPC functionally (Krumin et al., 2018;Mohan et al., 2018), and recent years have seen a drastic increase in the number of functional studies of PPC in mice due to technological advantages, such as large scale calcium imaging (see paper 3). However, studies in rodents do not always agree on the anatomical location of PPC, and can rely on the locations of extrastriate areas to approximate the location of PPC for neural recordings (Runyan et al., 2017). Thus, it would be of great interest to establish a coherent anatomical definition of PPC and to establish the correspondence between different nomenclatures and delineations from parallel lines of work (Paxinos and Franklin, 2012;Oh et al., 2014), in addition to its position relative to extrastriate areas in mice. This would provide as a resource applicable to any study to avoid confounding the interpretation of the wealth of new literature.

The first paper therefore describes the mouse PPC based on cyto- and chemoarchitecture as well as projections to the thalamus and cortico-cortical connectivity, and locates PPC relative to extrastriate areas to establish correspondence between differing nomenclatures used to refer to PPC.

Connectivity of the parieto-frontal system

Connections of PPC in rodents

The rodent PPC is considered a multimodal association cortex based on its vast connectivity with other cortical and subcortical regions (Figure 3). PPC receives input from many sensory cortices including the somatosensory, auditory as well as primary and secondary visual cortices (Whitlock, 2017). Lesion studies have suggested that reciprocally connected areas including PPC, the secondary motor cortex (M2), the anterior cingulate cortex (ACC), and the ventrolateral orbitofrontal cortex (VLO) are involved in directed attention (Kolb and Walkey, 1987;Chandler et al., 1992;Conte et al., 2008). Damage to either PPC, M2, VLO or the connections between PPC and M2 typically produce contralateral neglect – the inability to attend to the space contralateral to the lesion (King et al., 1989;Chandler et al., 1992;Burcham et al., 1997). Further, PPC receives input from M2, S1, V2, auditory, VLO as well as the medial orbitofrontal cortex (MO; Reep et al., 1994), and it is reciprocally connected with retrosplenial cortex (RSC; Olsen et al., 2017). The orbitofrontal cortex (OFC) is important for value based decision-making and behavioral flexibility (Rolls, 2000;Wallis, 2012), and could influence and inform PPC about appropriate actions and their expected outcomes. The posterior parietal connections with the parahippocampal system, a region important for spatial navigation, are weak, and the bulk of functional interactions are likely via postrhinal cortex (POR), presubiculum (PrS), or RSC (Reep et al., 1994;Burwell and Amaral, 1998b;Agster and Burwell, 2009;Olsen et al., 2017). Subcortical vestibular and cerebellar input reaches PPC via the thalamus and suggests involvement in motor functions (Giannetti and Molinari, 2002;Smith et al., 2005). PPC further projects to the intermediate layers of the superior colliculus, which is involved in directing gaze and orienting behavior (Wang and Burkhalter, 2013), and the dorsocentral striatum (Reep et al., 2003), important for directed attention and action selection.

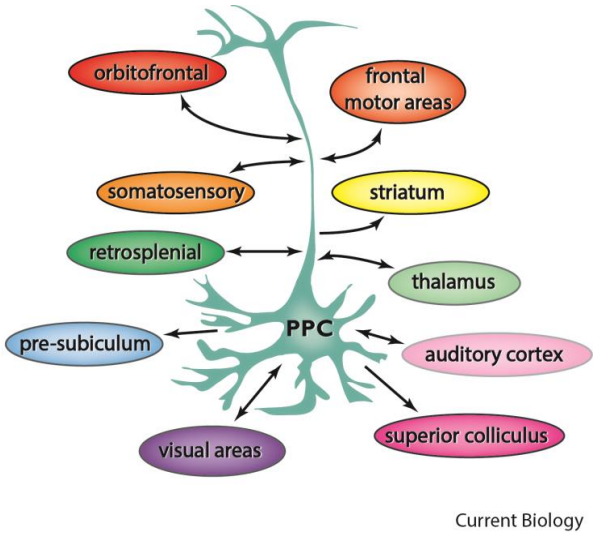

Figure 3. Connectivity of PPC with cortical and subcortical areas in rodents. Adapted from Whitlock, 2017.

Connections of the frontal motor cortex in rodents

The primate frontal cortex can be divided into an anterior portion, involved in higher order cognitive functions, and a posterior motor region that controls movements (Rizzolatti and Luppino, 2001). While it is still a matter of debate if rodents have truly homologous prefrontal cortical subdivisions (Carlén, 2017), they most certainly have a prominent frontal motor cortex including the primary (M1) and secondary motor cortices (M2), which are important for executing and voluntary control of actions, respectively. Homologs to the prefrontal cortex in rodents are therefore based on location and thalamic connectivity, in particular by receiving input from medial dorsal (MD) nucleus of the thalamus, which is a defining feature of prefrontal cortex in primates (Rose and Woolsey, 1948;Carlén, 2017). In rodents, connections with the MD nucleus are found with M2 as well as OFC, prelimbic (PL), infralimbic (IL), cingulate (ACC) and agranular insular regions, but not with M1 (Barthas and Kwan, 2017). Of these areas, M2 is of particular interest since it, similarly to PPC, is considered a critical area for linking sensory cues with motor actions, and thereby constitutes an important node in the circuitry for control of voluntary actions. M2 is also called medial agranular motor cortex (AGm) or secondary motor cortex (MOs), and based on physiological and anatomical features is thought to be a combination of or a precursor to the primate frontal eye fields and supplementary motor areas. As in primates, the rat M2 has extensive cortical connectivity including connections with visual, parietal, somatosensory, auditory, retrosplenial and orbital regions (Barthas and Kwan, 2017). The anterior regions of M2 process more somatosensory input, whereas the posterior region of M2 receives other

sensory input including visual (Reep et al., 1990). M2 also plays a role in controlling motor behavior, which is supported by projections along the cortico-spinal tract to the spinal cord, to the deep layers of the superior colliculus (SC), and to subcortical brainstem oculomotor nuclei. Interestingly, projections from PPC and M2 co-terminate in the same portions of the dorsocentral striatum, a region crucial for motor control, directed attention and multimodal processing (Reep et al., 2003).

Topographical connectivity of PPC

In primates, the input of somatosensory and visual information is topographically organized within the different subdivisions of PPC. Processing of visual information is more dominant in the posterior medial area 7a, whereas somatosensory information in preferentially processed in anterior-lateral areas 7b (Hyvärinen, 1981;Andersen et al., 1987;Cavada and Goldman-Rakic, 1989a;Andersen et al., 1990;Rozzi et al., 2008). Furthermore, the different subregions of PPC are preferentially connected to areas of motor cortex that control motor responses for corresponding body parts (Cavada and Goldman-Rakic, 1989b;Andersen et al., 1990;Neal et al., 1990;Rizzolatti and Luppino, 2001;Rozzi et al., 2006;Gharbawie et al., 2011a), which likely facilitates spatially-informed, goal-directed movements of the eye, hand, arm, and possibly the whole-body (Johnson et al., 1996;Andersen, 1997;Wise et al., 1997).

Similar to primates, recent studies have also shown that PPC and frontal cortices in rodents play a role in guiding behavior, with the firing patterns of neurons in each region seem to predict upcoming movements (Erlich et al., 2011;Whitlock et al., 2012;Raposo et al., 2014;Erlich et al., 2015;Hanks et al., 2015). PPC-frontal connections have previously been described in rats (Reep et al., 1984;Kolb and Walkey, 1987;Reep et al., 1987;Reep et al., 1990;Reep et al., 1994;Condé et al., 1995;Reep et al., 1996;Hoover and Vertes, 2007;2011) and mice (Harvey et al., 2012;Wang et al., 2012;Oh et al., 2014) using anatomical tracers. However, it is yet not known whether these connections are topographically organized like in primates, which limits functional analyses of PPC and frontal cortical areas. In particular, if the different subregions of PPC relate to frontal cortices in an organized manner, it would suggest heterogeneity in the parieto-frontal system in rodents, as seen in primates. Understanding how these areas interconnect in rodents would thus allow for more informed comparisons of the function of parieto-frontal network across species.

The second paper therefore aims to illuminate the topographical connectivity of the three different PPC subregions (mPPC, lPPC and PtP) with the frontal midline and motor cortices (OFC, ACC, M2, M1) in rats.

Neural representation of actions in the parieto-frontal system

More than a century of research in humans and primates has led to the identification of several brain areas crucial to the planning of actions, including supplementary, pre- and primary motor cortices as well as prefrontal and parietal areas (Wise, 1985;Andersen, 1997;Miller and Cohen, 2001). Among these, PPC processes high-level cognitive functions related to actions, including early movement planning, in the form of sensorimotor integrations and the formation of conscious intentions (Andersen and Buneo, 2002). Primate studies are nearly always carried out with head-fixed subjects that execute precise movements using their hands or eyes, and have traditionally focused on attention, decision making or other higher-order cognitive functions. Efforts over the past 15 years have made it possible to address similar questions using rodent paradigms, in which the subjects can move freely, by designing tasks that isolate decision-making and goal-directed behaviors. These include tests of visual attention (Broussard et al., 2006), working memory (Harvey et al., 2012), decision-making (Raposo et al., 2012;Brunton et al., 2013) and motor planning (Erlich et al., 2011), which have facilitated the unravelling of the neural circuit mechanisms supporting these functions.

One of the most remarkable properties of neurons in the primate parieto-frontal system is the ability to not only encode first-person, but also third-person actions. That is, the posterior parietal and premotor regions contain 'mirror' neurons, which fire both when an animal performs an action and when it observes a conspecific performing the same action (Gallese et al., 1996;Rizzolatti et al., 1996;Fogassi et al., 2005). Mirror neurons are thought to provide a cellular link between perception and action, which could be critical for several cognitive functions including observational learning, imitation and empathy. Mirror neurons were first discovered in monkeys, in a part of the ventral premotor cortex, area F5 (Gallese et al., 1996;Rizzolatti et al., 1996), but were later found in the monkey parietal lobe (Fogassi et al., 2005), in area HVC of swamp sparrows (Prather et al., 2008), as well as in several cortical regions in humans (Iacoboni and Mazziotta, 2007;Mukamel et al., 2010).

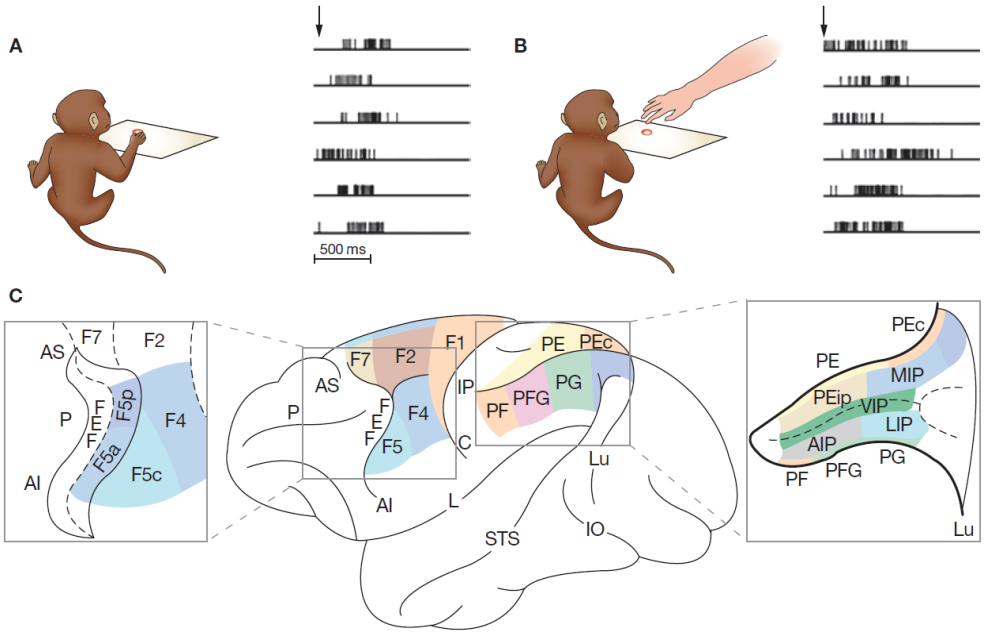

Figure 4. Lateral view of the macaque brain showing subdivisions of frontal motor and posterior parietal cortices. Boxed areas show the areas located on the inside of the arcuate and intraparietal sulci. Mirror neurons were first found in area F5 and PFG. Adapted from Rizzolatti et al. (2009).

The ventral premotor area F5 (Figure 4C) contains two different classes of visuo-motor neurons: 1) canonical neurons that fire when a monkey observes an object-directed action (Rizzolatti and Luppino, 2001), and, 2) mirror neurons, which are active 'both when the monkey performed a given action and when it observed a similar action performed by the experimenter' (Gallese et al., 1996). For mirror neurons to fire, goal-directed interactions between the object and the agent of action are required, and most commonly involves the hand and mouth as effective agents. In the classical studies, a monkey was trained to reach and grasp a piece of food and to watch the experimenter do the same task (Figure 4 A, B). Single neuron recordings showed that F5 neurons fired both when the animal reached for an object, and when the monkey observed the action being performed by another monkey or human.

Mirror neurons in inferior parietal lobule (IPL) area PFG (Figure 4C), which corresponds to Brodmann area 7 (as denoted in Figure 1), were found to encode sequences of goal-directed actions such as 'grasping-to-place' and 'grasping-to-eat' (Figure 5), responding differently when the same action was embedded in a different sequence of goal-directed behavior (Fogassi et al., 2005). It was concluded that mirror neurons with these properties would allow the observer to predict the intention of an action, enabling *action recognition*, and not only code for perceived motor acts per se.

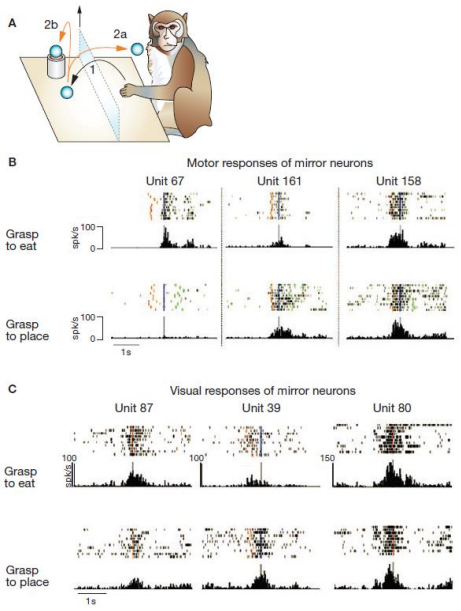

Figure 5. Action-constrained neurons in the monkey IPL. A) Experimental set-up. Grasping-to-eat and grasping-to-place mirror neurons fire during the performance of the action (B) and observation of the same actions being performed by the experimenter (C). Adapted from Rizzolatti et al. (2009).

Despite years of research and considerable speculation on the function of mirror neurons, a simple biological model for the mirror mechanism—of the neural pathways necessary for mirror neuron properties to emerge—is still lacking. Interestingly, several studies have revealed that the rodent parietal cortex and frontal motor cortices, as in primates, mediate functions consistent with the presence of a higher motor system for action control (Erlich et al., 2011;Harvey et al., 2012;Whitlock et al., 2012;Raposo et al., 2014), as well as the capacity for observational learning, basic forms of empathy and social modulation of learning (Panksepp and Lahvis, 2011;Zentall, 2012). Considering these similarities, in addition to comparable anatomical connectivity, it would be of interest to explore whether the rodent M2 and PPC are involved in action recognition as shown in monkeys and humans. That is, do rodents exhibit sensorimotor mirror matching in the parieto-frontal system in the form of mirror neurons, or is mirroring a more recent adaptation suited to the needs of only a few specific niches? Finding such representations in rodents would open the door to an array of investigations into the cellular and circuit basis of the mirror neuron, beyond what is currently feasible in monkeys and humans.

The third paper in this thesis aims to investigate whether the same neurons that represent first-person actions also code for observed actions, and whether 'mirror' neurons occur in the homologue areas M2 and PPC in mice as in primates.

OBJECTIVES

Integrating sensory information with motor output is essential to create meaningful behaviors, and the primate visuo-motor system is one of the best-studied examples of sensorimotor integration. Such computations enable the generation of movement intentions prior to motor output, as well as mirror neurons of the parieto-frontal system, at the end of the dorsal visual stream. In rodents, however, it is still unclear exactly whether or how PPC fits into a similar regime, both in terms of function and anatomy. For example, where PPC is located relative to the extrastriate areas in the dorsal stream, and whether the connections of the parieto-frontal network are topographically organized, are yet to be established. Similarities in anatomical connections would further suggest that sensorimotor integration could be implemented in a similar manner in rodents as in primates. The objectives of this thesis are thus threefold.

1) Paper 1 aims to characterize the mouse PPC based on cyto- and chemoarchitecture, thalamic projections and cortico-cortical connectivity. Further, it aims to register the location of PPC relative to extrastriate areas so as to establish correspondence between nomenclatures used to describe mouse PPC.
2) Paper 2 aims to determine if the reciprocal connections between PPC subregions and frontal midline and motor cortices are topographically organized rats as they are in primates.
3) Paper 3 aims to investigate whether neurons in mouse M2 and PPC encode both performed and observed actions, as a critical test of whether sensorimotor mirroring occurs in the parieto-frontal network, as described in primates.

SYNOPSIS OF METHODS

Paper 1 | Architecture and organization of the mouse posterior parietal cortex relative to extrastriate areas

In the first paper, I used 14 adult C57BL/6JBomTac mice to describe the anatomy of the posterior parietal cortex (PPC), its positioning in relation to higher visual areas, and its connectivity with other cortical areas. One mouse was perfused with PFA (4%) and the brain was cut in coronal sections to describe and delineate PPC and surrounding cortices based on cyto- and chemoarchitecture as revealed by nissl-, parvalbumin- (PV) and muscarinic acetylcholine receptor M2 (MAChR2)-staining. Anterograde tracing was performed using the tracers 10KD Biotinylated dextran amine (BDA), dextran-488 and dextran-546. Bilateral, triple injections were successfully made into the left and right hemispheres of the primary visual cortex (V1; N=5) *or* PPC by iontophoresis (N=4). After one week, the animals were transcardially perfused using ringer's solution and freshly prepared PFA (1%). Shortly after perfusion, the brains were cut in half along the midline and the right hemisphere was placed in a container with PFA (4%) to fixate overnight, followed by cryoprotective solution the next night. The hemisphere was cut in coronal sections (40µm) in three series on a freezing microtome. The first series was processed with nissl-staining, the second was stained histochemically against BDA (streptavidin-633), and the third was stained against MAChR2. The left hemisphere of the brain was dissected, the cortex was flattened and placed between two microscope glasses in PFA (4%) to fixate overnight, followed by a cryoprotective solution. It was cut in 50µm thick 'flattened tangential' sections in one series, which underwent histochemistry against BDA (streptavidin 633). Retrograde tracing was performed by first injecting a helper AAV virus into PPC (AAV1.CamKII0.4.Cre.SV40 + AAV5-syn-FLEX-splitTVA-EGFP-B19G) and, after 12 days, the rabies virus (EnvA-pseudotyped SAD-DeltaG-mCherry) was injected in the same location. After a survival time of 11 days, the animals (N=4) were perfused and subsequently the brains were cut in coronal sections (40µm). All brain sections were digitized with a scanner and selected sections were scanned with a confocal microscope for higher resolution images.

Paper 2 | Organization of the posterior parietal-frontal cortical connections in the rat

We analyzed data from 74 injections of anatomical tracers (BDA, PHA-L, FB, FG) in 61 Sprague Dawley rats. Most cases were obtained in previous work (65 cases), whereas some cases with successful injections of anterograde and retrograde tracers were incorporated to supplement this study (9 cases). In short, animals were anesthetized with isoflurane and injected with anterograde and/or retrograde tracers in orbitofrontal, posterior parietal and medial frontal cortices (Figure 6). After a survival time of 1-2 weeks, the animals were transcardially perfused using ringer's solution followed by PFA (4%). The brains were kept in fixative overnight, moved to a cryoprotective solution and later cut on a freezing microtome in 50µm coronal sections in six series. Two or more series of sections were processed to visualize the retrogradely labeled cells and anterogradely labeled fibers. Borders between brain areas were established on the adjacent Nissl stained sections, which were delineated based on the characteristic cytoarchitectonics of the areas. We carefully described the location and topography of cells and fibers in posterior parietal, frontal midline and orbitofrontal cortices. I also extrapolated digital flatmap representations of the locations of fibers in cingulate, secondary and primary motor cortices originating from the three subregions of the posterior parietal cortex (mPPC, lPPC and PtP). Cases with injections in the same areas were grouped together and average flatmaps were made to compare the topography of labeling in frontal cortices across the three groups.

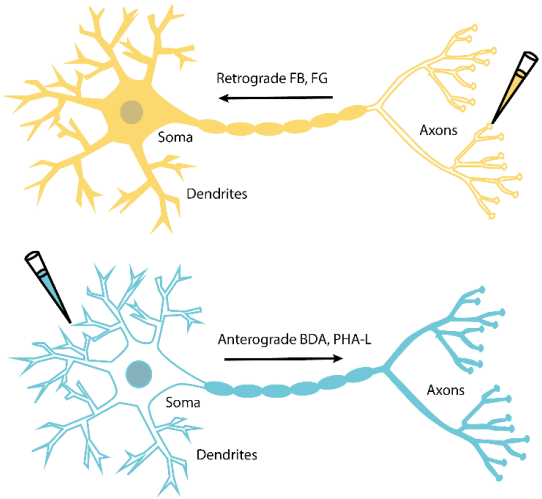

Figure 6. Traditional retrograde and anterograde anatomical tracing. *The retrograde FB and FG are taken up by axons and transported back to the soma. The anterograde tracers BDA and PHA-L are taken up by dendrites and soma and transported towards the axons. For abbreviations, see list of abbreviations. The figure is modified with permission from Hegstad (2019).*

Paper 3 | Action representation in the mouse parieto-frontal network

Data from eight wild type C57BL/6 female mice were included in the third paper. The animals were injected with a GCaMP6m-virus (AAV1.Syn.GCaMP6m.WPRE.SV40) into the secondary motor cortex (M2; Figure 7 A, left) or the posterior parietal cortex (PPC). GCaMP6m is a calcium indicator that, under the h-Syn promoter, expresses in all neuron types. One week post infection, a gradient refractive index lens (GRIN) attached to a prism (Inscopix) was implanted into the brain at the same location, and a headbar was cemented onto the skull to allow for head-fixation. The animals were trained gradually to (i) perform a pellet-reaching task in which they had to reach for food pellets and turn in a circle each time to get another, and (ii) be head-fixed in a tube during observation of the task. After approximately ten days, animals with strong GCaMP6m expression had a baseplate cemented onto the head above the craniotomy to hold the miniature microscope at a suitable distance from the prism to image neural activity during unrestrained behavior (Figure 7A, right). During recordings, the miniaturized microscopes shine LED-emitted blue light through the prism onto the cortical neurons expressing the calcium indicator. When the calcium indicator binds intracellular calcium it changes configuration and emits fluorescent light. In our experiments, this approach was used to approximate neural spiking activity across performance and observation of the pellet-reaching task (Figure 7B) and an open field/wheel-running task. On a given day, an animal would both perform and observe the task twice, allowing us to track the activity of the same neurons across conditions and evaluate the stability of their behavioral coding. In addition, the behavior of both animals and the pupil of three observers was recorded with high-resolution infrared cameras. After the experiments were done, the animals were perfused and the recording sites were confirmed. The neural activity, measured as calcium events (Figure 7B), was determined during performance and observation of up to nine naturalistic behaviors, allowing us to investigate whether the same neurons coded for both performed and observed behaviors.

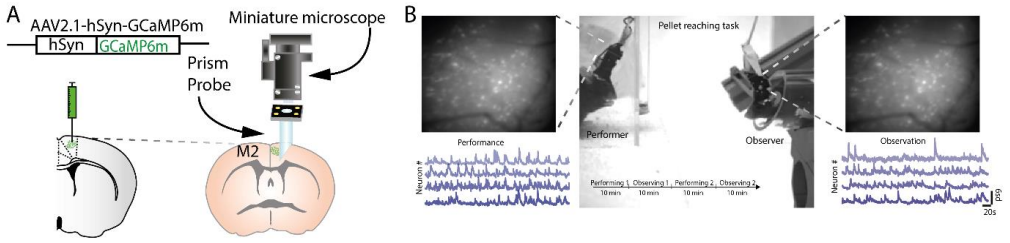

Figure 7. Experimental and behavioral design for calcium imaging in M2. *A) Virus injection in M2 and localization of virus expressing neurons, prism probe, baseplate and miniature microscope. B, middle) Two mice performing and observing the pellet-reaching task with miniature microscopes recording the neural activity from each of their brains (see field of view on each side). Below) extracted calcium traces of single neurons across time for performance and observation.*

SYNOPSIS OF RESULTS

Paper 1 | Architecture and organization of the mouse posterior parietal cortex relative to extrastriate areas

The technological advantages of rodent systems have led to a drastic increase in the number of studies utilizing mice to investigate PPC-dependent behaviors. However, a coherent anatomical definition of PPC in the mouse is still lacking. In the first paper, I delineate mouse PPC, as with rats, into three subregions consisting of mPPC, lPPC and PtP using cyto- and chemoarchitectural markers. PPC can be distinguished from neighboring regions by its very homogenous lamination in the nissl stain, with subtle differences between PPC subregions. These delineations are strongly supported by a sharp drop in parvalbumin and staining against the muscarinic acetylcholine receptor 2 in PPC compared neighboring areas. Several research groups currently use extrastriate areas to locate PPC in the brain, though the exact location of PPC relative to these areas is not known. I therefore performed bilateral triple anterograde tracer injections in primary visual cortex (V1) and prepared flattened tangential sections from one hemisphere (to locate extrastriate areas), and coronal sections from the other. This approach allowed me to co-register the cytoarchitectural features of PPC with projections from V1, revealing that extrastriate area A is largely contained within lPPC, that mPPC overlaps with the anterior portion of area AM, and that PtP overlaps partly with anterior RL. Furthermore, triple anterograde tracer injections in PPC showed strong projections to associative thalamic nuclei as well as higher visual areas, orbitofrontal, cingulate and secondary motor cortices. Retrograde circuit mapping with rabies virus further showed that all cortical connections are reciprocal. These combined approaches provide a coherent definition of mouse PPC that incorporates laminar architecture, extrastriate projections, thalamic and cortico–cortical connections, which is highly similar to rats and topologically comparable to primates (Figure 8).

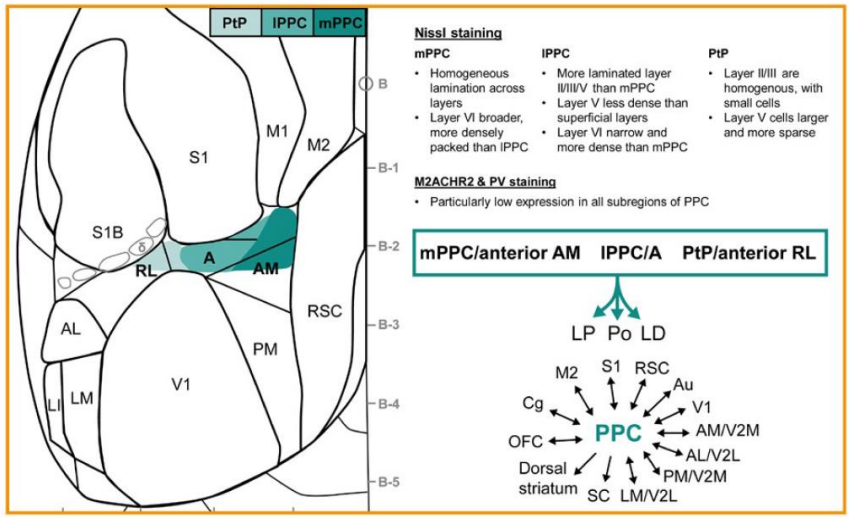

Figure 8. Summary of the location, architectural characteristics and connectivity of mouse PPC. (Left) approximation of PPC location relative to extrastriate areas. (Upper right) cyto- and chemoarchitectural characteristics of PPC. (Lower right) PPC projections to the thalamus and connectivity with cortical and subcortical areas. For abbreviations, see list of abbreviations.

Paper 2 | Organization of the posterior parieto-frontal cortical connections in the rat

Increasing evidence suggests that the rodent posterior parietal cortex (PPC) plays a role in guiding and controlling actions together with frontal cortical areas. In the second paper I describe the topography of anatomical connections between the three subregions of PPC, the medial (mPPC), the lateral (lPPC) and the posterolateral subregion (PtP), with frontal midline cortices using anterograde and retrograde tracers. I show that each PPC subregion projects to secondary motor cortex (M2), and that the reciprocal connections are arranged similarly. The connections follow a topographical organization, such that mPPC preferentially connects with anterior and caudal portions of M2, whereas lateral lPPC and PtP connect with the mid portion of M2. PPC is further connected with the cingulate cortex, mostly with the dorsal portion (24b), although these connections are sparser than those with M2. mPPC connects with rostral 24b, whereas lPPC and PtP connect with the more caudal portion of 24b. Connections with M1 and mPPC preferentially involve the caudal portions of M1, whereas lPPC connects with the mid portion and PtP with more rostral levels of M1, around the level of the genu of corpus callosum. In order to compare these topographical connections across cases and subregions, cases with injections into each of the three PPC subregions were grouped together and average flatmaps for each region were made to highlight the topography described above. I also show that PPC connections with the orbitofrontal cortex (OFC) are organized topographically in a medial-to-lateral manner. Specifically, mPPC is connected to the medial parts of OFC, including medial orbital (MO), ventral orbital (VO) and medial part of ventrolateral orbital (VLO) cortex. lPPC is connected to medial part of VLO, while PtP is preferentially connected with the central portion of VLO situated around the orbital notch. PPC is neither connected with lateral parts of OFC nor the prelimbic or infralimbic cortices. Taken together, these results demonstrate a topographical organization of connections between the different subregions of PPC and the frontal cortices (Figure 9). This could suggest functional differences between the subregions of PPC and the frontal areas to which they are connected; if so, it would be comparable to the heterogeneity seen in the primate parieto-frontal system.

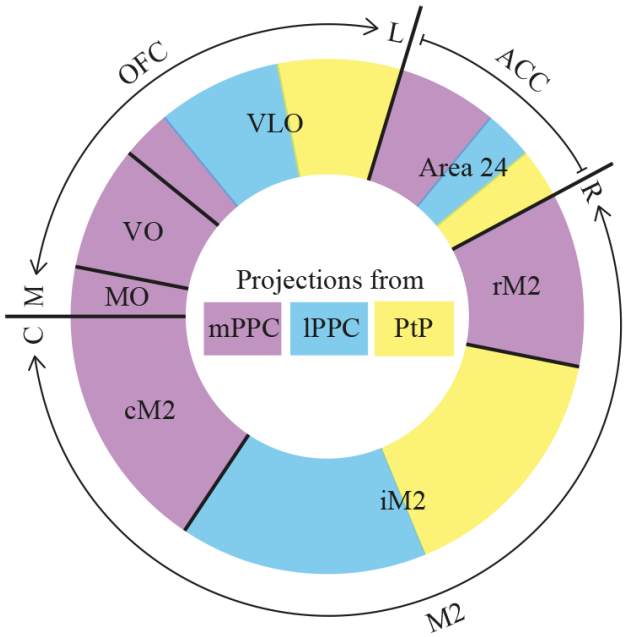

Figure 9. Summary diagram of PPC-frontal projections. *Projections from mPPC are marked in purple, projections from lPPC in blue and projections from PtP in yellow. The outer colored circle represents the relative proportion of projections, indicated by the size of the color-coded areas, from the three PPC subdivisions to frontal cortical areas that are separated with black lines. The outer edge indicates the total extent of OFC, ACC and M2, as well as their rostrocaudal (R–C) or mediolateral (M–L) organization. The reciprocal projections from OFC and M2 to PPC show comparable patterns. For abbreviations, see list of abbreviations.*

Paper 3 | Action representation in the mouse parieto-frontal network

The posterior parietal cortex (PPC), along with anatomically linked frontal areas, form a cortical network that supports sensorimotor transformations and goal-directed behavior. In primates, this network also links performed and observed actions via mirror neurons, which fire both when an animal performs an action and when they observe the same action performed by a conspecific. However, whether such sensorimotor mirror matching also happens in rodents is still unknown. In the third paper we therefore imaged calcium responses in large neural ensembles in secondary motor cortex (M2, four animals, 852 neurons) and PPC (four animals, 921 neurons) while mice performed and observed several naturalistic behaviors in either a pellet reaching or wheel running task. We found that large proportions of neurons in both brain regions robustly encoded a variety of behaviors including grasping for food, eating, nose poke, rearing, grooming, turning clockwise and counter clockwise. However, we found negligible neural tuning to the same actions when they were observed—across both brain areas and across animals—irrespective of whether the neurons encoded performed actions. An example of this is shown in Figure 10 for M2 neurons that discharged significantly when animals grasped a food pellet. To determine whether the lack of observational correlates of behaviors was due to low attention levels of observer mice, I estimated the attention level of observer animals (N=3) by quantifying their pupil diameter during task observation, and removed time intervals where the pupil was contracted (a proxy for low attentional levels), but this did not reveal any observational correlates of observed behaviors. Statistical modeling with a generalized linear model (GLM) also showed that performed actions, especially those that were task-specific (grasping and eating), outperformed observed actions in predicting neural responses. We conclude that performed and observed actions do not drive the same neurons in the parieto-frontal network in mice. This suggests that sensorimotor mirroring in the mammalian cortex may have evolved differently, or only in certain species.

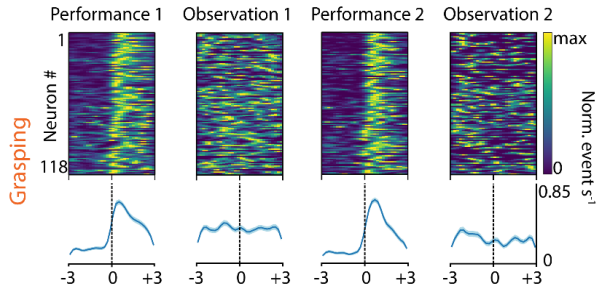

Figure 10. Paper 3 showed that cells with strong correlates for performed actions did not respond when the same actions were observed. An example of this phenomenology is shown above, with neurons in M2 stably coding for grasping a food pellet. Cells in 'Performance 1 and 2' do not respond when the animals watch a conspecific grasp for food in 'Observation 1 and 2'. Average responses for 118 neurons significantly coding for grasping are aligned to the onset of grasping.

METHODOLOGICAL CONSIDERATIONS

Anatomical tracing.

We used traditional anterograde and retrograde anatomical tracers and a retrograde, modified rabies virus to study cortical and subcortical connectivity in rats (paper 2) and mice (paper 1). In paper 1, I used combinations of the anterograde tracers Dextran amine 488, 546, 633 and 10 KD BDA for bilateral triple injections into either PPC or V1. In paper 2, we used two sensitive anterograde tracers - 10 KD biotinylated dextran amine (BDA) and *Phaseolus vulgaris* leucoagglutinin (PHA-L; Brandt and Apkarian, 1992;Veenman et al., 1992). Anterograde tracers are taken up by the neural dendrites and/or the somata and are transported toward the axon terminals (Lanciego and Wouterlood, 2011). 10 KD BDA is typically the preferred anterograde tracer since it is reliable, easy to combine with other tracers and is visualized in an efficient two-step histochemical procedure (Lanciego and Wouterlood, 2011), though in certain circumstances it may have a retrograde component. PHA-L also gives robust anterograde labeling and less retrograde labeling than BDA, but it requires more extensive immunohistochemical visualization procedures that often result in higher background signal, limiting the visualization of labeled fibers. This was overcome by analyzing the fibers at high magnification. A limitation of anterograde tracing is that retrograde uptake of the tracer by cells that project to the injection area may happen, which could lead to 'indirect' anterograde labeling from cells not located in the area where the injection was made (Chen and Aston-Jones, 1998). Precautions were made to minimize this possibility for indirect labeling. First, we used 10 KD BDA, which is the molecular weight version of BDA that is known to have the least retrograde component (Chen and Aston-Jones, 1998;Reiner et al., 2000), whereas PHA-L tends to have less retrograde labeling than BDA in general (Chen and Aston-Jones, 1998). Second, the microcapillary tip widths were kept at the minimum (20-25 µm for BDA and dextran tracers and 15-20 µm for PHA-L) to damage to the brain as little as possible. In paper 2, in cases where retrograde labeling was seen, which occurred mostly around the injection site, the possibility of indirect anterograde labeling was taken into account and the analysis was done with caution. Overall, the anterograde labeling location reflected the expected locations based on the placement of the injection sites and the volume of tracer injected, suggesting that true labeling was stronger than the potential indirect. I am therefore confident that the projection patterns shown in this study are from true PPC projections. The Dextran 633 used in paper 1 turned out to have a strong retrograde component and weak anterograde labeling, and was therefore excluded from the study in favor of BDA, which yielded robust and exclusively anterograde labeling. Dextran 488 and 546 both had moderate anterograde labeling and some retrograde component was seen in the same areas as the anterograde labeling, but not in other areas. Since we were looking at reciprocal connectivity

between PPC and cortical areas, this retrograde component provided positive confirmation of the projections seen from retrograde rabies tracing. The projection pattern was similar to the cases where no retrograde labeling was present and was only observed in areas with known connectivity. For injections in V1, some weak retrograde labeling was also seen in the extrastriate areas intermingled with the anterograde labeling. However, this did not interfere with the conclusions of the study and the connections were in accordance with those known from Montero (1993), who mapped the extrastriate areas in rats employing retrograde tracers in V1. Some triple injections were done bilaterally in the same area (PPC or V1), raising the question as to whether contralateral projections could contribute to the projections studied in the other hemisphere (coronal sections). I showed that there are weak contralateral projections between PPC in each hemisphere, but that contralateral projections to other brain areas were very weak. A hallmark of V1 is that it does not project contralaterally to itself, which is a feature used to locate V1 (Wang and Burkhalter, 2007), and I am therefore confident that the ipsilateral projection patterns shown in the study are representative.

For retrograde tracing in paper 2, we used Fast Blue (FB) and Fluorogold (FG), which are taken up by the axon terminals efficiently and transported retrogradely over long distances to fill the somata of projection neurons (Lanciego and Wouterlood, 2011). Possible uptake by damaged fibers passing through the area of the injection site and labeled cells that do not project to the injection site itself might constitute a challenge (Lanciego and Wouterlood, 2011). To limit this possibility, I used thin capillaries (40-50µm for FG, 80-100µm for FB) which were lowered very slowly into the brain. For injections into OFC to study input from PPC, this was likely not an issue since few fibers pass through OFC into olfactory domains as supported by our observations during the study. In all areas, the retrograde tracers tended to spread and create larger injection sites than the anterograde ones. Thus, for PtP, which is a very narrow area, no retrograde injections were successfully confined to PtP. Connections with PtP were therefore based mainly on anterograde data. Projections to PtP were also shown by anterograde tracer injections into M2 and VLO, whereas no such injections were done into 24b. However, since all other connections of PPC with frontal midline areas were reciprocal, it is very likely that it is the case for PtP as well.

For the rabies virus tracing in paper 1, I used a helper virus expressing the g-protein (AAV1.CamKII0.4.Cre.SV40 + AAV5-syn-FLEX-splitTVA-EGFP-B19G) and modified monosynaptic rabies virus (EnvA-pseudotyped SAD-DeltaG-mCherry), which were injected in the same location in PPC 12 days apart. The helper virus was under a CaMKII promoter that restricts viral expression to principle neurons, which constitute the majority of projecting neurons in cortex (Kirkcaldie, 2012). Rabies virus often labels only a subset of projecting cells, however, this was not an issue since we did not look to quantify the strength of projections, but merely show that the anterograde projections from PPC to

other cortical areas were reciprocal. Our use of rabies virus instead of traditional retrograde tracers also gave more confined injections in PPC, and the fact that this system requires both helper and rabies viruses to co-express within the same cells greatly reduced potential confounds stemming from uptake by passing fibers. The rabies tracing confirmed reciprocal connectivity between PPC and all cortical areas examined.

Calcium imaging.

In paper 3, I used *in vivo* calcium imaging in freely behaving mice to measure correlates of neural activity in M2 and PPC with the behaviors of the animals. Calcium imaging with miniaturized microscopes (Inscopix) is a state-of-the-art technique to study neural activity of hundreds of cells simultaneously in freely moving animals, and it allowed us to study naturalistic behaviors without the need for head restraint as with primate studies or two-photon imaging in rodents. Recording large numbers of neurons simultaneously allowed us to study the population activity of neurons while the animals performed and observing the tasks in addition to quantifying activity at the single-cell level.

For calcium imaging using a genetically encoded calcium indicator (GECI), a virus, typically an AAV, is injected into the area of interest to deliver the cDNA for the GECI into specific cell types. The GECI used in this study was GCaMP6m (Chen et al., 2013). Once the expression levels of the GECI are sufficiently high (2-3 weeks post-transfection), neural activity is measured indirectly via fleeting changes in calcium concentration when neurons are active. Specifically, during bouts of heightened spiking activity, calcium ions flow into the cell where they are bound by a calcium indicator that, upon calcium binding, changes conformation and fluoresces green light when excited by blue light from the LED in the microscope. The calcium events are recorded by the microscope and are distinguished by their sharp rise and a slow decay kinetics. For the present study, I injected a GCaMP6m-virus (AAV1.Syn.GCaMP6m.WPRE.SV40) into M2 (Figure 7A, left) or PPC of adult female mice; since GCaMP6 was under the h-Syn promoter it expressed in all neuron types. After testing many different AAV serotypes and configurations (e.g. Cre-dependent variants), this was the virus that gave the strongest and most reliable expression. To minimize photo bleaching of the calcium indicator, the recording sessions were separated by at least 4 hours to allow GaMP6m to recover. The sessions lasted no longer than 40 min and were recorded with a pre-tested LED power that was sufficiently high to detect calcium signals, but low enough to keep the cells throughout the sessions.

The miniaturized microscopes were one-photon, epifluorescent microscopes, meaning that photons from more than one focal plane were collected by the sensor, making it hard to distinguish cells that partly overlapped and/or were in different z-planes. To overcome this problem, we used an

established algorithm, CNMF-e (Pnevmatikakis et al., 2016;Zhou et al., 2018) that was specialized for extracting calcium signals spatially and temporally in high-background images, and was proven efficient at finding and distinguishing cells in miniature microscope recordings. Since the spatial resolution of the one-photon microscopes was rather poor, the ideal technique would have been miniaturized two-photon microscopes. Although prototypes of these microscopes now exist (Zong et al., 2017), they are yet not commercialized. Unlike with fluorescent imaging, in two-photon imaging the fluorophore is activated by the simultaneous absorption of two long wavelength photons, which brings the advantage of no out-of-focus light, deeper penetration in the tissue and less damage to the brain (Helmchen and Denk, 2005). The images are therefore much clearer than with the one-photon fluorescent imaging we used, and it is easier to detect individual cells. However, a recent study sought to compare the results from using a bench-top two-photon or a one-photon miniaturized microscope (Glas et al., 2019). They imaged orientation tuned neurons in V1 using the two techniques, identified the same neurons in image stacks and found that the tuning properties for each neurons was highly correlated between the two techniques even if the spatial resolution of one-photon was poorer.

Another limitation of calcium imaging is the slow decay time of calcium. The GCaMP6m that I used has a faster decay time than the 'slow' variant, GCaMP6s, but lower signal-to-noise, while having higher signal-to-noise than 'fast' GCaMP6 variant, GCaMP6f (Chen et al., 2013). To account for imperfect signal in our data, we applied a signal-to-noise algorithm to distinguish true calcium events from noise based on the shape as well as the amplitude of the calcium traces. I am thus confident that the calcium events in our analyses reflected the genuine calcium dynamics in the cells.

After perfusion, cutting and staining of the brains, I delineated the areas around the injection sites and prism tract based on Nissl-stained adjacent sections. This confirmed that the calcium recordings were done within M2 and PPC, as defined in the first paper of this thesis.

GENERAL DISCUSSION

The results in paper 1 show that mouse posterior parietal cortex (PPC) has similar connectivity and thalamic connections to rat PPC. It is divided into a medial, a lateral and a posterior subdivision (mPPC, lPPC and PtP), which partly overlap with anterior parts of extrastriate areas AM, A and RL, respectively. Although not studied in detail, our approach of using triple tracer injections revealed apparent gradients in some of the projections of PPC to other cortical areas. In paper 2, we confirm this to be the case in frontal cortex in rats, where the results showed that PPC subregions are differently connected with frontal midline cortices. In particular, mPPC is more strongly connected to the caudal portion of M2 and to MO and VO of the orbitofrontal cortex (OFC), whereas lPPC and PtP preferentially connect with the intermediate anterior-posterior portion of M2 (iM2) and the medial and central parts of ventrolateral orbitofrontal cortex (VLO). In terms of connectivity and architecture, the rodent PPC seems to be heterogeneous as it is in primates, strengthening the idea that parieto-frontal network in rodents may be homologous to those in primates. With this anatomical similarity in mind, in paper 3 we tested whether neurons in these areas in mice code for both performed and observed actions like in primates. The results showed that both M2 and PPC stably encode a variety of performed actions similar to primate areas, but we found no correlates for observed behaviors in either area. Thus, the capacity for PPC and pre-motor areas to code for observed actions may constitute a functional difference between species.

Organization of the rodent PPC

To my knowledge, paper 1 in this thesis is the first to systemically describe the cyto- and chemoarchitectural features of the mouse PPC that distinguishes it from neighboring areas, and investigate whether its anatomically defined subdivisions overlap with extrastriate areas. Since the mouse cortex is smooth and lacks gross anatomical landmarks, retinotopic mapping has become an important tool for locating higher visual areas (Garrett et al., 2014) and associative regions in the posterior cortex including PPC (Olcese et al., 2013;Driscoll et al., 2017). This functional mapping is not possible without intrinsic optical imaging or a broadly expressed calcium indicator, and the location of PPC relative to these areas has not been defined. Using anterograde anatomical tracing, I found that the anatomically defined mPPC overlaps with the anterior extrastriate area AM, that lPPC overlaps with area A, and PtP with the anterior part of area RL. This fits with PPC being part of the rodent 'dorsal stream', which includes areas PM, AM, A, RL and AL (Wang et al., 2011).

The extrastriate areas are known to have different functional responses, with AM and RL preferring fast temporal frequencies and lower spatial frequencies than V1 (Marshel et al., 2011). Retinotopic mapping of A has proven difficult (Zhuang et al., 2017), as the input from V1 is weaker and, likely, less topographically organized than other areas (Wang and Burkhalter, 2007). This view is supported by our study, which points to area A being largely contained within PPC, which itself supports a variety of movement-related (McNaughton et al., 1994;Whitlock et al., 2012), navigational (Nitz, 2006;2012) and cognitive functions (Harvey et al., 2012;Morcos and Harvey, 2016;Hwang et al., 2017;Akrami et al., 2018) that do not depend on visual stimuli. Microelectrode recordings have also shown that cells in the posterior extent of the rat PCC, which likely coincide with area AM, encode multipart movement motifs, for example running followed by a right or left turn (McNaughton et al., 1994), or track an animals' progress along navigational routes (Nitz, 2006). Others have used *in vivo* calcium imaging to demonstrate that more anterior sectors of mouse PPC are involved in higher-level sensory processing and decision making, as neurons in PPC were engaged during all phases of a virtual decision making T-maze task (Harvey et al., 2012). Together, these studies make it clear that PPC is involved in behaviors beyond visual processing, although it overlaps partly with several extrastriate areas.

To my knowledge, the only prior attempt to define PPC in the mouse was by Harvey and colleagues (2012), who located mouse PPC based on retrograde anatomical tracing and Bregma coordinates. Aside from showing that the anatomical afferents matched those known in rats, however, the work did not provide further specifications for locating or distinguishing PPC from neighboring areas. Different mouse atlases also refer to PPC area with different nomenclatures (e.g. PTLp, VISa, VISam, VISrl) and the anterior-posterior extent varies between them (Paxinos and Franklin, 2012;Oh et al., 2014). For this reason, referring to Bregma coordinates as the location of function recordings appears insufficient. This is why paper 1 provides simple anatomical criteria that can be used post-hoc to define where functional recordings were performed, which is increasingly important since many studies do not show their recording locations and may refer to different parts of cortex. This could result in allocating results to incorrect cortical positions, thus hampering a consistent interpretation and usage of individual datasets.

Based on our results, mouse PPC is organized similarly as rat PPC (Olsen and Witter, 2016). Furthermore, it has the preferred thalamic projections to the lateral posterior (LP), the lateral dorsal (LD) and the posterior complex (Po) of the thalamus, although mouse PPC is smaller and does not extend as far posterior as rat PPC in which PtP extends posteriorly lateral to V2L. Whether there are functional differences between PPC and posterior AM and RL is yet to be discovered. In a recent study, mice were head-fixed in a virtual reality environment to study their visual and navigational networks in posterior cortex (Minderer et al., 2019). The results showed that behavioral feature encoding is not

confined by retinotopic borders, but rather varies smoothly across the association regions. Another study showed that area RL contains a gradient of visual and somatosensory input, in which the whiskers are dominantly represented in the most anterior part that may overlap with PtP, whereas visual information is represented posteriorly in RL (Olcese et al., 2013). Thus, to use retinotopic mapping to characterize brain areas may be insufficient, and anatomical examination of recordings sites is therefore crucial to map functional specialization in cortex.

Topographical organization of the parieto-frontal cortices in rodents

Lesion studies in rats have typically included the whole PPC, thus do not allow to draw conclusions about potential functional differences between subregions (Kolb and Walkey, 1987;DiMattia and Kesner, 1988;Save and Moghaddam, 1996;Save and Poucet, 2000). Neurophysiological studies in PPC, on the other hand, have either been confined to mPPC (Chen et al., 1994;Nitz, 2006;2012;Whitlock et al., 2012) or did not find differences in coding properties between mPPC and lPPC (Wilber et al., 2014). More recent work, however, has started to shed light on functional differences in different sectors of PPC in rats. Specifically, Mimica et al. (2018) described a functional the distribution of body posture across PPC. The authors showed that neurons in PPC and M2 encode posture for the head and back in 3D, which was organized in a topographical manner, such that representations of the back were found mainly in the medial and anterior portions of PPC and the posterior portions of M2, whereas the lateral-posterior PPC and intermediate M2 shared a predominant sensitivity to the animals' head posture (Mimica et al., 2018). This gradient of responses appears to match the preferential connectivity of mPPC subregions with posterior M2 versus lPPC and PtP with intermediate M2, as described in Paper 2. Furthermore, a very recent study by Mohan et al. (2019) reported a coarse medial-to-lateral somatotopic correspondence between specific barrel fields in S1 and the location of electrophysiological responses in PPC evoked by whisker deflections.

Though functional studies are just beginning to report subregional differences in the rodent PPC, such differences have been proposed based on differences in anatomical connectivity patterns. The connectivity of mPPC with several cortical and subcortical regions hints at it being involved in visuospatial processing. First, it is strongly connected with the posterior portion of M2, which receives more visual input than the rostral portion (Reep et al., 1990), and lesions to the posterior M2 result in spatial neglect (King and Corwin, 1990). Furthermore, microstimulation of the posterior M2 elicits oculomotor movements as well as movement of the whiskers (Donoghue and Wise, 1982;Neafsey et al., 1986;Brecht et al., 2004). Second, it is connected with cingulate area 24b, which when stimulated

elicits eye, periocular and nose movements (Brecht et al., 2004). Third, it is connected with VO, a region of the OFC that receives strong visual input and is the only subregion of the OFC that is reciprocally connected with POR (Delatour and Witter, 2002;Agster and Burwell, 2009;Kondo and Witter, 2014). The POR relays processed visual information to the medial entorhinal cortex (MEC)(Kerr et al., 2007), a region known for spatial processing (Fyhn et al., 2004;Moser et al., 2008). Finally, mPPC is connected with the lateral posterior nucleus of the thalamus (LP), a higher order visual nucleus connected to several regions involved in spatial visual processing (Reep et al., 1994;Reep and Corwin, 1999;Reep et al., 2004;Conte et al., 2008;Kamishina et al., 2008;Kamishina et al., 2009;Juavinett et al., 2019). Based on these connections and other connections, PPC has been postulated as a critical node in a circuit for directed spatial attention that includes M2 and VLO in cortex (King et al., 1989;Chandler et al., 1992;Burcham et al., 1997), the LP nucleus of the thalamus (Kamishina et al., 2009) and the dorsocentral striatum (Cheatwood et al., 2003;Reep et al., 2003). Lesions to these regions or the fiber tracts between them also result in polymodal contralateral neglect (Reep and Corwin, 2009).

Less is known, however, about specific functions distinguishing lPPC and PtP which appear to have similar connection patterns, differing from those of mPPC, with the thalamus, the parahippocampal region (Olsen et al., 2017), and frontal cortices (paper 2). Both areas preferentially connect with the intermediate portion of M2 (paper 2), where somatosensory and visual information are intermingled (Reep et al., 1990). Interestingly, the projections from lPPC and PtP appeared to terminate in the transition zone on the border between M2 and M1, a sensory-input region that has been shown to respond to whisker deflections (Smith and Alloway, 2013). mPPC, in contrast, projects to M2 proper, which does not respond to whisker reflections but is rather effective at evoking whisking.

Topographical organization and the integrated representation of actions across parietal and frontal cortices in primates

Brodmann (1909) was the first to describe the anatomy of the macaque PPC, which surrounds the intraparietal sulcus and consists of an area 5, which is the superior parietal lobule (SPL), and area 7 on the inferior parietal lobule (IPL). Since then, several researchers have further subdivided PPC into finer subregions based on connectivity, microstimulation and functional recordings (Figure 11). While areas 5 and area 7b (PF) are predominately involved in somatosensory processing, area 7a (PG) is involved in oculomotor and visual responses (Hyvärinen, 1981). A recent study showed that there is a further topography of somatosensory, visual and motor representations within the cytoarchitecturally different areas on the IPL and that these regions are involved in motor control as well as being responsive to different sensory stimuli (Rozzi et al., 2008). Anteriorly on the IPL in area PF, motor acts related to the mouth and orofacial somatosensory responses area most prominent. Representations of hand motor acts and somatosensory responses of arm and trunk are dominant in PFG, whereas reaching movements and somatosensory responses of arm and hand are most prominently presented in the posterior area PG. There are also several specialized subregions inside the intraparietal sulcus, including area MIP, which is predominantly active during reaching, LIP, which is active during saccade planning and fixation and AIP, where visuomotor and motor neurons for grasping present (Andersen and Buneo, 2002;Rozzi et al., 2008).

Based on what is known about the heterogeneity of the primate PPC, lPPC and PtP in rodents may be comparable to area 7b, which processes somatosensory information. This idea is supported by the connectivity of lPPC and PtP with the transition zone of the motor cortex and their projections to intermediate M2, which receives mainly somatosensory input (paper 2). Also, lPPC and PtP are preferentially connected with the Po complex of the thalamus, which is also strongly connected with somatosensory cortices (Vertes et al., 2015;Olsen and Witter, 2016). mPPC, contrarily, could be more similar to the predominantly visual area 7a in primates, which is supported by its preferential connectivity with posterior M2 (paper 2) and connections with LP nucleus of the thalamus (Olsen and Witter, 2016). However, functional recordings targeting the specific subregions of PPC and testing these ideas specifically will be necessary in the future to draw firm conclusions.

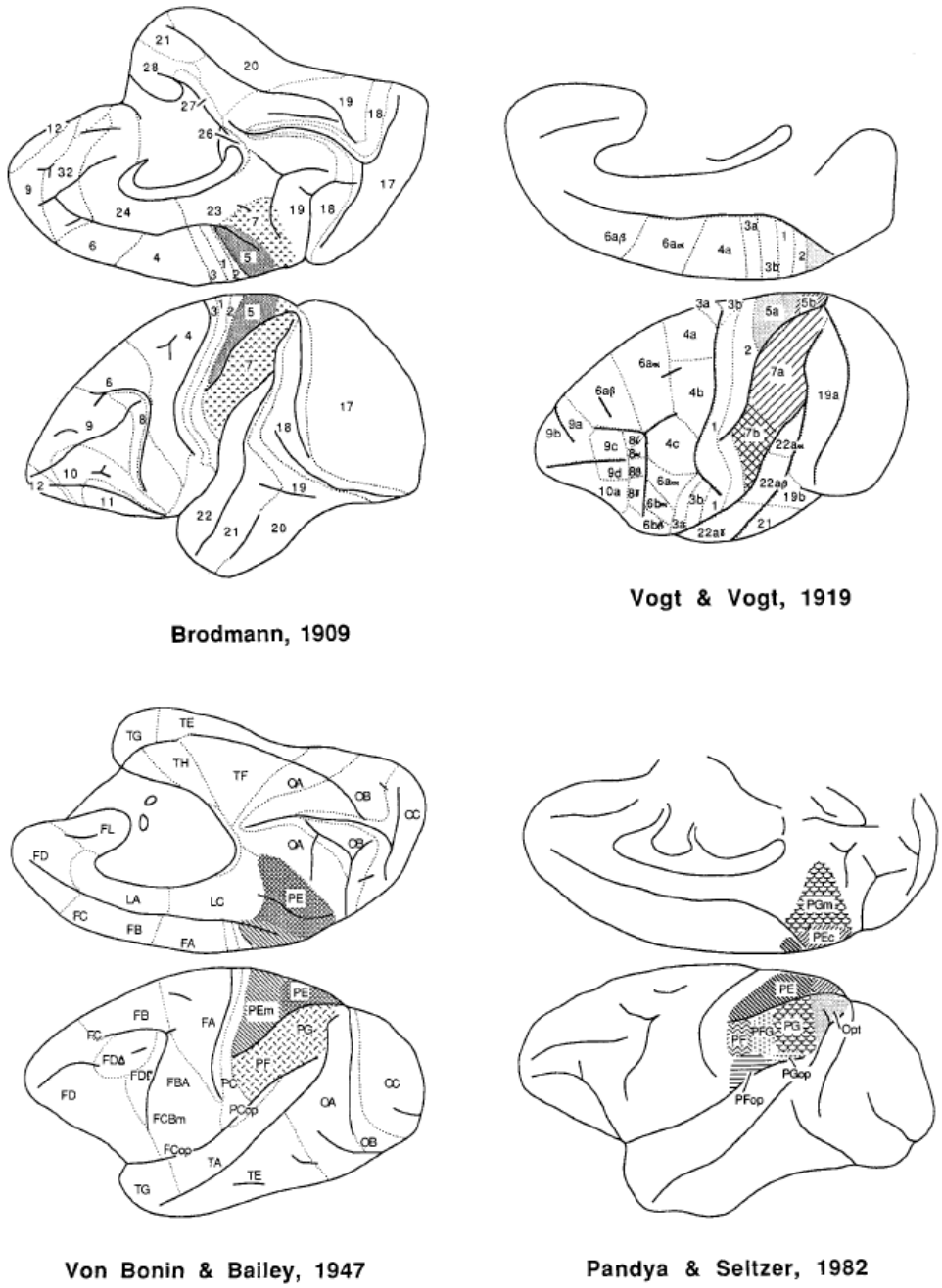

Figure 11. Different delineations of the posterior parietal cortex of primates by Brodmann (1909), Vogt and Vogt (1919), Von Bonin and Bailey (1947) and Pandya and Seltzer (1982). Adapted from Cavada and Goldman-Rakic (1989a).

Decades of anatomical and functional investigation have found that areas of PPC processing effector-specific information are linked anatomically with frontal motor areas which control the same parts of the body (see Wise et al., 1997 for review), and which show contemporaneous co-activation before or during specific movements such as reaching (Johnson et al., 1996) or moving the eyes (Pesaran et al., 2008). The macaque ventral premotor cortex (PMv) provides a classic example of this anatomical and functional pairing. It is located ventrally in front of the precentral sulcus and posterior to the arcuate sulcus, and can be subdivided into anterior and posterior areas termed 'F5' and 'F4', respectively (Matelli et al., 1985;Belmalih et al., 2009). Area F5 is strongly connected with PPC, and controls movements of the hand, arm and mouth as shown by focal electrical stimulation (Rizzolatti et al., 1988;Rizzolatti and Luppino, 2001). It consists of three cytoarchitectonically different subregions including anterior F5 (F5a), posterior F5 (F5p) and "convexity" F5 (F5c; Belmalih et al., 2009), which contain motor representations of the mouth (laterally) and hand (medially), and is important for goal-directed actions such as biting or grasping (Ferrari et al., 2017). Of particular interest is that mirror neurons were first found in the medial part of F5, which is anatomically connected with parietal areas PFG and AIP, which themselves represent reaching and grasping movements of the hand and also exhibit mirror properties. In the case of both first- and third-person action representation in the higher motor system in primates, high-order visual information enters the system via input from the superior temporal sulcus (STS), an area that encodes biological motion but does not contain the corresponding motor responses. This area feeds into posterior parietal areas PFG and AIP in the inferior parietal sulcus (IPS), which in turn project to the ventral premotor cortex. Furthermore, both F5 and AIP are connected with the prefrontal cortex, which is a region involved in the selection of stimulus and self-driven actions (Rizzolatti and Sinigaglia, 2010). A recent study recorded mirror neurons in macaque F5 and PFG (Bonini et al., 2010) and subsequently placed retrograde tracers in the two areas to confirm that they are reciprocally connected.

Although the rodent brain is less elaborate and much smaller than the macaque brain, the overall topology of visual - PPC - premotor connectivity is similar across species (Figure 12). The monkey parieto-frontal system contains a high number of subregions, of which each receives different inputs and drives specific motor outputs. Less is known about the rodent connectivity and function, although there is likely a similar, overall gradient of sensory and motor processing. In both species, higher order visual input reaches PPC and the resulting output of PPC computations is likely communicated to premotor cortex, with which it is strongly and reciprocally connected. The rodent premotor cortex/M2 seems to receive more direct visual input from higher visual areas than in the primate, which could be a result of the smaller size of the brain and the fact that distance separating each area is therefore smaller (Laramée and Boire, 2015).

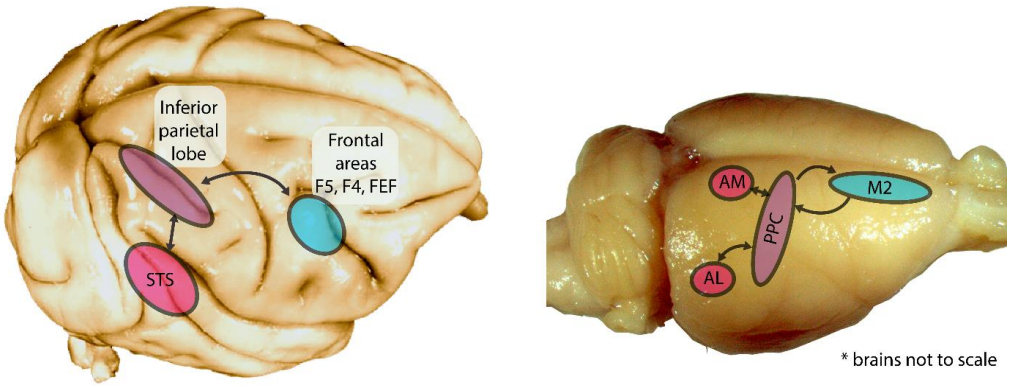

Figure 12. Topology of the visuo-parieto-frontal system in the macaque and rat. Higher visual areas are marked in pink, posterior parietal areas in purple and frontal motor areas in cyan. For abbreviations, see list of abbreviations.

Action representation in the parieto-frontal network

Neural correlates of performed actions

One of the most iconic representations of how the brain represents the body is the homunculus in primary motor and somatosensory cortices, in which the size of each body part is scaled according to its relative representation on the cortical surface (Graziano, 2016). The homunculus was mapped based on classic cortical microstimulation studies in the 1930's (Penfield and Boldrey, 1937), but in the early 2000s, Graziano and colleagues broke with this tradition and applied *prolonged* stimulation to different parts of the primate motor cortex. To their surprise, the stimulations did not produce individual muscular twitches, but instead resulted in complex, ethologically relevant, multi-effector motions such as moving the hand to the mouth or reaching to grasp (Graziano et al., 2002;Graziano, 2016). Other common actions were discovered in distinct zones in which, for example, movements of the upper body (e.g. hand-to-mouth, defense, chewing/licking) were represented in ventral motor cortex and movements of the lower body (e.g. climbing, hand in lower space) in dorsal motor cortex. This discovery led to a shift in belief from a purely somatotopic body map representation in motor cortex to that of 'ethological action maps', which represent both the body *and* the actions available in the animals' behavioral repertoire. These action maps were later found in several primate species in both motor- and posterior parietal cortices (Stepniewska et al., 2005;Stepniewska et al., 2009a;Stepniewska et al., 2009b;Gharbawie et al., 2011a;Gharbawie et al., 2011b). Furthermore, they

showed that the functionally mapped action zones in these areas are connected, including several multi-region pathways mediating reaching (Gharbawie et al., 2011b).

Both simple and more complex action maps have also been studied in rodents, where distinct frontal areas for whisking as well as grasping, reaching and other ethologically relevant actions have been described (Graziano, 2016). In addition, Brecht et al. (2004) used microstimulation to show that whisking behavior is contained in AGm (corresponding to M2), that head/body movements are represented in AGl (M1), while stimulation of the anterior or posterior cingulate cortices can evoke nose and periocular/eye movements, respectively. Most of the action map studies in rodents have focused on M1, while parallel work in M2 suggested an additional involvement in higher-order functions, such as enabling choice behavior by mapping antecedent sensory cues onto motor actions (Barthas and Kwan, 2017). This seems in line with the overall connectivity matrix known for M2, which is reciprocally connected with visual, somatosensory, parietal and retrosplenial areas, projects to several subcortical nuclei involved in motor behaviors, and has been linked to learning, decision-making and the use of sequences of actions (Barthas and Kwan, 2017).

Since many of the previous investigations of motor actions in rodents were executed in anesthetized animals or in the confines of restrictive tasks (Brecht et al., 2004;Rubin et al., 2019), paper 3 in this thesis sought to add to this knowledge by recording neuronal population activity in freely behaving mice that were allowed to engage in a variety of naturalistic actions. This allowed us to show that both M2 and PPC in mice stably encode a variety of performed behaviors, including grasping a food pellet (referred to as 'grasping'), eating, nose poke, rearing, turning clockwise (CW) and turning counterclockwise (CCW). In general, the proportions of cells coding for each behavior varied slightly between M2 and PPC, such that turning was well represented in both brain areas, whereas grasping was more prevalent in M2 and rearing was more prevalent in PPC, respectively. Due to limitations in the temporal precision of calcium imaging, we did not distinguish between the reaching and grasping components, and the fact that we did not image PPC and M2 simultaneously leaves open the question as to whether PPC, M2 or both code for the various stages of such movements. The caudal forelimb area, which is implicated in reaching, is located at the same anterior-posterior level as we recorded in M2, however, it is positioned more laterally in M1 (Ramanathan et al., 2006), yet we nevertheless found that the largest fraction of coding cells in M2 were tuned to reaching and grasping movements in recordings. More detailed analyses will be needed to characterize whether the cells were tuned to specific phases of reaching or grasping (e.g. raising the paw vs. bringing food to the mouth), or if the cells were rather tuned to the positioning of the head or trunk associated with reaching behavior. For the time being it remains an open question, as we counted 'grasping' events as beginning when the paw was lifted off the floor of the box and ending just as the animal started to withdraw the food from

the hole. We also found that around 15% of cells stably encoded more than one action, and that cells encoding different actions were anatomically dispersed among each other (paper 3). The heterogeneity of behavioral coding in PPC is also consistent with previous studies on decision-making (Raposo et al., 2014) and multisensory integration (Lippert et al., 2013) in rodents.

Macroscopic functional clustering is a hallmark of motor cortex in mammals, in that different subregions have been found to control different muscles (Asanuma and Rosen, 1972), the direction of hand movements (Georgopoulos et al., 1982) or ethologically related behaviors (Graziano et al., 2002). To study whether this holds at a cellular level in mice, a prior study by Dombeck et al. (2009) recorded calcium transients in mobile, head-fixed animals and found evidence for spatial intermingling of neurons in forelimb motor cortex during grooming and running. Consistent with this, we did not find spatial clustering of neurons coding for different behaviors in M2 or PPC (paper 3) but, unlike the Dombeck et al. (2009) study, we did not check for functional clustering of co-active cells. Whether or not that is the case with our data remains an open question. Notably, the absence of spatial clustering for the identified behaviors in these 'higher' motor areas is consistent with the absence of functional clustering of orientation selectivity in the rodent primary visual cortex (Ohki et al., 2005) and olfactory coding in the piriform cortex (Stettler and Axel, 2009).

Neural correlates of observed actions

One remarkable feature of mirror neurons in the primate parieto-frontal network, is the ability to encode not only performed, but also observed actions (Gallese et al., 1996;Fogassi et al., 2005). The parieto-frontal network supports a variety of functions necessary for goal-directed behaviors such as action planning, sensorimotor integration and decision-making (Andersen and Cui, 2009;Suzuki et al., 2015). An increasing number of studies has shown that the parieto-frontal network in rats and mice also is involved in higher cognitive functions such as decision-making (Raposo et al., 2014;Erlich et al., 2015), evidence accumulation (Hanks et al., 2015) and sensorimotor integration (Harvey et al., 2012), which for decades were studied mainly in primates. As in primates, PCC in rodents is strongly and reciprocally connected with M2 (Figure 12), and these connections are topographically organized (paper 2), meaning the similarities between the parieto-frontal pathway in rodents and primates are anatomical as well as functional. Also similar to primates, PPC and M2 both receive visual input from higher visual areas (AL, RL, AM, PM) as part of the dorsal stream (Wang et al., 2012), and have descending projections to the spinal cord and subcortical motor centers (Donoghue and Wise, 1982;Miller, 1987;Barthas and Kwan, 2017). The similarity of anatomical connections and the involvement of these areas in cognitive tasks could hint toward a role for these areas in action

recognition in rodents, similar to the representation of observed behaviors in primates (Gallese et al., 1996;Fogassi et al., 2005). In testing this idea, we recorded from hundreds of neurons in PPC and M2, specifically targeting the regions that interconnect with each other, while the animals performed and observed different naturalistic actions in two behavioral tasks. Although we did not see any correlates for observed behavior in either M2 or PPC (paper 3), and therefore no mirror neurons, it does not necessarily mean that mice do not have mirror neurons. A recent paper did tetrode recordings and reported emotional mirror-like neurons related to pain processing in the cingulate cortex of rats (Carrillo et al., 2019). That is, these neurons were activated both when a rat experienced pain applied by a laser to the paw and while observing another rat receive foot shocks (though it is notable that the study did not control for the sound of pain-evoked squeaks emitted by observers and demonstrators). It may conceivably be the case that the actions we studied were not appropriate to elicit neural activity in the observer, or that representations of observed and performed actions genuinely do not converge on the same neurons in PPC and M2 of mice. If the latter were the case, sensorimotor observational learning as described in mice (Carlier and Jamon, 2006;Jurado-Parras et al., 2012) may be facilitated by non-mirror-like associative mechanisms.

It is also possible that the negative results for action observation could stem from inappropriate task design or the behaviors we considered, though we noted over the course of the project that grasping to eat food was a natural behavior that the mice did without prior training in their home cages. Moreover, this behavior was encoded by the highest percentage of neurons in M2. Alternative experiments could have relied on more salient and basic behaviors like maternal caring behavior or fighting. If we can assume that at least some of the behaviors studied were comprehensible to observer animals, we are left with questions about the perceptual processing capacities of head-fixed mice. For example, is it possible for mouse mice to distinguish fast and fine scaled movements? While we did not task the observers with reporting behaviorally that they had observed an action, the distance separating the performers and observers in both tasks (~10-20cm; Figure 1, paper 3) was comparable to prior studies demonstrating sensorimotor observational learning in mice, including lever-pressing (Jurado-Parras et al., 2012) or manipulating a metal tab to retrieve food from a box (Carlier and Jamon, 2006). Moreover, at distances of 10-20cm, the relative size of the demonstrator animals in the observers' visual field was well above the measured threshold for visual behavioral acuity in wild-type mice (Gianfranceschi et al., 1999;Prusky et al., 2000). Based on this, and the fact that PPC cells responded reliably to forceps placing food in the pellet-reaching box, we conclude that the demonstrated behaviors, particularly larger behaviors like rearing, turning, grooming or eating, were likely within the perceptual capacity of the observers' visual systems.

Another factor is that the observer animals were head-fixed, which may have been stressful, and one can argue that it is challenging to determine whether the animals were paying attention to the behavior of the demonstrators. To rule out this possibility, I used the pupil diameter of three observer animals as a proxy for attention (Hoeks and Levelt, 1993;Reimer et al., 2014), and redid the analysis on only those parts of the recording when the pupils of the observers were dilating or at maximal dilation (indicative of an aroused state), but this did not uncover any observational correlates. More recent work demonstrated that the neural activity of socially interacting animals was synchronized and correlated (Kingsbury et al., 2019), suggesting that it may be necessary for mice to interact physically to show socially-driven neural responses. However, it would be very challenging in that case to determine whether neural activity in one animal is due to its own movement or due to the observation of another animal's behavior. This is precisely why the paradigm with head-fixation was utilized in paper 3. Yet another possibility is that the neural coding of observed actions happens in other parts of the brain which were not recorded, such as area AL or the caudal extent of AM, which also receive strong visual input and project in turn to M2 (Wang et al., 2012; paper 1). Another candidate area could be the ACC, the neighboring region of M2 that also receives visual input and, when stimulated, elicits eye, periocular and nose movements (Brecht et al., 2004). Such recordings could indeed be the topic of future investigations.

CONCLUDING REMARKS

In this thesis, I have shown that the mouse PPC is composed of three architectonically defined subdivisions, which overlap with anterior portions of extrastriate areas. The mouse PPC projects to the same thalamic nuclei and has the same reciprocal connectivity with other cortical areas as PPC of the rat. I further showed that PPC-frontal connections are topographically organized in the rat, in particular the connectivity with M2, which supports the notion of subdivisions within PPC. This prompted the final study in the thesis that tested whether neurons in mouse M2 and PPC encode performed as well as observed actions, like in primates. We found that neurons in M2 and PPC encode several naturalistic performed, but not observed, behaviors.

Taken together, I conclude that the rodent PPC is a heterogeneous region, which although overlapping partly with extrastriate areas, supports a variety of cognitive functions beyond visual processing. The heterogeneity of connections between PPC and frontal areas is comparable to that of the primate. Although rodents are capable of cognitive functions including basic forms of empathy and sensorimotor learning, there are limits to the functional similarity of PPC and frontal cortices in rodents and primates. This suggests that sensorimotor observational learning in mice may be facilitated by non-mirror-like associative mechanisms, or may take place in networks that do not include the parts of PPC and M2 recorded here.

REFERENCES

Agster, K.L., and Burwell, R.D. (2009). Cortical efferents of the perirhinal, postrhinal, and entorhinal cortices of the rat. *Hippocampus* 19**,** 1159-1186.

Akrami, A., Kopec, C.D., Diamond, M.E., and Brody, C.D. (2018). Posterior parietal cortex represents sensory history and mediates its effects on behaviour. *Nature* 554**,** 368-372.

Andersen, R.A. (1997). Multimodal integration for the representation of space in the posterior parietal cortex. *Philos Trans R Soc Lond B Biol Sci* 352**,** 1421-1428.

Andersen, R.A., Asanuma, C., Essick, G., and Siegel, R.M. (1990). Corticocortical connections of anatomically and physiologically defined subdivisions within the inferior parietal lobule. *J Comp Neurol* 296**,** 65-113.

Andersen, R.A., and Buneo, C.A. (2002). Intentional maps in posterior parietal cortex. *Annu Rev Neurosci* 25**,** 189-220.

Andersen, R.A., and Cui, H. (2009). Intention, action planning, and decision making in parietal-frontal circuits. *Neuron* 63**,** 568-583.

Andersen, R.A., Essick, G.K., and Siegel, R.M. (1987). Neurons of area 7 activated by both visual stimuli and oculomotor behavior. *Exp Brain Res* 67**,** 316-322.

Asanuma, H., and Rosen, I. (1972). Functional role of afferent inputs to the monkey motor cortex. *Brain Res* 40**,** 3-5.

Barthas, F., and Kwan, A.C. (2017). Secondary Motor Cortex: Where 'Sensory' Meets 'Motor' in the Rodent Frontal Cortex. *Trends Neurosci* 40**,** 181-193.

Belmalih, A., Borra, E., Contini, M., Gerbella, M., Rozzi, S., and Luppino, G. (2009). Multimodal architectonic subdivision of the rostral part (area F5) of the macaque ventral premotor cortex. *J Comp Neurol* 512**,** 183-217.

Bonini, L., Rozzi, S., Serventi, F.U., Simone, L., Ferrari, P.F., and Fogassi, L. (2010). Ventral premotor and inferior parietal cortices make distinct contribution to action organization and intention understanding. *Cereb Cortex* 20**,** 1372-1385.

Brandt, H.M., and Apkarian, A.V. (1992). Biotin-dextran: a sensitive anterograde tracer for neuroanatomic studies in rat and monkey. *J Neurosci Methods* 45**,** 35-40.

Brecht, M., Krauss, A., Muhammad, S., Sinai-Esfahani, L., Bellanca, S., and Margrie, T.W. (2004). Organization of rat vibrissa motor cortex and adjacent areas according to cytoarchitectonics, microstimulation, and intracellular stimulation of identified cells. *J Comp Neurol* 479**,** 360-373.

Brodmann, K. (1909). *Vergleichende Lokalisationslehre der Großhirnrinde in ihren Prinzipien dargestellt auf Grund des Zellenbaues.* Leipzig: Barth Verlag

Broussard, J., Sarter, M., and Givens, B. (2006). Neuronal correlates of signal detection in the posterior parietal cortex of rats performing a sustained attention task. *Neuroscience* 143**,** 407-417.

Brunton, B.W., Botvinick, M.M., and Brody, C.D. (2013). Rats and humans can optimally accumulate evidence for decision-making. *Science* 340**,** 95-98.

Burcham, K.J., Corwin, J.V., Stoll, M.L., and Reep, R.L. (1997). Disconnection of medial agranular and posterior parietal cortex produces multimodal neglect in rats. *Behav Brain Res* 86**,** 41-47.

Burwell, R.D., and Amaral, D.G. (1998a). Cortical afferents of the perirhinal, postrhinal, and entorhinal cortices of the rat. *J Comp Neurol* 398**,** 179-205.

Burwell, R.D., and Amaral, D.G. (1998b). Perirhinal and postrhinal cortices of the rat: interconnectivity and connections with the entorhinal cortex. *J Comp Neurol* 391**,** 293-321.

Carlén, M. (2017). What constitutes the prefrontal cortex? *Science* 358**,** 478-482.

Carlier, P., and Jamon, M. (2006). Observational learning in C57BL/6j mice. *Behav Brain Res* 174**,** 125-131.

Carrillo, M., Han, Y., Migliorati, F., Liu, M., Gazzola, V., and Keysers, C. (2019). Emotional Mirror Neurons in the Rat's Anterior Cingulate Cortex. *Curr Biol* 29**,** 1301-1312.e1306.

Cavada, C., and Goldman-Rakic, P.S. (1989a). Posterior parietal cortex in rhesus monkey: I. Parcellation of areas based on distinctive limbic and sensory corticocortical connections. *J Comp Neurol* 287**,** 393-421.

Cavada, C., and Goldman-Rakic, P.S. (1989b). Posterior parietal cortex in rhesus monkey: II. Evidence for segregated corticocortical networks linking sensory and limbic areas with the frontal lobe. *J Comp Neurol* 287**,** 422-445.

Chandler, H.C., King, V., Corwin, J.V., and Reep, R.L. (1992). Thalamocortical connections of rat posterior parietal cortex. *Neurosci Lett* 143**,** 237-242.

Cheatwood, J.L., Reep, R.L., and Corwin, J.V. (2003). The associative striatum: cortical and thalamic projections to the dorsocentral striatum in rats. *Brain Res* 968**,** 1-14.

Chen, L.L., Lin, L.H., Green, E.J., Barnes, C.A., and Mcnaughton, B.L. (1994). Head-direction cells in the rat posterior cortex. I. Anatomical distribution and behavioral modulation. *Exp Brain Res* 101**,** 8-23.

Chen, S., and Aston-Jones, G. (1998). Axonal collateral-collateral transport of tract tracers in brain neurons: false anterograde labelling and useful tool. *Neuroscience* 82**,** 1151-1163.

Chen, T.W., Wardill, T.J., Sun, Y., Pulver, S.R., Renninger, S.L., Baohan, A., Schreiter, E.R., Kerr, R.A., Orger, M.B., Jayaraman, V., Looger, L.L., Svoboda, K., and Kim, D.S. (2013). Ultrasensitive fluorescent proteins for imaging neuronal activity. *Nature* 499**,** 295-300.

Condé, F., Maire-Lepoivre, E., Audinat, E., and Crépel, F. (1995). Afferent connections of the medial frontal cortex of the rat. II. Cortical and subcortical afferents. *J Comp Neurol* 352**,** 567-593.

Conte, W.L., Kamishina, H., Corwin, J.V., and Reep, R.L. (2008). Topography in the projections of lateral posterior thalamus with cingulate and medial agranular cortex in relation to circuitry for directed attention and neglect. *Brain Res* 1240**,** 87-95.

Delatour, B., and Witter, M.P. (2002). Projections from the parahippocampal region to the prefrontal cortex in the rat: evidence of multiple pathways. *Eur J Neurosci* 15**,** 1400-1407.

Dimattia, B.V., and Kesner, R.P. (1988). Role of the posterior parietal association cortex in the processing of spatial event information. *Behav Neurosci* 102**,** 397-403.

Dombeck, D.A., Graziano, M.S., and Tank, D.W. (2009). Functional clustering of neurons in motor cortex determined by cellular resolution imaging in awake behaving mice. *J Neurosci* 29**,** 13751-13760.

Donoghue, J.P., and Wise, S.P. (1982). The motor cortex of the rat: cytoarchitecture and microstimulation mapping. *J Comp Neurol* 212**,** 76-88.

Driscoll, L.N., Pettit, N.L., Minderer, M., Chettih, S.N., and Harvey, C.D. (2017). Dynamic Reorganization of Neuronal Activity Patterns in Parietal Cortex. *Cell* 170**,** 986-999.e916.

Erlich, J.C., Bialek, M., and Brody, C.D. (2011). A cortical substrate for memory-guided orienting in the rat. *Neuron* 72**,** 330-343.

Erlich, J.C., Brunton, B.W., Duan, C.A., Hanks, T.D., and Brody, C.D. (2015). Distinct effects of prefrontal and parietal cortex inactivations on an accumulation of evidence task in the rat. *Elife* 4**,** e05457.

Ferrari, P.F., Gerbella, M., Coude, G., and Rozzi, S. (2017). Two different mirror neuron networks: The sensorimotor (hand) and limbic (face) pathways. *Neuroscience* 358**,** 300-315.

Fogassi, L., Ferrari, P.F., Gesierich, B., Rozzi, S., Chersi, F., and Rizzolatti, G. (2005). Parietal lobe: from action organization to intention understanding. *Science* 308**,** 662-667.

Fyhn, M., Molden, S., Witter, M.P., Moser, E.I., and Moser, M.B. (2004). Spatial representation in the entorhinal cortex. *Science* 305**,** 1258-1264.

Gallese, V., Fadiga, L., Fogassi, L., and Rizzolatti, G. (1996). Action recognition in the premotor cortex. *Brain* 119 (Pt 2)**,** 593-609.

Garrett, M.E., Nauhaus, I., Marshel, J.H., and Callaway, E.M. (2014). Topography and areal organization of mouse visual cortex. *J Neurosci* 34**,** 12587-12600.

Georgopoulos, A.P., Kalaska, J.F., Caminiti, R., and Massey, J.T. (1982). On the relations between the direction of two-dimensional arm movements and cell discharge in primate motor cortex. *J Neurosci* 2**,** 1527-1537.

Gharbawie, O.A., Stepniewska, I., and Kaas, J.H. (2011a). Cortical connections of functional zones in posterior parietal cortex and frontal cortex motor regions in new world monkeys. *Cereb Cortex* 21**,** 1981-2002.

Gharbawie, O.A., Stepniewska, I., Qi, H., and Kaas, J.H. (2011b). Multiple Parietal–Frontal Pathways Mediate Grasping in Macaque Monkeys. *J Neurosci.*31**,** 11660.

Gianfranceschi, L., Fiorentini, A., and Maffei, L. (1999). Behavioural visual acuity of wild type and bcl2 transgenic mouse. *Vision Research* 39**,** 569-574.

Giannetti, S., and Molinari, M. (2002). Cerebellar input to the posterior parietal cortex in the rat. *Brain Res Bull* 58**,** 481-489.

Glas, A., Hübener, M., Bonhoeffer, T., and Goltstein, P.M. (2019). Benchmarking miniaturized microscopy against two-photon calcium imaging using single-cell orientation tuning in mouse visual cortex. *PloS one* 14**,** e0214954-e0214954.

Goodale, M.A. (2011). Transforming vision into action. *Vision Res* 51**,** 1567-1587.

Goodale, M.A., and Milner, A.D. (1992). Separate visual pathways for perception and action. *Trends Neurosci* 15**,** 20-25.

Graziano, M.S. (2016). Ethological Action Maps: A Paradigm Shift for the Motor Cortex. *Trends Cogn Sci* 20**,** 121-132.

Graziano, M.S., Taylor, C.S., and Moore, T. (2002). Complex movements evoked by microstimulation of precentral cortex. *Neuron* 34**,** 841-851.

Hanks, T.D., Kopec, C.D., Brunton, B.W., Duan, C.A., Erlich, J.C., and Brody, C.D. (2015). Distinct relationships of parietal and prefrontal cortices to evidence accumulation. *Nature* 520**,** 220-223.

Harvey, C.D., Coen, P., and Tank, D.W. (2012). Choice-specific sequences in parietal cortex during a virtual-navigation decision task. *Nature* 484**,** 62-68.

Hegstad, A.M. (2019). *Anatomical organization of visuomotor projection pathways in mouse cortex.* MSc Neuroscience, Norwegian University of Science and Technology.

Helmchen, F., and Denk, W. (2005). Deep tissue two-photon microscopy. *Nature Methods* 2**,** 932-940.

Hoeks, B., and Levelt, W.J.M. (1993). Pupillary dilation as a measure of attention: a quantitative system analysis. *Behavior Research Methods, Instruments, & Computers* 25**,** 16-26.

Hoover, W.B., and Vertes, R.P. (2007). Anatomical analysis of afferent projections to the medial prefrontal cortex in the rat. *Brain Struct Funct* 212**,** 149-179.

Hoover, W.B., and Vertes, R.P. (2011). Projections of the medial orbital and ventral orbital cortex in the rat. *J Comp Neurol* 519**,** 3766-3801.

Hwang, E.J., Dahlen, J.E., Mukundan, M., and Komiyama, T. (2017). History-based action selection bias in posterior parietal cortex. *Nat Commun* 8**,** 1242.

Hyvärinen, J. (1981). Regional distribution of functions in parietal association area 7 of the monkey. *Brain Res* 206**,** 287-303.

Iacoboni, M., and Mazziotta, J.C. (2007). Mirror neuron system: basic findings and clinical applications. *Ann Neurol* 62**,** 213-218.

Johnson, P.B., Ferraina, S., Bianchi, L., and Caminiti, R. (1996). Cortical networks for visual reaching: physiological and anatomical organization of frontal and parietal lobe arm regions. *Cereb Cortex* 6**,** 102-119.

Jones, E.G. (2007). *The thalamus.* Cambridge: Cambridge University Press.

Juavinett, A.L., Kim, E.J., Collins, H.C., and Callaway, E.M. (2019). A systematic topographical relationship between mouse lateral posterior thalamic neurons and their visual cortical projection targets. *J Comp Neurol*.

Jurado-Parras, M.T., Gruart, A., and Delgado-Garcia, J.M. (2012). Observational learning in mice can be prevented by medial prefrontal cortex stimulation and enhanced by nucleus accumbens stimulation. *Learn Mem* 19**,** 99-106.
Kamishina, H., Conte, W.L., Patel, S.S., Tai, R.J., Corwin, J.V., and Reep, R.L. (2009). Cortical connections of the rat lateral posterior thalamic nucleus. *Brain Res* 1264**,** 39-56.
Kamishina, H., Yurcisin, G.H., Corwin, J.V., and Reep, R.L. (2008). Striatal projections from the rat lateral posterior thalamic nucleus. *Brain Res* 1204**,** 24-39.
Kerr, K.M., Agster, K.L., Furtak, S.C., and Burwell, R.D. (2007). Functional neuroanatomy of the parahippocampal region: the lateral and medial entorhinal areas. *Hippocampus* 17**,** 697-708.
King, V., and Corwin, J.V. (1990). Neglect following unilateral ablation of the caudal but not the rostral portion of medial agranular cortex of the rat and the therapeutic effect of apomorphine. *Behav Brain Res* 37**,** 169-184.
King, V., Corwin, J.V., and Reep, R.L. (1989). Production and characterization of neglect in rats with unilateral lesions of ventrolateral orbital cortex. *Exp Neurol* 105**,** 287-299.
Kingsbury, L., Huang, S., Wang, J., Gu, K., Golshani, P., Wu, Y.E., and Hong, W. (2019). Correlated Neural Activity and Encoding of Behavior across Brains of Socially Interacting Animals. *Cell* 178**,** 429-446.e416.
Kirkcaldie, M.T.K. (2012). "Neocortex. In: Watson C, Paxinos G, Puelles L (Eds). *The Mouse Nervous System*," in *The Mouse Nervous System*. Academic Press., 52–111.
Kolb, B., and Walkey, J. (1987). Behavioural and anatomical studies of the posterior parietal cortex in the rat. *Behav Brain Res* 23**,** 127-145.
Kondo, H., and Witter, M.P. (2014). Topographic organization of orbitofrontal projections to the parahippocampal region in rats. *J Comp Neurol* 522**,** 772-793.
Krieg, W.J. (1946). Connections of the cerebral cortex; the albino rat; structure of the cortical areas. *J Comp Neurol* 84**,** 277-323.
Krumin, M., Lee, J.J., Harris, K.D., and Carandini, M. (2018). Decision and navigation in mouse parietal cortex. *eLife* 7**,** e42583.
Lanciego, J.L., and Wouterlood, F.G. (2011). A half century of experimental neuroanatomical tracing. *J Chem Neuroanat* 42**,** 157-183.
Laramée, M.-E., and Boire, D. (2015). Visual cortical areas of the mouse: comparison of parcellation and network structure with primates. *Front Neural Circuits* 8.
Lashley, K.S. (1941). Thalamo-cortical connections of the rat's brain *J Comp Neurol* 75**,** 55.
Lippert, M.T., Takagaki, K., Kayser, C., and Ohl, F.W. (2013). Asymmetric multisensory interactions of visual and somatosensory responses in a region of the rat parietal cortex. *PLoS One* 8**,** e63631.
Marshel, J.H., Garrett, M.E., Nauhaus, I., and Callaway, E.M. (2011). Functional specialization of seven mouse visual cortical areas. *Neuron* 72**,** 1040-1054.
Matelli, M., Luppino, G., and Rizzolatti, G. (1985). Patterns of cytochrome oxidase activity in the frontal agranular cortex of the macaque monkey. *Behav Brain Res* 18**,** 125-136.
Mcnaughton, B.L., Mizumori, S.J., Barnes, C.A., Leonard, B.J., Marquis, M., and Green, E.J. (1994). Cortical representation of motion during unrestrained spatial navigation in the rat. *Cereb Cortex* 4**,** 27-39.
Miller, E.K., and Cohen, J.D. (2001). An integrative theory of prefrontal cortex function. *Annu Rev Neurosci* 24**,** 167-202.
Miller, M.W. (1987). The origin of corticospinal projection neurons in rat. *Exp Brain Res* 67**,** 339-351.
Mimica, B., Dunn, B.A., Tombaz, T., Bojja, V., and Whitlock, J.R. (2018). Efficient cortical coding of 3D posture in freely behaving rats. *Science* 362**,** 584-589.
Minderer, M., Brown, K.D., and Harvey, C.D. (2019). The Spatial Structure of Neural Encoding in Mouse Posterior Cortex during Navigation. *Neuron* 102**,** 232-248.e211.

Mohan, H., De Haan, R., Broersen, R., Pieneman, A.W., Helmchen, F., Staiger, J.F., Mansvelder, H.D., and De Kock, C.P.J. (2019). Functional architecture and encoding of tactile sensorimotor behavior in rat posterior parietal cortex. *J Neurosci*, 0693-0619.

Mohan, H., Gallero-Salas, Y., Carta, S., Sacramento, J., Laurenczy, B., Sumanovski, L.T., De Kock, C.P.J., Helmchen, F., and Sachidhanandam, S. (2018). Sensory representation of an auditory cued tactile stimulus in the posterior parietal cortex of the mouse. *Sci rep* 8, 7739-7739.

Montero, V.M. (1993). Retinotopy of cortical connections between the striate cortex and extrastriate visual areas in the rat. *Exp Brain Res* 94, 1-15.

Montero, V.M., Rojas, A., and Torrealba, F. (1973). Retinotopic organization of striate and peristriate visual cortex in the albino rat. *Brain Res* 53, 197-201.

Morcos, A.S., and Harvey, C.D. (2016). History-dependent variability in population dynamics during evidence accumulation in cortex. *Nat Neurosci.*

Moser, E.I., Kropff, E., and Moser, M.B. (2008). Place cells, grid cells, and the brain's spatial representation system. *Annu Rev Neurosci* 31, 69-89.

Mukamel, R., Ekstrom, A.D., Kaplan, J., Iacoboni, M., and Fried, I. (2010). Single-neuron responses in humans during execution and observation of actions. *Curr biol: CB* 20, 750-756.

Neafsey, E.J., Bold, E.L., Haas, G., Hurley-Gius, K.M., Quirk, G., Sievert, C.F., and Terreberry, R.R. (1986). The organization of the rat motor cortex: a microstimulation mapping study. *Brain Res* 396, 77-96.

Neal, J.W., Pearson, R.C., and Powell, T.P. (1990). The connections of area PG, 7a, with cortex in the parietal, occipital and temporal lobes of the monkey. *Brain Res* 532, 249-264.

Nitz, D.A. (2006). Tracking route progression in the posterior parietal cortex. *Neuron* 49, 747-756.

Nitz, D.A. (2012). Spaces within spaces: rat parietal cortex neurons register position across three reference frames. *Nat Neurosci* 15, 1365-1367.

Oh, S.W., Harris, J.A., Ng, L., Winslow, B., Cain, N., Mihalas, S., Wang, Q., Lau, C., Kuan, L., Henry, A.M., Mortrud, M.T., Ouellette, B., Nguyen, T.N., Sorensen, S.A., Slaughterbeck, C.R., Wakeman, W., Li, Y., Feng, D., Ho, A., Nicholas, E., Hirokawa, K.E., Bohn, P., Joines, K.M., Peng, H., Hawrylycz, M.J., Phillips, J.W., Hohmann, J.G., Wohnoutka, P., Gerfen, C.R., Koch, C., Bernard, A., Dang, C., Jones, A.R., and Zeng, H. (2014). A mesoscale connectome of the mouse brain. *Nature* 508, 207-214.

Ohki, K., Chung, S., Ch'ng, Y.H., Kara, P., and Reid, R.C. (2005). Functional imaging with cellular resolution reveals precise micro-architecture in visual cortex. *Nature* 433, 597-603.

Olavarria, J., Mignano, L.R., and Van Sluyters, R.C. (1982). Pattern of extrastriate visual areas connecting reciprocally with striate cortex in the mouse. *Exp Neurol* 78, 775-779.

Olcese, U., Iurilli, G., and Medini, P. (2013). Cellular and synaptic architecture of multisensory integration in the mouse neocortex. *Neuron* 79, 579-593.

Olsen, G.M., Ohara, S., Iijima, T., and Witter, M.P. (2017). Parahippocampal and retrosplenial connections of rat posterior parietal cortex. *Hippocampus* 27, 335-358.

Olsen, G.M., and Witter, M.P. (2016). The posterior parietal cortex of the rat: architectural delineation and thalamic differentiation. *J Comp Neurol*.

Panksepp, J.B., and Lahvis, G.P. (2011). Rodent empathy and affective neuroscience. *Neurosci Biobehav Rev* 35, 1864-1875.

Paxinos, G., and Franklin, K.B.J. (2012). *Paxinos and Franklin's the Mouse Brain in Stereotaxic Coordinates.* Elsevier Science.

Penfield, W., and Boldrey, E. (1937). Somatic motor and sensory representation in the cerebreal cortex of man as studied by electrical stimulation *Brain* 60, 389-443.

Pesaran, B., Nelson, M.J., and Andersen, R.A. (2008). Free choice activates a decision circuit between frontal and parietal cortex. *Nature* 453, 406-409.

Pnevmatikakis, E.A., Soudry, D., Gao, Y., Machado, T.A., Merel, J., Pfau, D., Reardon, T., Mu, Y., Lacefield, C., Yang, W., Ahrens, M., Bruno, R., Jessell, T.M., Peterka, D.S., Yuste, R., and

Paninski, L. (2016). Simultaneous Denoising, Deconvolution, and Demixing of Calcium Imaging Data. *Neuron* 89**,** 285-299.
Prather, J.F., Peters, S., Nowicki, S., and Mooney, R. (2008). Precise auditory-vocal mirroring in neurons for learned vocal communication. *Nature* 451**,** 305-310.
Prusky, G.T., West, P.W., and Douglas, R.M. (2000). Behavioral assessment of visual acuity in mice and rats. *Vision Res* 40**,** 2201-2209.
Ramanathan, D., Conner, J.M., and Tuszynski, M.H. (2006). A form of motor cortical plasticity that correlates with recovery of function after brain injury. *Proc Natl Acad Sci U S A* 103**,** 11370-11375.
Raposo, D., Kaufman, M.T., and Churchland, A.K. (2014). A category-free neural population supports evolving demands during decision-making. *Nat Neurosci* 17**,** 1784-1792.
Raposo, D., Sheppard, J.P., Schrater, P.R., and Churchland, A.K. (2012). Multisensory decision-making in rats and humans. *J Neurosci* 32**,** 3726-3735.
Reep, R.L., Chandler, H.C., King, V., and Corwin, J.V. (1994). Rat posterior parietal cortex: topography of corticocortical and thalamic connections. *Exp Brain Res* 100**,** 67-84.
Reep, R.L., Cheatwood, J.L., and Corwin, J.V. (2003). The associative striatum: organization of cortical projections to the dorsocentral striatum in rats. *J Comp Neurol* 467**,** 271-292.
Reep, R.L., and Corwin, J.V. (1999). Topographic organization of the striatal and thalamic connections of rat medial agranular cortex. *Brain Res* 841**,** 43-52.
Reep, R.L., and Corwin, J.V. (2009). Posterior parietal cortex as part of a neural network for directed attention in rats. *Neurobiol Learn Mem* 91**,** 104-113.
Reep, R.L., Corwin, J.V., Cheatwood, J.L., Van Vleet, T.M., Heilman, K.M., and Watson, R.T. (2004). A rodent model for investigating the neurobiology of contralateral neglect. *Cogn Behav Neurol* 17**,** 191-194.
Reep, R.L., Corwin, J.V., Hashimoto, A., and Watson, R.T. (1984). Afferent connections of medial precentral cortex in the rat. *Neurosci Lett* 44**,** 247-252.
Reep, R.L., Corwin, J.V., Hashimoto, A., and Watson, R.T. (1987). Efferent connections of the rostral portion of medial agranular cortex in rats. *Brain Res Bull* 19**,** 203-221.
Reep, R.L., Corwin, J.V., and King, V. (1996). Neuronal connections of orbital cortex in rats: topography of cortical and thalamic afferents. *Exp Brain Res* 111**,** 215-232.
Reep, R.L., Goodwin, G.S., and Corwin, J.V. (1990). Topographic organization in the corticortical connections of medial agranular cortex in rats. *J Comp Neurol* 294**,** 262-280.
Reimer, J., Froudarakis, E., Cadwell, C.R., Yatsenko, D., Denfield, G.H., and Tolias, A.S. (2014). Pupil fluctuations track fast switching of cortical states during quiet wakefulness. *Neuron* 84**,** 355-362.
Reiner, A., Veenman, C.L., Medina, L., Jiao, Y., Del Mar, N., and Honig, M.G. (2000). Pathway tracing using biotinylated dextran amines. *J Neurosci Methods* 103**,** 23-37.
Rizzolatti, G., Camarda, R., Fogassi, L., Gentilucci, M., Luppino, G., and Matelli, M. (1988). Functional organization of inferior area 6 in the macaque monkey. II. Area F5 and the control of distal movements. *Exp Brain Res* 71**,** 491-507.
Rizzolatti, G., Fabbri-Destro, M., and Cattaneo, L. (2009). Mirror neurons and their clinical relevance. *Nat Clin Pract Neurol* 5**,** 24-34.
Rizzolatti, G., Fadiga, L., Gallese, V., and Fogassi, L. (1996). Premotor cortex and the recognition of motor actions. *Brain Res Cogn Brain Res* 3**,** 131-141.
Rizzolatti, G., and Luppino, G. (2001). The cortical motor system. *Neuron* 31**,** 889-901.
Rizzolatti, G., and Sinigaglia, C. (2010). The functional role of the parieto-frontal mirror circuit: interpretations and misinterpretations. *Nat Rev Neurosci* 11**,** 264-274.
Rolls, E.T. (2000). The orbitofrontal cortex and reward. *Cereb Cortex* 10**,** 284-294.
Rose, J.E., and Woolsey, C.N. (1948). The orbitofrontal cortex and its connections with the mediodorsal nucleus in rabbit, sheep and cat. *Research publications - Association for Research in Nervous and Mental Disease* 1**,** 210-232.

Rozzi, S., Calzavara, R., Belmalih, A., Borra, E., Gregoriou, G.G., Matelli, M., and Luppino, G. (2006). Cortical connections of the inferior parietal cortical convexity of the macaque monkey. *Cereb Cortex* 16**,** 1389-1417.

Rozzi, S., Ferrari, P.F., Bonini, L., Rizzolatti, G., and Fogassi, L. (2008). Functional organization of inferior parietal lobule convexity in the macaque monkey: electrophysiological characterization of motor, sensory and mirror responses and their correlation with cytoarchitectonic areas. *Eur J Neurosci* 28**,** 1569-1588.

Rubin, A., Sheintuch, L., Brande-Eilat, N., Pinchasof, O., Rechavi, Y., Geva, N., and Ziv, Y. (2019). Revealing neural correlates of behavior without behavioral measurements. *bioRxiv***,** 540195.

Runyan, C.A., Piasini, E., Panzeri, S., and Harvey, C.D. (2017). Distinct timescales of population coding across cortex. *Nature* 548**,** 92-96.

Save, E., and Moghaddam, M. (1996). Effects of lesions of the associative parietal cortex on the acquisition and use of spatial memory in egocentric and allocentric navigation tasks in the rat. *Behav Neurosci* 110**,** 74-85.

Save, E., and Poucet, B. (2000). Involvement of the hippocampus and associative parietal cortex in the use of proximal and distal landmarks for navigation. *Behav Brain Res* 109**,** 195-206.

Smith, J.B., and Alloway, K.D. (2013). Rat whisker motor cortex is subdivided into sensory-input and motor-output areas. *Front Neural Circuits* 7**,** 4.

Smith, P.F., Horii, A., Russell, N., Bilkey, D.K., Zheng, Y., Liu, P., Kerr, D.S., and Darlington, C.L. (2005). The effects of vestibular lesions on hippocampal function in rats. *Prog Neurobiol* 75**,** 391-405.

Stepniewska, I., Cerkevich, C.M., Fang, P.C., and Kaas, J.H. (2009a). Organization of the posterior parietal cortex in galagos: II. Ipsilateral cortical connections of physiologically identified zones within anterior sensorimotor region. *J Comp Neurol* 517**,** 783-807.

Stepniewska, I., Fang, P.C., and Kaas, J.H. (2005). Microstimulation reveals specialized subregions for different complex movements in posterior parietal cortex of prosimian galagos. *Proc Natl Acad Sci U S A* 102**,** 4878-4883.

Stepniewska, I., Fang, P.C., and Kaas, J.H. (2009b). Organization of the posterior parietal cortex in galagos: I. Functional zones identified by microstimulation. *J Comp Neurol* 517**,** 765-782.

Stettler, D.D., and Axel, R. (2009). Representations of odor in the piriform cortex. *Neuron* 63**,** 854-864.

Suzuki, S., Adachi, R., Dunne, S., Bossaerts, P., and O'doherty, J.P. (2015). Neural mechanisms underlying human consensus decision-making. *Neuron* 86**,** 591-602.

Ungerleider, L., Mishkin, M., Ingle, D., Goodale, M., and Mansfield, R. (1982). Two cortical visual systems. In D. J. Ingle, M. A. Goodale, & R. J. W. Mansfield (Eds.), Analysis of visual behavior (pp. 549–586). Cambridge, MA: MIT Press.

Veenman, C.L., Reiner, A., and Honig, M.G. (1992). Biotinylated dextran amine as an anterograde tracer for single- and double-labeling studies. *J Neurosci Methods* 41**,** 239-254.

Vertes, R.P., Linley, S.B., Groenewegen, H.J., and Witter, M.P. (2015). "Thalamus," in *The Rat Nervous System,* ed. G. Paxinos. Fourth edition ed), 335-390.

Wallis, J.D. (2012). Cross-species studies of orbitofrontal cortex and value-based decision-making. *Nat Neurosci* 15**,** 13-19.

Wang, Q., and Burkhalter, A. (2007). Area map of mouse visual cortex. *J Comp Neurol* 502**,** 339-357.

Wang, Q., and Burkhalter, A. (2013). Stream-related preferences of inputs to the superior colliculus from areas of dorsal and ventral streams of mouse visual cortex. *J Neurosci* 33**,** 1696-1705.

Wang, Q., Gao, E., and Burkhalter, A. (2011). Gateways of ventral and dorsal streams in mouse visual cortex. *J Neurosci* 31**,** 1905-1918.

Wang, Q., Sporns, O., and Burkhalter, A. (2012). Network analysis of corticocortical connections reveals ventral and dorsal processing streams in mouse visual cortex. *J Neurosci* 32**,** 4386-4399.

Whitlock, J.R. (2017). Posterior parietal cortex. *Curr Biol* 27**,** R691-R695.

Whitlock, J.R., Pfuhl, G., Dagslott, N., Moser, M.B., and Moser, E.I. (2012). Functional split between parietal and entorhinal cortices in the rat. *Neuron* 73**,** 789-802.

Whitlock, J.R., Sutherland, R.J., Witter, M.P., Moser, M.B., and Moser, E.I. (2008). Navigating from hippocampus to parietal cortex. *Proc Natl Acad Sci USA* 105**,** 14755-14762.

Wilber, A., Clark, B.J., Demecha, A.J., Mesina, L., Vos, J.M., and Mcnaughton, B.L. (2015). Cortical Connectivity Maps Reveal Anatomically Distinct Areas in the Parietal Cortex of the Rat. *Front in Neural Circuits* 8.

Wilber, A.A., Clark, B.J., Forster, T.C., Tatsuno, M., and Mcnaughton, B.L. (2014). Interaction of egocentric and world-centered reference frames in the rat posterior parietal cortex. *J Neurosci* 34**,** 5431-5446.

Wise, S.P. (1985). The primate premotor cortex: past, present, and preparatory. *Annu Rev Neurosci* 8**,** 1-19.

Wise, S.P., Boussaoud, D., Johnson, P.B., and Caminiti, R. (1997). Premotor and parietal cortex: corticocortical connectivity and combinatorial computations. *Annu Rev Neurosci* 20**,** 25-42.

Zentall, T.R. (2012). Perspectives on observational learning in animals. *J Comp Psychol* 126**,** 114-128.

Zhou, P., Resendez, S.L., Rodriguez-Romaguera, J., Jimenez, J.C., Neufeld, S.Q., Giovannucci, A., Friedrich, J., Pnevmatikakis, E.A., Stuber, G.D., Hen, R., Kheirbek, M.A., Sabatini, B.L., Kass, R.E., and Paninski, L. (2018). Efficient and accurate extraction of in vivo calcium signals from microendoscopic video data. *eLife* 7**,** e28728.

Zhuang, J., Ng, L., Williams, D., Valley, M., Li, Y., Garrett, M., and Waters, J. (2017). An extended retinotopic map of mouse cortex. *Elife* 6.

Zong, W., Wu, R., Li, M., Hu, Y., Li, Y., Li, J., Rong, H., Wu, H., Xu, Y., Lu, Y., Jia, H., Fan, M., Zhou, Z., Zhang, Y., Wang, A., Chen, L., and Cheng, H. (2017). Fast high-resolution miniature two-photon microscopy for brain imaging in freely behaving mice. *Nat Methods* 14**,** 713.

PAPERS 1-3

Paper 1

Received: 5 July 2018 | Revised: 29 October 2018 | Accepted: 31 October 2018

DOI: 10.1111/ejn.14280

RESEARCH REPORT

WILEY EJN European Journal of Neuroscience FENS

Architecture and organization of mouse posterior parietal cortex relative to extrastriate areas

Karoline Hovde[1] | **Michele Gianatti**[1,2] | **Menno P. Witter**[1] | **Jonathan R. Whitlock**[1]

[1]Kavli Institute for Systems Neuroscience, Norwegian University of Science and Technology, Trondheim, Norway

[2]Faculty of Medicine, Univsersity of Oslo, Oslo, Norway

Correspondence
Karoline Hovde and Jonathan R. Whitlock, Kavli Institute for Systems Neuroscience, Norwegian University of Science and Technology, Trondheim, Norway.
Emails: karoline.hovde@ntnu.no and whitlock@ntnu.no

Funding information
Norges Forskningsråd, Grant/Award Number: Centre for Neural Computation, grant No. 223262, NORBRAIN, grant No. 197467 and Young Research Talents, grant No. 239963; FP7 Ideas: European Research Council, Grant/Award Number: Starting Grant, No. 335328

Abstract

The posterior parietal cortex (PPC) is a multifaceted region of cortex, contributing to several cognitive processes, including sensorimotor integration and spatial navigation. Although recent years have seen a considerable rise in the use of rodents, particularly mice, to investigate PPC and related networks, a coherent anatomical definition of PPC in the mouse is still lacking. To address this, we delineated the mouse PPC, using cyto- and chemoarchitectural markers from Nissl-, parvalbumin- and muscarinic acetylcholine receptor M2-staining. Additionally, we performed bilateral triple anterograde tracer injections in primary visual cortex (V1) and prepared flattened tangential sections from one hemisphere and coronal sections from the other, allowing us to co-register the cytoarchitectural features of PPC with V1 projections. This revealed that extrastriate area A was largely contained within lateral PPC, that medial PPC overlapped with the anterior portion of area AM, and that anterior RL overlapped partially with area PtP. Furthermore, triple anterograde tracer injections in PPC showed strong projections to associative thalamic nuclei as well as higher visual areas, orbitofrontal, cingulate and secondary motor cortices. Retrograde circuit mapping with rabies virus further showed that all cortical connections were reciprocal. These combined approaches provide a coherent definition of mouse PPC that incorporates laminar architecture, extrastriate projections, thalamic, and cortico–cortical connections.

KEYWORDS

anatomy, cortico–cortical connectivity, frontal cortex, parietal cortex, prefrontal cortex, tract tracing, visual cortex

Abbreviations: Cortical areas; Au, Auditory cortex; Cg, Cingulate cortex; EC, Entorhinal cortex; lPPC, Lateral posterior parietal cortex; M1, Primary motor cortex; M2, Secondary motor cortex; MO, Medial orbitofrontal cortex; mPPC, Medial posterior parietal cortex; POR, Postrhinal cortex; PPC, Posterior parietal cortex; PtP, Posterior part of parietal cortex; RSA, Agranular retrosplenial cortex; RSC, Retrosplenial cortex; RSG, Granular retrosplenial cortex; S1, Primary somatosensory cortex; S1B, Barrel fields of primary somatosensory cortex; Te, Temporal association cortex; V1, Primary visual cortex; V2L, Lateral secondary visual cortex; V2M, Medial secondary visual cortex; VLO, Ventrolateral orbitofrontal cortex; VO, Ventral orbitofrontal cortex.

Extrastriate areas; A, Anterior area; AL, Anterolateral area; AM, Anteromedial area; LI, Laterointermediate area; LM, Lateromedial area; MM, Mediomedial area; P, Posterior area; PM, Posteriomedial area; RL, Rostrolateral area.

Subcortical areas; DLG, Dorsal lateral geniculate nucleus; LD, Laterodorsal nucleus; LP, Lateral posterior nucleus; LPlr, Lateral posterior nucleus, anterolateral part; LPmr, Lateral posterior nucleus, anteromedial part; Po, Posterior thalamic nuclear group; SC, Superior colliculus; VPM, Ventral posterior nucleus, medial part.

Visualized protein; M2AChR, Muscarinic acetylcholine receptor type 2; PV, Parvalbumin.

Edited by Helen Barbas. Reviewed by John Aggleton and Leah Krubitzer.

All peer review communications can be found with the online version of the article.

1 | INTRODUCTION

The posterior parietal cortex (PPC) is one of the major associational cortical areas in the brain. Across mammalian species, it receives inputs from virtually all sensory modalities, frontal motor areas and prefrontal cortex (Krubitzer, 1995; Reep, Chandler, King, & Corwin, 1994; Stepniewska, Cerkevich, & Kaas, 2016; Wise, Boussaoud, Johnson, & Caminiti, 1997), and it supports a variety of cognitive functions, including sensorimotor transformations, spatial processing, decision-making and movement planning. For several decades, the monkey has served as the premiere model for investigating the behavioral and neurophysiological contributions of PPC, and while PPC in rodents is substantially smaller and less differentiated, recent years have seen an increase in the use of rats and mice. This has been motivated in part by the fact that rodents can be trained to perform a variety of highly specific, PPC-dependent tasks in real-world and virtual reality settings (Brunton, Botvinick, & Brody, 2013; Goard, Pho, Woodson, & Sur, 2016; Harvey, Coen, & Tank, 2012; Hwang, Dahlen, Mukundan, & Komiyama, 2017; Nitz, 2006; Raposo, Sheppard, Schrater, & Churchland, 2012; Whitlock, Pfuhl, Dagslott, Moser, & Moser, 2012; Wilber, Clark, Forster, Tatsuno, & McNaughton, 2014). The advantages of mice in particular include their genetic tractability and compatibility with large-scale recording and imaging techniques, leading to their widespread usage to study population coding and circuit function in every major sector of cortex, including PPC. Despite the popularity of the mouse for studying parietal cortex, there is little consensus on a coherent anatomical definition of PPC in the mouse, which is problematic because it complicates the interpretation of the wealth of new data.

As with rats, PPC in the mouse is located between visual and somatosensory cortices (Paxinos & Franklin, 2012), and the existing data suggests that it has similar patterns of cortico–cortical and thalamic connectivity (Harvey et al., 2012; Kolb & Walkey, 1987; Oh et al., 2014; Olsen & Witter, 2016; Reep et al., 1994; Wilber, Clark, Demecha et al., 2014). More detailed aspects of mouse PPC anatomy, including the boundaries which distinguish it from neighboring areas, its laminar organization and chemoarchitectural profile remain ill-defined. Recent strategies for targeting PPC in mice have therefore relied either on functionally mapping extrastriate areas (Olavarria, Mignano, & Van Sluyters, 1982) near PPC, or on stereotactic coordinates followed by post-hoc histological comparison to one of several reference atlases (e.g., Krieg, 1946; Paxinos & Franklin, 2012; Oh et al., 2014; http://connectivity.brain-map.org). These conventions may permit consistent anatomical targeting within a study, but hamper the comparison of PPC across studies since they are based on different labeling methodologies and unrelated nomenclatures.

We sought to resolve these discrepancies by first delineating mouse PPC using cytoarchitectural and laminar criteria obtained from Nissl-, parvalbumin (PV)-, and type-2 muscarinic acetylcholine receptor (M2AChR)-immunostained coronal sections. We next performed bilateral, triple anterograde tracer injections in mouse V1 as in earlier studies (Montero, 1993; Wang & Burkhalter, 2007), and prepared flattened sections from one hemisphere and coronal sections of the other. By labeling extrastriate projections in both flattened and coronal planes, and by comparing these alongside interleaved, annotated Nissl- and M2AChR-stained coronal sections, we located the mouse PPC with respect to the major projections from V1. Based on these coordinates, we performed triple anterograde tracer injections in PPC, revealing a previously undescribed topography in parietal output to higher visual areas. Additional monosynaptic retrograde tracing with rabies virus showed that the inputs to PPC largely matched that described in rats.

2 | MATRIALS AND METHODS

A total of 24 adult C57BL/6JBomTac mice (24–35 g, Taconic) were used in the study. Twenty-three were injected with tracers, of which 12 received injections in V1, and 11 were injected in PPC. Of these, 10 animals were excluded due to poor tracer uptake, transport, or off-target injections. Nine animals were used for anterograde tracing, and four animals were used for retrograde tracing, and one mouse was used for the architectural study (see Supportng information Table S1 for full listing). Mice were housed in separate cages with free access to water and food, and were kept on a reversed light-dark cycle. All surgical procedures were approved by the Norwegian Food Safety Authority as well as the local Animal Welfare Committee of the Norwegian University of Science and Technology, and followed the European Communities Council Directive and the Norwegian animal welfare act.

2.1 | Preparation and delineation of "atlas" brain

A 7-month-old female mouse, weighing 30 g, was given an overdose of pentobarbital and transcardially perfused using Ringer's solution (0.025% KCl, 0.85% NaCl, 0.02% NaHCO3, pH 6.9) followed by a freshly prepared paraformaldehyde solution (PFA, 4% in 0.125 M phosphate buffer, pH 7.4). The brain was carefully removed from the skull and post-fixed in 4% PFA overnight at 4°C. Subsequently, the brain was moved to a cryoprotective solution (2% dimethyl sulfoxide, DMSO in 0.125 M phosphate buffer, VWR) and stored again overnight at 4°C before sectioning. The brain was cut in 40 μm coronal sections on a freezing microtome (Microm HM430, Thermo Scientific, Waltham, USA) in three equally

spaced series. One series was used for Nissl staining, and the other two were used for immunohistochemistry against PV and M2AChR, respectively. Nissl staining and immunohistochemical procedures were the same for these and the anatomical tracing experiments, and are explained in detail in "Histology and immunochemistry" below. Delineations and cortical field designations for this and all other brains in the study were determined for each hemisphere individually in each analysis.

2.2 | Anterograde anatomical tracing

The coordinates for initial injections were based on Paxinos and Franklin (2012), and adjusted both to the size of the animal and according to the histology of injection sites in previous animals. All surgeries were performed under isoflurane anesthesia with the animal laying on a heating pad maintaining the body temperature at 37°C. Briefly, the animal was anesthetized in a box prefilled with isoflurane before being placed in a stereotaxic frame (Kopf Instruments). The analgesics Metacam (5 mg/kg, meloxicam, Boehringer Ingelheim Vetmedica) and Temgesic (0.1 mg/kg, buprenorphine, Indivior) were injected subcutaneously, as was the local anesthetic Marcain (1–3 mg/kg, bupivacaine, AstraZeneca) where the incision was to be made. The head of the animal was shaved, disinfected with 70% ethanol and iodine (Iodine NAF Liniment 2%, Norges Apotekerforening) and a small incision was made along the midline. The skull was cleaned with hydrogen peroxide (H_2O_2, 3%, Norges Apotekerforening) and 0.9% saline, the height of bregma and lambda were measured and adjusted to ensure the skull was levelled, and a craniotomy was made with a high-speed dental drill and 0.25 mm burr over the coordinates for injections.

The anterograde tracers used for triple injections were (a) 10 KD biotinylated dextran amine (BDA, Dextran, Biotin, 10,000 MW, Lysine Fixable (BDA-10,000), Thermo Fisher Scientific Cat. No. D1956, RRID:AB_2307337 in 5% solution in 0.125 M phosphate buffer) *or* Dextran, Alexa Fluor™ 647 (ThermoFisher, 10,000 MW, Anionic, Fixable, Catalog number D22914), (b) Dextran, Alexa Fluor™ 488 (ThermoFisher, 10,000 MW, Anionic, Fixable, Catalog number D22910) and (c) Dextran, Alexa Fluor™ 546 (ThermoFisher, 10,000 MW, Anionic, Fixable, Catalog number D22911). Tracers were injected iontophoretically by applying pulses of positive DC-current (6 s on/off alterations, 6 μA) for 10 min using glass micropipettes (20 μm tip, Harvard apparatus, 30-0044). In later experiments BDA replaced Dextran, Alexa Fluor™ 647 due to better transport and stronger signal. Different mice were used for injections in V1 (five animals) and PPC (four animals; see Table S1). Injections in V1 were spaced 0.3 mm apart beginning 2.30 mm lateral of the midline, immediately anterior to the transverse sinus. The injections in PPC were spaced 0.37 mm apart, beginning 1.25 mm lateral from of the midline and −1.90 mm posterior to bregma. Following the injections, the craniotomy was filled with Venus Diamond Flow (Kulzer, Mitsui chemical group), the skull was cleaned with saline, and the wound was stitched and disinfected with iodine. Animals were then transferred to a heating chamber until awake and active, before being moved back to its home cage. Postoperative pain management included Metacam (5 mg/kg) 12 hr postsurgery and, if deemed necessary, 24 hr post-surgery.

2.3 | Rabies tracing

Injections were made into PPC (B-2.00, L+ 1.50, D-0.50) following the general surgical procedure as described above (see Table S1 for injection details across animals). For the representative case, 300 nl helper virus (AAV1.CamKII0.4.Cre.SV40 + AAV5-syn-FLEX-splitTVA-EGFP-B19G, in a 1:1 ratio; Cre virus from U. Penn Vector Core; TVA virus was a generous gift from the laboratory of Cliff Kentros) was injected, using glass capillaries (World Precision Instruments (WPI), Cat. No. 4878), a Nanoliter2010 injector (WPI) and a Nanoliter2000 pump (WPI), with the glass tip left in place 10 min after the injection. 12 days later, 230 nl of rabies virus (EnvA-pseudotyped SAD-DeltaG-mCherry; gift from Kentros lab) was injected in the same location, and the animal was kept alive for 11 days before perfusion.

2.4 | Tissue collection and preparation

Animals receiving anterograde tracers were perfused one week after the injections. They were given an overdose of pentobarbital and perfused transcardially with Ringer's solution (0.025% KCl, 0.85% NaCl, 0.02% NaHCO3, pH 6.9) followed by freshly prepared paraformaldehyde solution (PFA, Sigma-Aldrich AS, 1% in 0.125 M phosphate buffer, pH 7.4). For brains with bilateral tracer injections, the left hemisphere was flattened and the right hemisphere was cut coronally (see below). Such brains were carefully removed from the skull and kept in a container with PFA (1%). Within one hour of the perfusion, the brain was cut in two along the midline to prepare coronal sections of the right hemisphere and tangential sections through flattened tissue (flat maps) from the left hemisphere. Brains with unilateral anterograde tracer injections and brains that received rabies injections were perfused and post-fixed with 4% PFA and always cut in the coronal plane (see below).

2.4.1 | Coronal sections

Coronal sections were prepared from brains that received (a) bilateral anterograde tracer injections, (b) unilateral anterograde injections, or (c) rabies injections. For bilateral injections, coronal sections were always made from the right

hemisphere. In all cases, brains were carefully removed from the skull following perfusions and transferred to a screw-top vial containing PFA (4%, 0.125 M phosphate buffer, pH 7.4), postfixed overnight at 4°C and transferred to cryoprotective solution (2% DMSO in 0.125 M phosphate buffer) the next day, and again stored overnight at 4°C. The hemisphere was then cut in 40 μm coronal sections on a freezing microtome (see above) in three equally spaced series. The first series was mounted directly onto Superfrost Plus microscope slides (Gergard Menzel GmbH, Braunschweig, Germany), dried overnight on a heating pad, and used for Nissl staining. Series two and three were each stored in cryoprotective solution at −20°C, and later used for visualizing anterograde tracers or rabies, and the other for immunohistochemistry against M2AChR.

2.4.2 | Tangential flattened sections

The left hemisphere was flattened to make "flat maps" of cortex, which first required that cortex was dissected from the rest of the subcortical structures. This was done by first resting the left hemisphere on the midline with the cortex upwards, and gently pressing the cortex flat. The brain was next flipped over to expose the midline, and a cut was made in fornix dorsal to the anterior commissure. Two brushes were used to push and separate cerebellum, cortex and the underlying subcortical areas from each other. The brainstem was held down with a brush, while dorsal cortex and hippocampus were pushed away with dissection scissors, and cuts were made at the same time along the white matter. The scissors were held parallel to the cutting plane and special care was taken to not damage ventral hippocampus. The brainstem and cerebellum were cut out and removed. One relief cut was made in the cingulate cortex and one ventral to the postrhinal cortex to facilitate the unfolding of the cortex. The cortex was then placed on a microscope glass covered with parafilm (Laboratory film, Pechiney, Plastic packaging, Chicago), and hippocampus and dorsal cortex were gently unfolded using two brushes. Another covered microscope glass was placed on top of the tissue and the two glasses were taped together. The preparation was placed in a container with PFA (4%) overnight at 4°C with a glass weight (52 g) on top to provide extra pressure. The following day, the flattened tissue was removed from the microscope glasses and kept in a screw-top container with 2% DMSO in 0.125 M phosphate buffer overnight at 4°C. One day later, the brain was mounted onto a freezing microtome stage using a sucrose solution (20%) with dorsal cortex facing down, and 50 μm thick sections of flattened cortex were cut and collected in one tube containing 2% DMSO in 0.125 M phosphate buffer. The sections were first used for studying projections from V1 to extrastriate areas in flat maps, and were stained subsequently with DAB against M2AChR for delineation purposes (as described in the following section). We defined all cortical boundaries based on myeloarchitecture and M2AChR staining in each hemisphere individually.

2.5 | Histology and immunochemistry

2.5.1 | Nissl staining

Series one from the right hemisphere was stained with cresyl violet (Sigma-Aldrich, St. Louis, MO). Briefly, the sections were dehydrated in increasing percentages of ethanol (50%, 70%, 80%, 90%, 3 × 100%, 10 dips each), cleared in xylene for 2 min, and rehydrated in decreasing concentration of ethanol. The sections were rinsed briefly in running water before being stained with cresyl violet (0.1%) on a shaker for 3 min. The sections were rinsed subsequently in running water and differentiated in an ethanol-acetic acid solution (0.5% acetic acid in 70% ethanol) until optimal staining was achieved. The sections were again dehydrated in increasing percentages of ethanol (as described above), cleared in xylene, and coverslipped with xylene solution (Merck KGaA, Darmstadt, Germany).

2.5.2 | Immunohistochemistry against BDA

Series two of the right hemisphere and all sections of the left hemisphere were used for triple-anterograde tracing experiments. Three of the tracers were conjugated with Alexa fluorophores Dextran, Alexa Fluor™ 488, Dextran, Alexa Fluor™ 546 and Alexa Fluor™ 647 whereas BDA was visualized, using fluorophore-tagged streptavidin (Thermo Fisher Scientific). This was done by first washing tissue sections 3 × 5 min in 0.125 M phosphate buffer (pH 7.4), followed by 3 × 5 min in TBS-Tx (0.5% Triton-X-100, 0.606% Tris(hydroxymethyl) aminomethane, 0.896% NaCl, pH 8.0). The sections were then incubated with primary antibody Streptavidin, Alexa Fluor 633 conjugate (1:400, Thermo Fisher Scientific Cat. No. S-21375, RRID:AB_2313500) in TBS-Tx for 90 min at room temperature, followed by 3 × 5 min rinsing in Tris buffer 0.606% (Tris(hydroxymethyl)aminomethane, pH 7.6). The tissue sections were then mounted on Menzel-glass slides (Thermo Scientific) using a Tris-gelatin solution (0.2% gelatin in Tris-buffer, pH 7.6), air dried overnight and coverslipped with an entellan-toluene solution the following day.

2.5.3 | DAB staining against M2AChR and PV

Tissue sections were stained with 3.3′-Diaminobenzidine tetrahydrochloride (DAB, Sigma-Aldrich, St. Louis, USA) to visualize M2AChR density in series three of the right hemisphere and flat map sections for the anterograde tracer experiments, as well as for series three of the "atlas" brain

(Figure 1). DAB staining was also used to visualize PV in series two of the "atlas" brain. The staining procedure for coronal sections was the same across experiments except for flat maps, for which staining was done on the slide, requiring a longer incubation time.

In brief, for immunostaining against M2AChR and PV, sections were first rinsed 2 × 5 min in phosphate buffer (0.125 M) followed by 2 × 5 min rinses in TBS-Tx. The sections were incubated with primary antibody (Rat anti-muscarinic acetylcholine receptor M2 monoclonal antibody, unconjugated, clone m2-2-b3, 1:750, Millipore Cat. No. MAB367, RRID:AB_94952; Mouse anti-parvalbumin monoclonal antibody, unconjugated, clone PARV-19, 1:1000, Sigma-Aldrich Cat. No. P3088, RRID:AB_477329) overnight at room temperature. They were then washed 2 × 5 min in TBS-Tx and incubated with mouse absorbed, rabbit-anti-rat secondary antibody (Anti-rat IgG (H+L), 1:300, Vector Laboratories Cat. No. BA-4001, RRID:AB_10015300; Goat anti-mouse IgG, biotin conjugated, 1:200, Sigma-Aldrich Cat. No. B7151, RRID:AB_258604) for 90 min at room temperature. The sections were then washed 2 × 5 min in TBS-Tx, 2 × 5 min in PB, 2 × 5 min in H_2O_2-metanol solution (0.08%, Sigma-Aldrich), 2 × 5 min TBS-Tx and incubated with a Vector ABC kit (Vector laboratories, Inc., Burlingame, USA) for 90 min at room temperature, per the manufacturer's instructions. Subsequently, the sections were washed 2 × 5 min in TBS-Tx, then 2 × 5 min in Tris-buffer before being incubated with DAB (10 mg in 15 mL Tris-buffer, Sigma-Aldrich) at room temperature. Just before the incubation, H_2O_2 (2 µL, 30%, Sigma-Aldrich) was added to the DAB solution and it was filtered. The sections were incubated in DAB until they reached the desired color, rinsed

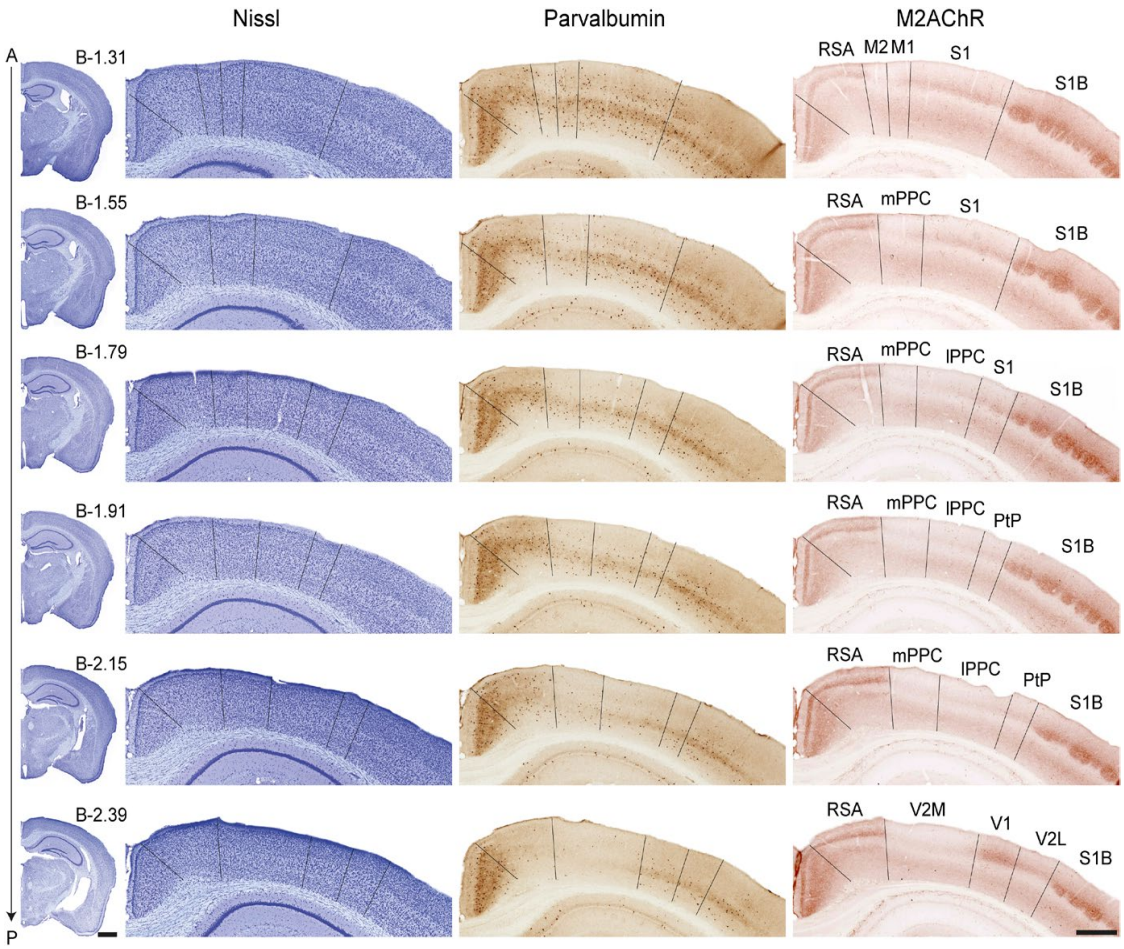

FIGURE 1 Delineation of posterior parietal cortex and surrounding areas. Coronal sections of Nissl- (left), parvalbumin- (middle) and M2AChR-stained (right) tissue from a single mouse are shown in 40 µm sections in three interleaved series. Approximate bregma levels, based on Paxinos and Franklin (2012), are indicated at the far left, along with a hemispheric overview of where the sections on the right were taken from. The nomenclature is also adapted from Paxinos and Franklin (2012); see list for abbreviations. Left scale bar = 1 mm, right scale bar = 500 µm

in Tris-buffer solution, and mounted on Menzel glass slides using a 0.2% gelatin solution. After drying overnight, the slides were coverslipped with an entellan-xylene solution.

2.5.4 | Immunohistochemistry against rabies

For brains used for rabies tracing, series two was stained against green fluorescent protein (GFP), and red fluorescent protein (RFP) to visualize the helper virus (AAV1.CamKII0.4.Cre.SV40 + AAV5-syn-FLEX-splitTVA-EGFP-B19G) and the rabies virus (EnvA-pseudotyped SAD-DeltaG-mCherry), respectively. In brief, the tissue was rinsed 3 × 5 min in phosphate buffered saline (PBS, 0.1 M, pH 7.4, Sigma-Aldrich) on a shaker at room temperature and rinsed 2 × 10 min in a 0.3% Triton solution (PBS 0.1 M and 0.3% Triton). Further, it was incubated with primary antibodies (Rabbit RFP Antibody Pre-adsorbed, 1:1000, Rockland Cat. No. 600-401-379, RRID:AB_2209751; Chicken anti-GFP, 1:500, Abcam Cat. No. ab13970, RRID:AB_300798) in a PBS 0.1 M + 0.3% Triton + 3% BSA solution on a shaker at 4°C overnight. The tissue was rinsed 2 × 5 min in 0.3% Triton solution and incubated with secondary antibodies (F(ab)2-goat anti-rabbit IgG (H+L) cross-adsorbed, Alexa Fluor 546, 1:1000, Thermo Fisher Scientific Cat. No. A-11071, RRID:AB_2534115; Goat anti-chicken IgY H&L, Alexa Fluor® 488, 1:1000, Abcam Cat# ab150169, RRID:AB_2636803) in a PBS 0.1 M + 0.3% Triton + 3% BSA solution on a shaker at room temperature for one hour. Finally, the tissue was rinsed 2 × 10 min in PBS (0.1 M) and mounted on gelatin-coated polysine slides (Thermo Scientific) using PBS (0.1 M). After drying for one hour, a Hoechst solution (1:5000 in PBS 0.1 M, bisBenzimid H 33258, catalog No. B1155, Sigma-Aldrich) was applied on the sections for 5 min in the dark, the slides were carefully rinsed with PBS

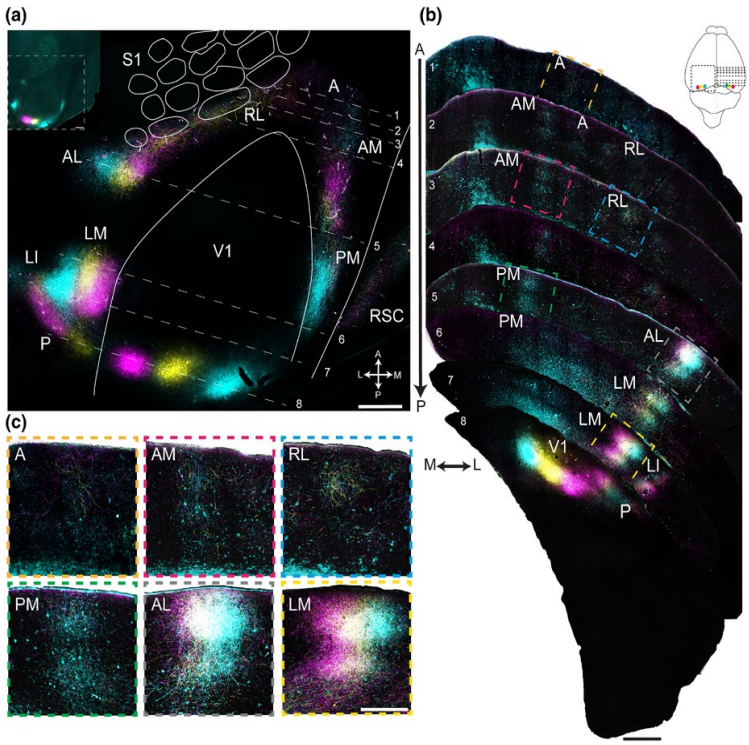

FIGURE 2 Projections from V1 viewed in flattened (left) and coronal (right) sections. (a) Left hemisphere: Section through layer IV of flattened cortex showing triple injections of anterograde tracers in V1 and the resulting projections to extrastriate areas. Insert: dark-field image from an unprocessed section for overview. Nomenclature for the visual projection fields is based on Montero (1993), and cortical field boundaries were established within-hemisphere. The outlines of V1 and barrels of S1 were drawn from M2AChR staining and myeloarchitecture from the dark-field image (see insert, top left). To avoid signal saturation from the injection sites, a shorter exposure time was used for injection sites than for projections as shown in the image (Methods). (b) Right hemisphere: triple injections of anterograde tracers in V1 (section 8, at bottom) as in a, visualized in coronal sections, as well as the resulting projections to extrastriate areas. Anterior-posterior levels of the coronal section are indicated by corresponding numbers (1 through 8) in a, the locations of which are estimates based on the similarity of labeling patterns and AP levels. Projections from V1 to areas LM, LI and AL were topographically organized, whereas labeling was intermingled in other subfields. (c) Magnified view of labeling from highlighted areas in coronal sections in b. The figure is for illustration purposes. See list for abbreviations. Scale bars in a and b = 500 μm, in c = 200 μm

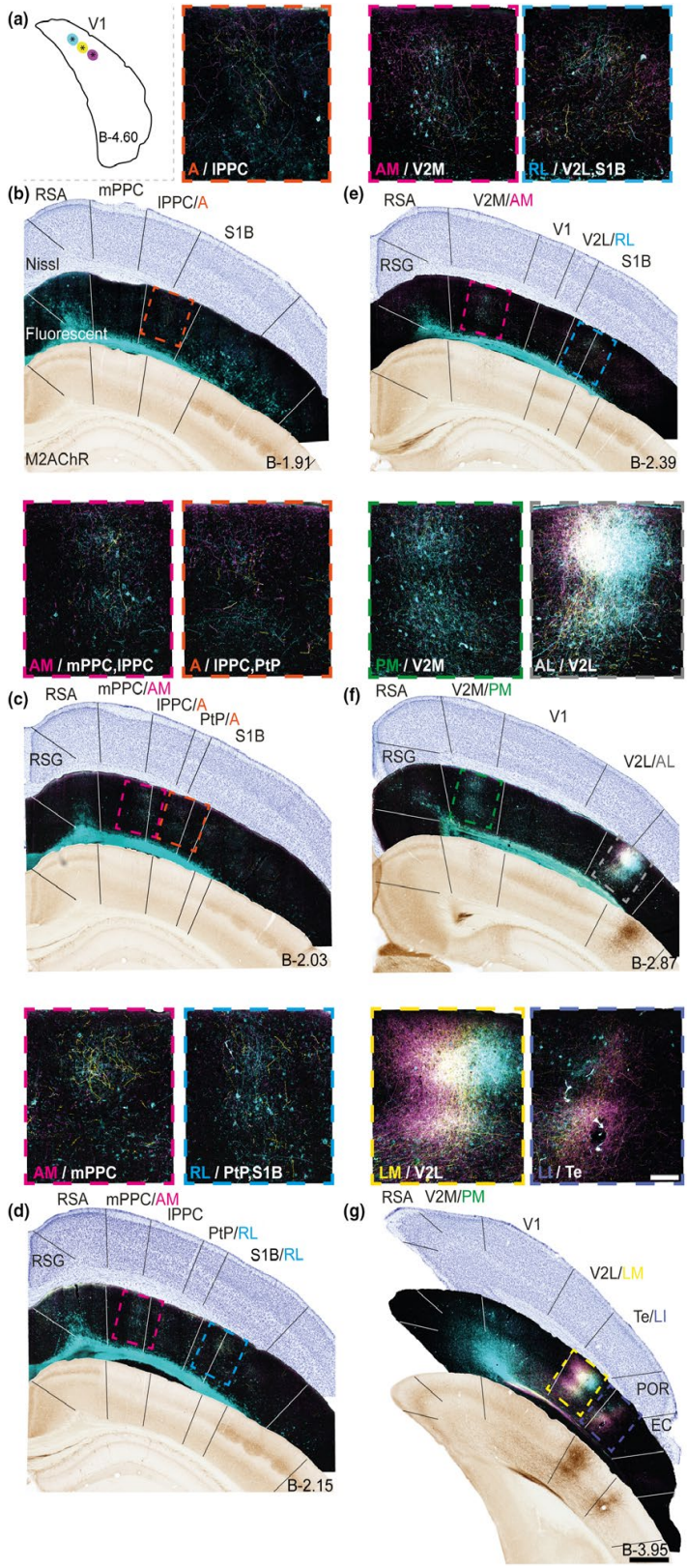

FIGURE 3 Co-registration of extrastriate areas with PPC and surrounding cortices. (a) Tissue from the same triple injections in V1 as in Figure 2 are shown, along with Nissl- and M2-stained sections from the same brain. Each panel consists of three immediately adjacent sections, with the series starting in PPC and proceeding posteriorly (AP coordinates estimated using Paxinos & Franklin, 2012). The nomenclature for extrastriate areas is based on Montero (1993) and Wang and Burkhalter (2007), and the cyto- and chemoarchitectonic labels are adapted from Paxinos and Franklin (2012). (b) A comparison of the three sections shows that mPPC at this level does not overlap with any extrastriate areas, whereas lPPC overlaps with area A. The enlarged inset above shows the fluorescent processes of area A/lPPC (nomenclatures juxtaposed at bottom left). (c–g) Similar comparisons from tissue sections spanning approximately −2 to −4 mm AP. Scale bar at bottom right of g = 500 μm; insert = 50 μm

and coverslipped with ProLong® Gold antifade reagent (REF P36934, Molecular probes, Life technologies™).

2.6 | Imaging and analysis

All brain sections were digitized using a Zeiss Axio Scan.Z1 scanner. Selected fluorescent coronal sections and fluorescent flat maps were scanned with a Zeiss confocal microscope (LSM800) in *z*-stacks and compiled using the max projection function to project all stacks onto a single plane. The scans were edited in Adobe Photoshop CC 2017 and figures were made in Adobe Illustrator CC 2017. Nissl and DAB-stained sections were optimized for brightness and contrast. Fluorescent flat maps and coronal sections in Figures 2–6 were used for illustration purposes, and were optimized in Adobe Photoshop for brightness and contrast levels for the whole image. Masks were applied to avoid overexposing the injection sites when enhancing the labeling. These were done to reduce background; no labeling was removed, only enhanced for visualization purposes. For Figures 2 and 3, dark field images were taken of the same sections and used as background underneath the fluorescent sections. Artifacts from blood vessels were removed by making them transparent against the background; see Figures 5 and 6 and Supporting information Figures S1–S3 for examples of when vascular artifacts were not removed. Descriptions of anterograde and retrograde labeling were intended to be descriptive in nature. We did not quantify the density of labeling or the injections, and therefore do not make assertions about the relative strengths of the connections.

Delineations in Figure 3 were performed on series one of the sections (Nissl) and series three (M2AChR stain).

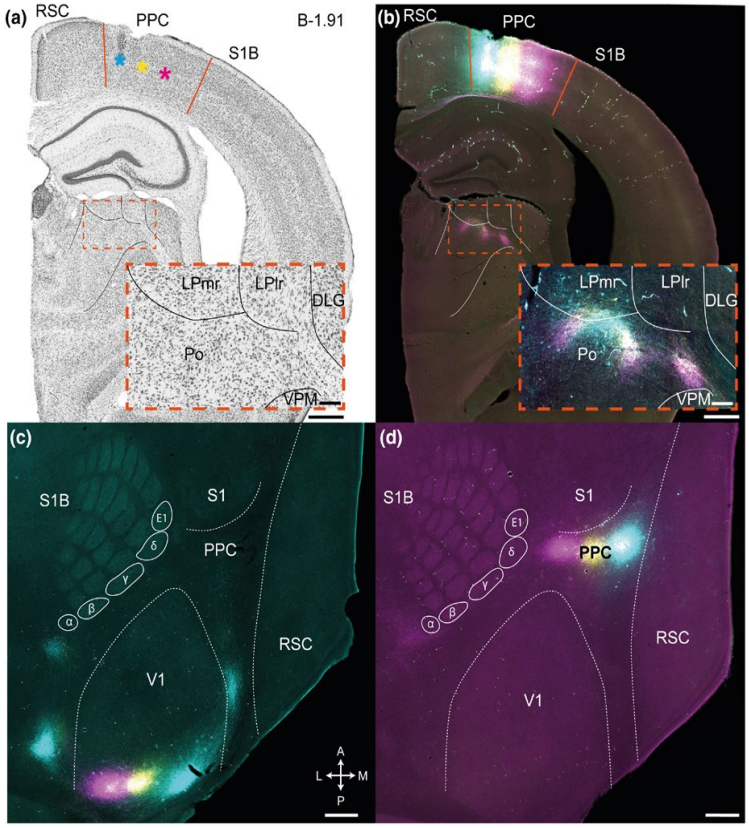

FIGURE 4 Validation of coordinates for PPC using thalamic labeling. (a) A Nissl-stained section from the right hemisphere showing triple injections of dextran amine tracers within cytoarchitectonic boundaries of PPC in that hemisphere, with the underlying thalamic nuclei delineated (inset). (b) Fluorescent image of the same section, showing fluorescent anterograde labeling in the associative thalamic nuclei LP and Po, with no staining in the DLG. (c) Overview of flattened cortex showing triple anterograde tracer injections in V1 in a different mouse, along with S1B, S1, RSC and an estimation of where PPC should fall. (d) Triple anterograde injections at the same coordinates as A and B, in the left hemisphere of the same animal, viewed in a flat map with the area estimated as PPC directly lateral to the δ barrel field. In both (c) and (d), cortical area boundaries are drawn based on within-hemisphere myeloarchitecture, and exposure times and saturation levels for the images were optimized to highlight injections sites, not labeled projections. Scale bars at bottom right of a–d = 500 μm; insert = 100 μm

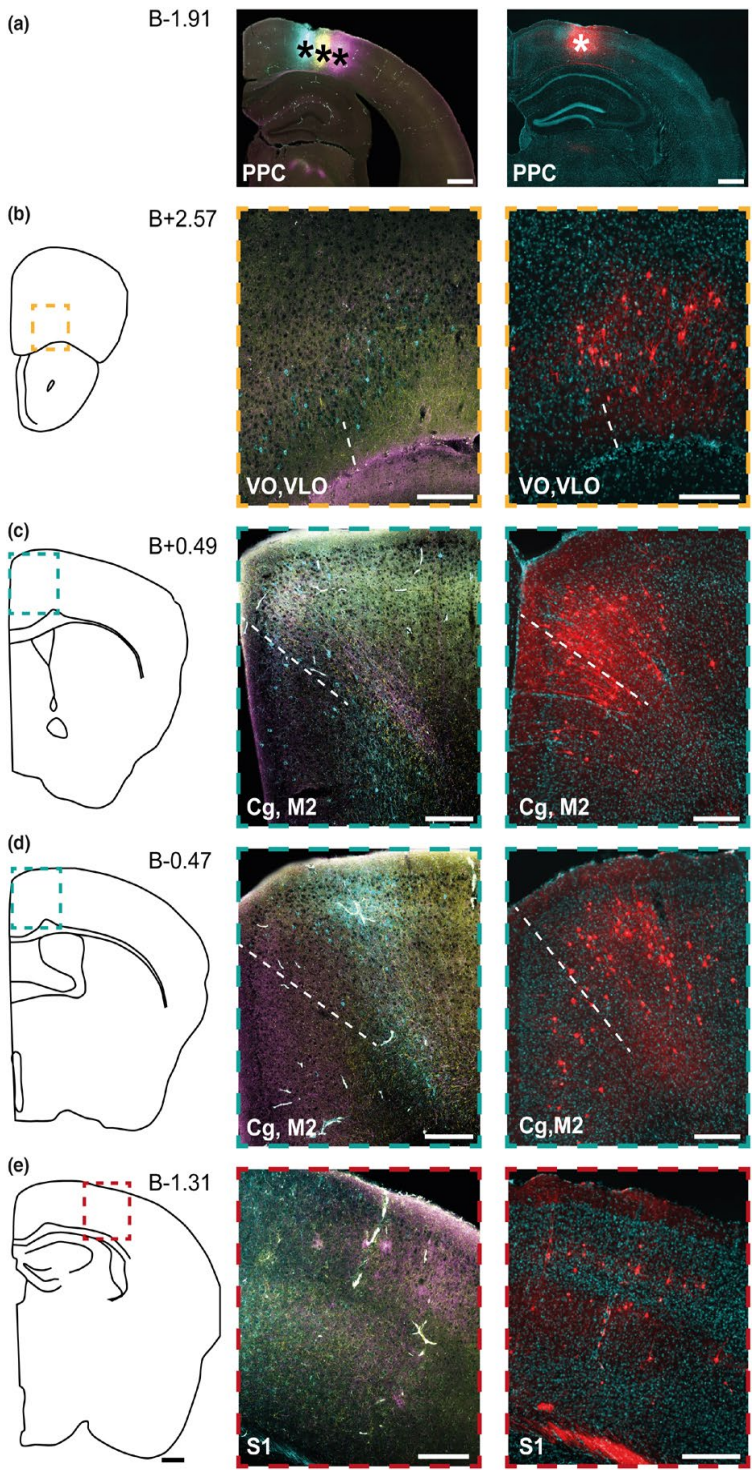

FIGURE 5 Efferent and afferent cortical connections anterior to PPC. (a) (left) Coronal section showing triple anterograde tracer injections in PPC of the right hemisphere; (right) injection site of TVAG and rabies viruses in the right hemisphere of a different mouse. Cortical boundaries were drawn based on cytoarchitectural features in Nissl-stained sections adjacent to each section with anterograde or retrograde labeling, in correspondence with Paxinos and Franklin (2012). (b) (left) Drawing of the right hemisphere at +2.57 mm from bregma, from which the middle and right panels were taken. (middle) Fluorescent images of PPC projections to VO and VLO, (right) retrograde rabies labeling (red) against Hoechst counterstaining (blue). (c) (left) Drawing of the right hemisphere at +0.49 mm from bregma. (middle) Strong anterograde labeling in Cg and M2, showing a rough topographical correspondence with injection sites in PPC. (right) Rabies labeling indicated dense monosynaptic projections from dorsal Cg cortex and medial M2 to PPC. (d) (left) Same as above, toward the posterior extent of M2, (middle) fluorescent anterograde projections from medial and lateral PPC; (right) retrogradely labeled neurons in posterior M2 and Cg that project to PPC. (e) (left) Drawing of the right hemisphere at −1.31 mm relative to bregma. (middle) At this level, PPC has robust projections to S1, and (right) rabies labeling in S1 shows the connection is reciprocal. Scale bars in b–e = 500 μm in left panels, 200 μm in middle and right panels

The sections were then overlaid on corresponding fluorescent sections from series two (anterograde or retrograde labeling) in Adobe Illustrator, and the borders where copied onto fluorescent sections. Special care was taken to overlay the sections exactly. Demarcations of cortical and thalamic subregions were performed for each experimental hemisphere individually; laminar and chemoarchitectural labeling in coronal sections was in correspondence with Paxinos and Franklin (2012); extrastriate areas in flattened sections were labeled in correspondence with Wang and Burkhalter (2007),

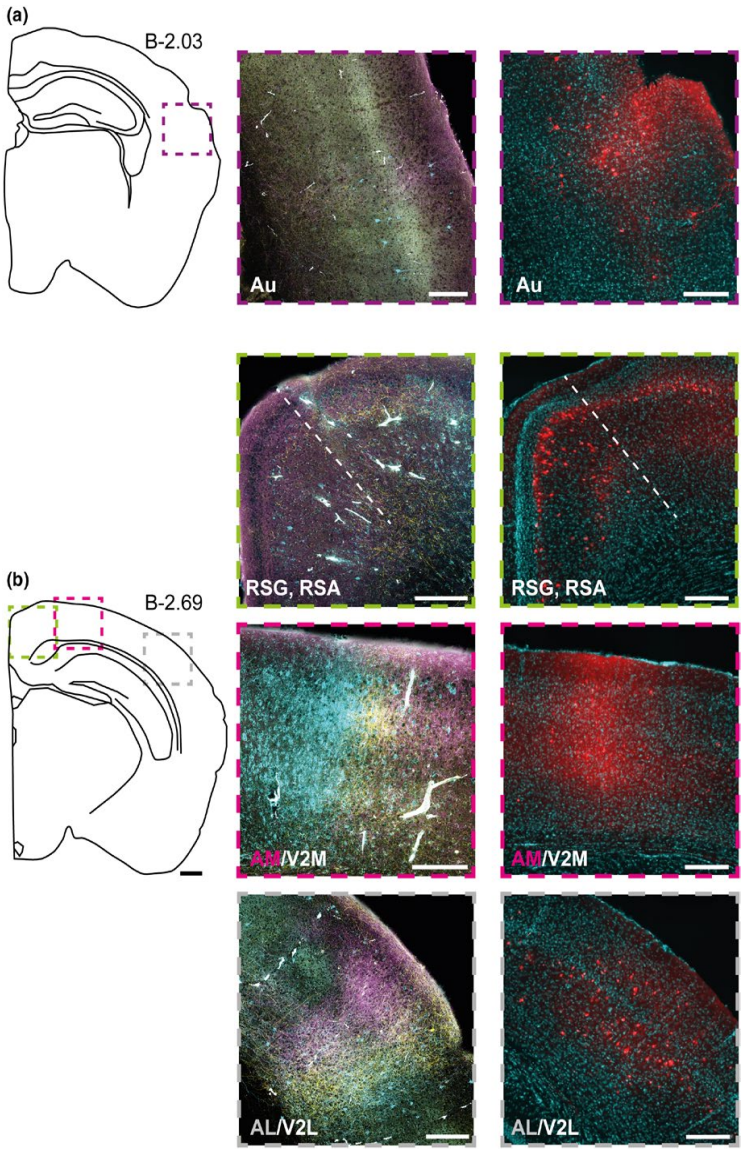

FIGURE 6 Efferent and afferent cortical connections posterior to PPC. Anterograde and retrograde labeling resulting from the same injections as in Figure 5; cortical boundaries were drawn based on adjacent Nissl-stained sections, in correspondence with Paxinos and Franklin (2012). (a) (left) Drawing of the right hemisphere at −2.03 mm from bregma, from which the middle and right panels were taken. (middle) PPC projects to deep and superficial layers of auditory cortex (Au); (right) Au provides monosynaptic input back to PPC, as indicated by rabies tracing. (b) (left) Same as above, at −2.69 mm relative to bregma. (middle) PPC projections were present in superficial and deep layers of RSC (top), but were stronger and clearly topographical in AM and AL (lower panels). (right) Deep and superficial RSC, as well as areas AM and AL provide monosynaptic input to PPC. Scale bar = 500 μm in left panels, 200 μm in middle and right panels

and in coronal sections with reference to D'Souza, Meier, Bista, Wang, and Burkhalter (2016). Boundaries for thalamic nuclei were in correspondence with Olsen and Witter (2016). A similar approach was used with Nissl-stained sections directly neighboring the fluorescent sections shown in Figures 5 and 6.

3 | RESULTS

3.1 | Architectural features of PPC and neighboring areas

Similar to the rat, the mouse PPC lies between primary somatosensory and visual cortices, spanning approximately 600 μm anterior-to-posterior, and has distinguishable medial (mPPC), lateral (lPPC) and posterior (PtP) divisions (Olsen & Witter, 2016; Paxinos & Watson, 2013). To define precisely the boundaries between PPC and neighboring cortical regions, and to discern parietal subareas, we examined laminar architecture using Nissl staining, and chemoarchitectonic patterns using immunostaining against PV and M2AChRs.

3.1.1 | Nissl staining

Posterior parietal cortex is bordered anteriorly by secondary motor cortex (M2), lateral to which is a narrow band of primary motor cortex (M1), and even more laterally by primary somatosensory cortex (S1). While cell density is mainly uniform in superficial and deep M2, M1 is conspicuous for a broad layer V with large pyramidal cell bodies,

and more homogenous lamination in superficial layers than M2. Lateral to M1, S1 is discernable by prominent lamination and a clearly distinguishable layer IV (Figure 1, top left). Medial to these areas and M2 is agranular retrosplenial cortex (RSA), which contains small, densely packed cell bodies in layer II and a loosely packed layer V that contrasts with the more homogenous distribution of cell bodies across layers in M2. Medial PPC (mPPC; Figure 1, row 2) first emerges at approximately −1.55 mm relative to bregma, and is apparent by its homogeneous lamination relative to the neighboring RSA, medially, and S1, laterally. Unlike mPPC, RSA has visibly different cell densities across layers II and III, with layer V having a sparse population of large cell bodies (Figure 1, rows 1 and 2). Somatosensory cortex is discernable by a well-developed granular layer IV and clearly stratified supragranular and infragranular layers.

The anterior tip of lPPC appears between mPPC and S1 (Figure 1, row 3). Unlike mPPC, lPPC has some discernable lamination between layers II/III and layer V, with layer V being less densely packed than superficial layers. Layer VI of lPPC is also slightly narrower and more densely packed than mPPC. The posterior part of the parietal cortex (PtP, from Paxinos & Franklin, 2012) is the most lateral subarea, and emerges between lPPC and S1 barrel cortex (Figure 1, row 4). Layers II/III of PtP are homogenous with small cells, whereas layer V cells are larger and more sparsely packed. Lateral to PtP is barrel cortex (Figure 1, row 5), which is distinguished by densely packed granular cells in layer IV forming the barrel fields. Posterior to mPPC and lPPC is the medial secondary visual cortex (V2M, Figure 1, row 6), which appears very similar to PPC in Nissl-staining. Considering the proximity and similarity of V2M and PPC with Nissl staining, we found that the emergence of V1, lateral to V2M, was the most useful indicator for being posterior to PPC. Primary visual cortex is characterized by a prominent, granular layer IV that is not present in V2M, and, unlike V2M, V1 is clearly laminated. Similar to S1, V1 contains large pyramidal cells in layer V, and has both superficial and deep cell-sparse zones.

3.1.2 | PV staining

In the section anterior to PPC (Figure 1, row 1, middle column), layers III and V of granular retrosplenial cortex (RSG) have very dense staining of cell bodies and neuropil which tapers into RSA and shows a gradual decrease in staining. The border to M2 can be noted by the drop in superficial neuropil staining, which becomes darker again in M1. Moving laterally, S1 has more pronounced stratification, with superficial layer V appearing as a clear stripe between densely stained deeper layers and layer II/III. Just posterior (Figure 1, row 2), the appearance of mPPC is marked by a salient decrease in PV staining in both cell bodies and the neuropil, which contrasts with the dense staining medially in layers II–V of RSA, and the darker staining in layers IV and V of S1. The neuropil in layer V of lPPC is slightly darker than mPPC (Figure 1, row 3), though both divisions have distinctly less PV staining than S1 and RSA. Laterally, PtP has slightly darker staining in deep layer III and layer V than lPPC (Figure 1, row 4–5), but it is markedly less than the neighboring S1 barrel fields, which have very dark staining in the neuropil of layers IV and V, and more PV+ cells in deeper layers (Figure 1, row 5). In posterior sections, V2M has even less PV staining than the neuropil and cell bodies of PPC. The near-total absence of PV staining is useful for distinguishing V2M from RSA, medially, and V1, laterally, which has a distinct band of staining in the layer V neuropil. Area V2L also has a darkly stained layer V, with weaker staining in superficial layers (Figure 1, row 6).

3.1.3 | M2AChR-stained sections

Similar to PV staining, RSG shows dense labeling for M2AChRs superficially in layer II as well as in deeper layers. Layer II continues to show prominent staining through RSA, but drops off abruptly at the border with M2 (Figure 2, top row, right column). The superficial staining returns in M1, remains clearly visible laterally through S1, and becomes extremely dense in superficial barrel cortex. Just posterior (Figure 2, row 2, right column), the appearance of mPPC is evidenced by a pronounced decrease in M2AChR staining in superficial layers relative to RSA, medially, and S1, laterally. Posterior to S1 (Figure 1, row 3), the emergence of lPPC is also indicated by a drop in M2AChR staining, and again so with PtP (Figure 1, row 4). The staining in PtP is slightly darker superficially than other parietal areas, but the appearance of S1B, lateral to PtP, is marked by a sharp increase in staining of the superficial barrel fields. Posterior to PPC, V2M virtually lacks M2AChR staining in superficial layers, and is bracketed by strong staining in RSA and V1 (Figure 1, row 6). Here, the emergence of V1 is marked by strong M2AChR staining directly posterior to lPPC and PtP; again the appearance of V1 is the best indicator of being posterior to all PPC subfields in the coronal plane.

3.2 | Topography of V1 projections in tangential flattened and coronal sections

Topographic maps of V1 projections were obtained in tangential sections from flattened hemispheres containing triple-tracer injections of dextran amines at the posterior pole of V1 (Wang & Burkhalter, 2007). Tracer injections were performed bilaterally in three mice and unilaterally in two, and a representative example of a tangential section through layer IV (Figure 2a) shows the injection sites and clusters of projections to extrastriate areas around the periphery of V1. The relative strengths of these projections were not quantified

here, but can be found in previous work (Wang & Burkhalter, 2007). The topography of the projections and delineations of V1 and S1 are with respect to myeloarchitectonic patterns (Figure 2, low-magnification inset) and M2AChRstaining (not shown) from the same sections.

The projections were identified in line with previous studies (Montero, 1993; Olavarria et al., 1982; Wang & Burkhalter, 2007) based on fluorescent labeling, orientation and topographical positioning, and were named using the same nomenclature as these previous studies (see Supporting information Table S2 for a nomenclatural comparison). Similar to their findings, we report a particularly strong projection from V1 to the lateromedial (LM) field, located immediately lateral to V1, and to the laterointermediate (LI) field lateral to LM (Figure 2a). Also consistent with prior reports (Wang & Burkhalter, 2007), LM showed a mirrored medial-to-lateral ordering of the labeling (Figure 2a), as did the prominently labeled anterolateral (AL) field, just posterior to the S1 barrels. The rostrolateral (RL) area contained a mixture of all tracers and ran parallel to the posterior barrel fields, while the anterior-most labeling was in the anterior (A) field, with labeling from all injections in V1 visible at higher magnifications (Figure 2c, top left). Posterior and medial to area A was the anteromedial (AM) field, with patches of labeling from each tracer stretched along the anterior–posterior axis, followed by the posteromedial (PM) field. While in this case the cyan labeling predominated at low magnification in PM, all tracers were evident at higher magnification (Figure 2c, bottom left).

Similar triple-injections were made in V1 of the right hemisphere, from which coronal sections were cut along the anterior-to-posterior extent of the extrastriate cortex (Figure 2b). Importantly, we verified that projection labeling from contralateral injections was negligible (Figure S1), indicating that labeling in coronal or flattened sections came almost entirely from ipsilateral injections. We identified fields in the coronal plane based on their labeling with respect to flat maps, and at levels corresponding to prior descriptions of extrastriate clusters in coronal sections (D'Souza et al., 2016). Consistent with the flat maps, area A was labeled sparsely following injections in V1, whereas the densest projections were to areas LM and AL, both of which exhibited topographically distributed labeling. Each extrastriate area (except LI) is shown at higher magnification in Figure 2c.

3.3 | Locations of extrastriate areas in relation to PPC

The main goal of this study was to describe the location of extrastriate areas described in classical studies (Montero, 1993; Olavarria & Montero, 1989; Olavarria et al., 1982; Wang & Burkhalter, 2007) in relation to the laminar, cyto- and chemoarchitectural features that distinguish PPC in the mouse. To do this, we stacked images of Nissl-stained, annotated PPC sections atop corresponding sections from the same animal with fluorescent V1 projections, and a third series of sections stained for M2AChR (Figure 3). As shown in Figure 3b, at −1.91 mm posterior to bregma the entire complement of labeled fibers for area A is contained in lPPC, with no apparent extrastriate labeling in mPPC. Proceeding posteriorly, area A continues to overlap primarily with the lateral areas lPPC and slightly with PtP, while AM overlaps mainly with mPPC and to a lesser extent lPPC (Figure 3c). The bulk of labeling in AM remained in mPPC along the full extent of PPC, while area RL overlapped with PtP and the medial edge of the S1 barrel fields (Figure 3d).

Posterior to PPC, labelling in area, AM was contained entirely in V2M (per the nomenclature of Paxinos & Franklin, 2012), and area RL continued to straddle the architectonic boundary between V2L and S1 barrels (Figure 3e). Even more posteriorly, at approximately −2.87 mm posterior to bregma, labeling in PM overlapped completely with Paxinos and Franklin's (2012) V2M, whereas V2L totally enveloped AL. We found that the splenium of the corpus callosum was a useful landmark for locating the transition from RL to AL, and that AL emerged at the level where the barrels disappeared in coronal sections. The farther posterior sections (Figure 3g) showed that area LM overlapped completely with posterior V2L, and area LI overlapped with the temporal association area (Te). Although we noted cross-reactivity between antibodies against M2-receptors and BDA labeling (Figures 3f–g), we confirmed that the patterns of M2AChR labeling in other sections matched staining patterns in tissue preparations without BDA injections (as in Figure 1).

3.4 | Thalamic and cortical connectivity of mouse PPC

One of the defining features of PPC in rats and other mammals is its connection with associative thalamic nuclei, namely the lateral posterior (LP), lateral dorsal (LD), and posterior (Po) nucleus (Bucci, Conley, & Gallagher, 1999; Cappe, Morel, & Rouiller, 2007; Chandler, King, Corwin, & Reep, 1992; Donoghue & Ebner, 1981; Kolb & Walkey, 1987; McDaniel, McDaniel, & Thomas, 1978; Olsen & Witter, 2016; Padberg & Krubitzer, 2006; Schmahmann & Pandya, 1990). Existing evidence indicates that PPC in mice receives input at least from LP (Harvey et al., 2012), so we used coordinates from our prior annotations (Figures 1 and 3) to target triple anterograde tracer injections in PPC (bilaterally in two animals, and unilaterally in two others), and cut the right hemisphere in coronal sections to investigate the patterns of thalamic labeling. In the two bilateral cases, the left hemisphere was used to prepare tangential flattened sections. The locations of PPC projections in all cases were identified using anatomical boundaries delineated in neighboring Nissl-stained sections,

and fluorescent labeling of the projections came nearly exclusively from injections in the ipsilateral hemisphere (Figure S1). Thalamic and cortical projections from PPC are shown for illustrative purposes, their densities were not quantified.

As seen in Figures 4a and b, tracer injections contained wholly within the cytoarchitectonic boundaries of PPC produced robust anterograde labeling in LP and Po, and farther anterior sections contained strong projections to LD (Figure S2). In all cases, thalamic projections were specific to associative nuclei with no staining in the immediately adjacent dorsal lateral geniculate nucleus (DLG), which receives projections from V1, nor in the ventral posterior medial nucleus (VPM), which receives projections from S1. Thus, the cortico-thalamic projections in the mouse appeared highly similar to those described in rats (Chandler et al., 1992; Olsen & Witter, 2016). To visualize the position of the injection sites in PPC relative to other cortical areas, we examined flattened sections from the left hemisphere, which had similar triple injections at the same coordinates as the coronal sections. The myeloarchitecture in the flattened sections showed that our coordinates for PPC fell anterior and largely medial to V1, and tangential to the barrel fields of S1, in particular the δ barrel (Figure 4d).

To verify the projection targets of PPC, we next examined labeling resulting from triple-injections in coronal sections of the right hemisphere (Figure 5a, left), which showed prominent labeling in several cortical and subcortical regions. Anterior to PPC, this included projections targeting medial, ventral and ventrolateral orbitofrontal cortex (MO, VO, VLO; Figure 5b, left, MO not shown), with the most prominent labeling in superficial layers of VLO. The injections also produced strong labeling in cingulate (Cg) and secondary motor (M2) cortices, which appeared to follow a coarsely topographical distribution, with medial PPC projecting medially toward Cg, and lateral PPC projecting more laterally into M2 (Figure 5c–d, left). The projections from PPC to M2 were particularly strong posterior to bregma, though whether labeling was topographical at this level varied across animals (Figure S3). We also noted that the projections to M2 corresponded well with prior descriptions of outputs from areas A and RL (Wang, Sporns, & Burkhalter, 2012). These connections, along with robust projections to primary somatosensory cortices (Figure 5e), and subcortical projections to the dorsal striatum and intermediate layers of the superior colliculus (Figure S2), are strongly consistent with the complement of connections described in rats (Chandler et al., 1992; Kolb & Walkey, 1987; Olsen & Witter, 2016; Wilber, Clark, Demecha et al., 2014). To determine whether these cortical outputs of PPC were reciprocal, we performed monosynaptic circuit tracing with rabies virus in a parallel series of mice ($n = 4$, Figure 5a, right; Wickersham et al., 2007), which showed unequivocally that PPC received monosynaptic inputs from each cortical area with anterograde labeling (Figure 5b–e, right).

Posteriorly, PPC projections were labeled in both superficial and deep layers of primary auditory cortex (Figure 6a), and in granular and agranular retrosplenial cortex (Figure 6b, top), which is consistent with observations in rats (Kolb & Walkey, 1987; Olsen & Witter, 2016; Reep et al., 1994; Wilber, Clark, Demecha et al., 2014) and could correspond to RSC projections from areas A and AM in mice (Wang et al., 2012; Wilber, Clark, Demecha et al., 2014). The densest projections from PPC were to extrastriate areas AM/V2M and AL/V2L (Figure 6b, middle and bottom), with AM/V2M showing a medial-to-lateral topography in line with the location of tracer injections in PPC, and AL/V2L in some cases showing a mirrored ordering (Figure 6b, bottom; Figure S3, bottom). Although labeling from PPC was present more posteriorly in areas PM and LM, it was weaker than in AM/V2M and AL/V2L, and did not appear topographical (not shown). As with cortical connections anterior to PPC, monosynaptic tracing with rabies virus confirmed these connections were reciprocal, originating from both deep and superficial layers in all upstream areas (Figure 6a and b, right).

4 | DISCUSSION

In this study, we described laminar, cytoarchitectonic and chemoarchitectonic criteria for defining the mouse PPC and surrounding cortices which, to our knowledge, have not been established previously. By providing a characterization of PPC and its boundaries using intrinsic architectural features, this study differs from previous, large-scale investigations of the organization of mouse cortex based on functional connectivity and projection patterns (Lim et al., 2012; Oh et al., 2014; Zingg et al., 2014). Importantly, we reconciled widely used but disparate nomenclatures that refer to PPC (Paxinos & Franklin, 2012) *versus* the extrastriate areas around it (Montero, 1993; Olavarria & Montero, 1989; Olavarria et al., 1982; Wang & Burkhalter, 2007). We further confirmed our coordinates for PPC on the basis of projections to associative thalamic nuclei, which corresponded to thalamic projection patterns in rats (Bucci et al., 1999; Chandler et al., 1992; Kolb & Walkey, 1987; Olsen & Witter, 2016), mice (Harvey et al., 2012) and several other mammalian species (Donoghue & Ebner, 1981; Olson & Lawler, 1987; Padberg & Krubitzer, 2006; Schmahmann & Pandya, 1990).

Considering the growing use of mice to study PPC and the networks with which it connects, advancing a straightforward cytoarchitectonic definition of the mouse PPC in relation to nearby areas is increasingly critical. The two major aims of this study were therefore (a) to provide a resource for identifying mouse PPC with anatomical criteria that are evident using ubiquitously available staining methods, such as a Nissl stain, and (b) to define where PPC falls in relation to extrastriate areas around V1. The

first evidence for such areas in mice came from studies of retinotopic processing in striate and extrastriate cortices (Wagor, Mangini, & Pearlman, 1980), with subsequent investigations characterizing them based on anatomical projection patterns from V1 (Olavarria & Montero, 1989; Olavarria et al., 1982). Later work established their connection strengths and retinotopic response properties systematically and at larger scales (Andermann, Kerlin, Roumis, Glickfeld, & Reid, 2011; Garrett, Nauhaus, Marshel, & Callaway, 2014; Marshel, Garrett, Nauhaus, & Callaway, 2011; Wang & Burkhalter, 2007), and their projections to other cortical areas were also mapped (Wang et al., 2012). Since the dorsal cortical surface in rodents lacks gross anatomical landmarks, the pattern of responses in extrastriate areas have provided increasingly-used functional landmarks for locating higher visual (Garrett et al., 2014) and associative regions in the posterior cortex (Driscoll, Pettit, Minderer, Chettih, & Harvey, 2017; Olcese, Iurilli, & Medini, 2013). However, functional mapping of this kind is not feasible in the absence of a broadly expressed calcium indicator or intrinsic optical imaging, and the location of these areas relative to PPC had not been defined explicitly until now.

By characterizing the architectural boundaries of PPC and cross-referencing them with projections from V1, we established that the anterior pole of PPC does not overlap with any extrastriate areas, whereas the posterior sectors of PPC overlap with areas A and AM (see Figure 7 for summary). The most lateral and posterior extent of PPC, area PtP (Paxinos & Franklin, 2012), overlapped partly with anterior area RL. These areas are referred to as "extrastriate", implying a primacy of visual processing (Andermann et al., 2011; Garrett et al., 2014; Marshel et al., 2011; Wang & Burkhalter, 2007), though they overlap considerably with PPC, which has cognitive (Akrami, Kopec, Diamond, & Brody, 2018; Harvey et al., 2012; Hwang et al., 2017; Morcos & Harvey, 2016), navigational (Nitz, 2006, 2012), and movement-related (McNaughton et al., 1994; Whitlock et al., 2012) functions that can be expressed independently of visual input. For example, tetrode recordings in unrestrained rats targeting the posterior extent of PPC—appearing to coincide with area AM—showed widespread tuning to self-motion and angular head velocity in addition to visual landmarks (Chen, Lin, Barnes, & McNaughton, 1994; Chen & McNaughton, 1988). Subsequent work spanning similar cortical territory also reported robust coding of self-motion and landmark positions in egocentric coordinates (Wilber, Skelin, Wu, & McNaughton, 2017; Wilber, Clark, Forster et al., 2014), again indicating roles in behavior beyond purely visual processing, though visual signals or optic flow could contribute to such representations. The exact functions of PPC and surrounding extrastriate areas therefore merit further, systematic investigation outside of passive perceptual tasks, with substantial information likely to be gained from active or freely behaving animals.

Nevertheless, considerable portions of mouse PPC indeed receive input from V1, and its additional connections

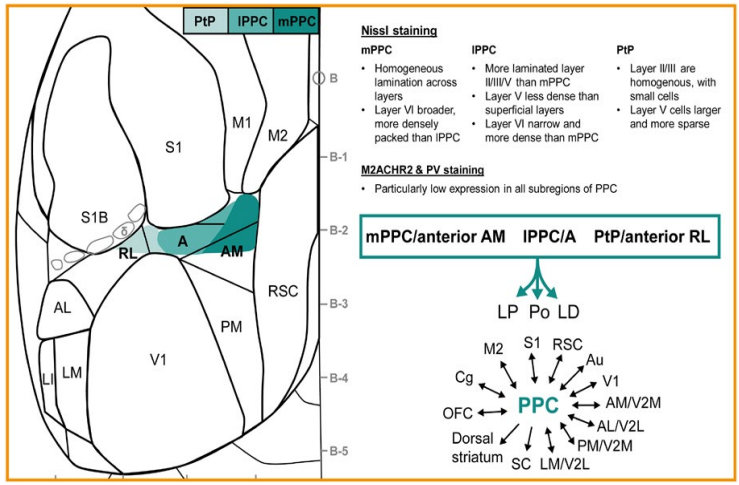

FIGURE 7 Summary of the location, architectural characteristics and connectivity of mouse PPC. (left) Schematic of the dorsal cortical surface with boundaries outlined for major sensory, motor and associative regions. The seven extrastriate areas considered in this study are drawn around V1. Each of the PPC subareas, defined architectonically, are superimposed in color. The anterior pole of PPC does not overlap with any extrastriate areas while, more posteriorly, mPPC overlaps with the anterior portion of area AM, lPPC overlaps extensively with area A, and PtP overlaps with the anterior pole of area RL. Laterally, the posterior row of S1 barrel fields are drawn with the delta barrel labeled. Dimensions are in millimeters and referenced to bregma (B). (right, top) Brief description of distinguishing laminar and cytoarchitectonic features for each PPC subarea. (right, bottom) Summary of thalamic, cortical and subcortical connections of PPC described in the present study, including connections for LM and PM as described by Wang and Burkhalter (2007)

with auditory and somatosensory areas (Zingg et al., 2014) are fully consistent with a role in multisensory processing (Olcese et al., 2013; Raposo, Kaufman, & Churchland, 2014). The parietal connections with frontal cortex likely support a role in elaborating movement, whereas connections with retrosplenial cortex and the dorsal presubiculum (Olsen, Ohara, Iijima, & Witter, 2017; Zingg et al., 2014; Wilber et al., 2014) likely contribute to navigation (Save & Poucet, 2009; Whitlock, Sutherland, Witter, Moser, & Moser, 2008) and, possibly, transformations from first-person to third-person reference frames (Alexander & Nitz, 2015; Byrne, Becker, & Burgess, 2007). The general topological relationship between PPC and these extrinsic systems has been described to various extents across species, including rats (Kolb & Walkey, 1987), cats (Olson & Lawler, 1987), ferrets (Manger, Masiello, & Innocenti, 2002), galagos (Stepniewska et al., 2016), shrews (Remple, Reed, Stepniewska, & Kaas, 2006), new world (Gharbawie, Stepniewska, & Kaas, 2011) and old world monkeys (Cavada & Goldman-Rakic, 1989), and humans (Kaas & Stepniewska, 2016). Assuming that hodology is indicative of information flow, the connections of PPC would enable it to support potentially similar cognitive and behavioral functions in different species (Brunton et al., 2013; Goldring & Krubitzer, 2017; Kaas, 1995; Krubitzer, 1995; Raposo et al., 2012; Whitlock, 2014, 2017), though the relative weight of sensory inputs, for example, could vary according to evolutionary niches. The size and differentiation of PPC also differs substantially across species; in humans it consists of four distinct Brodmann areas 5, 7, 39, and 40 (Brodmann, 1909), while in macaques it includes areas 5 and 7, and in rats only an area 7 has been well described (Krieg, 1946; Olsen & Witter, 2016). Since the vast majority of recording studies in PPC have been in primates, and macaques in particular, the true degree of functional homology across species requires further recordings particularly in rodents, and with a detailed consideration of the animals' sensory processing and behavior.

As for mice, it remains to be mapped more fully where inputs from associative, motor, and sensory areas are integrated synaptically within PPC, and whether graded topographies exists for different sensory modalities, as shown for visual and vibrissal afferents in area RL (Olcese et al., 2013). While the present study focused on characterizing PPC relative to extrastriate projections, comparable mapping could likely be performed in the context of somatosensory, auditory or motor inputs.

ACKNOWLEDGEMENTS

This work was supported by an ERC starting grant (agreement No 335328) to J.R.W., a Research Council of Norway grant to J.R.W. (agreement No 239963), the Centre of Excellence scheme of the Research Council of Norway (Centre for Neural Computation, grant No 223262) and the National Infrastructure scheme of the Research Council of Norway – NORBRAIN, grant No 197467. We thank M. Carandini for helpful comments on the manuscript; G. M. Olsen for technical assistance, aiding with annotation and helpful discussions on comparative labeling in rats and mice; A. Burkhalter for generously sharing the flat map protocol; R.R. Nair and C. Kentros for generously sharing TVA and rabies viruses; H. Kleven and H. Waade for technical and IT assistance; members of the Whitlock lab for helpful discussions.

CONFLICT OF INTERESTS

The authors declare no competing financial interests.

DATA ACCESSIBILITY

Scans and confocal images of tissue used in this study can be made available upon request.

AUTHOR CONTRIBUTIONS

JRW and MPW conceived of and designed the study. KH performed all surgeries and histology. KH and MG analyzed the data. JRW and KH drafted the manuscript with input from MPW and MG.

ORCID

Menno P. Witter https://orcid.org/0000-0003-0285-1637
Jonathan R. Whitlock https://orcid.org/0000-0003-2642-8737

REFERENCES

Akrami, A., Kopec, C. D., Diamond, M. E., & Brody, C. D. (2018). Posterior parietal cortex represents sensory history and mediates its effects on behaviour. *Nature*, *554*, 368–372. https://doi.org/10.1038/nature25510

Alexander, A. S., & Nitz, D. A. (2015). Retrosplenial cortex maps the conjunction of internal and external spaces. *Nature Neuroscience*, *18*, 1143–1151. https://doi.org/10.1038/nn.4058

Andermann, M. L., Kerlin, A. M., Roumis, D. K., Glickfeld, L. L., & Reid, R. C. (2011). Functional specialization of mouse higher visual cortical areas. *Neuron*, *72*, 1025–1039. https://doi.org/10.1016/j.neuron.2011.11.013

Brodmann, K. (1909). *Vergleichende Lokalisationslehre der Grosshirnrinde in ihren Prinzipien dargestellt auf Grund des Zellenbauers*. Leipzig: Verlag von Johann Ambrosius Barth.

Brunton, B. W., Botvinick, M. M., & Brody, C. D. (2013). Rats and humans can optimally accumulate evidence for decision-making. *Science*, *340*, 95–98. https://doi.org/10.1126/science.1233912

Bucci, D. J., Conley, M., & Gallagher, M. (1999). Thalamic and basal forebrain cholinergic connections of the rat

posterior parietal cortex. *NeuroReport*, *10*, 941–945. https://doi.org/10.1097/00001756-199904060-00009

Byrne, P., Becker, S., & Burgess, N. (2007). Remembering the past and imagining the future: A neural model of spatial memory and imagery. *Psychological Review*, *114*, 340–375. https://doi.org/10.1037/0033-295X.114.2.340

Cappe, C., Morel, A., & Rouiller, E. M. (2007). Thalamocortical and the dual pattern of corticothalamic projections of the posterior parietal cortex in macaque monkeys. *Neuroscience*, *146*, 1371–1387. https://doi.org/10.1016/j.neuroscience.2007.02.033

Cavada, C., & Goldman-Rakic, P. S. (1989). Posterior parietal cortex in rhesus monkey: i. Parcellation of areas based on distinctive limbic and sensory corticocortical connections. *The Journal of Comparative Neurology*, *287*, 393–421. https://doi.org/10.1002/(ISSN)1096-9861

Chandler, H. C., King, V., Corwin, J. V., & Reep, R. L. (1992). Thalamocortical connections of rat posterior parietal cortex. *Neuroscience Letters*, *31*, 237–242. https://doi.org/10.1016/0304-3940(92)90273-A

Chen, L. L., Lin, L. H., Barnes, C. A., & McNaughton, B. L. (1994). Head-direction cells in the rat posterior cortex. ii. Contributions of visual and ideothetic information to the directional firing. *Experimental Brain Research. Experimentelle Hirnforschung*, *101*, 24–34. https://doi.org/10.1007/BF00243213

Chen, L. L., & McNaughton, B. L. (1988). Spatially selective discharge of vision and movement modulated posterior parietal neurons in the rat. *Society for Neuroscience*, *14*, 818. https://doi.org/10.1016/j.cell.2014.02.023

Donoghue, J. P., & Ebner, F. F. (1981). The organization of thalamic projections to the parietal cortex of the Virginia opossum. *The Journal of Comparative Neurology*, *198*, 365–388. https://doi.org/10.1002/(ISSN)1096-9861

Driscoll, L. N., Pettit, N. L., Minderer, M., Chettih, S. N., & Harvey, C. D. (2017). Dynamic reorganization of neuronal activity patterns in parietal cortex. *Cell*, *170*, 986–999. https://doi.org/10.1016/j.cell.2017.07.021

D'Souza, R. D., Meier, A. M., Bista, P., Wang, Q., & Burkhalter, A. (2016). Recruitment of inhibition and excitation across mouse visual cortex depends on the hierarchy of interconnecting areas. *Elife*, *5*, e19332.

Garrett, M. E., Nauhaus, I., Marshel, J. H., & Callaway, E. M. (2014). Topography and areal organization of mouse visual cortex. *The Journal of Neuroscience*, *34*, 12587–12600. https://doi.org/10.1523/JNEUROSCI.1124-14.2014

Gharbawie, O. A., Stepniewska, I., & Kaas, J. H. (2011). Cortical connections of functional zones in posterior parietal cortex and frontal cortex motor regions in new world monkeys. *Cerebral Cortex*, *21*, 1981–2002. https://doi.org/10.1093/cercor/bhq260

Goard, M. J., Pho, G. N., Woodson, J., & Sur, M. (2016). Distinct roles of visual, parietal, and frontal motor cortices in memory-guided sensorimotor decisions. *Elife*, *5*, e13764.

Goldring, A., & Krubitzer, L. (2017). Evolution of parietal cortex in mammals: From manipulation to tool use. In L. Krubitzer, & J. H. Kaas (Eds.), *The evolution of nervous systems* (pp. 259–286). London: Elsevier. https://doi.org/10.1016/B978-0-12-804042-3.00086-5

Harvey, C. D., Coen, P., & Tank, D. W. (2012). Choice-specific sequences in parietal cortex during a virtual-navigation decision task. *Nature*, *484*, 62–68. https://doi.org/10.1038/nature10918

Hwang, E. J., Dahlen, J. E., Mukundan, M., & Komiyama, T. (2017). History-based action selection bias in posterior parietal cortex. *Nature Communications*, *8*, 1242. https://doi.org/10.1038/s41467-017-01356-z

Kaas, J. H. (1995). The evolution of isocortex. *Brain, Behavior and Evolution*, *46*, 187–196. https://doi.org/10.1159/000113273

Kaas, J. H., & Stepniewska, I. (2016). Evolution of posterior parietal cortex and parietal-frontal networks for specific actions in primates. *The Journal of Comparative Neurology*, *524*, 595–608. https://doi.org/10.1002/cne.23838

Kolb, B., & Walkey, J. (1987). Behavioural and anatomical studies of the posterior parietal cortex in the rat. *Behavioural Brain Research*, *23*, 127–145. https://doi.org/10.1016/0166-4328(87)90050-7

Krieg, W. J. S. (1946). Connections of the cerebral cortex: I. The albino rat. B. Structure of the cortical areas. *Journal of Comparative Neurology*, *84*, 277–323. https://doi.org/10.1002/(ISSN)1096-9861

Krubitzer, L. (1995). The organization of neocortex in mammals: Are species differences really so different? *Trends in Neuroscience*, *18*, 408–417. https://doi.org/10.1016/0166-2236(95)93938-T

Lim, D. H., Mohajerani, M. H., Ledue, J., Boyd, J., Chen, S., & Murphy, T. H. (2012). In vivo large-scale cortical mapping using Channelrhodopsin-2 stimulation in transgenic mice reveals asymmetric and reciprocal relationships between cortical areas. *Frontiers in Neural Circuits*, *6*, 11.

Manger, P. R., Masiello, I., & Innocenti, G. M. (2002). Areal organization of the posterior parietal cortex of the ferret (*Mustela putorius*). *Cerebral Cortex*, *12*, 1280–1297. https://doi.org/10.1093/cercor/12.12.1280

Marshel, J. H., Garrett, M. E., Nauhaus, I., & Callaway, E. M. (2011). Functional specialization of seven mouse visual cortical areas. *Neuron*, *72*, 1040–1054. https://doi.org/10.1016/j.neuron.2011.12.004

McDaniel, W. F., McDaniel, S. E., & Thomas, R. K. (1978). Thalamocortical projections to the temporal and parietal association cortices in the rat. *Neuroscience Letters*, *7*, 121–125. https://doi.org/10.1016/0304-3940(78)90154-4

McNaughton, B. L., Mizumori, S. J., Barnes, C. A., Leonard, B. J., Marquis, M., & Green, E. J. (1994). Cortical representation of motion during unrestrained spatial navigation in the rat. *Cerebral Cortex*, *4*, 27–39. https://doi.org/10.1093/cercor/4.1.27

Montero, V. M. (1993). Retinotopy of cortical connections between the striate cortex and extrastriate visual areas in the rat. *Experimental Brain Research*, *94*, 1–15.

Morcos, A. S., & Harvey, C. D. (2016). History-dependent variability in population dynamics during evidence accumulation in cortex. *Nature Neuroscience*, *19*, 1672–1681. https://doi.org/10.1038/nn.4403

Nitz, D. A. (2006). Tracking route progression in the posterior parietal cortex. *Neuron*, *49*, 747–756. https://doi.org/10.1016/j.neuron.2006.01.037

Nitz, D. A. (2012). Spaces within spaces: Rat parietal cortex neurons register position across three reference frames. *Nature Neuroscience*, *15*, 1365–1367. https://doi.org/10.1038/nn.3213

Oh, S. W., Harris, J. A., Ng, L., Winslow, B., Cain, N., Mihalas, S., … Zeng, H. (2014). A mesoscale connectome of the mouse brain. *Nature*, *508*, 207–214. https://doi.org/10.1038/nature13186

Olavarria, J., Mignano, L. R., & Van Sluyters, R. C. (1982). Pattern of extrastriate visual areas connecting reciprocally with striate cortex in the mouse. *Experimental Neurology*, *78*, 775–779. https://doi.org/10.1016/0014-4886(82)90090-5

Olavarria, J., & Montero, V. M. (1989). Organization of visual cortex in the mouse revealed by correlating callosal and striate-extrastriate connections. *Visual Neuroscience*, *3*, 59–69. https://doi.org/10.1017/S0952523800012517

Olcese, U., Iurilli, G., & Medini, P. (2013). Cellular and synaptic architecture of multisensory integration in the mouse neocortex. *Neuron*, *79*, 579–593. https://doi.org/10.1016/j.neuron.2013.06.010

Olsen, G. M., Ohara, S., Iijima, T., & Witter, M. P. (2017). Parahippocampal and retrosplenial connections of rat posterior parietal cortex. *Hippocampus*, *27*, 335–358. https://doi.org/10.1002/hipo.22701

Olsen, G. M., & Witter, M. P. (2016). Posterior parietal cortex of the rat: Architectural delineation and thalamic differentiation. *The Journal of Comparative Neurology*, *524*, 3774–3809. https://doi.org/10.1002/cne.24032

Olson, C. R., & Lawler, K. (1987). Cortical and subcortical afferent connections of a posterior division of feline area 7 (area 7p). *The Journal of Comparative Neurology*, *259*, 13–30. https://doi.org/10.1002/(ISSN)1096-9861

Padberg, J., & Krubitzer, L. (2006). Thalamocortical connections of anterior and posterior parietal cortical areas in New World titi monkeys. *The Journal of Comparative Neurology*, *497*, 416–435. https://doi.org/10.1002/(ISSN)1096-9861

Paxinos, G., & Franklin, K. (2012). *Paxino's and Franklin's the mouse brain in stereotaxic coordinates*. (7th edn). San Diego: Elsevier Academic Press.

Paxinos, G., & Watson, C. (2013). *The rat brain in stereotaxic coordinates*. (7th edn). San Diego: Elsevier Academic Press.

Raposo, D., Kaufman, M. T., & Churchland, A. K. (2014). A category-free neural population supports evolving demands during decision-making. *Nature Neuroscience*, *17*, 1784–1792. https://doi.org/10.1038/nn.3865

Raposo, D., Sheppard, J. P., Schrater, P. R., & Churchland, A. K. (2012). Multisensory decision-making in rats and humans. *The Journal of Neuroscience*, *32*, 3726–3735. https://doi.org/10.1523/JNEUROSCI.4998-11.2012

Reep, R. L., Chandler, H. C., King, V., & Corwin, J. V. (1994). Rat posterior parietal cortex: Topography of corticocortical and thalamic connections. *Experimental Brain Research*, *100*, 67–84.

Remple, M. S., Reed, J. L., Stepniewska, I., & Kaas, J. H. (2006). Organization of frontoparietal cortex in the tree shrew (Tupaia belangeri). I. Architecture, microelectrode maps, and corticospinal connections. *The Journal of Comparative Neurology*, *497*, 133–154. https://doi.org/10.1002/(ISSN)1096-9861

Save, E., & Poucet, B. (2009). Role of the parietal cortex in long-term representation of spatial information in the rat. *Neurobioligy of Learning and Memory*, *91*, 172–178. https://doi.org/10.1016/j.nlm.2008.08.005

Schmahmann, J. D., & Pandya, D. N. (1990). Anatomical investigation of projections from thalamus to posterior parietal cortex in the rhesus monkey: A WGA-HRP and fluorescent tracer study. *The Journal of Comparative Neurology*, *295*, 299–326. https://doi.org/10.1002/(ISSN)1096-9861

Stepniewska, I., Cerkevich, C. M., & Kaas, J. H. (2016). Cortical connections of the caudal portion of posterior parietal cortex in Prosimian Galagos. *Cerebral Cortex*, *26*, 2753–2777. https://doi.org/10.1093/cercor/bhv132

Wagor, E., Mangini, N. J., & Pearlman, A. L. (1980). Retinotopic organization of striate and extrastriate visual cortex in the mouse. *The Journal of Comparative Neurology*, *193*, 187–202. https://doi.org/10.1002/(ISSN)1096-9861

Wang, Q., & Burkhalter, A. (2007). Area map of mouse visual cortex. *The Journal of Comparative Neurology*, *502*, 339–357. https://doi.org/10.1002/(ISSN)1096-9861

Wang, Q., Sporns, O., & Burkhalter, A. (2012). Network analysis of corticocortical connections reveals ventral and dorsal processing streams in mouse visual cortex. *The Journal of Neuroscience*, *32*, 4386–4399. https://doi.org/10.1523/JNEUROSCI.6063-11.2012

Whitlock, J. R. (2014). Navigating actions through the rodent parietal cortex. *Frontiers in Human Neuroscience*, *8*, 293.

Whitlock, J. R. (2017). Posterior parietal cortex. *Current Biology*, *27*, R691–R695. https://doi.org/10.1016/j.cub.2017.06.007

Whitlock, J. R., Pfuhl, G., Dagslott, N., Moser, M. B., & Moser, E. I. (2012). Functional split between parietal and entorhinal cortices in the rat. *Neuron*, *73*, 789–802. https://doi.org/10.1016/j.neuron.2011.12.028

Whitlock, J. R., Sutherland, R. J., Witter, M. P., Moser, M. B., & Moser, E. I. (2008). Navigating from hippocampus to parietal cortex. *Proceedings of the National Academy of Sciences of the United States of America*, *105*, 14755–14762. https://doi.org/10.1073/pnas.0804216105

Wickersham, I. R., Lyon, D. C., Barnard, R. J., Mori, T., Finke, S., Conzelmann, K. K., … Callaway, E. M. (2007). Monosynaptic restriction of transsynaptic tracing from single, genetically targeted neurons. *Neuron*, *53*, 639–647. https://doi.org/10.1016/j.neuron.2007.01.033

Wilber, A. A., Clark, B. J., Demecha, A. J., Mesina, L., Vos, J. M., & McNaughton, B. L. (2014). Cortical connectivity maps reveal anatomically distinct areas in the parietal cortex of the rat. *Frontiers in Neural Circuits*, *8*, 146.

Wilber, A. A., Clark, B. J., Forster, T. C., Tatsuno, M., & McNaughton, B. L. (2014). Interaction of egocentric and world-centered reference frames in the rat posterior parietal cortex. *The Journal of Neuroscience*, *34*, 5431–5446. https://doi.org/10.1523/JNEUROSCI.0511-14.2014

Wilber, A. A., Skelin, I., Wu, W., & McNaughton, B. L. (2017). Laminar organization of encoding and memory reactivation in the parietal cortex. *Neuron*, *95*, 1406–1419 e1405. https://doi.org/10.1016/j.neuron.2017.08.033

Wise, S. P., Boussaoud, D., Johnson, P. B., & Caminiti, R. (1997). Premotor and parietal cortex: Corticocortical connectivity and combinatorial computations. *Annual Review of Neuroscience*, *20*, 25–42. https://doi.org/10.1146/annurev.neuro.20.1.25

Zingg, B., Hintiryan, H., Gou, L., Song, M. Y., Bay, M., Bienkowski, M. S., … Dong, H. W. (2014). Neural networks of the mouse neocortex. *Cell*, *156*, 1096–1111.

SUPPORTING INFORMATION

Additional supporting information may be found online in the Supporting Information section at the end of the article.

How to cite this article: Hovde K, Gianatti M, Witter MP, Whitlock JR. Architecture and organization of mouse posterior parietal cortex relative to extrastriate areas. *Eur J Neurosci*. 2018;00:1–17. https://doi.org/10.1111/ejn.14280

Paper 2

frontiers in Systems Neuroscience

ORIGINAL RESEARCH
published: 21 August 2019
doi: 10.3389/fnsys.2019.00038

Organization of Posterior Parietal–Frontal Connections in the Rat

*Grethe M. Olsen†, Karoline Hovde†, Hideki Kondo‡, Teri Sakshaug, Hanna Haaland Sømme, Jonathan R. Whitlock and Menno P. Witter**

The Faculty of Medicine, Kavli Institute for Systems Neuroscience, Centre for Neural Computation, Egil and Pauline Braathen and Fred Kavli Centre for Cortical Microcircuits, NTNU—Norwegian University of Science and Technology, Trondheim, Norway

OPEN ACCESS

Edited by:
Gilad Silberberg, Karolinska Institute (KI), Sweden

Reviewed by:
Jared Brent Smith, Salk Institute for Biological Studies, United States
Paolo Medini, Umeå University, Sweden

***Correspondence:**
Menno P. Witter
menno.witter@ntnu.no

†These authors have contributed equally to this work and share the first authorship

‡Present Address:
Hideki Kondo, CSHL Cold Spring Harbor Laboratory, One Bungtown Road, Cold Spring Harbor, NY, United States

Received: *26 May 2019*
Accepted: *29 July 2019*
Published: *21 August 2019*

Citation:
Olsen GM, Hovde K, Kondo H, Sakshaug T, Sømme HH, Whitlock JR and Witter MP (2019) Organization of Posterior Parietal–Frontal Connections in the Rat. Front. Syst. Neurosci. 13:38. doi: 10.3389/fnsys.2019.00038

Recent investigations of the rat posterior parietal cortex (PPC) suggest that this region plays a central role in action control together with the frontal cortical areas. Posterior parietal-frontal cortical connections have been described in rats, but little is known about whether these connections are topographically organized as in the primate. Here, we injected retrograde and anterograde tracers into subdivisions of PPC as well as the frontal midline and orbital cortical areas to explore possible topographies within their connections. We found that PPC projects to several frontal cortical areas, largely reciprocating the densest input received from the same areas. All PPC subdivisions are strongly connected with the secondary motor cortex (M2) in a topographically organized manner. The medial subdivision (medial posterior parietal cortex, mPPC) has a dense reciprocal connection with the most caudal portion of M2 (cM2), whereas the lateral subdivision (lateral posterior parietal cortex, lPPC) and the caudolateral subdivision (PtP) are reciprocally connected with the intermediate rostrocaudal portion of M2 (iM2). Sparser reciprocal connections were seen with anterior cingulate area 24b. mPPC connects with rostral, and lPPC and PtP connect with caudal parts of 24b, respectively. There are virtually no connections with area 24a, nor with prelimbic or infralimbic cortex. PPC and orbitofrontal cortices are also connected, showing a gradient such that mPPC entertains reciprocal connections mainly with the ventral orbitofrontal cortex (OFC),

Abbreviations: Brain areas: 24a, anterior cingulate area 24a; 24b, anterior cingulate area 24b; ACC, anterior cingulate cortex; Cl, claustrum; cM2, caudal secondary motor cortex; DLO, dorsolateral orbitofrontal cortex; iM2, intermediate secondary motor cortex; IL, infralimbic cortex; Ins, insular cortex; LO, lateral orbitofrontal cortex; lPPC, lateral posterior parietal cortex; M1, primary motor cortex; M2, secondary motor cortex; MO, medial orbitofrontal cortex; mPPC, medial posterior parietal cortex; OFC, orbitofrontal cortex; PL, prelimbic cortex; PPC, posterior parietal cortex; PtP, caudolateral posterior parietal cortex; rM2, rostral secondary motor cortex; RSC, retrosplenial cortex; S1, primary somatosensory cortex; V1, primary visual cortex; V2, secondary visual cortex; V2L, lateral secondary visual cortex; V2M, medial secondary visual cortex; VLO, ventrolateral orbitofrontal cortex; VO, ventral orbitofrontal cortex. **Others:** BDA, biotinylated Dextran amine; C, caudal; DAB, 3,3′-diaminobenzidine tetrahydrocholoride; DMSO, dimethylsulfoxide; FB, Fast Blue; FG, Fluorogold; L, lateral; M, medial; PHA-L, *Phaseolus vulgaris* agglutinin; R, rostral.

whereas lPPC and PtP are preferentially connected with medial and central portions of ventrolateral OFC, respectively. Our results thus indicate that the connections of PPC with frontal cortices are organized in a topographical fashion, supporting functional heterogeneity within PPC and frontal cortices.

Keywords: anterograde tracer injections, retrograde tracer injections, immunohistochemistry, cingulate cortex, motor cortex, orbitofrontal cortex, posterior parietal cortex

INTRODUCTION

The posterior parietal cortex (PPC) is a multimodal association area, proposed to play a role in a variety of higher cognitive functions. In the rat, many functional studies of PPC have focused on its role in spatial navigation (Kolb and Walkey, 1987; Chen et al., 1994a,b; Save and Moghaddam, 1996; Save and Poucet, 2000; Save et al., 2005; Nitz, 2006, 2012). In contrast, in the non-human primate, the focus has been on a presumed function in action control and therefore on the interaction between PPC and frontal cortices (Cavada and Goldman-Rakic, 1989b; Andersen et al., 1990; Pesaran et al., 2008; Gharbawie et al., 2011; Stepniewska et al., 2011). In humans, the early exemplary role of parts of PPC were described in terms of contralateral neglect (Mesulam, 1999; Corbetta and Shulman, 2011) and, interestingly, comparable deficits have been reported in monkeys (Deuel and Regan, 1985) and rats (King and Corwin, 1993; Burcham et al., 1997).

Probing and comparing the functional relevance of PPC has been complicated by the fact that the physical location and delineation of PPC in different species is disputed, and an overall consensus on whether the PPC in different species actually is a homologous area is lacking (Olsen and Witter, 2016). For example, even within the rat, the delineation and functional division of PPC has been variable (for a review, see Whitlock et al., 2008). In a recent study, we defined PPC in the rat on the basis of a combination of cyto- and chemo-architectonic criteria and patterns of thalamic connectivity. This resulted in a reliable subdivision into three domains: a medial (mPPC), lateral (lPPC) and caudolateral (PtP) subdivision (Olsen and Witter, 2016). In the mouse, the position and definition of the main borders of PPC with its neighbors, the visual, somatosensory, and motor cortices and the subdivisions used here are comparable (Hovde et al., 2018), although some authors additionally differentiate nearby subareas in mice based on projections from primary visual cortex and their specific visual properties (areas RL, A, AM, Wang and Burkhalter, 2007; Wang et al., 2011).

Since early functional studies of the rat PPC focused on the role of this region in spatial navigation, we recently investigated the connections between PPC and the cortical regions most critical for such behavior, the hippocampal and parahippocampal regions, and found that this connectivity in general, was sparse, with the exception of projections to the presubiculum. We additionally described projections to retrosplenial cortex (RSC; Olsen et al., 2017). It is therefore unlikely that PPC provides a functional signal that is directly relevant for the emergence of spatially modulated neurons found in the hippocampal-projecting medial entorhinal cortex, such as grid cells, border cells, head direction cells or speed cells (Fyhn et al., 2004; Hafting et al., 2005; Sargolini et al., 2006; Solstad et al., 2008; Kropff et al., 2015). In parallel, there has been an increasing interest in the communication between PPC and frontal cortex in rodents (King and Corwin, 1992, 1993; Burcham et al., 1997; Erlich et al., 2015; Hanks et al., 2015), especially their respective roles in decision-making, which complements the long history of work on similar topics in primates. Recent work has also confirmed that similar projections link PPC and frontal cortical areas in mice (Hovde et al., 2018). However, in contrast to thorough analyses in the non-human primate, where these connections have been found to be topographically organized (Pandya and Kuypers, 1969; Petras, 1971; Mesulam et al., 1977; Cavada and Goldman-Rakic, 1989b; Andersen et al., 1990; Neal et al., 1990; Lewis and Van Essen, 2000; Rozzi et al., 2006), data on posterior parietal-frontal cortical connectivity in rodents is less detailed, confounding functional analyses of their interactions. Reciprocal connections of PPC with frontal midline and orbital cortices have been described (Reep et al., 1984, 1987, 1990, 1994, 1996; Kolb and Walkey, 1987; Condé et al., 1995; Hoover and Vertes, 2007, 2011), but to our knowledge no studies have systematically investigated the specificity of the organization of these connections, in particular how the three PPC subdivisions described previously (Olsen and Witter, 2016) relate to the frontal cortex. Thus, the present study aims to illuminate the topographical organization of the posterior parietal-frontal cortical connections in the rat.

MATERIALS AND METHODS

Animals and Surgeries

All experimental procedures followed approved protocols that adhere to national and EU regulations. We analyzed 74 injections of anatomical tracers in 61 Sprague–Dawley rats (58 females, three males, 180–230 g at the time of surgery; Charles River, Sulzfeld/Kisslegg, Germany). The majority of the material (65 cases) described here was obtained in previous studies and methods for tracer injections, perfusions and histology are described in detail there (Kondo and Witter, 2014; Olsen and Witter, 2016). To complement the already existing material, a few cases were prepared with successful injections of anterograde tracers in the dorsolateral part of the orbitofrontal cortex (DLO; $N = 1$) and M2 ($N = 3$), as well as injections of retrograde tracers in the ventral and ventrolateral orbital cortex (VO/VLO region; $N = 5$).

In short, animals were deeply anesthetized and injected with retrograde and/or anterograde tracers in the parietal,

orbitofrontal and medial frontal domains of the cortex. As retrograde tracers, we used Fast Blue (EMS Chemie, Domat/Ems, Switzerland, catalog number 9000002; 1% in 0.125 M phosphate buffer), and Fluorogold (Fluorochrome, Denver, CO, USA; 2.5% in H_2O). For anterograde tracing, *Phaseolus vulgaris* Leucoagglutinin (PHA-L, Vector Laboratories, Burlingame, CA, USA, catalog number L-1110; 2.5% in 0.01 M phosphate buffer) and 10 kDa biotinylated dextran amine (BDA, Invitrogen, Molecular Probes, Eugene, OR, USA, catalog number D1956, RRID:AB_2307337; 5% solution in 0.125 M phosphate buffer) were used.

Rats were anesthetized with Isoflurane and injected i.p. with atropine (Nycomed, Zürich, Switzerland, 0.04 mg/kg) and rimadyl (Pfizer, New York, NY, USA, 5 mg/kg) and placed in a stereotaxic frame (Kopf Instruments, Tujunga, CA, USA). During surgery, we maintained a constant body temperature of 37°C. Stereotaxic coordinates were determined using Bregma and the mid-sagittal sinus as rostral-caudal and medial-lateral reference points, respectively, using a stereotaxic atlas as a guide (Paxinos and Watson, 2007). Retrograde tracers were pressure-injected into the brain through 1 μl Hamilton syringes. Iontophoretic injections of anterograde tracers were performed using glass micropipettes with an outer tip diameter of 15–25 μm (alternating currents, 6 s on/6 s off, 6 μA for BDA and 7 μA for PHA-L). During the surgery, the rat was given saline subcutaneously to avoid dehydration. Upon completion of injections, the wound was cleaned and sutured, and the animal was allowed to recover in a heat chamber before being returned to its home cage.

Perfusion and Tissue Processing

After a survival time of 1–2 weeks to allow for complete transport of the tracers, the animals were anesthetized and transcardially perfused with Ringer solution (37°C) followed by freshly depolymerized 4% paraformaldehyde (pH 7.4). The brains were extracted and post-fixed in the perfusion fixative overnight. After being cryoprotected in a DMSO/glycerol solution at least overnight, six equally spaced series of 50 μm coronal sections were prepared on a freezing microtome. One series was mounted on Superfrost plus-slides and stained with cresyl violet for cytoarchitectural orientation. For brains containing fluorescent retrograde tracers, one series was mounted on uncoated microscope slides for analysis of labeling without any further processing, and one series of the brains containing anterograde tracers was processed to reveal the transport of BDA and PHA-L following standard (immuno)histochemical protocols for free-floating sections. Fluorescent molecules or the photostable molecule 3,3′-diaminobenzidine tetrahydrochloride (DAB, Sigma-Aldrich, St. Louis, MO, USA; catalog number D5905) were used as chromophores (for further details see Olsen and Witter, 2016).

Imaging and Analyses

In order to delineate the PPC, the frontal midline cortex, and the OFC, we used Nissl stained sections at appropriate levels. Images were obtained using a Mirax-midi scanner with a white light source (objective 20×, NA0.8; Carl Zeiss MicroImaging, Jena, Germany), or a Zeiss Axio Imager M2 microscope (Carl Zeiss MicroImaging). Using Adobe Photoshop CS6 (Adobe Systems Incorporated, San Jose, CA, USA), the images were converted to grayscale images, and the images were adjusted using the Levels function to improve the illustration of the cytoarchitecture of the cortical areas. Mainly, the black point was set to higher values whereas the gamma value was decreased to better visualize Nissl labeled cell bodies. The adjusted images were imported to Adobe Illustrator CS6 (Adobe Systems Incorporated), and borders of cortical areas were added.

Representative cases were selected for illustration of labeling patterns. For all tracer injections, labeling patterns are shown in the ipsilateral hemisphere, and for illustration purposes, all injections are shown as being in the right hemisphere although a few were in the left hemisphere. Retrogradely labeled cell bodies were mapped using a microscope connected to a computer with Neurolucida software (MicroBrightField, Colchester, VT, USA). The resulting maps were overlaid with images of adjacent Nissl-stained sections in Adobe Illustrator CS6 and the regions of interest were delineated. To illustrate anterogradely labeled fibers, images were obtained using a Mirax-midi scanner with a fluorescent or white light source, or a Zeiss Axio Imager M2 microscope. Pictures of DAB labeled fibers were turned into pseudo-dark-field images or grayscale images, whereas images of fluorescent labeled fibers were exported as grayscale images. Brightness and contrast were adjusted in Adobe Photoshop CS6 to improve visualization of the labeled fibers. Due to the generally dim nature of the images, the white point was shifted to lower values and the gamma value was increased. The position of labeled elements was determined using adjacent Nissl stained sections from the same brains allowing for the delineation of regions of interest with the use of Adobe Illustrator CS6.

Flatmap Illustrations

To illustrate connections between PPC and frontal midline cortex, three different representations were used. First, we illustrated the location and density of labeled neurons and fibers in actual histological sections, either as drawings or as images. Second, a grayscale table was produced for each representative case of retrograde tracer injected in PPC. To this end, every section along the rostrocaudal axis of a specific cortical area was delineated, and the density of retrogradely labeled cells was scored subjectively for each cortical area with the densest labeling in each experiment being indicated by the darkest gray. The results were plotted in an Excel table, where each column represents a coronal section and each row represents a cortical area in that section. Third, standardized representations of the location of projections/labeled fibers from each subregion of PPC to the superficial layers of frontal midline cortex were produced. These normalized "flatmaps" contained the average of projections across five cases for each PPC subregion. Seven cases were excluded from this analysis due to tilted cutting angle, poor images or missing tissue. However, the overall labeling in the excluded brains was the same as for the included cases. To create the flatmap representations, every section along the rostrocaudal axis of areas 24a, 24b, M2 and M1 was delineated. The distance from the medial border to labeled fibers was measured through

layer 2/3, and the density of labeling was subjectively scored on a scale from 0 to 5 for each cortical area, 0 indicating no labeling. Further, the scale was normalized for each brain such that "5" corresponded to the strongest labeling in M2 in that brain, since M2 contained the heaviest labeling in all cases. The sections across brains were aligned using the level at which the forceps minor, the genu of corpus callosum and CA3 appeared in coronal sections. The sections were spaced 0.3 mm apart and assigned corresponding Bregma levels that were then used by a custom-made Matlab script to generate the flatmaps as described in detail below.

Individual Flatmaps

Given that the thickness of each brain section was 50 μm and the distance between brain sections was slightly variable, the intermediate values for the total lengths of the region borders were linearly interpolated using 50 μm intervals. In order to use an equilateral square pixel as the basic unit of the reconstructed flatmap of the regions, the total lengths at each point in the rostro-caudal axis were divided by 50 μm units. The intermediary product, the region outline flatmap, consisted of a row of contiguous columns of pixels, with the number of pixels in each column given by the total length of that region at that rostrocaudal coordinate. Next, the region outline flatmap was filled with the values of labeled fiber densities. Taking into consideration that the density values were registered at non-contiguous points in the rostrocaudal axis of the flatmap, it was necessary to assign them at the corresponding columns in the map and interpolate the values of the columns in between. For the columns where labeled fiber intensity data were available, the partial lengths for each block were divided by 50 μm units, and rounded to the nearest integer, which gave the number of pixels that was assigned to the corresponding value of intensity measured. The blocks were assigned starting at the unit nearest to the region's 24b/M2 border and moving laterally. Once the assigned columns were filled, a three-step process was used to fill the intermediary columns. (1) For each pair of consecutively filled columns, the length of the longest column of the two was taken as reference. The shortest of the two columns was then stretched to the same length as the reference, using a nearest neighbor interpolation algorithm with rounding to the nearest integer, such that the proportional size of the blocks was preserved in the stretched column. This step was tested with examples in order to assure that the process is faithful during reversal, i.e., the block distribution is similar to the original when the column is set back to its original length. When both columns were adjusted to the same length, they were set as the first and the last column in a rectangle. This rectangle width was dependent on the distance between two consecutive filled sections, divided by the lateral length of the unitary pixel (50 μm). (2) A linear interpolation algorithm was used to fill the intermediary pixels on each row of the rectangle, followed by rounding each pixel to the nearest integer. (3) Every column of the group being processed was adjusted back to the length value calculated previously for the corresponding position of the rostrocaudal axis in the region outline flatmap. This step was achieved using the same nearest neighbor interpolation algorithm, with rounding to the nearest integer that was used on the first step of the process. This process was repeated for all pairs of consecutively filled columns. At the end of this iterative process, a region flatmap with continuous values of labeled fiber density had been created. The four regions (regions 24a, 24b, M2 and M1) were assembled into a final flatmap. This was done by iteratively joining the rostrocaudal coordinates of the corresponding columns of each of the individual flatmaps, starting at the most medial region at the bottom and proceeding through all the regions to the most lateral at the top. White lines were plotted at the junction points in order to visually separate the four regions. Regions with the densest labeling in each experiment are indicated by the brightest color. For individual maps, see **Supplementary Figure S1**.

Two important arbitrary aspects were assumed in order to calculate the average flatmaps. The first was that the process of averaging was done individually for every region, and the final result was the product of assembling the four region maps together. The second was that the areas of the average region maps did not reflect the mean of the areas of all the individual maps. Rather, the largest of all the individual maps was used as reference and the data from the smaller maps was stretched to its size. This was done because stretching and interpolating a set of two-dimensional data does not lead to loss of data, whereas the opposite process can. Another reason was that there were small variations in the shapes of the individual maps, so by doing this, the average flatmaps were close to the ones of their origin. The algorithm used is similar to that used for flatmaps in Sugar and Witter (2016), where a graphical representation of the algorithm is provided.

RESULTS

Topography and Delineations of Cortical Areas

The PPC in the rat is situated dorsally in the brain, between the somatosensory parietal and visual occipital domains, and comprises three subdivisions, the medial (mPPC), lateral (lPPC) and the caudolateral (PtP) PPC (**Figure 1**; Olsen and Witter, 2016). mPPC is characterized by a homogenous appearance, whereas lPPC is perceived as slightly more laminated due to a sparsely populated layer 5. A defining feature of area PtP is the small and weakly stained cells of layer 3/4.

The medial surface of the rat frontal cortex comprises several distinct areas (**Figure 2**; Jones et al., 2005; Vogt and Paxinos, 2014). At rostral levels, prelimbic cortex (PL) is found ventral to the rostral secondary motor cortex (rM2) and dorsal to orbitofrontal cortex (OFC). Throughout most of its rostrocaudal extent, M2 is bordered laterally by primary motor cortex (M1). Approximately at the level of the forceps minor of the corpus callosum, the anterior cingulate cortical (ACC) area 24b is wedged between PL and rM2, and infralimbic cortex (IL) is seen ventral to PL (**Figure 2B**). At the level of the genu of the corpus callosum, IL and PL disappear and ACC area 24a is situated between the corpus callosum and area 24b (**Figure 2D**). Caudally, at the level where the hippocampus appears, areas 24a

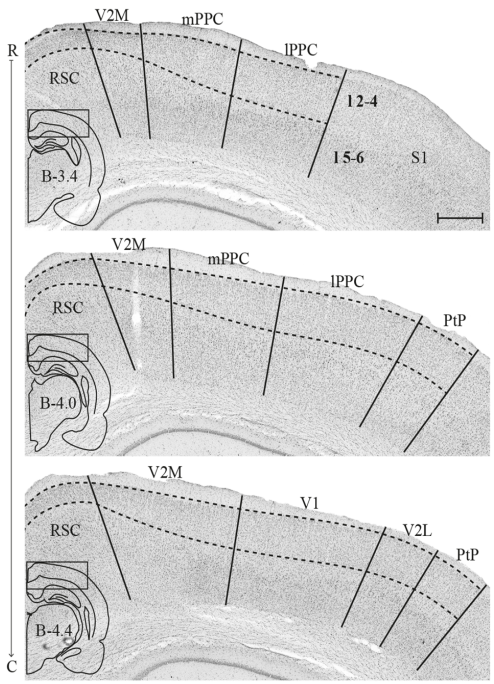

FIGURE 1 | Delineation of posterior parietal cortex (PPC) and adjacent areas. Coronal sections containing PPC, arranged from rostral to caudal (indicated as R–C). Solid lines indicate borders between cortical areas and dashed lines demarcate cortical layers. Insets outline the hemisphere of the depicted coronal section and the area shown. Bregma levels are approximate and according to Paxinos and Watson (2007). Scale bar: 500 μm.

and 24b are replaced by retrosplenial cortex (RSC, not shown). The IL is the least differentiated of the frontal midline areas, it is poorly laminated and the border between layers 1 and 2/3 is particularly irregular. The dorsally adjacent PL is characterized by large, darkly stained cells in layer 5 and densely packed cells in layer 2. In area 24b, dorsal to PL in rostral sections, cells in layer 2 are darkly stained. Layer 5 is broad and contains a large number of pyramidal neurons. In area 24a, ventral to 24b at more caudal levels, cells are distributed homogenously across layers and 24a thus appears less laminated than 24b. In addition, superficial cells have larger somata in area 24a than in area 24b. Lateral to 24b, M2 comprises narrow superficial layers where layer 3 is weakly stained, and layer 5 appears homogenous and densely packed. On the basis of differences in connectivity, M2 has been divided into three parts along its rostrocaudal axis, the rostral part (rM2) being situated rostral to the genu of the corpus callosum, the intermediate part extending from the genu to the anterior commissure (iM2), and the caudal M2 (cM2) that extends from the anterior commissure until it is replaced caudally by the medial secondary visual cortex (Reep et al., 1990; Olsen and Witter, 2016). Similarly, area 24b has been hypothesized to contain three rostrocaudal divisions, of which the rostral portion is situated rostral to the genu of the corpus callosum (Jones et al., 2005).

The OFC is situated ventrally and rostrally in the rat brain, on the dorsal bank of the rostral extension of the rhinal fissure. From medial to lateral, OFC comprises a medial (MO), ventral (VO), ventrolateral (VLO), lateral (LO), and dorsolateral (DLO) subdivision (**Figure 3**; Kondo and Witter, 2014). MO and VO constitute the medial bank of the rhinal fissure, VLO sits around the notch of the fissure, and LO and DLO are situated on the lateral bank. MO is bordered dorsally by PL at rostral levels and IL at caudal levels, whereas the insular cortex constitutes the dorsolateral border of DLO. OFC subdivisions are most easily distinguished based on the morphology of their superficial layers, whereas deep layers of this cortex are more homogenous and thus difficult to separate. MO layer 2 is sparsely populated with patches of cells, and the transition between layers 2 and 3 is diffuse. In the laterally adjacent area VO, superficial layers contain smaller cells than in MO. VO is overall more sparsely populated than its neighboring areas, giving it a homogenous appearance. VLO is densely packed with cells across layers and is particularly characterized by columns of cells in layer 2, organized perpendicular to the pia. LO layer 2 contains large, clustered cells, whereas layer 3 cells are small and densely clustered. DLO is distinguished from LO by comparatively larger cells in layer 3.

Characterization of Injection Sites

Tracer injections in the PPC were described in detail in a previous study where the positions of the injections were characterized based on the cytoarchitecture of the area as well as the resulting thalamic labeling pattern (Olsen and Witter, 2016). A surface representation of the cores of the retrograde and anterograde injection sites is given in **Figures 3G,P** and **Figures 5–7G**, respectively. In general, retrograde tracer injections tended to diffuse more and were more likely to extend into adjacent cortical areas compared to anterograde tracer injections.

Injections of anterograde tracers in MO, VO, VLO and LO of OFC were part of a previous study, in which the injections were described extensively (Kondo and Witter, 2014). However, the latter study did not include tracer injections in DLO, nor did it include injections of retrograde tracers in OFC. Therefore, we supplemented the material with one injection of anterograde tracer in DLO (not shown) as well as five injections of retrograde tracers in the VO/VLO areas. In addition to the surface representations of the injection sites illustrated here and in previous studies, all illustrations of labeled neurons or fibers in the present study include a representation of the core of the tracer injection site as seen in a coronal section.

Connections of PPC with Frontal Midline Areas

Input to PPC From Frontal Midline Areas

We analyzed seven injections of retrograde tracers in PPC, four in mPPC and three in lPPC, since we, unfortunately, did not obtain selective injections of retrograde tracers in PtP. All injections resulted in highest densities of labeled cells in M2, with less labeling in other frontal midline areas (mPPC; **Figures 3A–F,I**, lPPC; **Figures 3J–O,P**). In a representative case, Fast Blue was

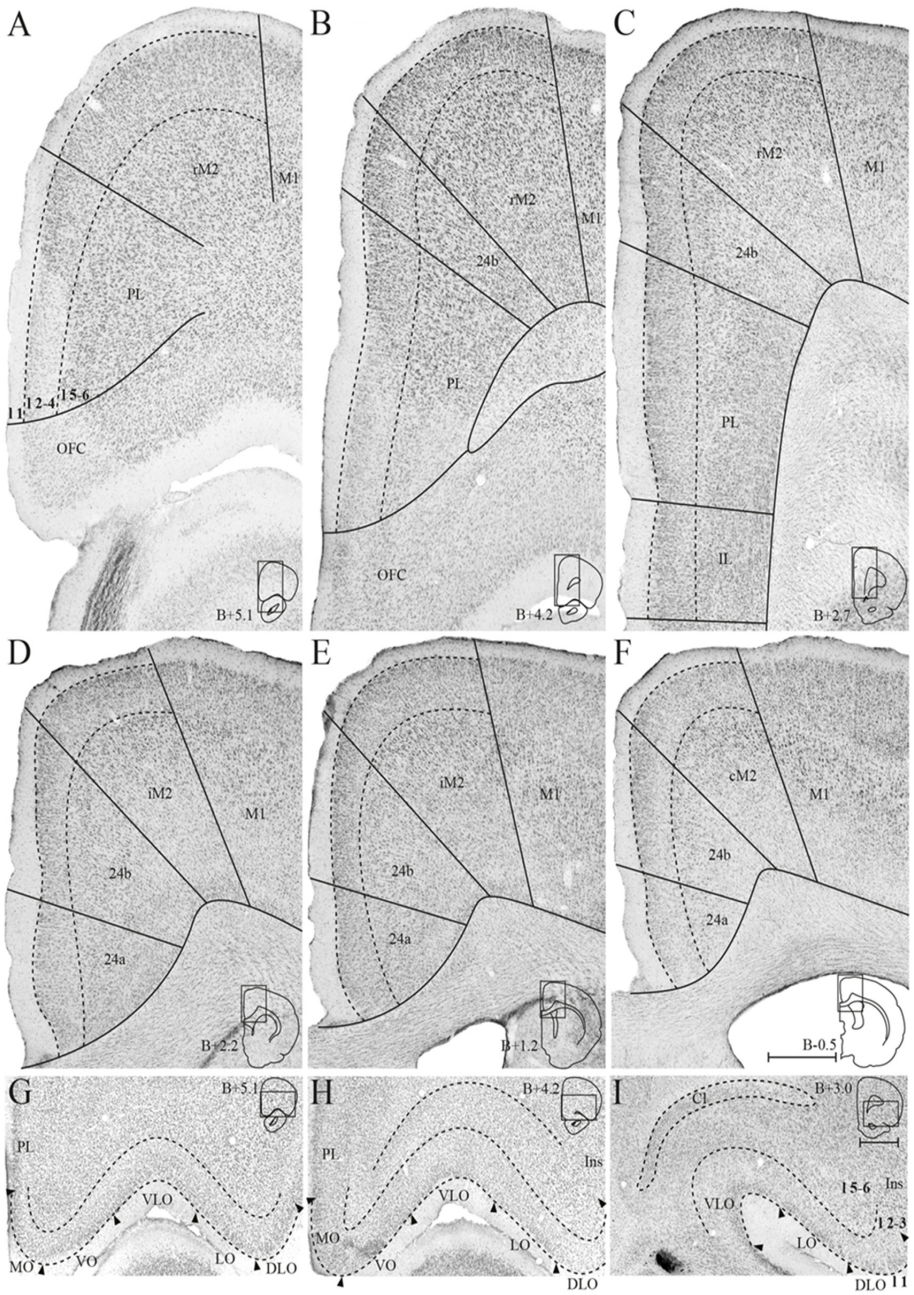

FIGURE 2 | Delineation of the frontal midline and orbitofrontal cortices. Coronal sections containing the frontal midline cortex **(A–F)** and the orbitofrontal cortex (OFC; **G–I**), arranged from rostral to caudal. Solid lines **(A–F)** and black arrowheads **(G–I)** indicate borders between cortical areas and dashed lines demarcate cortical layers. Insets on the right outline the hemisphere of the depicted coronal section and the area shown. Bregma levels are approximate and according to Paxinos and Watson (2007). Scale bar: 500 μm.

injected rostrally in mPPC (**Figures 3G,H**). Throughout the rostrocaudal length of the frontal midline cortex, retrogradely labeled cells were seen in M2 (**Figures 3A–F,I**), though labeling was especially dense in the most caudal parts (**Figure 3F**). We observed labeled neurons across all layers but with a denser concentration in layer 5. Retrogradely labeled cells were also

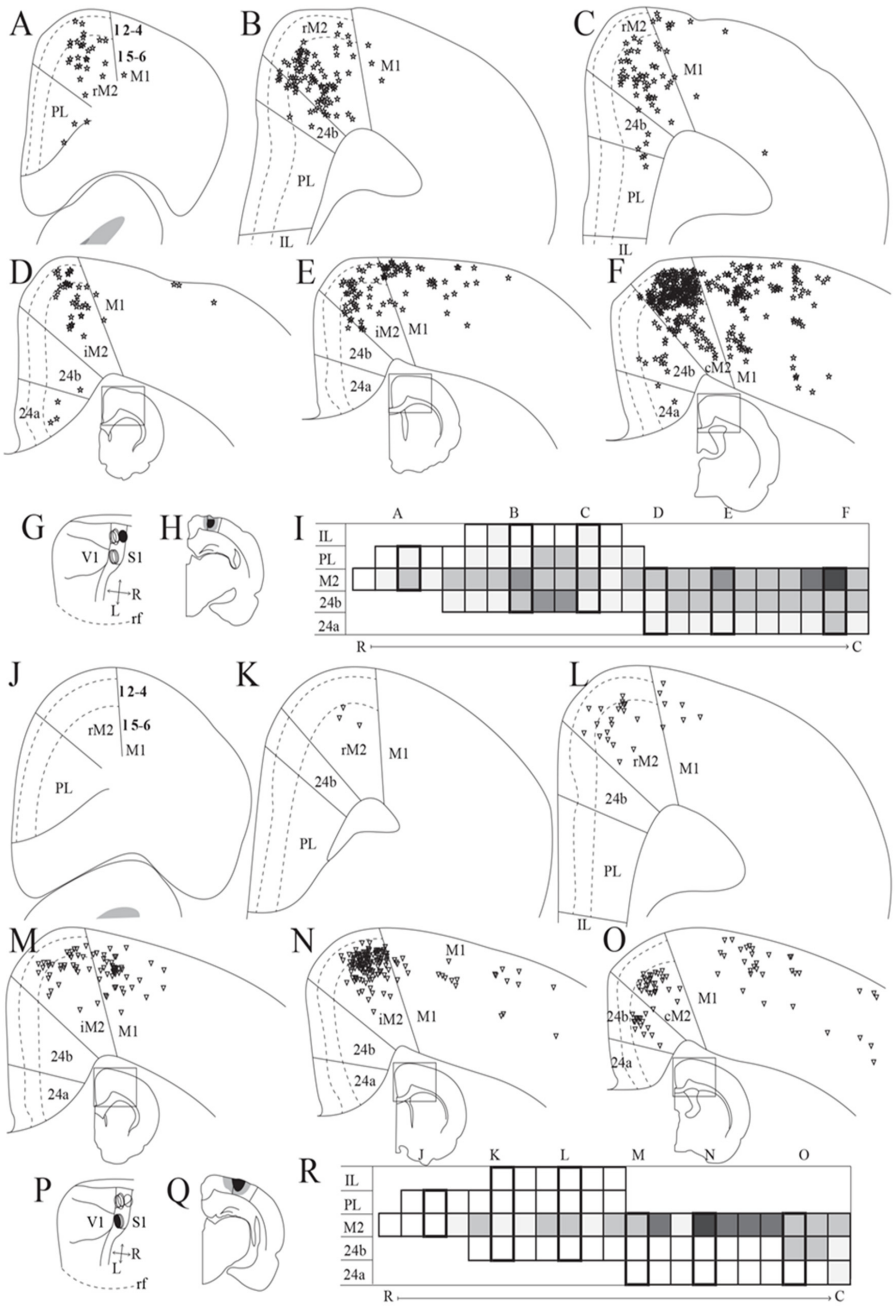

FIGURE 3 | Frontal midline cortical input to PPC. Retrogradely labeled cells in the frontal midline cortex resulting from an injection of Fast Blue in medial PPC (mPPC; **A–F**, labeled cells represented with stars) and Fluorogold in lateral PPC (lPPC; **J–O**, labeled cells represented with triangles). **(A–F)** and **(J–O)** Coronal sections arranged from rostral **(A,J)** to caudal **(F,O)**. Solid lines indicate borders between cortical areas and dashed lines demarcate cortical layers. Insets in panels **(D–F)** and **(M–O)** indicate the rostrocaudal position of the section and the approximate area shown. Densest labeling was seen in area M2 throughout the rostrocaudal axis for both injections. **(G,P)** The respective injection sites represented in a surface rendering of the brain. **(H,Q)** Drawings of the respective injection sites in a coronal section of the brain. **(I,R)** Grayscale representation of the density of labeling in frontal midline areas from rostral to caudal (R–C), darker gray indicates a denser cluster of labeled cells. Each row represents a cortical area and columns represent coronal sections along the rostrocaudal axis. Columns representing sections visualized in the figure are boxed and indicated by their appropriate letter.

found in area 24b but in much lower numbers than in M2 (**Figures 3B–F**). Occasionally labeled cells were encountered in PL and 24a (**Figures 3A,C,D,F**).

Retrograde tracer injections in lPPC also resulted in retrogradely labeled cells mainly in M2, showing a slightly different pattern than seen in mPPC cases. In a representative case, Fluorogold was injected caudally in lPPC on the border with mPPC and impinging on visual areas (**Figures 3P,Q**). Retrogradely labeled cells were found almost throughout the rostrocaudal extent of M2 (**Figures 3J–O,R**) with the exception of the part rostral to the forceps minor of the corpus callosum, where only low numbers of neurons were labeled (**Figures 3J,K,O**). Similar to mPPC cases, the majority of the labeled cells were encountered in layer 5, but in contrast, their rostrocaudal position was different such that the densest M2 labeling was concentrated at a slightly more rostral level in the lPPC cases compared to the labeling seen in mPPC cases (**Figures 3I,R**). In area 24b labeled cells were found only at the most caudal levels and no labeled cells were observed in PL, IL or 24a (**Figures 3J–O,R**).

In three animals, PHA-L was injected in M2 (**Figure 4**). Although the cores of the injections were at different rostrocaudal levels, all injections extended along the rostrocaudal axis and partially overlapped. All injections covered deep layers, which in our retrograde data were shown to be the main origin of projections to PPC, whereas involvement of superficial layers was more variable between cases. Although the injections were largely confined to M2, they did impinge on the medially adjacent 24b and laterally adjacent M1. All three cases resulted in dense labeling in PPC. In the case with the most rostrally located injection in iM2, one dense plexus of labeled fibers were found in mPPC and another in lPPC (**Figure 4A**). Labeling was particularly dense in layers 1 and 6, where the fibers appeared to branch strongly, indicating that this was where the fibers terminated. Fibers going through other layers were largely straight with minimal branching but did show swellings and thus showed a beaded morphology. These are believed to represent mitochondria although en passant synapses cannot be excluded. In the two cases with more caudally positioned injections, in iM2 and on the border between iM2 and cM2, sparser labeling was seen in mPPC and a dense plexus of labeled fibers spanning across layers was observed in lPPC (**Figures 4B,C**). Similar to the results from the more rostral case with the injection located in M2, terminating fibers were particularly focused in layers 1 and 6 of PPC. In all three cases, labeling was sparser within area PtP than in mPPC and lPPC. Also, in all three cases, labeled fibers were observed in PPC of the hemisphere contralateral to the injection, but the density was drastically reduced. Similar to the ipsilateral labeling, labeled contralateral fibers terminated mainly in layers 1 and 6 although sparse plexuses of labeled fibers were seen stretching across the cortical layers at positions homotopic to the ipsilateral plexuses (**Supplementary Figure S2**).

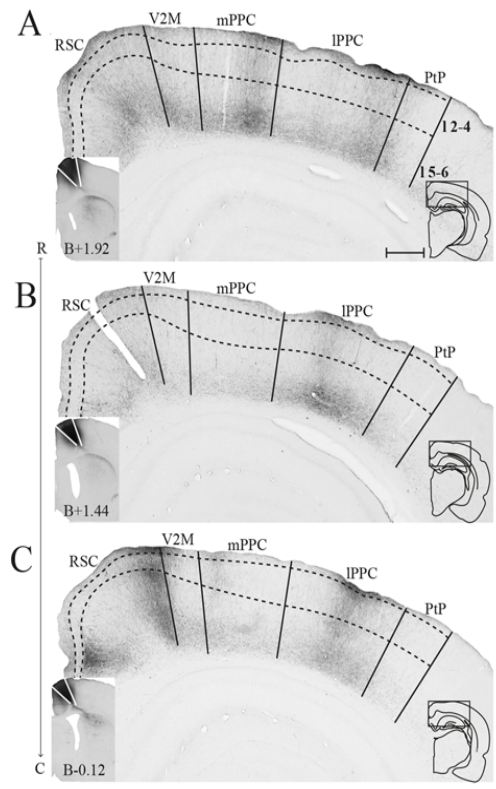

FIGURE 4 | M2 projections to PPC. Anterogradely labeled fibers in PPC and nearby areas resulting from three injections of PHA-L, each at a different rostrocaudal level of M2 (indicated by R–C). Although the cores of the injections were located at different levels, all injections extended in the rostrocaudal axis and partially overlapped. The most rostral injection in iM2 **(A)** resulted in dense plexuses of labeled fibers in mPPC and lPPC, whereas the more caudal injections in iM2 **(B)** and at the border between iM2 and cM2 **(C)** resulted in densest labeling in lPPC. Solid lines indicate borders between cortical areas and dashed lines demarcate cortical layers. Insets are images of the core of the injection sites with the borders of M2 indicated by solid lines (left) and outlines of the hemisphere of the depicted section and the area shown containing labeled fibers (right). Bregma levels are approximate and according to Paxinos and Watson (2007). Scale bar: 500 μm.

PPC Projections to Frontal Midline Areas

We analyzed 22 injections of anterograde tracers in PPC, seven in mPPC, nine in lPPC and six in PtP. Injections of anterograde tracers in PPC resulted in dense anterograde labeling in M2, with less labeling in other frontal midline areas (**Figures 5–8**).

mPPC

In a representative case, PHA-L was injected rostrally in mPPC, covering all layers (**Figures 5G,H**). In the most rostral parts of area rM2, sparse terminal labeling was present in superficial layers (**Figure 5A**). More caudally, labeling was denser and present across layers (**Figure 5E**). The densest labeling was seen in cM2 (**Figures 5F,I**), where terminal fibers branched strongly in layers 1, 3, and deep 5. It is worth noting that this densely labeled plexus appears to be located at approximately the same rostrocaudal position as the dense patch of labeled cells after injecting a retrograde tracer in mPPC (**Figure 3F**). In area 24b, a restricted plexus of terminating fibers was found

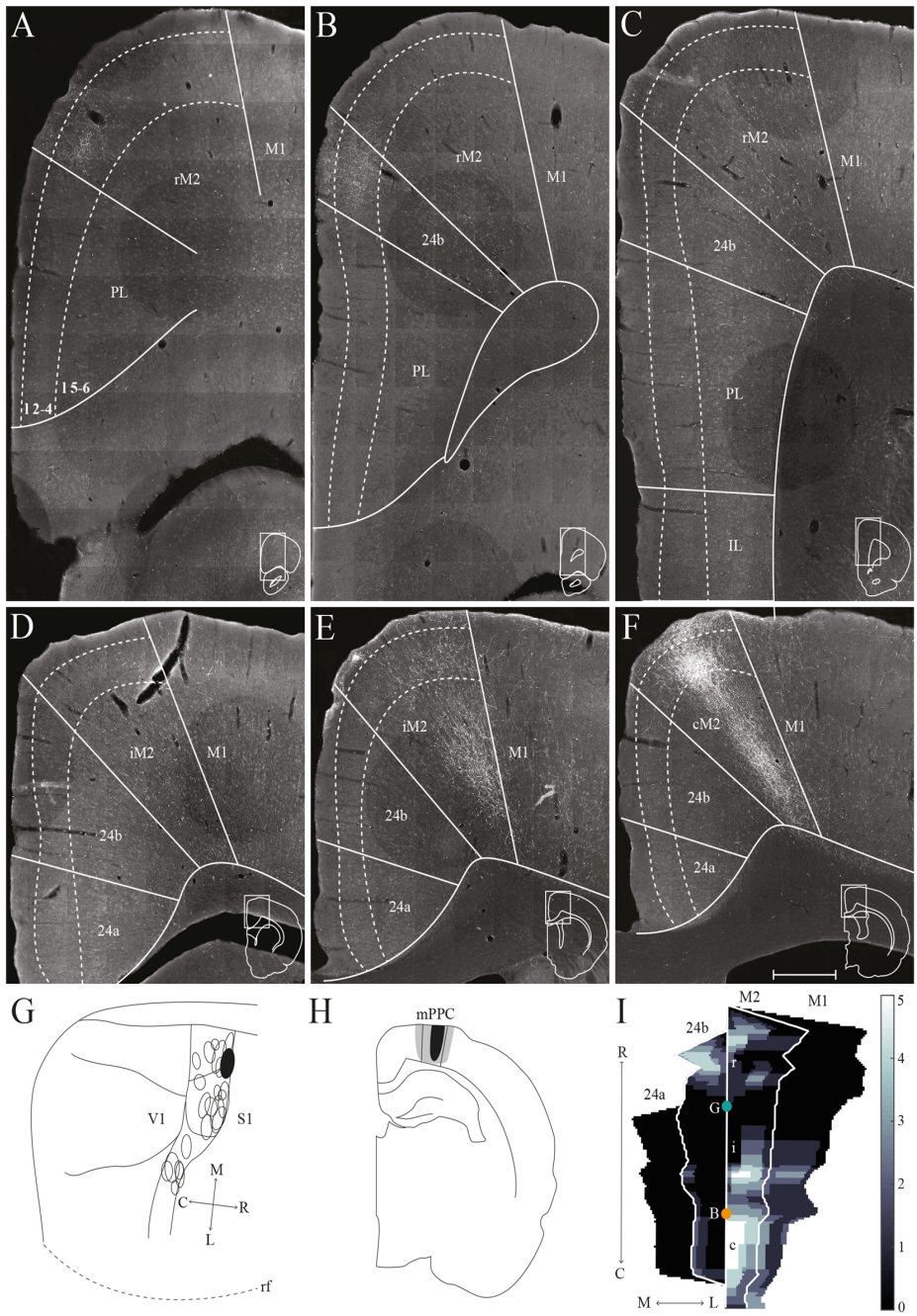

FIGURE 5 | mPPC projections to frontal midline cortex. Anterogradely labeled fibers in the frontal midline cortex resulting from an injection of PHA-L in mPPC. **(A–F)** Coronal sections arranged from rostral **(A)** to caudal **(F)**. Solid lines indicate borders between cortical areas and dashed lines demarcate cortical layers. Insets in all panels indicate the rostrocaudal position of the section and the approximate area shown. Densest labeling was seen in area cM2. **(G)** PHA-L injection site in mPPC shown as a filled circle in a surface rendering of the brain and all injection sites. **(H)** Drawing of the injection site in a coronal section with the borders of mPPC indicated by solid lines. **(I)** Intensity representation of the density of labeling in frontal midline areas from rostral to caudal (R–C), Lighter color indicates a denser plexus of labeled fibers. The scale bar relates the color code in the flatmaps to the density scores initially assigned to each pixel in the digitized sections (for details, see "Materials and Methods" section). Bregma is indicated by an orange dot and the genu of the corpus callosum, which coincides with the border between rM2 and iM2, by a green dot. Scale bar: 500 μm.

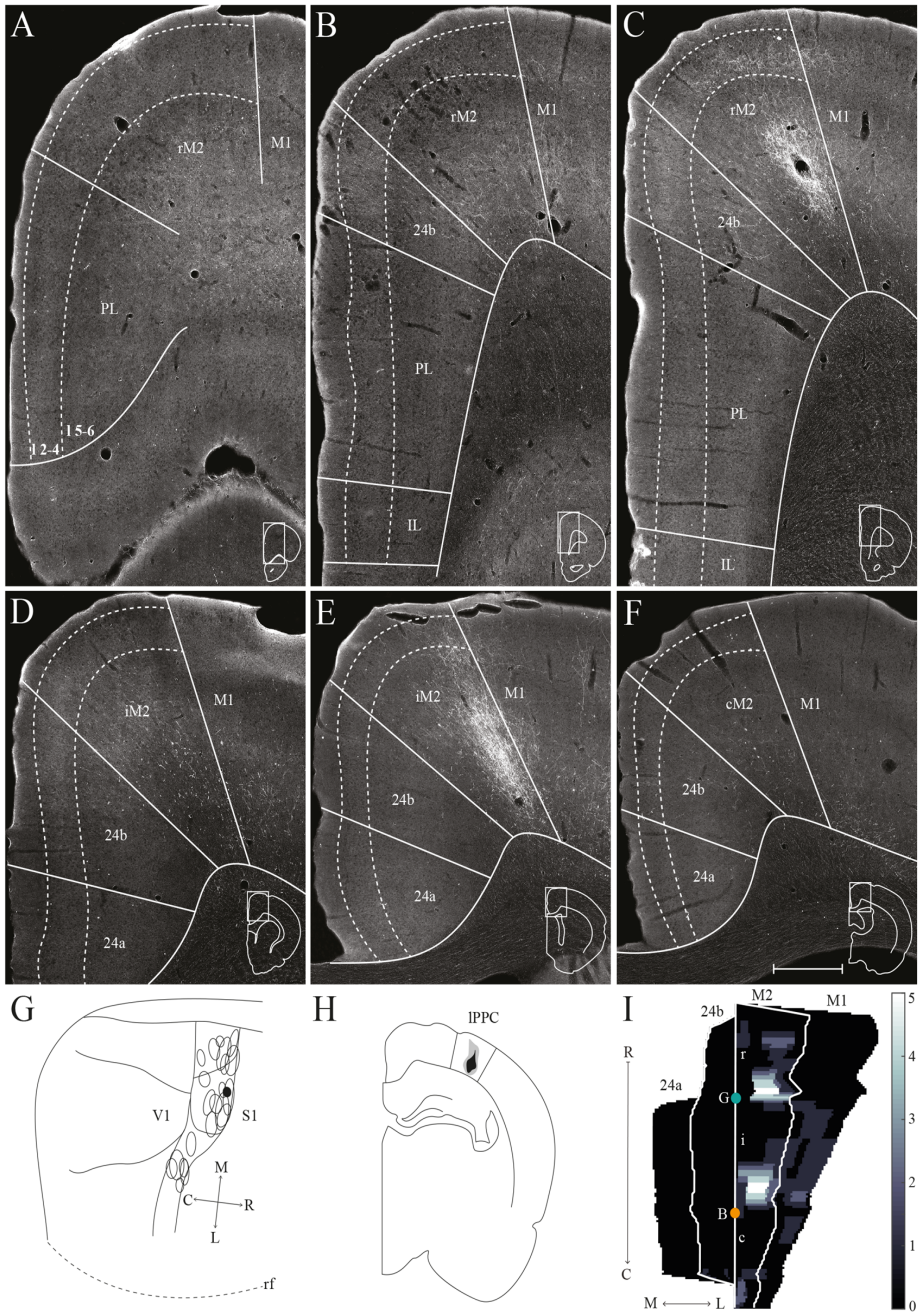

FIGURE 6 | lPPC projections to frontal midline cortex. Anterogradely labeled fibers in the frontal midline cortex resulting from an injection of BDA in lPPC. **(A–F)** Coronal sections arranged from rostral **(A)** to caudal **(F)**. Solid lines indicate borders between cortical areas and dashed lines demarcate cortical layers. Insets in all panels indicate the rostrocaudal position of the section and the approximate area shown. Densest labeling was seen in area iM2. **(G)** BDA injection site in lPPC shown as a filled circle in a surface rendering of the brain and all injection sites. **(H)** Drawing of the injection site in a coronal section with the borders of lPPC indicated by solid lines. **(I)** Intensity representation of the density of labeling in frontal midline areas from rostral to caudal (R–C), lighter color indicates a denser plexus of labeled fibers. The scale bar relates the color code in the flatmaps to the density scores initially assigned to each pixel in the digitized sections (for details, see "Materials and Methods" section). Bregma is indicated by an orange dot and the genu of the corpus callosum, which coincides with the border between rM2 and iM2, by a green dot. Scale bar: 500 μm.

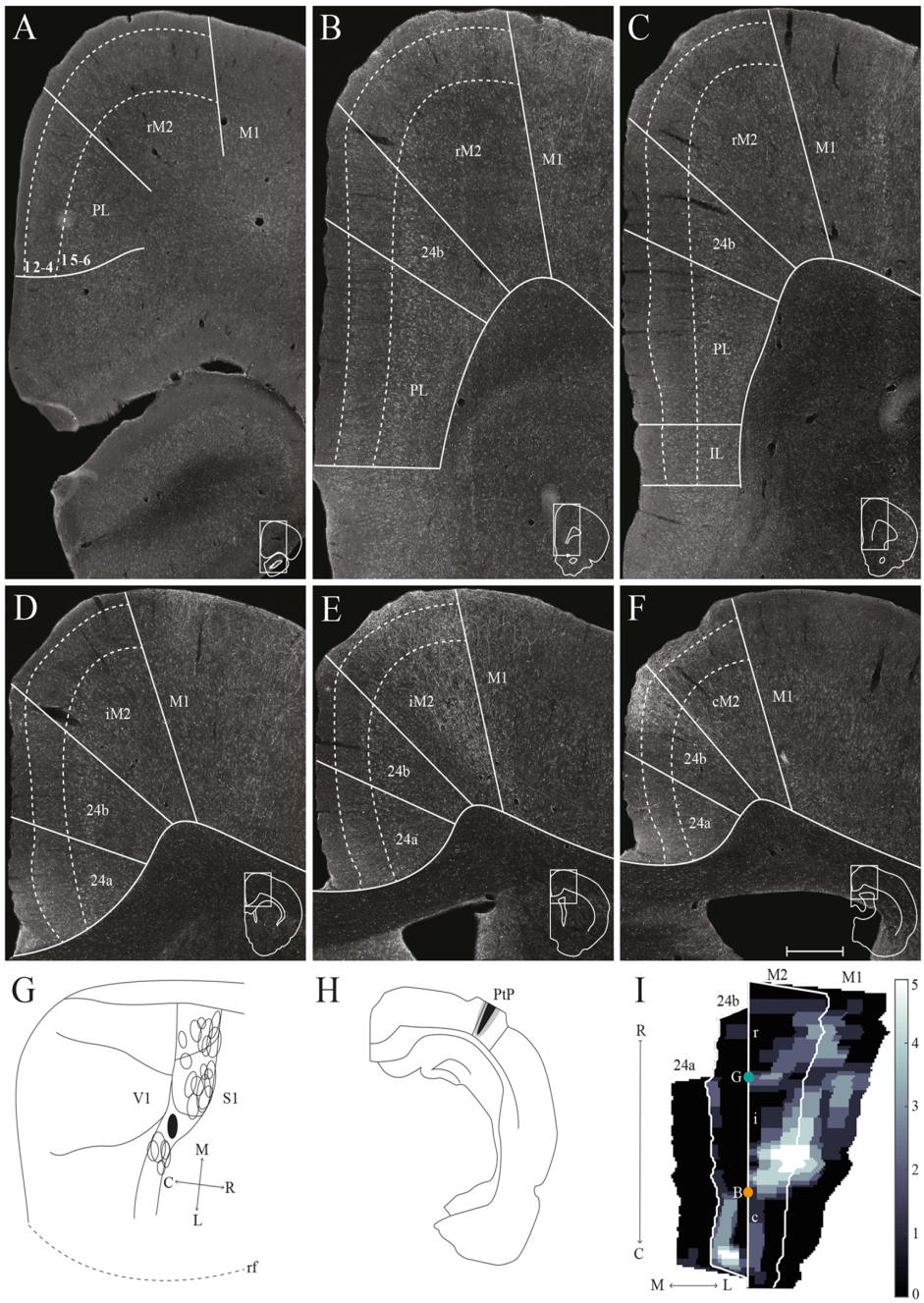

FIGURE 7 | PtP projections to frontal midline cortex. Anterogradely labeled fibers in the frontal midline cortex resulting from an injection of PHA-L in PtP. **(A–F)** Coronal sections arranged from rostral **(A)** to caudal **(F)**. Solid lines indicate borders between cortical areas and dashed lines demarcate cortical layers. Insets in all panels indicate the rostrocaudal position of the section and the approximate area shown. Densest labeling was seen in area iM2. **(G)** PHA-L injection site in PtP shown as a filled circle in a surface rendering of the brain and all injection sites. **(H)** Drawing of the injection site in a coronal section with the borders of PtP indicated by solid lines. **(I)** Intensity representation of the density of labeling in frontal midline areas from rostral to caudal (R–C), lighter color indicates a denser plexus of labeled fibers. The scale bar relates the color code in the flatmaps to the density scores initially assigned to each pixel in the digitized sections (for details, see "Materials and Methods" section). Bregma is indicated by an orange dot and the genu of the corpus callosum, which coincides with the border between rM2 and iM2, by a green dot. Scale bar: 500 μm.

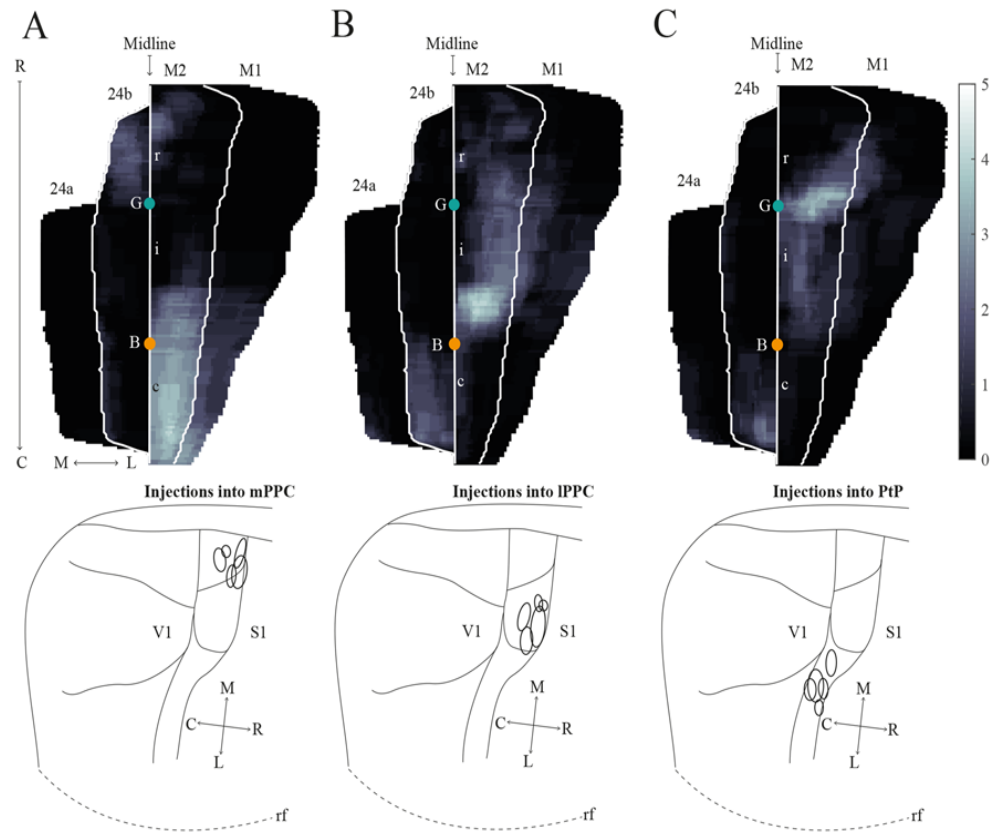

FIGURE 8 | Average projections from PPC to midline frontal cortices. **(A–C)** Top: average intensity representation of the density of labeling in frontal midline areas from rostral to caudal (R–C), resulting from injections of anterograde tracers into mPPC **(A)**, lPPC **(B)**, and PtP **(C)**. Lighter color indicates a denser plexus of labeled fibers. The scale bar relates the color code in the flatmaps to the density scores initially assigned to each pixel in the digitized sections (for details, see "Materials and Methods" section). Bregma is indicated by an orange dot and the genu of the corpus callosum, which coincides with the border between rM2 and iM2, by a green dot. Bottom: surface representations of injection sites in cases that make up the average map.

in superficial layers at its most rostral level (**Figures 5B,I**) and sparse labeling was observed in superficial and deep layers at the most caudal level of area 24b (**Figures 5E,F,I**), extending ventrally into area 24a and caudally into RSC (not shown). No labeled fibers were encountered in IL, and only a few were observed in PL (**Figures 5A–C**). In the contralateral hemisphere, sparse labeling reflected the ipsilateral labeling and was most frequently found in M2 at the same rostrocaudal levels as the strongest ipsilateral labeling (not shown). The majority of the contralateral labeled fibers were located in layers 1 and 3, and comparably fewer fibers were observed in layer 5. Other cases of tracer injections in mPPC yielded similar labeling patterns. In several cases, sparse to moderate labeling was observed in rM2 rostral to the forceps minor, with some fibers also located in area 24b, and comparably less labeling was found in iM2. The densest labeling was most frequently found caudal to the crossing of the anterior commissure although the exact rostrocaudal level of the densest plexus could vary between cases.

lPPC

A representative, small BDA injection in lPPC with a core mainly in deep layers was centered at a mid rostrocaudal level (**Figures 6G,H**). Similar to the results in case of the injection in mPPC, dense labeling was observed in M2, however, the labeling was shifted along the rostrocaudal axis (**Figures 6C–E,I**). No labeling was encountered at the most rostral levels (**Figures 6A,I**), and only sparse labeling was observed in rM2 at the level of the forceps minor of the corpus callosum (**Figures 6B,I**). A moderately dense plexus of terminal fibers in layers 3 and 5 were present rostral to the level of the genu of the corpus callosum, with fewer fibers in layers 1 and 6 (**Figures 6C,I**). At more caudal levels, another moderately dense plexus of terminating fibers was seen in iM2 with a similar laminar pattern (**Figures 6E,I**). This plexus was located at a similar rostrocaudal level as the dense patch of labeled cells seen after retrograde tracer injections in lPPC (**Figures 3N,R**), and thus at a slightly more rostral level compared to the densest plexus of labeled fibers in the above-described mPPC case.

Labeled fibers were occasionally observed in area 24b, at the most caudal level they extended into area 24a (**Figures 6F,I**) and extended caudally into RSC (not shown). No labeled fibers were present in areas PL or IL (**Figures 6A–C**). Only a few labeled fibers were observed contralaterally, mainly in layer 5 of iM2 (not shown). Other cases with injections in lPPC produced similar labeling patterns. In all cases, although the exact rostrocaudal position varied slightly, the densest labeling in M2 was found in iM2. In addition, injections involving more superficial layers resulted in relatively more labeling in superficial layers of M2.

PtP

Similar to tracer injections in mPPC and lPPC, injections of anterograde tracers into PtP resulted in labeled fibers in M2. Following a representative injection impinging on the lateral secondary visual cortex (V2L, **Figures 7G,H**), very few labeled fibers were observed in rM2 at levels rostral to the genu of the corpus callosum (**Figures 7A–C,I**). More caudally, a dense plexus of labeled fibers were seen in area iM2, terminating mainly in layers 1, 3, and 5 (**Figures 7E,I**). This plexus appeared at a level similar to the dense plexus of labeled fibers that was seen after injecting tracer in lPPC (**Figures 6E,I**). At the most caudal level of the frontal midline cortex, a small but dense plexus of terminal fibers was found in superficial layers of area 24b with a few fibers extending into area 24a (**Figures 7E,F,I**) and continuing caudally into RSC (not shown). No labeled fibers were seen in areas PL or IL (**Figures 7A–C**). Very sparse labeling was seen in the contralateral hemisphere, homotopic to the densest ipsilateral labeling in M2 and 24b. Other cases of anterograde tracer injections into PtP yielded less labeling in M2, and although the densest labeling was consistently found within the iM2, labeling in several cases was shifted more rostrally, closer to the genu of the corpus callosum. Most cases had sparse labeling at caudal levels of area 24b/a continuing into RSC, however, two cases failed to yield labeling in area 24. In both cases, the injection was focused in layer 6 and deep layer 5 and overall cortical labeling was sparse.

In order to verify that the projection patterns presented for individual cases were representative of all animals, standardized representations of the location of labeled fibers in cingulate and motor areas were made in the form of flatmaps. Note that such flatmaps were made to illustrate and compare the preferred location of projections as well as relative strength. In each case, strength throughout the flatmap was represented in relation to the strongest labeling in M2, which was represented by a value of 5. The flatmaps were created by averaging the projection pattern across five brains with injections into mPPC (**Figure 8A**), five brains with injections into lPPC (**Figure 8B**) and five brains with injections into PtP (**Figure 8C**). For individual case maps see **Supplementary Figure S1**. The flatmaps confirmed the results from the representative cases and showed that mPPC, lPPC and PtP preferentially target different rostrocaudal portions of cingulate and motor cortices. mPPC preferentially targets cM2, with the strongest projections caudal to Bregma (**Figure 8A**). M2 labeling is accompanied by labeling in M1, which is strongest most caudally and tapers off rostral to Bregma. mPPC also has moderate projections targeting the most medial rM2, as well as to rostromedial 24b. Weak labeling was found on the medial border of 24b extending from the genu of the corpus callosum to the caudal extent of 24b. lPPC, in contrast, preferentially targets iM2 with the strongest projection observed in sections just rostral to Bregma, with moderate labeling continuing rostral and laterally in M2 (**Figure 8B**). Weaker projections are also seen medially in cM2, caudal to Bregma. Area 24b is labeled at the level of Bregma, with labeling extending caudally to where retrosplenial cortex appears. lPPC projections to M1 are weaker than to iM2 and 24b and target the mid rostrocaudal portion along the border of iM2. PtP also targets the iM2, though more weakly than lPPC, while its strongest projections are to more rostral levels near the genu of corpus callosum (**Figure 8C**). PtP projects weakly to caudal 24b, mainly terminating lateral to the projections from lPPC. Very weak labeling was also observed in caudal 24a for both lPPC and PtP injections.

Connections of PPC With Orbitofrontal Cortex

Orbitofrontal Input to PPC

To analyze the termination pattern of orbitofrontal input to PPC, we analyzed our dataset of 36 anterograde tracer injections (Kondo and Witter, 2014), supplemented with one injection in DLO. Anterograde tracer injections in LO and DLO did not yield labeled fibers in PPC.

MO

We analyzed seven anterograde tracer injections in MO, out of which only one injection of BDA yielded anterogradely labeled fibers in PPC (**Figure 9A**). This injection involved all layers and covered a large portion of the rostrocaudal extent of MO. The resulting labeling in PPC was sparse and mainly confined to mPPC, with only occasional labeled fibers in lPPC. No labeled fibers were encountered in PtP, whereas weak labeling was observed in the medial secondary visual cortex (V2M).

VO

Seven out of 11 anterograde tracer injections in VO resulted in labeled fibers in PPC. Generally, tracer injections situated medially within VO yielded less robust labeling in PPC than injections located more laterally in this area. In one representative case, PHA-L was injected laterally in VO on the border with VLO, where the core of the injection was confined to superficial layers (**Figure 9B**). The injection site slightly involved the anterior olfactory nucleus, which according to our retrograde data does not project to PPC. In this representative case, a moderately dense plexus of terminal fibers was observed in mPPC, sparser labeling was seen in lPPC, and only a few labeled fibers were encountered in PtP (**Figure 9B**). V2M, as well as primary visual cortex (V1), contained moderate labeling. In all areas, the majority of the labeled fibers were located in layers 2 and 3, whereas sparser labeling was seen in layers 1 and 5. Following a BDA injection in VO at the border with VLO, a moderately dense cluster of terminating fibers was located medially in mPPC, with clearly branching fibers in layers 2, 3, and 5 (see **Figure 11A** for exemplary micrograph). Only a few

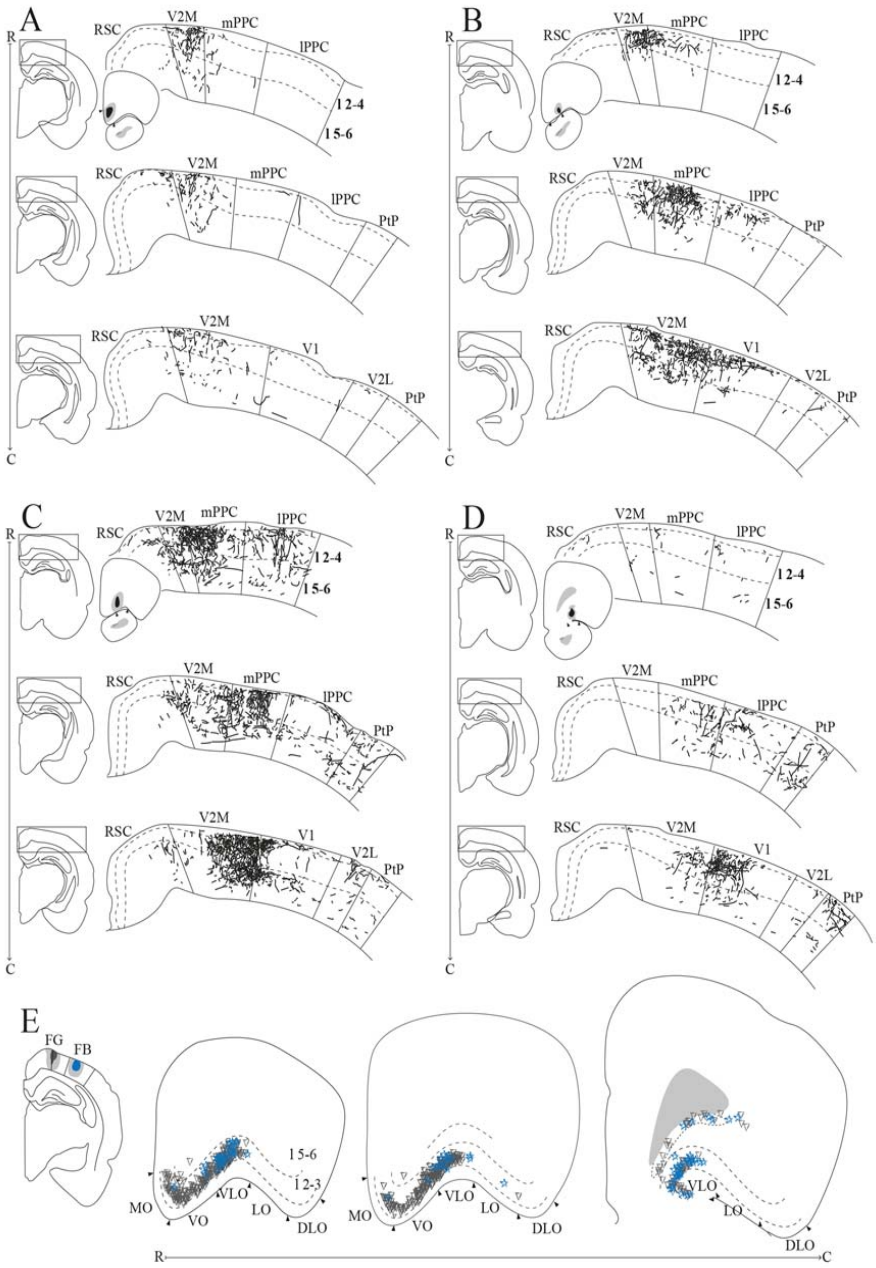

FIGURE 9 | OFC projections to PPC. **(A–D)** Anterogradely labeled fibers at three different rostrocaudal levels of PPC (R–C, respectively) and adjacent areas resulting from injections of anterograde tracers in MO (**A**, BDA), VO (**B**, PHA-L), rostral VLO (**C**, PHA-L), and caudal VLO (**D**, BDA). As injection sites shifted from medial to lateral and caudal within OFC, anterogradely labeled fibers extended progressively more lateral and caudal in PPC. Solid lines indicate borders between cortical areas and dashed lines demarcate cortical layers. Right insets indicate the position of the core of the injection and the borders of MO **(A)**, VO **(B)**, and VLO **(C,D)** are marked by arrowheads. Left insets indicate the rostrocaudal position of the depicted area. **(E)** Retrogradely labeled cells in OFC, represented at three different rostrocaudal levels (indicated by R–C), resulting from an injection of Fluorogold in mPPC (represented by gray triangles) and injection of Fast Blue in lPPC (represented by blue stars) in the same animal. Both injections resulted in dense labeling in VLO, and the Fluorogold injection also resulted in dense labeling in VO and MO. Arrowheads indicate borders between cortical areas and dashed lines demarcate cortical layers. Inset indicates the position of the cores of the injection sites, with borders of mPPC and lPPC outlined with solid lines.

scattered labeled fibers were observed in lPPC, whereas in PtP labeling was absent.

VLO

Out of 13 injections of anterograde tracers in VLO, eight yielded anterogradely labeled fibers in PPC. From the cases with no labeled fibers in PPC, one injection was placed medially to the notch of the rhinal fissure, and the remaining four were placed lateral to the notch. A slight shift in the location of labeled fibers was observed between injections placed rostrally in VLO vs. injections situated at the more caudal portion of this area. A representative injection of PHA-L rostrally in VLO on the border with VO involved the medial bank of the rhinal fissure (**Figure 9C**). In mPPC, a moderately dense cluster of terminal fibers was observed, and more dispersed labeling was found in lPPC and PtP. Moderate to dense labeling was seen in V2M, whereas sparse labeling was encountered in V1 and V2L. Similar to what was seen in case of injections into VO, the majority of labeled fibers were located in layers 2 and 3, and labeling in layers 1 and 5 was somewhat sparser. An injection of BDA placed more caudally in VLO yielded sparse anterograde labeling in mPPC, lPPC, and PtP (**Figure 9D**). Only weak labeling was found in V2M, and a moderately dense plexus of labeled fibers was seen in V1. Terminating fibers were located mainly in layers 2 and 3, with sparser labeling in layers 1 and 5. A large injection of PHA-L placed caudally in VLO resulted in a moderately dense cluster of labeled fibers in mPPC and adjacent medial portions of lPPC, with sparser labeling more laterally in lPPC (**Figure 11B**) and PtP (not shown). Fibers tended to branch mainly in layers 2, 3, and 5.

To investigate the origin of orbitofrontal input to PPC, we reviewed the same dataset of retrograde tracers used to describe the projections from frontal midline areas to PPC, four cases of injections in mPPC and three cases of injections in lPPC (**Figures 3G,P**). All injections resulted in strong retrograde labeling in OFC, mainly in superficial layers. In one animal, Fluorogold was injected in mPPC and Fast Blue was injected in lPPC, with the cores of both injections located in superficial layers (**Figure 9E**). Both tracer injections resulted in dense labeling throughout the rostrocaudal extent of OFC. Cells labeled after the injection in mPPC spanned a substantial medial-to-lateral extent of OFC, from the medially located MO to the centrally located VLO. In contrast, the injection in lPPC yielded labeled cells mainly confined to VLO. Labeled cells from both injections were spatially intermingled, and occasional cells were found to be double-labeled. In view of the sparsity of these double-labeled neurons, we did not quantify these results. We observed very few labeled neurons in LO or DLO, in line with the results of anterograde tracers injected in either of the two areas.

PPC Projections to Orbitofrontal Cortex

To analyze the distribution of PPC projections to OFC, we made use of the anterograde dataset with injections in PPC, described above (**Figures 5–7G**). Injections of anterograde tracers in PPC resulted in sparse to moderately dense terminal labeling in OFC with a distribution that matches that of retrogradely labeled neurons in OFC following injections in PPC, in that anterograde labeling was mainly found in MO, VO and VLO. Labeled fibers were largely observed in the hemisphere ipsilateral to the injection, although some fibers were encountered contralaterally in cases with strong orbitofrontal projections, terminating mainly in layer 1.

mPPC

In a representative case, PHA-L was injected rostrally in mPPC (**Figure 10A**). Anterogradely labeled fibers were observed in MO, VO and medially in VLO, across layers. At rostral levels of OFC, terminal fibers were mostly located in superficial layers, and at the most caudal level labeled fibers were seen to extend from the claustrum into VLO. Following an injection of BDA caudally in mPPC (**Figure 11C**), terminating fibers were mainly seen in the lateral portion of VO, extending into the medial portion of VLO. Fibers branched most densely in layer 3 but also extended into layers 2 and 1.

lPPC

An injection of PHA-L laterally in lPPC at a mid rostrocaudal position resulted in labeling largely confined to the medial half of VLO with a few fibers extending into the medially adjacent VO (**Figure 10B**). Terminating fibers were located mainly in layers 1, 3 and 6 throughout the rostrocaudal extent of VLO. **Figure 11D** shows labeled fibers after injection of PHA-L in lPPC in another case. A moderately dense cluster of terminal fibers was confined to the part of VLO located on the medial bank of the rhinal fissure. The fibers were seen to branch most densely in layer 1, and labeled fibers were scarcer in layers 2, 3 and 6. A few labeled fibers were also seen in deep layers of VO.

PtP

Similar to cases with injections in lPPC, injections of anterograde tracers in PtP yielded anterogradely labeled fibers mainly in VLO. In a representative case, PHA-L was injected rostrally and medially in PtP, slightly impinging on V2L (**Figure 10C**). The resulting labeled fibers were located mainly within VLO, with a slightly more lateral position in VLO than was seen following injections in lPPC. The labeled fibers were observed not only on the medial bank and notch of the rhinal fissure but extended into the lateral bank of the fissure as well. Terminating fibers were seen in layers 1–3, and 5/6. In another case, BDA was injected at a more caudal level of PtP (**Figure 11E**). As was seen following the more rostral injection, anterogradely labeled fibers, in this case, were mainly seen in medial VLO, with terminal branching largely in superficial layers.

In order to investigate the origin of PPC projections to OFC, retrograde tracers were injected in OFC in five cases. In a representative case, a large injection of Fast Blue was placed in the VO/VLO region, medial to the notch of the rhinal fissure (**Figure 10D**). Tracer leaked into the claustrum and the anterior olfactory nucleus, the latter was shown in our anterograde data to not receive projections from PPC. Across all subdivisions of PPC, retrogradely labeled cells were found in large numbers in deep layers and only occasionally were labeled cells found in superficial layers. In line with the sparse contralateral PPC-OFC projections observed in the anterograde tracer cases, very few labeled cells were observed in the

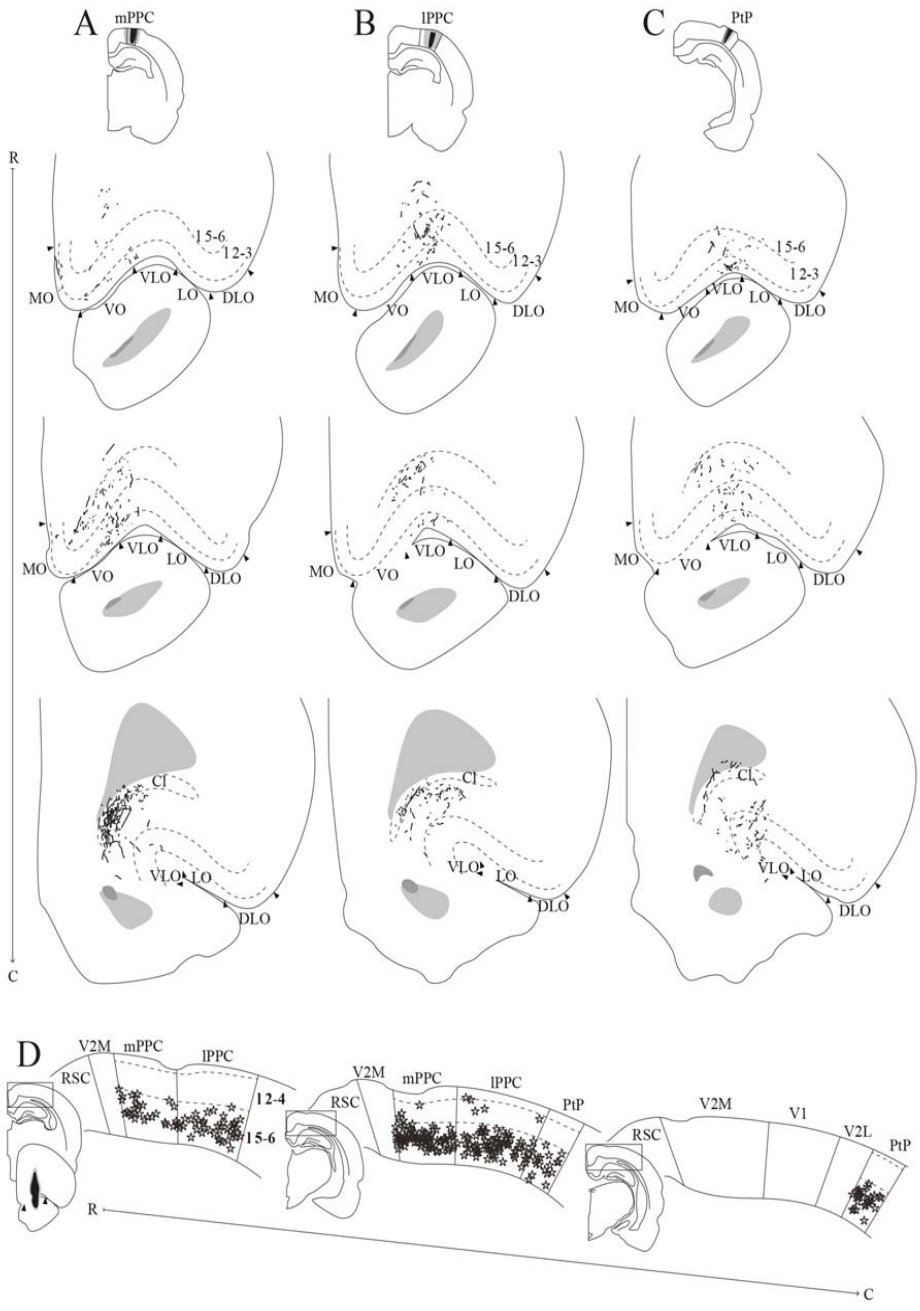

FIGURE 10 | PPC projections to OFC. **(A–C)** Anterogradely labeled fibers at three different rostrocaudal levels (indicated by R–C) of OFC resulting from injections of PHA-L in mPPC **(A)**, lPPC **(B)**, and PtP **(C)**. As injections shifted from medial to lateral in PPC, anterogradely labeled fibers extended progressively more lateral and caudal in OFC. Arrowheads indicate borders between cortical areas and dashed lines demarcate cortical layers. Top insets indicate the position of the core of each injection with the borders of the mPPC **(A)**, lPPC **(B)**, and PtP **(C)** outlined with solid lines. **(D)** Retrogradely labeled cells represented by stars at three different rostrocaudal levels (indicated by R–C) of PPC resulting from a big injection of Fast Blue in the VO/VLO region. Labeled cells were primarily located in layer 5 across all PPC subdivisions. Solid lines indicate borders between cortical areas and dashed lines demarcate cortical layers. Bottom left inset shows a drawing of the injection site in a coronal section, arrowheads indicate the medial border of VO and lateral border of VLO. Insets at the left of each section indicate the rostrocaudal position of the depicted areas.

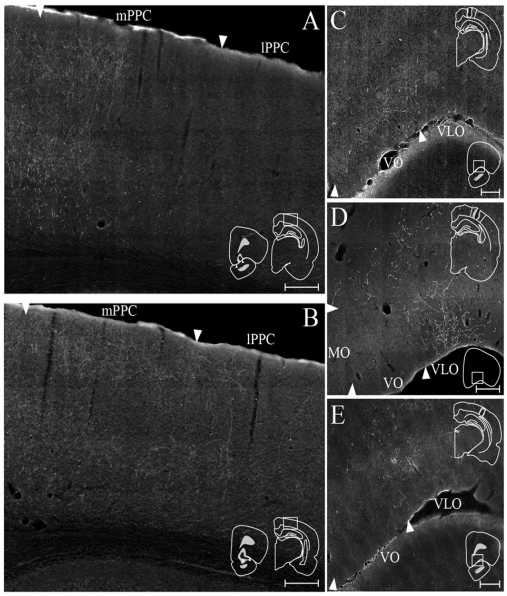

FIGURE 11 | OFC-PPC connections. **(A,B)** Examples of labeled fibers in PPC resulting from injections of anterograde tracer in VO (**A**, BDA) and VLO (**B**, PHA-L). Insets indicate the position of the injection site in OFC with the borders of VO **(A)** and VLO **(B)** marked by arrowheads (left) and the portion of PPC containing the labeled fibers (right). **(C–E)** Examples of labeled fibers in OFC resulting from injections of anterograde tracer in mPPC (**C**, BDA), lPPC (**D**, PHA-L), and PtP (**E**, BDA). Insets indicate the position of the injection site in PPC with the borders of mPPC **(C)**, lPPC **(D)**, and PtP **(E)** outlined with solid lines (top) and the position in OFC of the depicted area (bottom). Arrowheads indicate borders of cortical areas. All scale bars: 200 μm.

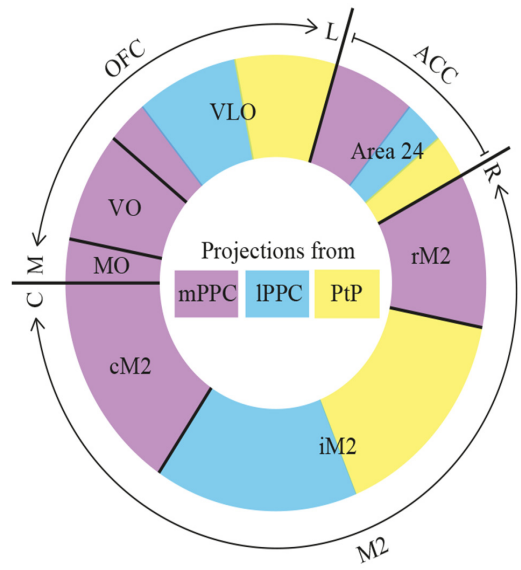

FIGURE 12 | Summary. Diagram of parietal-frontal projections. The center of the circle shows a color-coded representation of the three PPC subdivisions, mPPC (purple), lPPC (blue), and PtP (yellow). The outer colored circle represents the relative proportion of projections, indicated by the size of the color-coded areas, from the three PPC subdivisions to frontal cortical areas that are separated with black lines. The outer edge indicates the total extent of orbitofrontal cortex (OFC), anterior cingulate cortex (ACC) and secondary motor cortex (M2), as well as their rostrocaudal (R–C) or mediolateral (M–L) organization. The reciprocal projections from OFC and M2 to PPC show comparable patterns. rM2, rostral portion of M2; iM2, intermediate portion of M2; cM2, caudal portion of M2.

contralateral PPC following injection of retrograde tracer in OFC (not illustrated).

DISCUSSION

The current data show that PPC projects to several frontal cortical areas (summarized in **Figure 12**), largely reciprocating the densest input received from the same areas. The laminar connection patterns are summarized in **Supplementary Figure S3**. Within the frontal midline areas, all PPC subdivisions appear to be strongly connected with M2. mPPC preferentially targets cM2 in addition to moderate labeling at rM2, whereas lPPC and PtP target iM2. Sparser connections were found with area 24b. mPPC projects to rostral 24b, whereas lPPC and PtP project to caudal regions. There were virtually no connections with area 24a, IL or PL. Within OFC, a gradient was revealed in which medial areas of OFC connects with mPPC, and the more central portion of OFC preferentially connects with lateral PPC subdivisions lPPC and PtP. PPC connections with the more lateral portions LO and DLO were absent. Our results are overall in line with previous studies, but as detailed below, our data uncover a topographical organization of the connections of the three subdivisions of PPC.

Connections of PPC With Frontal Midline Cortices

Area M2

The current data corroborate previous reports that M2 projects to PPC, and that these projections originate from the entire rostrocaudal extent of M2 (Kolb and Walkey, 1987; Reep et al., 1994). Regarding the laminar origin of the M2 to PPC projections, we conclude that there is a slight preference for a deep origin, which seems disparate from what can be seen in the figures in the study of Reep et al. (1994), showing a more even laminar origin, although this is not specifically mentioned by the authors. The difference may be a result of the lower detail provided in the latter study compared to ours. In addition, our data showed that M2 projections to PPC originated in superficial layers at specific rostrocaudal levels. Projections from M2 to PPC have previously been shown to travel through layer 6 of the cortex (Reep et al., 1987), which is confirmed by our observations after injections of anterograde tracer in M2. Further, our data show that these projections terminate in layers 1 and 6 across mPPC and lPPC, with sparse, more diffuse labeling in PtP although, interestingly, the bilaminar labeling sometimes extends throughout all layers in a columnar pattern in mPPC and lPPC. Such an alternating bilaminar and

columnar termination pattern of cortical projections of M2 has been described previously (Reep et al., 1987). With respect to possible connectional differences between the three subdivisions of PPC, the present data indicate that M2 projections to PtP are weak, whereas lPPC and mPPC both receive dense projections from M2. This differs from another study (Wilber et al., 2015), which reported that lPPC received much stronger M2 input than mPPC. A close evaluation of the latter study revealed that only one out of five retrograde tracer injections in lPPC showed particularly dense input from M2, one showed sparse input and the other three appeared to receive very little input. We consider it likely that the results of the one case showing strong labeling in M2 are due to the involvement of layer 6 in the injection site, since, as mentioned above, M2 projections to adjacent cortical areas have a preferred path through layer 6.

To our knowledge, we are the first to describe the laminar termination pattern of PPC projections within M2 and potential differences between projections from the three PPC subdivisions, although projections from PPC to M2 have been described in previous studies following injections of retrograde tracers in M2 in rats (Reep et al., 1984, 1990; Kolb and Walkey, 1987; Condé et al., 1995; Hoover and Vertes, 2007). These studies showed that the projections originated in layers 2/3 and 5 of PPC, however, one study found that projections to rM2 arose from deep layers only (Hoover and Vertes, 2007). Unfortunately, these studies provided little detail regarding the question of whether the three subdivisions of PPC contributed differentially to these projections, or whether topographical differences might be present. Moreover, detailed comparisons between the various studies are difficult since applied cortical delineations differ between studies, including our previous study in which we established the borders and subdivisions of PPC used here (Olsen and Witter, 2016). In mice, it was shown that extrastriate areas corresponding to PPC (anterior parts of A, AM and RL) also project to M2 (Wang et al., 2012) and, that the connectivity is reciprocal (Zingg et al., 2014; Hovde et al., 2018). The present results show that all PPC subdivisions project to superficial and deep layers of M2. In a previous study, it was reported that projections from nearby higher-order visual areas terminate in superficial layers of M2 (Miller and Vogt, 1984), but the authors did not include data on PPC projections.

As mentioned previously, M2 has been divided into three parts along its rostrocaudal axis. Injections of retrograde tracers showed that the rostral part of M2, rM2, received extensive somatosensory input whereas the caudal part, cM2, had an overweight of visual cortical input and the mid-portion, iM2, received a mixture of both (Reep et al., 1990). Our current data add to this by showing that PPC projections terminate at specific rostrocaudal levels within M2 as well. We further show that the terminal distribution of the PPC-M2 projection overlaps with the main origin of the reciprocating M2 projections to PPC. Thus, mPPC has minor reciprocal connections with a small portion at the rostral extreme of rM2, moderate reciprocal connections with the mid-portion and strongest reciprocal connections with the most caudal portion, cM2. lPPC is also sparsely reciprocally connected with rM2, but at a level much closer to the genu of the corpus callosum. In addition, strong reciprocal connections were found between lPPC and iM2, as well as a sparser connection with cM2. While we did not obtain any retrograde tracer injections confined to PtP, considering that PtP projects mainly to iM2, we expect that the densest input from iM2 to PtP originates here. However, it should be noted that, in our hands, three anterograde tracer injections in M2, located at different rostrocaudal levels of iM2 and cM2, yielded only sparse labeling in PtP compared to mPPC and lPPC.

PL, IL and Area 24

Our observations indicate that reciprocal connections between PPC and the prefrontal midline areas PL and IL are very sparse, in line with previous studies (Reep et al., 1994; Condé et al., 1995; Vertes, 2004; Hoover and Vertes, 2007; Wilber et al., 2015). Differing from the sparse or non-existent IL and PL connections, our data indicate that PPC has slightly stronger connections with ACC area 24, supporting previous reports (Condé et al., 1995; Hoover and Vertes, 2007). According to these studies, area 24 has corticocortical connections that overall are sparser than those of M2. Moreover, within ACC, area 24b has more widespread corticocortical connections than 24a (Vogt and Miller, 1983). Both notions are supported by our results.

Interconnections have been found between the IL and PL as well as the most rostral portion of area 24b (Condé et al., 1995; Fisk and Wyss, 1999; Jones et al., 2005; but see Vertes, 2004). These areas are only sparsely connected with the rest of the ACC as well as other cortical areas and are thought to constitute the medial prefrontal cortex in the rat. The mid- and caudal portions of area 24b are reciprocally connected with rostral and caudal area 24a in a complex manner (Jones et al., 2005), and receive input from several cortical areas (Reep et al., 1990). Data on connections between PPC and area 24 do not emphasize a particular preference to connect with any of these three rostrocaudal subdivisions. One might expect a relatively weak connection with the very rostral part of area 24, in line with the weak to absent connections with the connected PL and IL. However, our data suggest that mPPC receives input from the entire rostrocaudal extent of area 24b and has a small projection to the rostral extreme of area 24b as well as a very sparse projection to the most caudal portion that has been shown to originate mainly in deep layers (Finch et al., 1984; Condé et al., 1995; Hoover and Vertes, 2007). Regarding lPPC, it receives input only from the most caudal level of area 24b, and sends a minor reciprocating projection. The data on area 24 projections to PPC reported by us are in line with previously published ones, showing that injections of retrograde tracers in mPPC resulted in labeled cells throughout area 24b, and injections in lPPC yielded labeled cells confined to the caudal third of area 24b (Reep et al., 1994; see also Kolb and Walkey, 1987). PtP has a small projection to the caudal extreme of area 24b and currently, no data are available addressing a potential reciprocating projection in rodents. Thus, among the PPC subdivisions, mPPC appears to have the strongest connections

with the ACC, including unique connections with the most rostral part.

Connections of PPC With Orbitofrontal Cortex

Our data suggest that PPC is reciprocally connected with OFC, specifically to parts of OFC located medial to the orbital notch, in line with previous studies in rats and mice (Kolb and Walkey, 1987; Reep et al., 1994; Hoover and Vertes, 2011; Zingg et al., 2014; Wilber et al., 2015; Hovde et al., 2018). Retrograde tracer injections in PPC yielded retrogradely labeled cells largely in superficial layers of MO, VO and VLO, but not in the more lateral parts, LO and DLO (Kolb and Walkey, 1987; Reep et al., 1994; Wilber et al., 2015). Labeled cells in these three subdivisions of OFC appeared to be dispersed throughout, irrespective of whether the injection was placed in mPPC or lPPC (see especially Reep et al., 1994 for details). This contrasts with our data, where injections of retrograde tracer in mPPC resulted in labeled cells that were most concentrated in VO but were observed also in neighboring MO and medial VLO, and injections in lPPC yielded labeled cells mainly confined to medial VLO. Corroborating the retrograde data, our anterograde tracer data suggest that MO projects sparsely to PPC since only one out of seven injections yielded scattered anterogradely labeled fibers in PPC. In contrast, VO and VLO project progressively more lateral and caudal within PPC as injection sites shift from VO through rostral VLO to caudal VLO. Our findings replicate the results of a previous study where only a few labeled fibers were observed in layer 6 of PPC after injection of PHA-L in MO, whereas injections in VO produced labeled fibers, albeit sparse, in superficial and deep layers of PPC (Hoover and Vertes, 2011). Unfortunately, these authors did not include injections of anterograde tracers in VLO.

The topography of projections from PPC to OFC have not been studied in detail previously. To our knowledge, only one study employing retrograde tracers in OFC showed that MO, VO and VLO subdivisions received input from PPC, whereas LO did not (Reep et al., 1996). Our anterograde tracing data corroborate these observations in showing that PPC projections are confined to MO, VO and medial parts of VLO, with a strong preference for VO and medial VLO. Moreover, in line with the figures shown in the article by Reep et al. (1996), we showed that projections to VO and MO originate mainly from mPPC, whereas lPPC and PtP project almost exclusively to medial and central parts of VLO.

Interconnectivity Between Frontal Midline and Orbital Cortices

Areas M2 and the medial half of OFC not only have reciprocal connections with PPC, they are also interconnected with each other. In particular, the rostrocaudal extent of M2 receives projections from superficial and deep layers of MO, VO, and VLO (Reep et al., 1984, 1990; Condé et al., 1995; Hoover and Vertes, 2007) that mainly terminate in layers 1 and 6 of M2 (Hoover and Vertes, 2011). Reciprocating projections from M2 to OFC target the same medial parts of OFC with preferred termination in layers 1, 3 and 5 of VLO, whereas only sparse projections were observed to LO (Reep et al., 1987). The preferred M2 projection to VLO/VO over MO or LO/DLO was corroborated by a retrograde study which showed that the projection originates from neurons in preferentially superficial but also deep layers of M2 along its rostrocaudal extent (Reep et al., 1996). In conclusion, M2 is reciprocally connected with the same portion of OFC as PPC is.

Whether or not connections between area 24 and OFC exist has been debated. One retrograde tracing study failed to observe projections from OFC to caudal parts of area 24a (Reep et al., 1990), whereas other studies have found projections to rostral area 24b that originate in MO, VO, and VLO (Condé et al., 1995; Hoover and Vertes, 2007). The first, negative report likely is caused by the fact that connections between OFC and area 24a, particularly its caudal portions, are overall very sparse (Hoover and Vertes, 2011).

Retrograde tracing studies consistently show that sparse reciprocal connections between area 24b and M2 exist, with cells in superficial and deep layers of both areas projecting to its neighbor, but details on their rostrocaudal topographical organization are not known (Reep et al., 1984, 1990; Condé et al., 1995; Hoover and Vertes, 2007). In an anterograde tracing study, projections from rostral M2 to area 24b were shown terminating sparsely across layers of 24b (Reep et al., 1987). However, results should be interpreted with caution since the two areas are adjacent to each other, and tracer injections in one area are at risk of leaking into the other.

Functional Considerations

As mentioned previously, the focus of functional studies in the rodent PPC, along with frontal cortical areas, has shifted towards roles played by these areas in action control (Whitlock et al., 2008; Erlich et al., 2011; Harvey et al., 2012; Raposo et al., 2014), evidence accumulation (Hanks et al., 2015) and decision making (Raposo et al., 2014; Erlich et al., 2015). In the monkey, numerous anatomical and functional studies have suggested that a coarse somatotopy exists in sensory and motor responses within PPC, such that visual representations are located caudomedially, largely in area 7a, whereas somatic representations are dominant more rostrolaterally, in area 7b (Hyvärinen, 1981; Andersen et al., 1987; Rozzi et al., 2008). Such an organization is also reflected in the connections of areas 7a and 7b with respectively visual and somatosensory cortical areas (Cavada and Goldman-Rakic, 1989a; Andersen et al., 1990). Moreover, monkey PPC subdivisions are preferentially connected with different areas of the frontal cortex containing motor responses for the same part of the body (Cavada and Goldman-Rakic, 1989b; Andersen et al., 1990; Neal et al., 1990; Rozzi et al., 2006; Gharbawie et al., 2011; Stepniewska et al., 2011). The thalamic connections of the rat PPC suggest that mPPC may be homologous to monkey area 7a, whereas lPPC and PtP may be homologous to monkey area 7b (Olsen and Witter, 2016).

The results from the present study suggest that the three subdivisions of the rat PPC have topographically organized connections with frontal cortical areas which could be homologous to those of the monkey. Particularly dense connections exist with area M2, such that mPPC has strong

reciprocal connections with cM2 and lPPC is reciprocally connected with iM2. Similarly, PtP projects to iM2 but details of reciprocal projections are still lacking. Within the rat M2, the distribution of somatosensory and visual input varies along its rostrocaudal axis (Reep et al., 1990), but whether the topography in somatic and visual sensory as well as posterior parietal connections translates into a functional topography remains unknown. Whisker, as well as eye motor responses, have been elicited by microstimulation of this area (Donoghue and Wise, 1982; Neafsey et al., 1986; Brecht et al., 2004), and the entire M2 has been suggested by some to be homologous to the primate frontal eye field (Neafsey et al., 1986; Reep et al., 1990), which is extensively interconnected with PPC. Another study examined the functional organization of motor cortex relative to input from S1, S2 and PPC (Smith and Alloway, 2013). By use of intracortical microstimulations, these authors found that motor cortex can be divided into a sensory processing zone and a motor-output area. Neurons in the transition zone between M1 and M2 were responsive to passive whisker deflections whereas M2 neurons were not. In contrast, the latter were more adequate at evoking whisker responses. Our results showed that lPPC and PtP partly target the transition zone in iM2, which would support their role in sensory integration and the homology to monkey area 7b.

Functional studies have also shown that activity in the rat M2 predicts upcoming movements (Erlich et al., 2011), as does activity in the rodent PPC (Whitlock et al., 2008; Harvey et al., 2012; Raposo et al., 2014), suggesting that the two areas are involved in similar functions. Interestingly, in a perceptual two-choice decision-making task, PPC activity reflected the upcoming action but was not essential for decision-making itself (Hanks et al., 2015). Rather, PPC neurons were constantly evaluating the sum of the presented stimulus. On the other hand, M2 activity was crucial for transforming the total value of the presented stimulus into a motor response (Erlich et al., 2015; Hanks et al., 2015). Further evidence for a functional relationship between PPC and M2 comes from a recent study in rats, which showed that both areas represent posture of the head and back and that spiking activity in PPC anticipates that of M2 (Mimica et al., 2018). Interestingly, the postural representations showed a strong topographical organization that appeared to correspond to the anatomical organization described in our study. Namely, the medial and rostral-most sectors of PPC and the caudal-most regions of M2 shared a predominant sensitivity to the posture of the animals' backs, while the more lateral and caudal regions of PPC were dominated by signals for 3D head position, which was matched by similar tuning in mid-rostral coordinates in M2. This functional organization is specifically in line with the preferred connectivity of lPPC with iM2, and the strong connectivity of mPPC with cM2.

Whether ACC area 24b in the rat is a pure motor area may be debated, though microstimulation of neurons in this region elicits periocular, eye, and nose movements (Brecht et al., 2004). The most rostral part of area 24b is considered part of the medial prefrontal cortex based on its extensive connections with other medial frontal areas (Condé et al., 1995; Fisk and Wyss, 1999; Vertes, 2004; Jones et al., 2005), and our results suggest that this portion is connected exclusively with mPPC. This resembles the organization of monkey PPC-ACC connections where only area 7a receives area 24b input (Pandya et al., 1981). It should be mentioned that these authors described strong projections to area 7a as well as 7b from cingulate area 23, but a homolog of this area has thus far not been found in rodents.

Our data further indicate that the rat PPC is reciprocally connected with OFC medial to the orbital notch in a topographical manner. Anatomical studies have suggested that the connectivity of primate OFC subdivisions is organized in two distinct networks, a medial prefrontal and an orbital one, each of which subserves different functions, and these observations have been extended to the rat OFC (Floyd et al., 2000, 2001; Öngur and Price, 2000; Price, 2007). However, the interpretation of the functional relevance of these networks is confounded by the fact that several OFC subdivisions have connections within both networks. Nevertheless, it is interesting to note in our results that the rat PPC is connected with only a subset of OFC subdivisions located medial to the orbital notch, suggesting a functional specialization of this portion of OFC. It has been suggested that the lateral half of the OFC evaluates individual options for choosing behavior, whereas the medial half compares the choices according to their reward size and probability (for review, see Rudebeck and Murray, 2014). Functional studies in primates have indicated that (pre)frontal cortices, in general, exert a top-down control over PPC during goal-directed actions (Buschman and Miller, 2007; Crowe et al., 2013). Thus, OFC could inform PPC about the value of expected outcomes and perhaps influence the evaluation of appropriate actions within PPC, which would then guide the execution of actions along with motor regions. Even though PPC subdivisions and frontal cortical areas may be interconnected within the same networks, the topographical organization of connections between them found in the present study suggests that functional differences between PPC subdivisions exist. However, further work is required to establish precisely what these differences entail.

DATA AVAILABILITY

All datasets generated for this study are included in the manuscript and/or the **Supplementary Files**.

ETHICS STATEMENT

Animal Subjects

The animal study was reviewed and approved by Norwegian Food Safety Authority Animal Welfare Committee of the Norwegian University of Science, and Technology European Communities Council Directive and the Norwegian animal welfare act.

AUTHOR CONTRIBUTIONS

All authors had full access to all the data in the study and take responsibility for the integrity of the data and the accuracy of the data analysis. MW: obtained funding, study supervision, study concept and design. GO, KH, HK, TS and HS: acquisition of data.

GO, KH, TS, HS and MW: analysis and interpretation of the data. GO and KH: drafting of the manuscript. MW and JW: critical revision of the manuscript for important intellectual content.

FUNDING

This study was supported by the Kavli Foundation and Centre of Excellence (#145993), equipment (#181676), and research (#191929) grants from the Norwegian Research Council. This work was supported by the Centre of Excellence scheme of the Research Council of Norway (Norges Forskningsråd; Centre for Neural Computation, grant No. 223262) and the National Infrastructure scheme of the Research Council of Norway—NORBRAIN, grant No. 197467; JW and KH were supported by a European Research Council (ERC) starting grant (agreement No. 335328), and a Research Council of Norway grant (agreement No. 239963).

ACKNOWLEDGMENTS

We are indebted to Bruno Monterotti and Paulo Girão for their excellent technical assistance in sectioning and histological processing of parts of the material. We thank Paulo Girão for assistance with generating the flatmaps.

SUPPLEMENTARY MATERIAL

The Supplementary Material for this article can be found online at: https://www.frontiersin.org/articles/10.3389/fnsys.2019.00038/full#supplementary-material

REFERENCES

Andersen, R. A., Asanuma, C., Essick, G., and Siegel, R. M. (1990). Corticocortical connections of anatomically and physiologically defined subdivisions within the inferior parietal lobule. *J. Comp. Neurol.* 296, 65–113. doi: 10.1002/cne.902960106

Andersen, R. A., Essick, G. K., and Siegel, R. M. (1987). Neurons of area 7 activated by both visual stimuli and oculomotor behavior. *Exp. Brain Res.* 67, 316–322. doi: 10.1007/bf00248552

Brecht, M., Krauss, A., Muhammad, S., Sinai-Esfahani, L., Bellanca, S., and Margrie, T. W. (2004). Organization of rat vibrissa motor cortex and adjacent areas according to cytoarchitectonics, microstimulation and intracellular stimulation of identified cells. *J. Comp. Neurol.* 479, 360–373. doi: 10.1002/cne.20306

Burcham, K. J., Corwin, J. V., Stoll, M. L., and Reep, R. L. (1997). Disconnection of medial agranular and posterior parietal cortex produces multimodal neglect in rats. *Behav. Brain Res.* 86, 41–47. doi: 10.1016/s0166-4328(96)02241-3

Buschman, T. J., and Miller, E. K. (2007). Top-down versus bottom-up control of attention in the prefrontal and posterior parietal cortices. *Science* 315, 1860–1862. doi: 10.1126/science.1138071

Cavada, C., and Goldman-Rakic, P. S. (1989a). Posterior parietal cortex in rhesus monkey: I. Parcellation of areas based on distinctive limbic and sensory corticocortical connections. *J. Comp. Neurol.* 287, 393–421. doi: 10.1002/cne.902870402

Cavada, C., and Goldman-Rakic, P. S. (1989b). Posterior parietal cortex in rhesus monkey: II. Evidence for segregated corticocortical networks linking sensory and limbic areas with the frontal lobe. *J. Comp. Neurol.* 287, 422–445. doi: 10.1002/cne.902870403

Chen, L. L., Lin, L. H., Barnes, C. A., and Mcnaughton, B. L. (1994a). Head-direction cells in the rat posterior cortex: II. Contributions of visual and ideothetic information to the directional firing. *Exp. Brain Res.* 101, 24–34. doi: 10.1007/bf00243213

Chen, L. L., Lin, L. H., Green, E. J., Barnes, C. A., and Mcnaughton, B. L. (1994b). Head-direction cells in the rat posterior cortex. I. Anatomical distribution and behavioral modulation. *Exp. Brain Res.* 101, 8–23. doi: 10.1007/bf00243212

Condé, F., Maire-Lepoivre, E., Audinat, E., and Crépel, F. (1995). Afferent connections of the medial frontal cortex of the rat: II. Cortical and subcortical afferents. *J. Comp. Neurol.* 352, 567–593. doi: 10.1002/cne.903520407

Corbetta, M., and Shulman, G. L. (2011). Spatial neglect and attention networks. *Annu. Rev. Neurosci.* 34, 569–599. doi: 10.1146/annurev-neuro-061010-113731

Crowe, D. A., Goodwin, S. J., Blackman, R. K., Sakellaridi, S., Sponheim, S. R., MacDonald, A. W., et al. (2013). Prefrontal neurons transmit signals to parietal neurons that reflect executive control of cognition. *Nat. Neurosci.* 16, 1484–1491. doi: 10.1038/nn.3509

Deuel, R. K., and Regan, D. J. (1985). Parietal hemineglect and motor deficits in the monkey. *Neuropsychologia* 23, 305–314. doi: 10.1016/0028-3932(85)90017-X

Donoghue, J. P., and Wise, S. P. (1982). The motor cortex of the rat: cytoarchitecture and microstimulation mapping. *J. Comp. Neurol.* 212, 76–88. doi: 10.1002/cne.902120106

Erlich, J. C., Bialek, M., and Brody, C. D. (2011). A cortical substrate for memory-guided orienting in the rat. *Neuron* 72, 330–343. doi: 10.1016/j.neuron.2011.07.010

Erlich, J. C., Brunton, B. W., Duan, C. A., Hanks, T. D., and Brody, C. D. (2015). Distinct effects of prefrontal and parietal cortex inactivations on an accumulation of evidence task in the rat. *Elife* 4:e05457. doi: 10.7554/eLife.05457

Finch, D. M., Derian, E. L., and Babb, T. L. (1984). Afferent fibers to rat cingulate cortex. *Exp. Neurol.* 83, 468–485. doi: 10.1016/0014-4886(84)90116-x

Fisk, G. D., and Wyss, J. M. (1999). Associational projections of the anterior midline cortex in the rat: intracingulate and retrosplenial connections. *Brain Res.* 825, 1–13. doi: 10.1016/s0006-8993(99)01182-8

Floyd, N. S., Price, J. L., Ferry, A. T., Keay, K. A., and Bandler, R. (2000). Orbitomedial prefrontal cortical projections to distinct longitudinal columns of the periaqueductal gray in the rat. *J. Comp. Neurol.* 422, 556–578. doi: 10.1002/1096-9861(20000710)422:4%3C556::AID-CNE6%3E3.0.CO;2-U

Floyd, N. S., Price, J. L., Ferry, A. T., Keay, K. A., and Bandler, R. (2001). Orbitomedial prefrontal cortical projections to hypothalamus in the rat. *J. Comp. Neurol.* 432, 307–328. doi: 10.1002/cne.1105

Fyhn, M., Molden, S., Witter, M. P., Moser, E. I., and Moser, M. B. (2004). Spatial representation in the entorhinal cortex. *Science* 305, 1258–1264. doi: 10.1126/science.1099901

Gharbawie, O. A., Stepniewska, I., and Kaas, J. H. (2011). Cortical connections of functional zones in posterior parietal cortex and frontal cortex motor regions in new world monkeys. *Cereb. Cortex* 21, 1981–2002. doi: 10.1093/cercor/bhq260

Hafting, T., Fyhn, M., Molden, S., Moser, M. B., and Moser, E. I. (2005). Microstructure of a spatial map in the entorhinal cortex. *Nature* 436, 801–806. doi: 10.1038/nature03721

Hanks, T. D., Kopec, C. D., Brunton, B. W., Duan, C. A., Erlich, J. C., and Brody, C. D. (2015). Distinct relationships of parietal and prefrontal cortices to evidence accumulation. *Nature* 520, 220–223. doi: 10.1038/nature14066

Harvey, C. D., Coen, P., and Tank, D. W. (2012). Choice-specific sequences in parietal cortex during a virtual-navigation decision task. *Nature* 484, 62–68. doi: 10.1038/nature10918

Hoover, W. B., and Vertes, R. P. (2007). Anatomical analysis of afferent projections to the medial prefrontal cortex in the rat. *Brain Struct. Funct.* 212, 149–179. doi: 10.1007/s00429-007-0150-4

Hoover, W. B., and Vertes, R. P. (2011). Projections of the medial orbital and ventral orbital cortex in the rat. *J. Comp. Neurol.* 519, 3766–3801. doi: 10.1002/cne.22733

Hovde, K., Gianatti, M., Witter, M. P., and Whitlock, J. R. (2018). Architecture and organization of mouse posterior parietal cortex relative to extrastriate areas. *Eur. J. Neurosci.* 49, 1313–1329. doi: 10.1111/ejn.14280

Hyvärinen, J. (1981). Regional distribution of functions in parietal association area 7 of the monkey. *Brain Res.* 206, 287–303. doi: 10.1016/0006-8993(81)90533-3

Jones, B. F., Groenewegen, H. J., and Witter, M. P. (2005). Intrinsic connections of the cingulate cortex in the rat suggest the existence of multiple functionally segregated networks. *Neuroscience* 133, 193–207. doi: 10.1016/j.neuroscience.2005.01.063

King, V. R., and Corwin, J. V. (1992). Spatial deficits and hemispheric asymmetries in the rat following unilateral and bilateral lesions of posterior parietal or medial agranular cortex. *Behav. Brain Res.* 50, 53–68. doi: 10.1016/s0166-4328(05)80287-6

King, V. R., and Corwin, J. V. (1993). Comparisons of hemi-inattention produced by unilateral lesions of the posterior parietal cortex or medial agranular prefrontal cortex in rats: neglect, extinction and the role of stimulus distance. *Behav. Brain Res.* 54, 117–131. doi: 10.1016/0166-4328(93)90070-7

Kolb, B., and Walkey, J. (1987). Behavioural and anatomical studies of the posterior parietal cortex in the rat. *Behav. Brain Res.* 23, 127–145. doi: 10.1016/0166-4328(87)90050-7

Kondo, H., and Witter, M. P. (2014). Topographic organization of orbitofrontal projections to the parahippocampal region in rats. *J. Comp. Neurol.* 522, 772–793. doi: 10.1002/cne.23442

Kropff, E., Carmichael, J. E., Moser, M. B., and Moser, E. I. (2015). Speed cells in the medial entorhinal cortex. *Nature* 523, 419–424. doi: 10.1038/nature14622

Lewis, J. W., and Van Essen, D. C. (2000). Corticocortical connections of visual, sensorimotor and multimodal processing areas in the parietal lobe of the macaque monkey. *J. Comp. Neurol.* 428, 112–137. doi: 10.1002/1096-9861(20001204)428:1%3C112::AID-CNE8%3E3.0.CO;2-9

Mesulam, M. M. (1999). Spatial attention and neglect: parietal, frontal and cingulate contributions to the mental representation and attentional targeting of salient extrapersonal events. *Philos. Trans. R. Soc. Lond. B Biol. Sci.* 354, 1325–1346. doi: 10.1098/rstb.1999.0482

Mesulam, M. M., Van Hoesen, G. W., Pandya, D. N., and Geschwind, N. (1977). Limbic and sensory connections of the inferior parietal lobule (area PG) in the rhesus monkey: a study with a new method for horseradish peroxidase histochemistry. *Brain Res.* 136, 393–414. doi: 10.1016/0006-8993(77)90066-x

Miller, M. W., and Vogt, B. A. (1984). Direct connections of rat visual cortex with sensory, motor and association cortices. *J. Comp. Neurol.* 226, 184–202. doi: 10.1002/cne.902260204

Mimica, B., Dunn, B. A., Tombaz, T., Bojja, V., and Whitlock, J. R. (2018). Efficient cortical coding of 3D posture in freely behaving rats. *Science* 362, 584–589. doi: 10.1126/science.aau2013

Neafsey, E. J., Bold, E. L., Haas, G., Hurley-Gius, K. M., Quirk, G., Sievert, C. F., et al. (1986). The organization of the rat motor cortex: a microstimulation mapping study. *Brain Res.* 396, 77–96. doi: 10.1016/s0006-8993(86)80191-3

Neal, J. W., Pearson, R. C., and Powell, T. P. (1990). The ipsilateral corticocortical connections of area 7 with the frontal lobe in the monkey. *Brain Res.* 509, 31–40. doi: 10.1016/0006-8993(90)90305-u

Nitz, D. A. (2006). Tracking route progression in the posterior parietal cortex. *Neuron* 49, 747–756. doi: 10.1016/j.neuron.2006.01.037

Nitz, D. A. (2012). Spaces within spaces: rat parietal cortex neurons register position across three reference frames. *Nat. Neurosci.* 15, 1365–1367. doi: 10.1038/nn.3213

Olsen, G. M., Ohara, S., Iijima, T., and Witter, M. P. (2017). Parahippocampal and retrosplenial connections of rat posterior parietal cortex. *Hippocampus* 27, 335–358. doi: 10.1002/hipo.22701

Olsen, G. M., and Witter, M. P. (2016). The posterior parietal cortex of the rat: architectural delineation and thalamic differentiation. *J. Comp. Neurol.* 524, 3774–3809. doi: 10.1002/cne.24032

Öngur, D., and Price, J. L. (2000). The organization of networks within the orbital and medial prefrontal cortex of rats, monkeys and humans. *Cereb. Cortex* 10, 206–219. doi: 10.1093/cercor/10.3.206

Pandya, D. N., and Kuypers, H. G. (1969). Cortico-cortical connections in the rhesus monkey. *Brain Res.* 13, 13–36. doi: 10.1016/0006-8993(69)90141-3

Pandya, D. N., Van Hoesen, G. W., and Mesulam, M. M. (1981). Efferent connections of the cingulate gyrus in the rhesus monkey. *Exp. Brain Res.* 42, 319–330. doi: 10.1007/bf00237497

Paxinos, G., and Watson, C. (2007). *The Rat Brain in Stereotaxic Coordinates*. 6th Edn. San Diego, CA: Academic press.

Pesaran, B., Nelson, M. J., and Andersen, R. A. (2008). Free choice activates a decision circuit between frontal and parietal cortex. *Nature* 453, 406–409. doi: 10.1038/nature06849

Petras, J. M. (1971). Connections of the parietal lobe. *J. Psychiatr. Res.* 8, 189–201. doi: 10.1016/0022-3956(71)90018-5

Price, J. L. (2007). Definition of the orbital cortex in relation to specific connections with limbic and visceral structures and other cortical regions. *Ann. N Y Acad. Sci.* 1121, 54–71. doi: 10.1196/annals.1401.008

Raposo, D., Kaufman, M. T., and Churchland, A. K. (2014). A category-free neural population supports evolving demands during decision-making. *Nat. Neurosci.* 17, 1784–1792. doi: 10.1038/nn.3865

Reep, R. L., Chandler, H. C., King, V., and Corwin, J. V. (1994). Rat posterior parietal cortex: topography of corticocortical and thalamic connections. *Exp. Brain Res.* 100, 67–84. doi: 10.1007/bf00227280

Reep, R. L., Corwin, J. V., Hashimoto, A., and Watson, R. T. (1984). Afferent connections of medial precentral cortex in the rat. *Neurosci. Lett.* 44, 247–252. doi: 10.1016/0304-3940(84)90030-2

Reep, R. L., Corwin, J. V., Hashimoto, A., and Watson, R. T. (1987). Efferent connections of the rostral portion of medial agranular cortex in rats. *Brain Res. Bull.* 19, 203–221. doi: 10.1016/0361-9230(87)90086-4

Reep, R. L., Corwin, J. V., and King, V. (1996). Neuronal connections of orbital cortex in rats: topography of cortical and thalamic afferents. *Exp. Brain Res.* 111, 215–232. doi: 10.1007/bf00227299

Reep, R. L., Goodwin, G. S., and Corwin, J. V. (1990). Topographic organization in the corticortical connections of medial agranular cortex in rats. *J. Comp. Neurol.* 294, 262–280. doi: 10.1002/cne.902940210

Rozzi, S., Calzavara, R., Belmalih, A., Borra, E., Gregoriou, G. G., Matelli, M., et al. (2006). Cortical connections of the inferior parietal cortical convexity of the macaque monkey. *Cereb. Cortex* 16, 1389–1417. doi: 10.1093/cercor/bhj076

Rozzi, S., Ferrari, P. F., Bonini, L., Rizzolatti, G., and Fogassi, L. (2008). Functional organization of inferior parietal lobule convexity in the macaque monkey: electrophysiological characterization of motor, sensory and mirror responses and their correlation with cytoarchitectonic areas. *Eur. J. Neurosci.* 28, 1569–1588. doi: 10.1111/j.1460-9568.2008.06395.x

Rudebeck, P. H., and Murray, E. A. (2014). The orbitofrontal oracle: cortical mechanisms for the prediction and evaluation of specific behavioral outcomes. *Neuron* 84, 1143–1156. doi: 10.1016/j.neuron.2014.10.049

Sargolini, F., Fyhn, M., Hafting, T., Mcnaughton, B. L., Witter, M. P., Moser, M. B., et al. (2006). Conjunctive representation of position, direction and velocity in entorhinal cortex. *Science* 312, 758–762. doi: 10.1126/science.1125572

Save, E., and Moghaddam, M. (1996). Effects of lesions of the associative parietal cortex on the acquisition and use of spatial memory in egocentric and allocentric navigation tasks in the rat. *Behav. Neurosci.* 110, 74–85. doi: 10.1037/0735-7044.110.1.74

Save, E., Paz-Villagran, V., Alexinsky, T., and Poucet, B. (2005). Functional interaction between the associative parietal cortex and hippocampal place cell firing in the rat. *Eur. J. Neurosci.* 21, 522–530. doi: 10.1111/j.1460-9568.2005.03882.x

Save, E., and Poucet, B. (2000). Involvement of the hippocampus and associative parietal cortex in the use of proximal and distal landmarks for navigation. *Behav. Brain Res.* 109, 195–206. doi: 10.1016/S0166-4328(99)00173-4

Smith, J. B., and Alloway, K. D. (2013). Rat whisker motor cortex is subdivided into sensory-input and motor-output areas. *Front. Neural Circuits* 7:4. doi: 10.3389/fncir.2013.00004

Solstad, T., Boccara, C. N., Kropff, E., Moser, M. B., and Moser, E. I. (2008). Representation of geometric borders in the entorhinal cortex. *Science* 322, 1865–1868. doi: 10.1126/science.1166466

Stepniewska, I., Friedman, R. M., Gharbawie, O. A., Cerkevich, C. M., Roe, A. W., and Kaas, J. H. (2011). Optical imaging in galagos reveals parietal-frontal circuits underlying motor behavior. *Proc. Natl. Acad. Sci. U S A* 108, E725–E732. doi: 10.1073/pnas.1109925108

Sugar, J., and Witter, M. P. (2016). Postnatal development of retrosplenial projections to the parahippocampal region of the rat. *Elife* 5:e13925. doi: 10.7554/eLife.13925

Vertes, R. P. (2004). Differential projections of the infralimbic and prelimbic cortex in the rat. *Synapse* 51, 32–58. doi: 10.1002/syn.10279

Vogt, B. A., and Miller, M. W. (1983). Cortical connections between rat cingulate cortex and visual, motor and postsubicular cortices. *J. Comp. Neurol.* 216, 192–210. doi: 10.1002/cne.902160207

Vogt, B. A., and Paxinos, G. (2014). Cytoarchitecture of mouse and rat cingulate cortex with human homologies. *Brain Struct. Funct.* 219, 185–192. doi: 10.1007/s00429-012-0493-3

Wang, Q., and Burkhalter, A. (2007). Area map of mouse visual cortex. *J. Comp. Neurol.* 502, 339–357. doi: 10.1002/cne.21286

Wang, Q., Gao, E., and Burkhalter, A. (2011). Gateways of ventral and dorsal streams in mouse visual cortex. *J. Neurosci.* 31, 1905–1918. doi: 10.1523/JNEUROSCI.3488-10.2011

Wang, Q., Sporns, O., and Burkhalter, A. (2012). Network analysis of corticocortical connections reveals ventral and dorsal processing streams in mouse visual cortex. *J. Neurosci.* 32, 4386–4399. doi: 10.1523/JNEUROSCI.6063-11.2012

Whitlock, J. R., Sutherland, R. J., Witter, M. P., Moser, M. B., and Moser, E. I. (2008). Navigating from hippocampus to parietal cortex. *Proc. Natl. Acad. Sci. U. S. A.* 105, 14755–14762. doi: 10.1073/pnas.08042 16105

Wilber, A., Clark, B. J., Demecha, A. J., Mesina, L., Vos, J. M., and Mcnaughton, B. L. (2015). Cortical connectivity maps reveal anatomically distinct areas in the parietal cortex of the rat. *Front. Neural Circuits* 8:146. doi: 10.3389/fncir.2014.00146

Zingg, B., Hintiryan, H., Gou, L., Song, M. Y., Bay, M., Bienkowski, M. S., et al. (2014). Neural networks of the mouse neocortex. *Cell* 156, 1096–1111. doi: 10.1016/j.cell.2014.02.023

Conflict of Interest Statement: The authors declare that the research was conducted in the absence of any commercial or financial relationships that could be construed as a potential conflict of interest.

Paper 3

Action representation in the mouse parieto-frontal network

Tuce Tombaz[1†*], Benjamin A. Dunn[1,2*], Karoline Hovde[1§], Ryan J. Cubero[1§], Bartul Mimica[1§], Pranav Mamidanna[3], Yasser Roudi[1], Jonathan R. Whitlock[1†]

1. Kavli Institute for Systems Neuroscience & Centre for Neural Circuits, Norwegian University of Science and Technology, Olav Kyrres Gate 9, 7489 Trondheim, Norway.

2. Department of Mathematical Sciences, Norwegian University of Science and Technology, Alfred Getz' Vei 1, 7034 Trondheim, Norway.

3. Department of Health Science and Technology, Center for Sensory-Motor Interaction, Aalborg University, D3, Fedrik Bajers Vej 7, 9920 Aalborg, Denmark.

Running title: Action coding in mouse cortex

Total number of characters with spaces (significance statement, abstract, main text, references, main and supporting figure legends): 70 781

No. figures: 5

*These authors contributed equally to the work
§ These authors contributed equally to the work

† Correspondance:
Tuce Tombaz: Tel +47 91887550, fax +47 73598294; e-mail: tuce.tombaz@ntnu.no
Jonathan Whitlock: Tel +47 45164390, fax +47 73598294; e-mail: jonathan.whitlock@ntnu.no

Keywords: posterior parietal cortex, motor cortex, mouse, action, mirror neuron

Significance statement

The parieto-frontal network in mammals mediates several functions supporting goal-directed behavior, which in primates can include representing the actions of conspecifics. Mirror neurons, discovered in monkeys, are postulated to fulfill this role since they respond when the same actions are performed and observed, but whether mirror neurons occur in other social mammals, such as rodents, is unknown. Here we show that neural ensembles in the mouse posterior parietal and frontal motor cortices robustly encode a variety of natural actions when they are performed, yet do not respond when the same behaviors are observed. These findings invite further research into the physiological basis of observational learning in rodents, and raise important questions about species-specific adaptations in cortical circuits.

Abstract

The posterior parietal cortex (PPC), along with anatomically linked frontal areas, form a cortical network which mediates several functions that support goal-directed behavior, including sensorimotor transformations and decision making. In primates, this network also links performed and observed actions via mirror neurons, which fire both when an individual performs an action and when they observe the same action performed by a conspecific. Mirror neurons are thought to be important for social learning and imitation, but it is not known whether mirror-like neurons occur in similar networks in other species that can learn socially, such as rodents. We therefore imaged Ca^{2+} responses in large neural ensembles in PPC and secondary motor cortex (M2) while mice performed and observed several actions in pellet reaching and wheel running tasks. In all animals, we found spatially overlapping neural ensembles in PPC and M2 that robustly encoded a variety of naturalistic behaviors, and that subsets of cells could stably encode multiple actions. However, neural responses to the same set of observed actions were absent in both brain areas, and across animals. Statistical modeling analyses also showed that performed actions, especially those that were task-specific, outperformed observed actions in predicting neural responses. Overall, these findings show that performed and observed actions do not drive the same cells in the parieto-frontal network in mice, and suggest that sensorimotor mirroring in the mammalian cortex may have evolved more recently, and only in certain species.

Introduction

A key function of any motor system is the rapid and flexible production of actions in response to external stimuli, including the behavior of other individuals. Having robust representations of performed and observed behaviors has therefore been hypothesized to add survival value in a number of species since it facilitates an array of behavioral functions, including optimal action selection, gaining access to food sources or avoiding predators (1). However, which neural circuits integrate performed and observed actions, and how, are not well understood. In different species of primates and songbirds, a striking manifestation of such interactions has been described in the form of mirror neurons. Mirror neurons, first characterized in pre-motor cortex (2, 3) then PPC (4) in monkeys, and later reported in humans (5) and birds (6)**,** respond reliably both when an individual performs a specific action and when they observe the same action performed by a conspecific. Based on these properties, they have been postulated to enable skills requiring conjoint coding of observed and performed behaviors, such as imitation and action understanding (7, 8). The striking specificity of mirror coding requires that sensory and motor processing streams are combined precisely at the level of single cells, which prompts the question as to how such a mechanism arose originally. That is, did prototypical sensory and motor processing pathways become linked early in evolution, in which case most species should exhibit sensorimotor mirror matching, or is it a more recent adaptation suited to the needs of a few specific niches?

To address this question, we tested whether neurons in PPC and frontal motor cortex (M2) of mice encode the performance and observation of unrestrained motor behaviors. We chose rodents since they fall between primates and avians phylogenetically, they can socially acquire both sensorimotor and fear-based behaviors (9-14), and they have proven effective models for studying the neurobiology of empathetic social learning (15-19). Emerging evidence also suggests that PPC and M2 in rodents, like primates, comprise a cortical network supporting several aspects of goal-directed behavior,

including decision making (20, 21), sensorimotor transformations (22, 23), and movement planning (24, 25). Rodent models also bring methodological advantages, including large-scale neural recordings in unrestrained subjects, which enables the analysis of neural ensemble dynamics during any number of self-initiated actions. In turn, it is possible to uncover intrinsic features of neural population activity driven by behavior, such as state space structure (26), independently of experimenter bias.

Here, we used miniaturized, head-mounted fluorescent microscopes (27) to image the activity of hundreds of individual neurons at a time while mice performed or observed pellet reaching and wheel-running tasks. First, using dimensionality reduction (28), we saw clear differences in the structure of ensemble responses during performed and observed behaviors. This motivated the subsequent quantification of single-cell selectivity to specific behaviors using shuffling analyses as well as statistical modeling with a generalized linear model (GLM). All tests indicated that PPC and M2 were driven strongly by performed behaviors, similar to what has been shown in more stereotypical tasks (26), but extended here to freely behaving animals. The neural coding of observed behavior, on the other hand, was below chance levels in both brain areas, even in neurons with strong performance correlates. These results indicate that the representation of the observed actions we tested occurs outside the parieto-frontal circuit in mice, which suggests a divergence in action recognition mechanisms between primates and rodents. By extension, this supports the view that sensorimotor mirroring evolved independently in birds and primates.

Results

To determine whether neurons in the mouse PPC and M2 reliably responded to the performance and observation of the same set of behaviors, we used one-photon epifluorescence microscopy to image the activity of neuronal ensembles expressing the genetically encoded calcium indicator GCaMP6m (AAV1.Syn.GCaMP6m.WPRE.SV40) via AAV-mediated transfection (921 neurons in PPC in 4 mice; 852 neurons in M2 in 4 mice; Fig. S1, Table 1). Cellular responses were monitored through a chronically implanted gradient refractive index lens attached to a prism (Fig. 1 *A* and *C*). All animals were trained to perform the pellet reaching task (29) in an 8.5 x 15 x 20 cm box (Fig. 1*B*), in which they were taught to reach through a 1 cm diameter hole to grasp food pellets (Fig. 1*B*). They were trained to asymptotic performance levels prior to experimental recordings (maximum of 10 days; Methods) and, concurrently, were habituated to head-fixation and to observe a sibling perform the same task. In the experiments, each animal's cortical activity was imaged during four sessions, with performance (P) and observation (O) conditions interleaved (following a P1-O1-P2-O2 scheme). In parallel, we recorded from each mouse while they behaved freely in a wall-less open arena (30 x 30 cm) with a running wheel, and while they observed a sibling doing the same (Fig. 1*B*). The calcium imaging data were paired with high-resolution behavioral recordings made during both performance and observation sessions.

Having imaged large ensembles of neurons in PPC and M2, as a prelude to our analysis, we visualized how performance and observation conditions affected the population activity. To this end, we applied the uniform manifold approximation and projection (UMAP) method on downsampled population activity vectors (Methods) (28). As shown in Fig. 2 *A* and *B*, this revealed structural discrepancies in the dimensionally-reduced activity space between performance and observation sessions, with population activity states being closer to each other for time points belonging to the same behavior during performance, but not observation conditions (Movie S1). We measured the degree to which time points labeled by the same behaviors were clustered using the Dunn Index (Methods), which

produced clustering indices between 2.4 and 10.9 times higher during performance than observation sessions across animals (3 mice in PPC, 1 mouse in M2). This suggested that there were clear signatures of the representation of performed behavior but not observed behavior in PPC and M2 activity. Due to the dependence of the quantitative aspects of the UMAP results on several initial parameters, such as the dimension of the projective space, a more careful quantification of these effect required going beyond this visualization, which is what we report in the rest of the paper.

To determine if the UMAP results reflected behavioral selectivity at the single-cell level, we quantified the tuning of individual neurons to different actions the animals engaged in while performing the tasks. We labelled the onset and offset of discrete, recurring behaviors, including turning left or right, nose poking, grasping to eat, eating, rearing or grooming (Fig. 3 *A*; Movie S2; Methods). A cell was considered stably tuned to a behavior if its in-behavior event rate exceeded 95% of the shuffled in-behavior rates in two consecutive performing sessions (Methods). Approximately half the neurons in both PPC (430 of 921 cells; 46.6% in 4 mice) and M2 (439 of 852 cells, 51.5%, 4 mice) were reliably driven by performed behaviors (Fig. 3 *B* and *C*; Table S1). While the majority of neurons were uniquely tuned to individual behaviors, subsets of cells were selective for multiple actions, and in all cases, tuning was invariant to the duration of the behavior (Fig. S2). In the open field task, 67 of 724 PPC cells (9.3%; 3 mice) in PPC were stably tuned to clockwise (CW) and counter-clockwise (CCW) wheel running, while 21 out of 216 neurons (9.7%, running CCW only; 1 mouse) were stably tuned in M2. The proportion of cells representing each behavior varied between animals, with larger groups of cells encoding turning in both PPC and M2, and a larger proportion of cells tuned to grasping in M2 than PPC (Figs. 3 *B-D*, S2).

The heterogeneity of tuning properties, and the tuning of some cells to multiple behaviors, raised the question as to whether cells with similar coding clustered anatomically, as suggested by prior work in parietal and motor areas in different mammalian species (30-32). Ensemble imaging allowed us to

assess the spatial micro-organization of behaviorally responsive neurons according to their tuning preference in each brain region of each animal. However, an analysis of the quality of clustering by behavioral tuning (Dunn Index; Methods) showed no clear tendency of grouping between cells with similar properties, nor any clear mapping based on cortical depth or location in the imaging field of view (Fig. S3 and S4).

Since PPC and M2 showed robust tuning to a variety of performed behaviors, we next assessed whether they responded during observation of the same actions. We compared trial-averaged responses to specific behaviors across all four recording sessions: P1, O1, P2 and O2 (Fig. 4 *A* and *B* upper panels). However, in both brain areas and across mice, we saw negligible neural tuning to observed actions, irrespective of whether the cells stably encoded performed actions (Fig. 4 *A* and *B* lower panels, Fig.S5). Specifically,15 of 921 neurons (1.6%) in PPC and 13 out of 852 neurons (1.5%) in M2 exhibited stable observational correlates for the pellet reaching task, even though the total amount of time the animals spent observing behaviors was comparable to the time spent performing them (Table S1). To test whether the proportion of cells reliably tuned to observed behaviors exceeded chance levels, we paired neural activity with behavior labels from the wrong sessions and computed false positive rates in this manner for all sessions and all animals (Methods). This approach identified 27/921 (2.9%) PPC cells and 32/852 (3.8%) M2 cells as stably tuned to mismatched observed behaviors, demonstrating that the low number of stable observational correlates was less than expected by chance (PPC: U= 286.5, $p > 0.05$, M2: U = 228, $p > 0.05$; Mann-Whitney U test). Similarly, in the open field task, only three out of 724 neurons (0.4%) and one out of 216 neurons (0.5%) had reliable observational tuning to running behaviors in PPC and M2, respectively. Fewer than 1% of cells had stable, matched correlates for performed and observed actions in the pellet reaching task in either area, which again was below mismatched data rates (U = 364, $p > 0.05$ for PPC; U = 287.5, $p > 0.05$ for M2). Moreover, no cells showed matched tuning for wheel-running behavior in the open field task (Table S1).

To investigate whether the lack of neural responsiveness to observed actions stemmed from fluctuations in arousal state, we measured variations in pupil diameter, a proxy for arousal and attention (33), in a subset of mice. Since prior work established that contraction of the pupil is associated with reduced attentiveness and neural responsiveness (34), we restricted our analyses of observation sessions to exclude epochs when the pupil diameter was smallest (Fig. S6; n = 3 animals). Consistent with our prior findings, however, this did not affect the number of cells showing stable tuning (9 of 621 cells (1.5%) with all timepoints included, 8 cells (1.3%) when excluding pupil contraction), indicating the lack of effect did not relate to low arousal of the observers.

To further assess whether activity patterns during performance sessions related to observation, we sought to characterize how well cellular activity could be predicted from one task condition to another. When cells were selected based on their behavioral tuning in the first performing session, and their z-scored firing rates were correlated to those in the second performing session, we saw in every case that the responses of cells correlated positively (Pearson's correlations for same-behavior comparisons ranged from 0.22 to 0.75 for PPC and 0.08 to 0.48 for M2; Fig. 4*C*). Likewise, selecting cells based on their tuning in the second session and correlating those rates back to the first yielded similar results (r-values ranged from 0.20 to 0.71 in PPC and 0.1 to 0.44 for M2; Fig. 4*C*). By comparison, the correlations of activity rates between performance and observation sessions centered around zero in all cases (r-values ranged from -0.09 to 0.12 for PPC and -0.24 to 0.22 for M2; Fig. 4*C*).

Lastly, we wished to determine the extent to which each of the behaviors explained the activity rates of the cells during performance and observation conditions, for which we used a generalized linear model (GLM) framework (Methods) (35). The model was designed to incorporate all labelled behaviors as predictors of each neuron's time-varying activity. To quantify how well the behavioral variables accounted for the activity of the neurons, we computed cross-validated negative log-likelihood ratios

by normalizing the negative log-likelihoods of single variable models to that of the null-model (Methods). For each of the behaviors considered, and in both pellet reaching and open field tasks, we found that neural responses in PPC and M2 were better predicted by performed behaviors compared to a model with only the constant term (i.e. the mean firing rate; Fig. 5 *A* and *B*). We also noted that the proportions of neurons that were stably tuned to task-dependent behaviors such as grasping (10% in PPC and 24% in M2) and eating (7% in PPC and 6% in M2) fared better than those with task-independent behaviors, such as grooming or rearing. Predictions based on observed behaviors, on the other hand, were in all cases worse than the null-model (Fig. 5 *A* and *B*), which was contrasted strongly by the significant improvement in model performance for the observers' own movements.

Discussion

The results of our study demonstrate that PPC and M2 were reliably modulated by the execution of various natural behaviors in both pellet-reaching and wheel-running tasks, which was juxtaposed sharply by the low number of neurons responding to observed behaviors, which neither exceeded chance levels nor aided in predicting neural activity. Our analysis was inspired by exploration of dimensionally reduced network state dynamics across task conditions, which revealed that population activity in both brain areas was more structured during performance than observation of behaviors. We note that the behavioral clusters in the dimensionality-reduced manifold of performance sessions were not fully separated, which could suggest that the population vectors do not lie completely on a two-dimensional non-linear manifold, that other tunable parameters of UMAP were not ideally chosen, or that variables which we did not measure, such as posture or decision-making, bind separate behaviors more closely together. In contrast, action observation did not elicit any appreciable structure in population activity. This led us to perform a GLM analysis which confirmed that action observation does not predict neural activity. In fact, the bodily movement of the observers was the most influential factor in the statistical model, which was consistent with results from the performance sessions, and could have been part of a larger wave of neural activation in the brain, as described in recent work in head-fixed animals (36,37).

The fact that the animals were freely moving when performing the tasks allowed us to measure how cells responded to a variety of actions, revealing new features of behavioral coding in both PPC and M2. First, just under 15% of cells in both areas stably represented more than one behavior (Fig. S2), and cells coding for different behaviors were intermingled anatomically. This indicates that cell ensembles in PPC or M2 are apt to participate in more than one behavioral representation, though any overarching organization of tuning based on somatotopy (30), posture (38) or ethological organization (31, 39) was not apparent at the microscales at which we were imaging. Furthermore, while the exact proportion of represented behaviors varied per animal, we generally found turning

represented strongly in both PPC and M2, while rearing was more prevalent in PPC and grasping was stronger in M2. In both areas, however, eating was the best predictor of population calcium events in the GLM (Fig. 5), despite that it was coded by comparatively few neurons. Since this predictability could not be attributed to the over-expression of eating epochs relative to other behaviors (Fig S2), it could reflect the salience of the consumptive behavior. It could also imply a population coding strategy where increased single-neuron selectivity compensates for the small population size or, conversely, that a small population size is all that is used because the neurons are strongly tuned (40). On the whole, the heterogeneous response selectivity of cells across distinct behavioral categories is consistent with previous work on multisensory coding and decision making in the rodent PPC (41, 42), while the absence of spatial clustering for similarly tuned neurons is consistent with the dispersed anatomical organization of orientation tuning in primary visual cortex (43), and olfactory coding in the piriform cortex (44).

As for mirror neurons, they have been best characterized across primate species in pre-motor cortex and PPC which, together, comprise the parieto-frontal network (2, 4, 45, 46). This network supports several functions required for goal-directed behavior including sensorimotor transformations, action planning and decision making (47, 48). Although it was long thought that rodent brains lacked the prerequisite complexity to subserve higher cognitive functions, a growing body of work shows that both rats and mice exhibit accomplished performance in sensory-motor tasks such as virtual navigation (49) and evidence-based decision making (20, 50), and they show stimulus history effects (51-53). In terms of anatomy, although PPC and M2 are considerably less elaborate in mice than primates, there are several features common to both species which could support action recognition, including strong input from higher visual areas (54, 55) and dense reciprocal connectivity between PPC and M2 (56-59). Given the anatomical and functional similarities, we reasoned that neurons in the rodent PPC-M2 circuit might exhibit mirror-like responses to the observation and execution of the same actions, and were surprised by the effective absence of observational tuning in both areas.

To our understanding, there are at least two possibilities why this could be the case. One is that the range of behaviors considered was of the wrong kind to elicit mirror responses in rodents. While the pellet reaching task encapsulated the grasping and eating behaviors which evoked mirror neuron activation in primates, it also allowed for the expression of several other natural behaviors, such as grooming and rearing, and wheel running was strongly encoded, particularly in PPC. The absence of observational responses in such tasks suggests that mice may be a species where representations of observed and performed actions do not converge on the same neurons, at least not in the PPC-M2 network, and their capacity for sensorimotor observational learning (13, 14) may depend on non-mirror associative mechanisms. This contrasts with affective learning paradigms, where, for example, mirror-like responses have been shown for pain in the anterior cingulate of rats (19). Thus, distinct anatomical pathways might utilize different neural mechanisms to support different forms of social learning. Another possibility for our findings is that observed actions are encoded in areas outside or upstream of where we imaged. For example, extrastriate areas AL and RL receive the same, if not more, input from V1 as the more medial regions we imaged in PPC, and they project to frontal motor cortices, and could be potential targets for similar experiments in the future.

If the cortical motor system in mice indeed lacks mirror neurons it could also have implications for the evolutionary lineage of sensorimotor mirroring (60). To date, such a phenomenon has been shown in songbirds (6), new (46) and old world monkeys (2, 45), and humans (5, 61). This variety of species raises questions about the phylogenetic development of the capacity for mirroring, and the systems supporting these functions. For example, neurons jointly encoding the vocalization of self and others were found in the telencephalic nucleus HVC of swamp sparrows and zebra finches (6, 62), while audio-vocal mirror neurons were shown in the human inferior frontal gyrus (63). Though avian and primate circuits are not structurally homologous, the question of whether the capacity for mirroring evolved independently or originated in a common ancestor has remained open. Our results suggest the former scenario. Unlike sensorimotor mirroring, vicarious responses for affective states, such as

disgust or pain, have been reported in corresponding areas in humans (64, 65) and rodents (19), which is consistent with conserved mirroring involving more ancient sub-cortical systems. This suggests that fundamentally different neural computations may support emotional vs. sensorimotor learning, at least in rodents, and that the likelihood of finding mirror neurons within a system will vary depending on the species in question.

Materials and methods

Subjects and virus injection. All procedures were approved by and in accordance with the Norwegian Animas Act and the European Convention for the Protection of Vertebrate Animals for Experimental and Other Scientific Purposes. Experimental mice were 3 to 7 month old wild type C56BL/6 females (6 from Taconic Bioscience, 2 from The Jackson Laboratory), individually housed on a 12 hr inverted light/dark cycle with ad libitum access to food and water. Surgeries were performed under sterilized conditions and body temperature was maintained at 37°C with a heating pad. Anesthesia was induced using isoflurane mixed with oxygen (5% for induction, 1-1.5% for maintenance) on a stereotactic frame (David Kopf Instruments). Prior to surgery, mice were injected with analgesics subcutaneously (Metacam 1 mg/kg, Temgesic 0.1mg/kg weight) and with a local anesthetic (Marcain 0.5mg/ml) under the skin surface above the skull before making an incision. Following the initial induction and drug administration, the dorsal surface of the head was shaved and ophthalmic ointment was applied to the eyes. The incision area was scrubbed with cotton swabs dipped in 70% Ethanol followed by betadine (2 x each), and a small incision was made along the midline. All measurements were made relative to bregma for virus and prism probe implant surgeries. A craniotomy (1.2 x 1.2mm) was made and each animal was injected with 300nl of AAV1.Syn.GCaMP6m.WPRE.SV40 (University of Pennsylvania Vector Core; item # AV-1-PV2823) at multiple locations in the right hemisphere of the posterior parietal cortex (AP: -1.95, ML: 1.5, DV: 0.35 and 0.7; AP: -1.95, ML: 1.9, DV: 0.35 and 0.7mm relative to bregma) or secondary motor cortex (AP:+0.5, ML: 0.5, DV: 0.5; AP: +0.2, ML: 0.5, DV: 0.5mm relative to bregma) using a Nanoject II Injector (WPI, USA), delivering virus at a rate of 35nl per min with a controller (Micro4; WPI). The glass injection pipette was left in place for 10 min post-injection, after which it was slowly withdrawn. Following the viral injections, the craniotomy was filled with Kwik-Sil silicone elastomer (WPI) and the incision was closed with nylon sutures. After surgery, mice were kept in a heated chamber until they regained consciousness and began moving.

Prism probe implantation. One week post virus-injection, a 1mm diameter gradient refractive index lens (GRIN) attached to a prism (Inscopix) was lowered stereotaxically into the craniotomy at a rate of 10µm/s while the tissue was treated constantly with saline to minimize desiccation. The prism lens was positioned 1.2-1.3mm deep and 0.15 - 0.2mm away from the injection site. Lens implants were secured to the skull with a thin layer of Kwik-Sil silicone elastomer, followed by a thick layer of adhesive cement (super-bond C&B, Sun Medical). The lens cuff was filled with Kwik-Cast (WPI) for protection during a 1-2 week interval to allow for viral expression. A custom made head bar was cemented to the skull with dental acrylic for head fixation in behavioral experiments.

Once viral expression was confirmed, mice underwent anesthesia to secure a baseplate (Inscopix), which was cemented on the prism probe to support the connection of the miniaturized microscope during in vivo imaging under freely moving conditions. During the procedure, a baseplate was attached to the miniature epifluorescence microscope (nVista HD, Inscopix) and stereotaxically positioned to a desired focal plane with the help of visible landmarks (GCaMP6m-expressing neurons and blood vessels) using 20-30% LED power, a frame rate of 5Hz and digital gain of 4. Once the focal plane was identified, the microscope and baseplate were raised by ~50µm to compensate for shrinkage of the adhesive cement, and were subsequently fixed in place using the same compound, followed by a thin layer of dental acrylic mixed with black carbon spherical powder (Sigma Aldrich) to minimize the light interference of the imaging field. The baseplate was covered with a protective cap (Inscopix), and imaging began within 1-2 days.

Behavioral training and recording. Animal training. Pairs of sibling animals were used in all experiments, and were housed together for one week prior to the start of training. During this period, each animal was habituated to the experimenter and handled extensively on a daily basis. Subsequently, mice were housed individually and food restricted to maintain 90% initial body weight throughout the training period. They were trained daily for 7-10 days in a modified version of the pellet reaching task (29). The chamber used for the task was built from clear plexiglass (3mm thick, 20

x 8.5 x 15cm) with a rectangular cylinder attached externally through which food pellets were delivered (Fig.1). After one day of habituation to the box with no pellets, animals underwent 2 stages of task acquisition; shaping and training. During shaping (2 days, 2 sessions per day), mice were presented with multiple chocolate pellets (20mg per pellet, TestDiet) in the reaching compartment to reinforce reaching behavior. During the subsequent training period (5 days, twice per day), a single pellet was placed in the reaching compartment and the animals' performance was monitored during 15 min sessions. In this task, each mouse learned spontaneously to turn in a circle in place to elicit pellet delivery (leading to a turn-grasp-eat motif), though this was not explicitly shaped by reinforcement. Trials in which animals retrieved the food pellet with their tongue were excluded from the analysis. Experiments began once mice exceeded 40 successful trials in at least 2 consecutive sessions.

Following head bar placement, the same cohort of animals was gradually habituated to head-fixation over an 8-10 day period. First, they were allowed to move freely in and out of a 4.5 cm diameter acrylic tube, and were subsequently head-fixed with their body in the tube for 15 min. Over 7 days this was increased to 45 min until body movement was minimal. Finally, animals were habituated to head fixation while another conspecific performed the pellet reaching task in front of them. This process typically required ~10 days.

After the pellet reaching task, mice were placed in a wall-less, open, squared arena (30 x 30 cm) with a running wheel, and allowed to behave freely during 20 min sessions. The animals were pre-trained until they exhibited full coverage of the arena, and the same cohort was head-fixed in the tube and, alternately, performed or observed siblings perform the open field task.

Behavioral recording setup. The animals' behavior was recorded with 5 high-resolution, near-infrared (NIR) cameras (4MP, 100fps, 850nm; Simi Reality Motion Systems GmbH, Germany): one capturing both the performer and observer, one solely on the observer and three exclusively on the performer.

The cameras were angled to minimize redundancy of view, and infrared illumination was aided by 8-10 additional NIR LED lamps (850nm, 48 LEDs each; Banggood). All experiments were performed in dim visible light with the experimenter hidden from the view of the animal.

Pupil measurements. To control for changes in arousal state and neural responsiveness during observation sessions (Reimer et al., 2014), variations in pupil size were measured for 3 mice using close-up video from the camera positioned specifically on the observer, with additional NIR (850nm) illumination of the left eye (Fig. S6). ImageJ software (NIH, version 1.52e) was used to trace a region of interest (ROI) at the lateral edge where the pupil, which was black, met the lighter-colored sclera, which changed dynamically when the pupil dilated or contracted (as in (66)). The mean pixel intensity of the ROI was registered as a negative number that was closest to zero (i.e. largest) when the pupil was dilated maximally, and was most negative when the pupil was contracted (Fig. S6). For each mouse, a binary threshold was determined that captured periods when the pupil was contracting to the smallest size; this was used to flank epochs when the pupil was most contracted, typically when animals were quiescent and motionless.

Behavioral labeling. Videos were decompressed and downsampled by a factor of 5 (except for one animal which had a 25fps image acquisition rate) to reduce file size and match calcium imaging sampling frequency. The videos of several behavioral sessions were reviewed closely to determine which behaviors were sufficiently frequent and reliable to label manually, including task-specific (e.g. grasping a pellet) and non-specific (e.g. rearing) behaviors. The behaviors were manually labelled using a Jython-based, custom-developed graphical user interface (GUI). For each recording session, videos with different fields of view (with at least one of the performer and one of the observer) were loaded into the GUI, and two experimenters scored behaviors from the same sessions frame by frame. The behaviors used for subsequent neural analyses included nose poke, grasping, eating, grooming, turning (with clockwise and counter-clockwise turning separated) and rearing (Movie S2). In the open field we only quantified wheel-running behavior, but again discretized clockwise and counter-

clockwise directions. We also labeled epochs when observer animals moved their limbs or bodies during the observation experiments, allowing us to measure neuronal activity during observer movement.

Calcium imaging. One photon imaging of intracellular calcium activity was acquired at a rate of 20-25Hz, with LED power set to 20-30% and a gain of 1; the same image acquisition parameters were maintained for a given set of sessions (4 x 10 min) to allow for comparison of neural activity (27). Calcium imaging timestamps were synchronized with the behavioral recording system for offline behavioral analyses. Synchronization was done using the nVista DAQ box (Inscopix), which enabled triggering of external hardware (behavioral recording system; Simi) using a TTL system. GCaMP6m-expressing C57BL/6 mice were imaged while performing the pellet reaching task (2 x 10 min), and again while observing the task (2 x 10 min) while head-fixed. The following day, the same animals were imaged while freely exploring the open field with the running wheel (2 x 10 min), and again while head-fixed, observing a conspecific doing the same (2 x 10 min).

Image processing. Fluorescence movies were processed using Mosaic Software (v.1.1.2, Inscopix). Raw videos were spatially downsampled by a factor of 4 to reduce file size and processing time; temporal downsampling was not applied. Dropped frames were isolated and interpolated, and the movies were cropped to remove regions lacking cells. For pellet-reaching and open field experiments, performance and observation recordings of the same task were concatenated to generate a single 40 min recording. Motion artifacts were corrected using a single reference image (typically obtained by drawing a border around a large blood vessel or selecting bright neurons) using the Turboreg image registration algorithm within Mosaic software. The movies were further cropped to remove post-registration black borders.

Fluorescence trace extraction. Motion-corrected, cropped recordings were saved as .tiff files for subsequent signal extraction using the constrained non-negative matrix factorization algorithm for

endoscopic recordings (CNMF-E) (67). CNMF-E was designed to isolate large fluctuations in background fluorescence and facilitate the accurate extraction of cellular signals by simultaneously denoising, deconvolving and demixing one photon calcium imaging data. The CNMF-E framework can be summarized by the following steps: (1) initialize the spatial and temporal components of all neurons without explicit estimation of the background, (2) approximate the background given the activity of all neurons, (3) update spatial and temporal components by subtracting background from the raw image using alternating matrix factorization, (4) delete neurons and merge neurons with high temporal correlations, (5) repeat steps 2-4 (for quantitative detail see Zhou, et al., 2018). Similar parameters (gSig = 3, gSiz = 13, mincorr = 0.9) were used across different data sets to extract fluorescence signals. After calcium signal extraction with CNMF-E, fluorescence traces were deconvolved to approximate relative firing rates in each imaging frame using 'Online Active Set methods for Spike Inference' (OASIS) (68). For this, the fluorescence data was modelled using an autoregressive (AR(1)) process due to the fast rising time of calcium. The decay time of the calcium signal (g hyperparameter) was estimated from the autocorrelation, and the optimized g hyperparameter was set to 0. Lastly, a strict threshold of 5 standard deviations from the mean event was used for further calcium event estimation. All subsequent analyses used the inferred calcium events to minimize the effect of decay kinetics of calcium signals.

Signal-to-noise ratio. A signal-to-noise ratio (SNR) analysis was performed to estimate the quality of the deconvolved output relative to raw traces. Every raw trace value in the interval spanning one second before to seven seconds after a registered calcium event (to accommodate the sharp rise and slow decay of the calcium signal) was considered as signal, and everything outside that range was considered as noise. The SNR was defined as the ratio of the mean of the traces related to calcium events and the standard deviation of the noise. Any cell that failed to exceed or match the SNR minimum value of 3.5 for all sessions was discarded from further analyses.

Behavioral tuning and shuffling. Calcium event rates were calculated for each cell during each behavior by dividing the total number of events within a behavior by the total time spent in that behavior (in seconds). The calcium event trains were then offset by a random interval between 20 and 60 sec one thousand times, and event rates for each behavior were re-calculated for each permutation, generating a shuffled distribution. The observed firing rates were z-scored relative to the shuffled distribution, and a cell was considered significantly tuned if its z-scored rate was 2 standard deviations above its shuffled mean during a given behavior. Only cells meeting this criterion for two of the same type of session were considered stably tuned. During observation sessions, the observers' body movements were registered in addition to the behavior of the performer. Cells tuned to the observer's movement in any session were discarded from the analysis as potentially showing tuning to observed actions.

Peri-event time histograms. Calcium events were binned in 200 ms windows relative to the onset of a given behavior, converted into rates and convolved with a Gaussian kernel with a width of 1 bin. Behavioral epochs shorter than 100 ms were excluded from the analysis. For each bin, the mean and the standard error of mean were calculated over epochs. After averaging over epochs, each cell was normalized to its peak rate and cells were ordered according to the magnitude of their z-scored rate in the first performing session (P1).

False positive estimations. For either brain area, we assessed whether the number of stably tuned neurons across different conditions (performance, observation and matched) was statistically different from chance (i.e. false positive) rates. The false positive rate was estimated empirically by swapping behavioral labels between two sessions of the same kind (e.g. O1 and O2) and re-computing calcium rates for each behavior, thus determining the "false" proportion of stably tuned cells across all animals. The significance of the difference between the distributions of true and false positive proportions was determined with the Mann-Whitney U test.

Correlation matrices. To assess the predictability of representations across different session types, data from all animals within a region were pooled and significantly tuned cells for each behavior (e.g. rearing) in each session (e.g. P1) were selected. A given z-scored calcium rate series (e.g. all rearing cells in P1) was then correlated with the series of z-scored rates of all the behaviors in all the other sessions (e.g. all grooming cells in O1).

Cell registration. To identify discrete states in neuronal population activity using dimensionality reduction (Uniform Manifold Approximation and Projection, UMAP; Mclnnes et al., 2018), the stability and identity of cells across all sessions were first confirmed using methods recently published by Sheintuch et al. (69), which uses a probabilistic approach to register the spatial location of cells across sessions. After extraction of spatial components of the imaged data for each recording, spatial footprints were loaded into a graphical user interface (GUI) provided by Sheintuch et al. (2017) for further alignment and characterization of the similarity measure. For this analysis, a pixel value of 2.3μm, maximal distance of 15μm (due to sparsity) and Psame threshold of 0.95 (to be conservative) were used.

Dimensionality reduction. The fast, non-linear dimensionality reduction algorithm, UMAP, was applied to visualize the high-dimensional neural state space using a lower-dimensional manifold while preserving high-dimensional local and global structures. To do this, cells were first registered across a total of 60 minutes of combined pellet reaching and open field recordings (described in "Cell registration") to ensure similarity. The calcium event trains were then binned to the resolution of the imaging sampling rate (20Hz for PPC, 25Hz for M2) and the activities were convolved using a Gaussian kernel with a width of 2 bins. Neural data was downsampled to every 2 bins, then further downsampled by keeping only the time points when >10% of the population for performing sessions and >5% for observing sessions had non-zero convolved events. Dimensionality reduction with UMAP was performed assuming a Manhattan distance metric, and the parameters (n_neighbors=5, min_distance=0.5, spread=1.0) were kept the same for all neural data sets.

Dunn Index. The compactness of the behavioral clusters (i.e., cluster of time points corresponding to the same hand-labeled behavior) in the dimensionality-reduced representation was assessed using the Dunn Index (DI) (70). To this end, the centroids were first calculated for every behavioral cluster. Distances between each point within a behavioral cluster and the cluster's centroid (intra-cluster distances) and the distances between centroids of different clusters (inter-cluster distances) were measured. The DI was then calculated as the ratio between the minimum inter-cluster distance and the maximum intra-cluster distance (as defined above). The DI provides a measure of overall clustering quality, i.e., a high Dunn index corresponds to tight clustering in the data.

Generalized linear model. For performed behaviors, the neural calcium event data from performing sessions was fitted with generalized linear models (GLMs) to determine whether a given performed behavior explained the calcium events better than the neurons' mean calcium events rate. To do this, the events were binned to the resolution of the imaging sampling rate (20Hz). The calcium event data were then fitted with a Bernoulli GLM (35) assuming the neurons were independent. Each GLM contained a parameter corresponding to a hand-labeled behavior (nose poke, pellet grasping, eating, grooming, turning CW, turning CCW, rearing, running CW or running CCW) as well as a constant term. The likelihood of the data given each of the models was maximized across 10 folds of the data. Calcium events recorded from each neuron were also fitted with a Bernoulli GLM (which we call the null model) with only the constant term, which corresponded to the neuron's mean calcium event rate. The out-of-sample likelihood was calculated for each fitted GLM. The cross-validated negative log-likelihood ratio (cross-val nLLR) was then calculated as the difference between the out-of-sample model likelihood, which was obtained from the GLM with a parameter attached to a hand-labeled behavior, and the out-of-sample null model likelihood, which was from the GLM with only the constant term, normalized over the out-of-sample null model likelihood and averaged over 10 folds of the data.

For observed behaviors, the neural calcium event data from observing sessions were also fitted with Bernoulli GLMs to determine whether a given observed behavior could account for the calcium events

beyond what can be explained with the observer's own behavior (i.e., body movement). The cross-val nLLRs were calculated as with performed behaviors, but with the out-of-sample model likelihood obtained from the GLM with parameters attached to an observed behavior and to body movement, plus the out-of-sample null model likelihood from the GLM with a parameter attached to only the body movement.

Spatial clustering of behaviorally selective neurons. To calculate the spatial distribution of significantly tuned neurons, each neuron's centroid location was first identified using TrakEM2 software (71). To do this, neurons identified as responsive to any given behavior were stacked together in ImageJ, and image stacks for each behavior were averaged to obtain a single image with the physical locations of tuned neurons. These images were subsequently loaded into TrakEM2 and the position of each cell in each image was manually traced as a circle. The XY location of each circle was calculated to obtain the position of each cell in each animal. Next, Euclidean distances between stably tuned cells in the imaging field for each mouse were calculated. To evaluate spatial clustering of cells based on their behavioral correlates, the Dunn Index (DI; see Dimensionality reduction: Dunn index) of each animal's recorded dataset was compared against the distribution of DIs generated from shuffled data. A behavioral cluster was defined as the cluster of cells that was stably tuned to a given behavior. The shuffled distribution of DIs was obtained by randomly permuting cell IDs one thousand times and recalculating the DI for each permutation.

Anatomical verification of imaging locations. For perfusions, animals were anaesthetized deeply using isoflurane (5%) and subsequently injected with sodium pentobarbital (200 mg/kg; intraperitoneal injection) and transcardially perfused using ~25 ml saline followed by ~50 ml of 4% paraformaldehyde (PFA). Each mouse was decapitated and the brain was removed carefully from the skull. Brains were kept in 4% PFA at 4 °C overnight, then transferred to 2% dimethyl sulfoxide (DMSO: VWR, Radnor, PA) solution for cryoprotection for 1-2 days. The brains were cut in coronal sections in 3 series of 40µm on a freezing sliding microtome (HM-430 Thermo Scientific, Waltham, MA). The first

series was mounted directly onto the superfrost slides (Thermo Scientific) to perform Nissl-staining for delineation purposes. The remaining series of sections were collected in vials containing 2% DMSO and 20% glycerol in phosphate buffer (PB) and stored at -20° C until further usage.

For immunohistochemical staining, the second series of sections was used to visualize GCaMP6m viral expression. The brain sections were first rinsed 3 x 5 min in PBS on a shaker, incubated in blocking buffer (PBS plus 0.3% Triton, 2 x 10 min), followed by incubation in primary antibody solution (rabbit anti-GFP, 1:1000, ThermoFisher Scientific, A-11122, in PBS and 0.3% Triton) overnight at 4 °C. Sections were further washed in PBS containing 0.3% Triton and 3% bovine serum albumin (BSA; Sigma Aldrich) for 2 x 5 min at room temperature (RT), and subsequently incubated in secondary antibody solution (AlexaFluor 488-tagged goat anti-rabbit Ab, 1:1000, ThermoFisher Scientific, A-11008) for 1 h at RT. Sections were washed 2 x 10 min in PBS and mounted on gelatin-coated polysine microscope slides and dried in the dark overnight. Next, sections were treated with Hoechst solution (1:5000; Sigma Aldrich) for 5 min in the dark and immediately rinsed with PBS. Slides were air dried overnight in the dark at RT and cover-slipped using entellan-toluene solution (Merck Chemicals) the following day.

For anatomical delineation of recording locations, all brain sections were digitized using an automated scanner for fluorescence and brightfield images at the appropriate illumination wavelengths (Zeiss Axio Scan.Z1, Jena, Germany). Corresponding Nissl stained sections were used to delineate PPC, M2 and neighboring cortical regions in each animal in accordance with Hovde et al. (2018), the borders of which were copied onto the GFP-stained images in Adobe Illustrator CC 2017. Bregma coordinates were estimated in correspondence with Paxinos & Franklin (72).

Acknowledgements

We thank C. Keyser and E. Moser for helpful comments on the manuscript; S. Gonzalo Congo and H. Obenhaus for fruitful discussions on the analysis. H. Kleven, M. Gianatti, C. Bjørkli, and H. Waade for technical and I.T. assistance; E. Demirci for assistance with behavioral labeling; M. Witter for helpful discussions on anatomy; S. Eggen for veterinary oversight. This study was supported by the European Research Council ('RAT MIRROR CELL', Starting Grant Agreement N^{o} 335328), the Research Council of Norway (FRIPRO Young Research Talents, Grant Agreement N^{o} 239963), the Kavli Foundation, and the Center of Excellence scheme of the Research Council of Norway (Center for Neural Computation).

Author contributions: J.R.W., T.T. and B.A.D. designed the project; T.T., B.A.D., K.H. designed aspects of experiments; T.T. and K.H. contributed half the data each. B.A.D., B.M., R.J.C., Y.R. and P.M. designed the analyses, T.T., K.H., R.J.C., and B.M. performed the analyses. T.T., B.M., J.R.W. wrote the paper with assistance from R.J.C., Y.R., K.H., and B.A.D.

The authors declare no conflict of interest.

References

1. B. G. Galef, Jr.; Laland, K. N., Social Learning in Animals: Empirical Studies and Theoretical Models. *BioScience* **55**, 489-499 (2005).
2. G. di Pellegrino, L. Fadiga, L. Fogassi, V. Gallese, G. Rizzolatti, Understanding motor events: a neurophysiological study. *Experimental brain research* **91**, 176-180 (1992).
3. V. Gallese, L. Fadiga, L. Fogassi, G. Rizzolatti, Action recognition in the premotor cortex. *Brain* **119 (Pt 2)**, 593-609 (1996).
4. L. Fogassi *et al.*, Parietal lobe: from action organization to intention understanding. *Science (New York, N.Y* **308**, 662-667 (2005).
5. R. Mukamel, A. D. Ekstrom, J. Kaplan, M. Iacoboni, I. Fried, Single-neuron responses in humans during execution and observation of actions. *Curr Biol* **20**, 750-756 (2010).
6. J. F. Prather, S. Peters, S. Nowicki, R. Mooney, Precise auditory-vocal mirroring in neurons for learned vocal communication. *Nature* **451**, 305-310 (2008).
7. G. Rizzolatti, L. Craighero, The mirror-neuron system. *Annual review of neuroscience* **27**, 169-192 (2004).
8. M. Iacoboni, Imitation, empathy, and mirror neurons. *Annu Rev Psychol* **60**, 653-670 (2009).
9. J. D. Russo, Observational learning in hooded rats. *Psychonomic Science* **24**, 37-38 (1971).
10. O. Zohar, Terkel, J., Acquisition of pine cone stripping behavior in black rats (rattus rattus). *International Journal of Comparative Psychology* **5**, 1-6 (1991).
11. M. G. Leggio *et al.*, A new paradigm to analyze observational learning in rats. *Brain Res Brain Res Protoc* **12**, 83-90 (2003).
12. M. Kavaliers, E. Choleris, D. D. Colwell, Learning from others to cope with biting flies: social learning of fear-induced conditioned analgesia and active avoidance. *Behav Neurosci* **115**, 661-674 (2001).
13. P. Carlier, M. Jamon, Observational learning in C57BL/6j mice. *Behavioural brain research* **174**, 125-131 (2006).
14. M. T. Jurado-Parras, A. Gruart, J. M. Delgado-Garcia, Observational learning in mice can be prevented by medial prefrontal cortex stimulation and enhanced by nucleus accumbens stimulation. *Learn Mem* **19**, 99-106 (2012).
15. D. J. Langford *et al.*, Social modulation of pain as evidence for empathy in mice. *Science* **312**, 1967-1970 (2006).

16. T. Sakaguchi, S. Iwasaki, M. Okada, K. Okamoto, Y. Ikegaya, Ethanol facilitates socially evoked memory recall in mice by recruiting pain-sensitive anterior cingulate cortical neurons. *Nat Commun* **9**, 3526 (2018).
17. D. Jeon *et al.*, Observational fear learning involves affective pain system and Cav1.2 Ca2+ channels in ACC. *Nature neuroscience* **13**, 482-488 (2010).
18. S. A. Allsop *et al.*, Corticoamygdala Transfer of Socially Derived Information Gates Observational Learning. *Cell* **173**, 1329-1342 e1318 (2018).
19. M. Carrillo *et al.*, Emotional Mirror Neurons in the Rat's Anterior Cingulate Cortex. *Curr Biol* **29**, 1301-1312 e1306 (2019).
20. T. D. Hanks *et al.*, Distinct relationships of parietal and prefrontal cortices to evidence accumulation. *Nature* **520**, 220-223 (2015).
21. A. M. Licata *et al.*, Posterior Parietal Cortex Guides Visual Decisions in Rats. *J Neurosci* **37**, 4954-4966 (2017).
22. H. Mohan, R. de Haan, H. D. Mansvelder, C. P. J. de Kock, The posterior parietal cortex as integrative hub for whisker sensorimotor information. *Neuroscience* **368**, 240-245 (2018).
23. F. Barthas, A. C. Kwan, Secondary Motor Cortex: Where 'Sensory' Meets 'Motor' in the Rodent Frontal Cortex. *Trends Neurosci* **40**, 181-193 (2017).
24. J. C. Erlich, M. Bialek, C. D. Brody, A cortical substrate for memory-guided orienting in the rat. *Neuron* **72**, 330-343 (2011).
25. J. R. Whitlock, G. Pfuhl, N. Dagslott, M. B. Moser, E. I. Moser, Functional split between parietal and entorhinal cortices in the rat. *Neuron* **73**, 789-802 (2012).
26. A. Rubin, Sheintuch, L., Brande-Eilat, N., Pinchasof, O., Rechavi, Y., Geva, N., Ziv, Y., Revealing neural correlates of behavior without behavioral measurements. *biorXiv* https://doi.org/10.1101/540195 (2019).
27. K. K. Ghosh *et al.*, Miniaturized integration of a fluorescence microscope. *Nat Methods* **8**, 871-878 (2011).
28. L. McInnes, Healy, J., Melville, J., UMAP: Uniform Manifold Approximation and Projection for Dimension Reduction. *arXiv* (version 2 of preprint), arXiv:1802.03426 (2018).
29. T. Xu *et al.*, Rapid formation and selective stabilization of synapses for enduring motor memories. *Nature* **462**, 915-919 (2009).
30. R. D. Hall, Lindholm, E.P., Organization of motor and somatosensory neocortex in albino rat. *Brain research* **66**, 23-38 (1974).

31. D. F. Cooke, C. S. Taylor, T. Moore, M. S. Graziano, Complex movements evoked by microstimulation of the ventral intraparietal area. *Proc Natl Acad Sci U S A* **100**, 6163-6168 (2003).
32. D. A. Dombeck, M. S. Graziano, D. W. Tank, Functional clustering of neurons in motor cortex determined by cellular resolution imaging in awake behaving mice. *J Neurosci* **29**, 13751-13760 (2009).
33. B. Hoeks, Levelt, W.J.M., Pupillary dilation as a measure of attention: A quantitative system analysis. *Behavior Research Methods, Instruments, & Computers* **25**, 16-26 (1993).
34. J. Reimer *et al.*, Pupil fluctuations track fast switching of cortical states during quiet wakefulness. *Neuron* **84**, 355-362 (2014).
35. J. A. Nelder, Wedderburn, W.M., Generalized Linear Models. *Journal of the Royal Statistical Society. Series A* **135**, 370-384 (1972).
36. C. Stringer *et al.*, Spontaneous behaviors drive multidimensional, brainwide activity. *Science* **364**, 255 (2019).
37. S. K. Musall, M. T., Gluf, S., Churchland, A. K., Single-trial neural dynamics are dominated by richly varied movements. *biorXiv,* https://doi.org/10.1101/308288 (2019).
38. B. Mimica, B. A. Dunn, T. Tombaz, V. Bojja, J. R. Whitlock, Efficient cortical coding of 3D posture in freely behaving rats. *Science* **362**, 584-589 (2018).
39. S. Rozzi, P. F. Ferrari, L. Bonini, G. Rizzolatti, L. Fogassi, Functional organization of inferior parietal lobule convexity in the macaque monkey: electrophysiological characterization of motor, sensory and mirror responses and their correlation with cytoarchitectonic areas. *The European journal of neuroscience* **28**, 1569-1588 (2008).
40. B. A. Olshausen, D. J. Field, Sparse coding of sensory inputs. *Curr Opin Neurobiol* **14**, 481-487 (2004).
41. M. T. Lippert, K. Takagaki, C. Kayser, F. W. Ohl, Asymmetric multisensory interactions of visual and somatosensory responses in a region of the rat parietal cortex. *PLoS One* **8**, e63631 (2013).
42. D. Raposo, M. T. Kaufman, A. K. Churchland, A category-free neural population supports evolving demands during decision-making. *Nature neuroscience* **17**, 1784-1792 (2014).
43. K. Ohki, S. Chung, Y. H. Ch'ng, P. Kara, R. C. Reid, Functional imaging with cellular resolution reveals precise micro-architecture in visual cortex. *Nature* **433**, 597-603 (2005).
44. D. D. Stettler, R. Axel, Representations of odor in the piriform cortex. *Neuron* **63**, 854-864 (2009).
45. E. E. Hecht *et al.*, Differences in neural activation for object-directed grasping in chimpanzees and humans. *J Neurosci* **33**, 14117-14134 (2013).

46. W. Suzuki *et al.*, Mirror Neurons in a New World Monkey, Common Marmoset. *Front Neurosci* **9**, 459 (2015).
47. J. I. Gold, M. N. Shadlen, The neural basis of decision making. *Annual review of neuroscience* **30**, 535-574 (2007).
48. R. A. Andersen, H. Cui, Intention, action planning, and decision making in parietal-frontal circuits. *Neuron* **63**, 568-583 (2009).
49. C. D. Harvey, P. Coen, D. W. Tank, Choice-specific sequences in parietal cortex during a virtual-navigation decision task. *Nature* **484**, 62-68 (2012).
50. B. W. Brunton, M. M. Botvinick, C. D. Brody, Rats and humans can optimally accumulate evidence for decision-making. *Science* **340**, 95-98 (2013).
51. A. S. Morcos, C. D. Harvey, History-dependent variability in population dynamics during evidence accumulation in cortex. *Nature neuroscience* **19**, 1672-1681 (2016).
52. E. J. Hwang, J. E. Dahlen, M. Mukundan, T. Komiyama, History-based action selection bias in posterior parietal cortex. *Nat Commun* **8**, 1242 (2017).
53. A. Akrami, C. D. Kopec, M. E. Diamond, C. D. Brody, Posterior parietal cortex represents sensory history and mediates its effects on behaviour. *Nature* **554**, 368-372 (2018).
54. Q. Wang, O. Sporns, A. Burkhalter, Network analysis of corticocortical connections reveals ventral and dorsal processing streams in mouse visual cortex. *J Neurosci* **32**, 4386-4399 (2012).
55. K. Hovde, M. Gianatti, M. P. Witter, J. R. Whitlock, Architecture and organization of mouse posterior parietal cortex relative to extrastriate areas. *The European journal of neuroscience* 10.1111/ejn.14280 (2018).
56. R. L. Reep, G. S. Goodwin, J. V. Corwin, Topographic organization in the corticocortical connections of medial agranular cortex in rats. *The Journal of comparative neurology* **294**, 262-280 (1990).
57. R. L. Reep, H. C. Chandler, V. King, J. V. Corwin, Rat posterior parietal cortex: topography of corticocortical and thalamic connections. *Experimental brain research* **100**, 67-84 (1994).
58. S. P. Wise, D. Boussaoud, P. B. Johnson, R. Caminiti, Premotor and parietal cortex: corticocortical connectivity and combinatorial computations. *Annual review of neuroscience* **20**, 25-42 (1997).
59. G. Rizzolatti, L. Fogassi, V. Gallese, Parietal cortex: from sight to action. *Curr Opin Neurobiol* **7**, 562-567 (1997).
60. L. Bonini, P. F. Ferrari, Evolution of mirror systems: a simple mechanism for complex cognitive functions. *Ann N Y Acad Sci* **1225**, 166-175 (2011).

61. L. Fadiga, L. Fogassi, G. Pavesi, G. Rizzolatti, Motor facilitation during action observation: a magnetic stimulation study. *J Neurophysiol* **73**, 2608-2611 (1995).

62. T. F. Roberts, S. M. Gobes, M. Murugan, B. P. Olveczky, R. Mooney, Motor circuits are required to encode a sensory model for imitative learning. *Nature neuroscience* **15**, 1454-1459 (2012).

63. S. M. Wilson, A. P. Saygin, M. I. Sereno, M. Iacoboni, Listening to speech activates motor areas involved in speech production. *Nature neuroscience* **7**, 701-702 (2004).

64. B. Wicker *et al.*, Both of us disgusted in My insula: the common neural basis of seeing and feeling disgust. *Neuron* **40**, 655-664 (2003).

65. T. Singer *et al.*, Empathy for pain involves the affective but not sensory components of pain. *Science* **303**, 1157-1162 (2004).

66. C. Bennett *et al.*, Higher-Order Thalamic Circuits Channel Parallel Streams of Visual Information in Mice. *Neuron* **102**, 477-492 e475 (2019).

67. P. Zhou *et al.*, Efficient and accurate extraction of in vivo calcium signals from microendoscopic video data. *Elife* **7** (2018).

68. J. Friedrich, P. Zhou, L. Paninski, Fast online deconvolution of calcium imaging data. *PLoS Comput Biol* **13**, e1005423 (2017).

69. L. Sheintuch *et al.*, Tracking the Same Neurons across Multiple Days in Ca(2+) Imaging Data. *Cell Rep* **21**, 1102-1115 (2017).

70. J. C. Dunn, Well-Separated Clusters and Optimal Fuzzy Partitions. *Journal of Cybernetics* **4**, 95-104 (1974).

71. A. Cardona *et al.*, TrakEM2 software for neural circuit reconstruction. *PLoS One* **7**, e38011 (2012).

72. G. Paxinos, Franklin K. (2012) Paxino's and Franklin's the Mouse Brain in Stereotaxic Coordinates. (Academic Press).

Figure legends

Fig. 1. Experimental paradigm for imaging neural populations in PPC and M2 in freely behaving mice. (*A*) PPC and M2 were transfected virally to express GCaMP6m (*Left*), and miniature prism probes were implanted to image tangentially across cortical layers (*Right*) during different behavioral tasks. (*B*) In the experiments, mice alternated between performing and observing a conspecific in a pellet-reaching task (*Top*) and wheel-running task in an open arena (*Below*). Dynamic calcium fluctuations were monitored in each mouse during four 10-min recording sessions, two of which were during performance and two during observation of each task. (*C*) (*Left*) Average of 500 images of the entire FOV after image pre-processing. Scale bar, 100μm. Shaded arrows indicate 6 cells whose calcium traces are shown (*Middle*) during performance and (*Right*) observation of the pellet-reaching task.

Fig. 2. UMAP projections of population activity in both PPC and M2 reveal structural segregation for performed but not observed behaviors. (*A*) PPC ensemble activity separated in the reduced dimensional space during specific performed behaviors, including wheel-running (beige dots), counter-clockwise turning (light green) and rearing (blue). By contrast, the distribution of points during observed behaviors (*Right*) was spread homogenously in UMAP space. Each dot corresponds to the activity state of the entire population of recorded neurons at a given time point; color-coding for each behavior is shown at bottom. (*B*) Recordings from M2 were similar to *A*, showing a stronger tendency to cluster during performed than observed behaviors.

Fig. 3. Cell populations in PPC and M2 robustly encode actions performed in the pellet-reaching task. (*A*) Representative neural map (*Left*) and Ca^{2+} transients of 7 PPC neurons (*Right*) tuned to each of the behaviors in the pellet reaching task; color coding for each behavior is shown above. (*B*) (*Top*) Temporal profiles of behaviorally evoked responses of single cells for each behavior are shown as heat maps; immediately beneath are behaviorally aligned average activity rates for each cell over the entire session. (*Bottom*) Normalized responses for all behaviorally tuned PPC neurons from all animals aligned to behavior onset; population means are shown in the row underneath. Color bars indicate

max event/s; blue shaded regions around averaged rates denote ± SEM. (*C*) Same as *B*, for single cells (*Top row*) and cell populations (*Bottom row*) imaged in M2. (*D*) Color coded pie charts indicating the proportion of stably tuned neurons for each behavior; a total of 1674 cells were imaged in 4 mice in PPC; 1082 cells were imaged in 4 mice in M2.

Fig. 4. Neural ensembles in PPC and M2 stably represent performed, but not observed actions. (*A*) (*Above*) Session-averaged Ca^{2+} responses of individual cells aligned to the onset of specific actions in the pellet- reaching task, and ranked by z-scored firing rate during the first performance session (P1). (*Below*) Population average (± SEM) of responses of all cells for each behavior. Virtually none of the cells with stable correlates across the two performance sessions responded when the same actions were observed (Observation sessions 1 and 2), yielding a flat activity rate in the ensemble average. (*B*) Same as *A*, but for cells recorded in M2. (*C*) Correlation matrices, with each square corresponding to a particular behavior, show the sustained specificity of behavioral tuning in PPC across performance sessions (P1 and P2). The conserved correlation structure is reflected by the red diagonal in P1 vs. P2, which is notably absent across performance and observation conditions. (*D*) Same as *C*, for recordings in M2.

Fig 5. Bar plots show the cross-validated negative log-likelihood ratios for single behavior Bernoulli generalized linear model of calcium events from neural populations in the PPC (*Top panels*) and M2 (*Bottom panels*) of mice during pellet-reaching task (*Left panels*) and wheel running task (*Right panels*). Hand-labeled behaviors from performance sessions are shown as empty boxes while behaviors from observation sessions as hatched boxes. Bars represent the mean ± SEM over animal subjects (pellet-reaching task: 4 mice for PPC and 4 animals for M2; wheel-running task: 3 mice for PPC and 1 mouse for M2).

Supplementary figure legends

Fig. S1. (*A*) (*Left*) Histological sections (40µm) showing GCaMP6m expression in M2, with prism probe locations depicted by the white dashed line. (*Right*) Same, for animals in PPC. In both areas, schematics of the tissue were drawn to show the extent of GCaMP6 expression in green. Anatomical boundaries for PPC, M2 and surrounding regions were established using lamination and cytoarchitectural profiles in adjacent, Nissl-stained sections. Scale bar denotes 200 µm. (*B*) Dorsal view of estimated recording planes in M2 (red rectangles) and PPC (blue) in all 8 animals. Bregma (”B”) is indicated on the midline, and black dots indicate 1 mm.

Fig. S2. Subsets of cells in PPC and M2 were stably tuned to multiple behaviors. (*A*) Color-coded pie charts show the proportion of PPC neurons significantly tuned to each behavior in the pellet reaching task, with the number of cells in each category written around the ring periphery, and the total time in each behavior (summed across both performance sessions) shown in the center. To display the relative proportions graphically, cells tuned to multiple behaviors (e.g. “Nose poke” and “Grasping”) appear in more than one pie chart. Cells stably tuned to three or more behaviors are denoted by dark blue, while cells not tuned to the behavior of interest are shaded in grey. (*B*) Same as in *A*, but for M2.

Fig. S3. Behaviorally tuned neurons in PPC did not cluster anatomically. (*A*) Cell maps for each animal, color-coded by their behavioral correlates (legend at bottom). Scale bars = 100µm. (*B*) Matrices showing pairwise Euclidean distances between neurons grouped by their tuning preferences (colored boxes); shortest distances are shown in white and longer distances are darker. Functional-anatomical clustering would produce lighter shading within-behavior and darker colors outside. (*C*) The quality of clustering by behavior was quantified using the Dunn index (Methods), which assessed Euclidean distances between cells with similar vs. different behavioral classifications. The distribution of actual intra- vs. inter-cluster distances was compared against a shuffled distribution in which cell identities were permuted, which indicated below-chance levels of clustering in each animal. Dashed lines indicate the 99th percentile of the shuffled distribution; black circles denote the Dunn index value.

Fig. S4. Behaviorally tuned neurons in M2 were not clustered anatomically. (*A*) Cell maps for each animal, color-coded by their behavioral correlates (legend at bottom). Scale bars = 100µm. (*B*) Same matrices as for PPC cells in Figure S3, showing pairwise Euclidean distances between neurons grouped by tuning preferences. (*C*) The quality of clustering by behavior was quantified using the Dunn index (Methods), as with PPC neurons in the previous Supplementary figure; none of the animals showed neural clustering exceeding the 99th percentile of the shuffled distribution (dashed lines); black circles denote the observed Dunn index value.

Fig. S5. Additional behavioral conditions in relation to Figure 4 comparing PPC and M2 ensemble activation during performance and observation sessions. (*A*) As with Figure 4, PPC cells responded during performed, but not observed actions. (*B*) Same as *A*, but for cells recorded in M2; insufficient data were collected to test for stable tuning for Running CW for recordings in M2, so that condition was omitted. Note that the behaviors here are included in the cross-correlation matrices for performance and observation sessions in Figure 4 *C* and *D*.

Fig. S6. Arousal state did not influence neural responses to observed actions. (*A*) Pupil size was measured as a proxy for arousal state during observation of the pellet-reaching task in three mice with prisms in M2. (*Left*) A region of interest (ROI) was drawn over a close-up video of the eye using ImageJ software, and pupil size (red circle) was reported via pixel intensity inside the ROI (*Right*). For each mouse, a threshold was determined to capture epochs when the pupil was constricting to its smallest size (red line in graph), typically when animals were quiescent and motionless. (*B*) The number of cells with stable correlates for observed behavior was below the false positive rate regardless of whether epochs with small pupil diameter were included in the analysis.

Supplementary movies

Movie S1. (left panel) The momentary state of neural population activity is indicated by the blue cursor, while the dimensionally-reduced manifold of population activity for the entire session is shown as grey dots. Darker areas correspond to denser regions in the reduced space. Note that the cursor (i.e. the state of population activity) occupies a stable location when the animal performs clockwise and counter-clockwise running, but that it moves unpredictably over the manifold when the same animal observes a cohort running on the wheel. (right panel) Corresponding in-session videos of wheel-running epochs from performance and observation sessions. For display purposes, calcium events were convolved with a Gaussian kernel with width of 5 bins before down sampling and manifold learning using UMAP (Methods).

Movie S2. Video showing a side-view of a mouse performing the pellet reaching task. Each behavior included in the neural data analyses is demonstrated in the video.

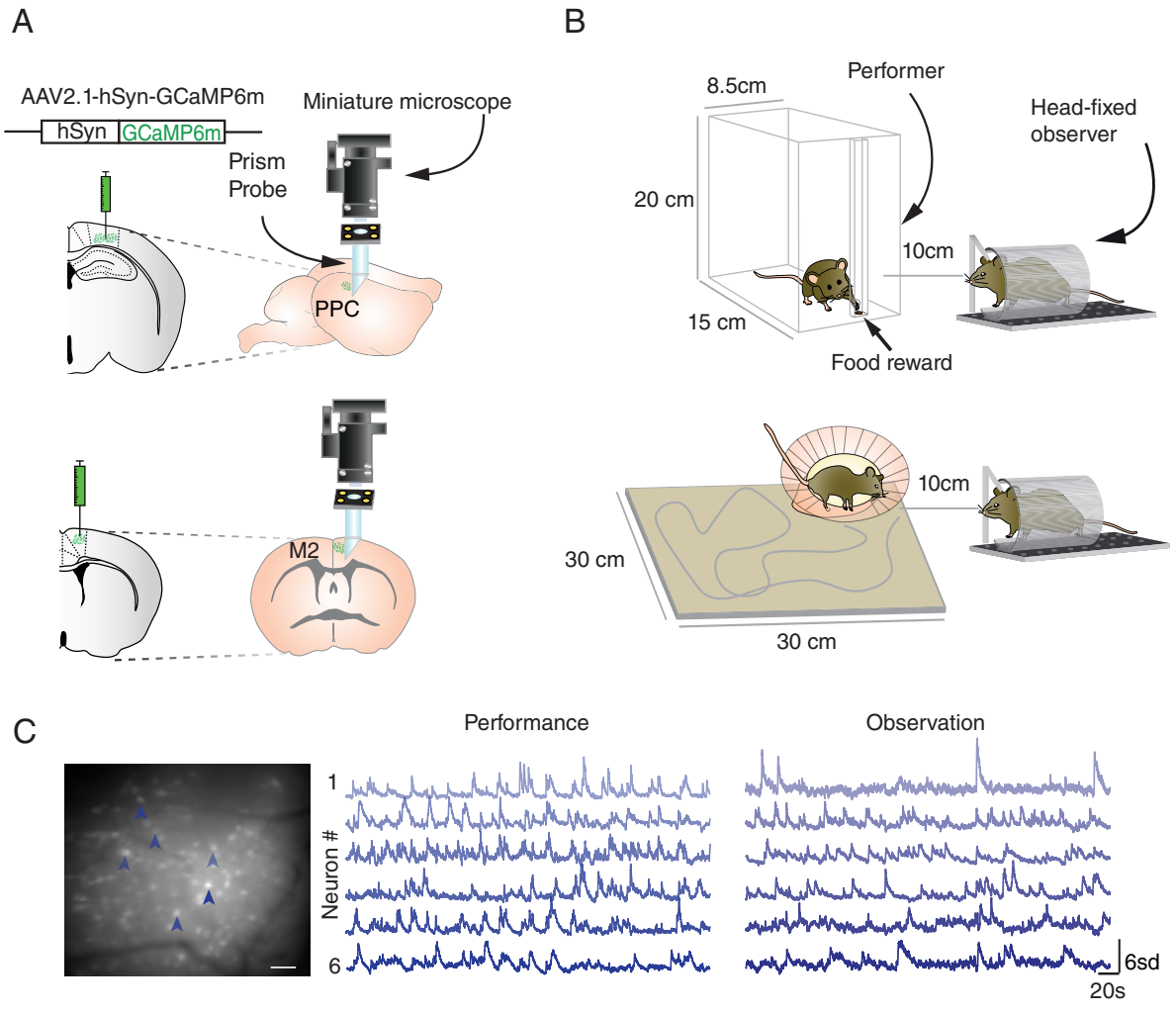
A
AAV2.1-hSyn-GCaMP6m
hSyn
GCaMP6m
Miniature microscope
Prism
Probe
PPC
M2
B
8.5cm
Performer
Head-fixed
observer
20 cm
10cm
15 cm
Food reward
10cm
30 cm
30 cm
C
Performance
Observation
Neuron #
1
6
6sd
20s

Figure 1

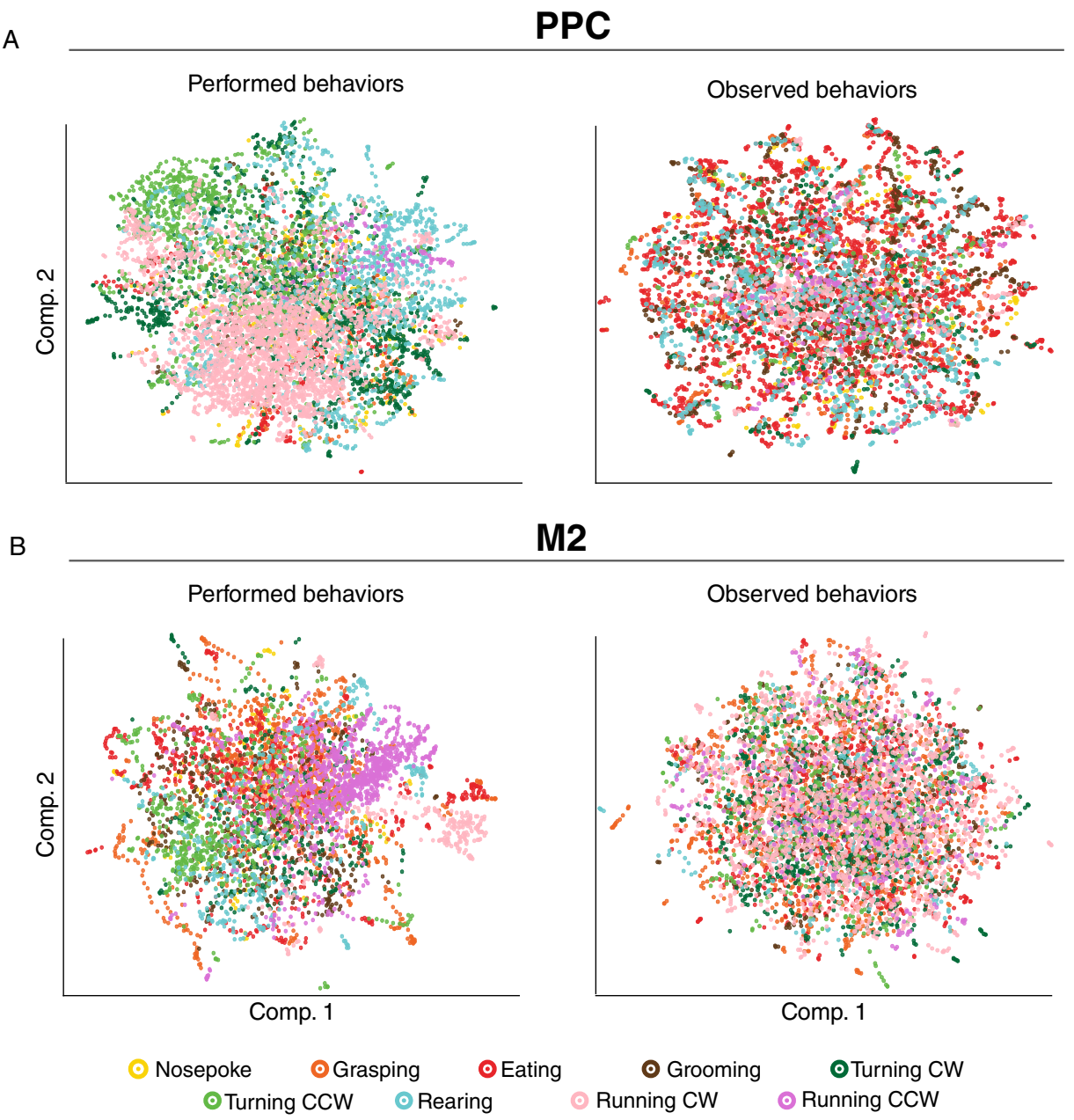
A
PPC
Performed behaviors
Observed behaviors
Comp. 2
B
M2
Performed behaviors
Observed behaviors
Comp. 2
Comp. 1
Comp. 1
Nosepoke
Grasping
Eating
Grooming
Turning CW
Turning CCW
Rearing
Running CW
Running CCW

Figure 2

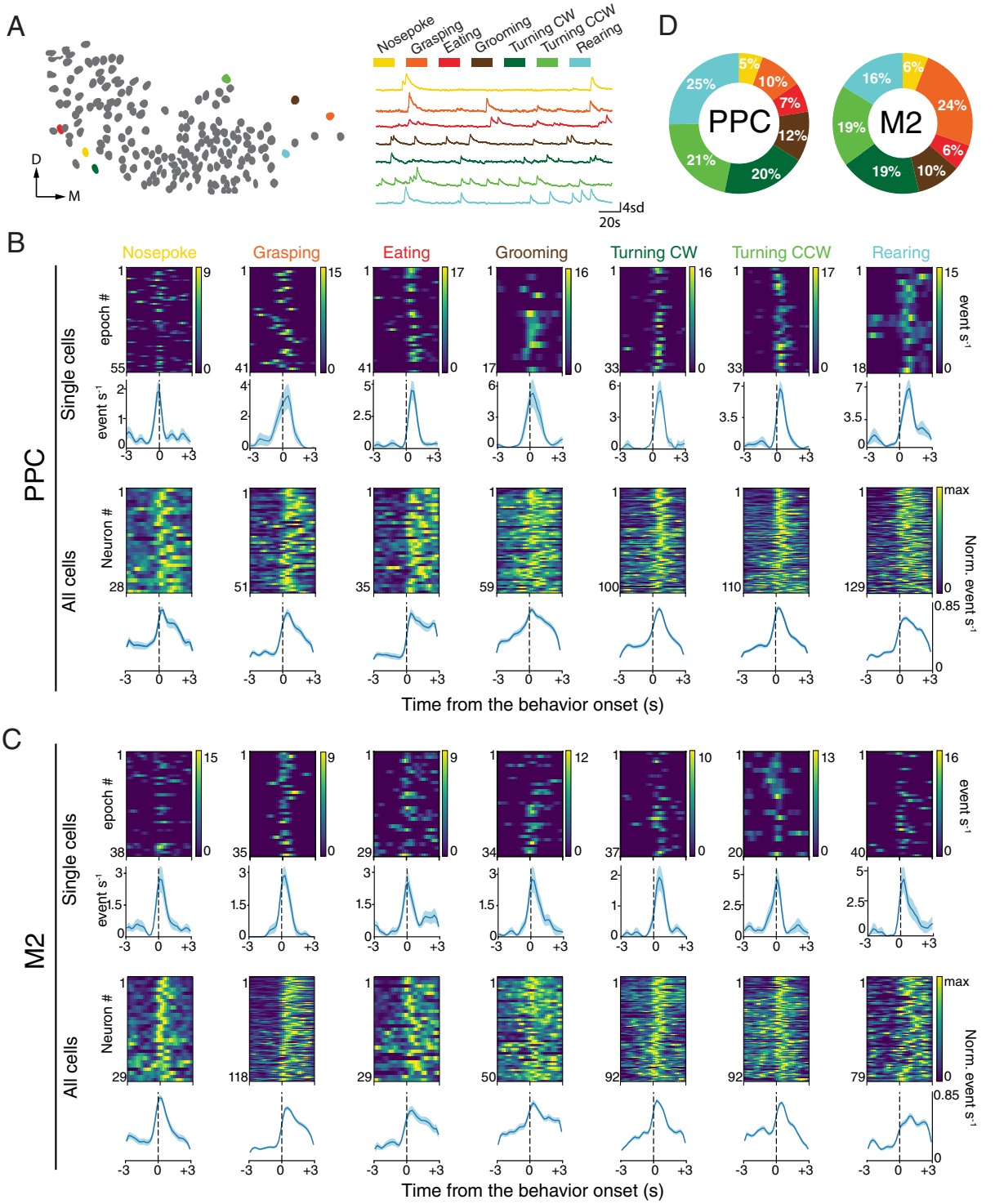
A
D
M
Nosepoke
Grasping
Eating
Grooming
Turning CW
Turning CCW
Rearing
4sd
20s
D
PPC
5%
10%
7%
12%
20%
21%
25%
M2
6%
24%
6%
10%
19%
19%
16%
B
PPC
Single cells
All cells
epoch #
Neuron #
event s-1
Norm. event s-1
max
Time from the behavior onset (s)
C
M2
Single cells
All cells
epoch #
Neuron #
event s-1
Norm. event s-1
max
Time from the behavior onset (s)

Figure 3

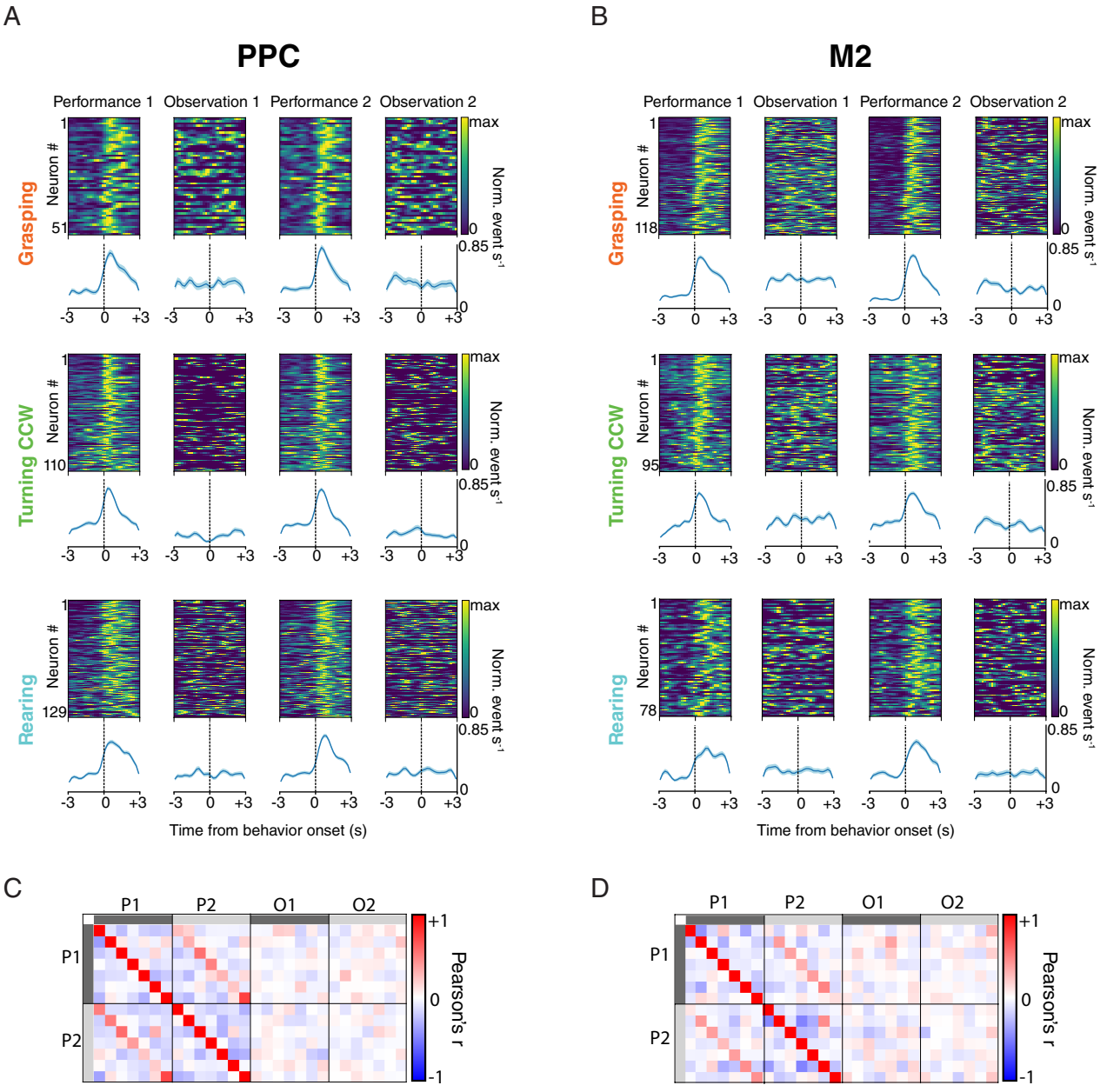
A
PPC
B
M2
Performance 1
Observation 1
Performance 2
Observation 2
Grasping
Turning CCW
Rearing
Neuron #
max
Norm. event s-1
0.85
Time from behavior onset (s)
C
D
P1
P2
O1
O2
Pearson's r
+1
0
-1

Figure 4

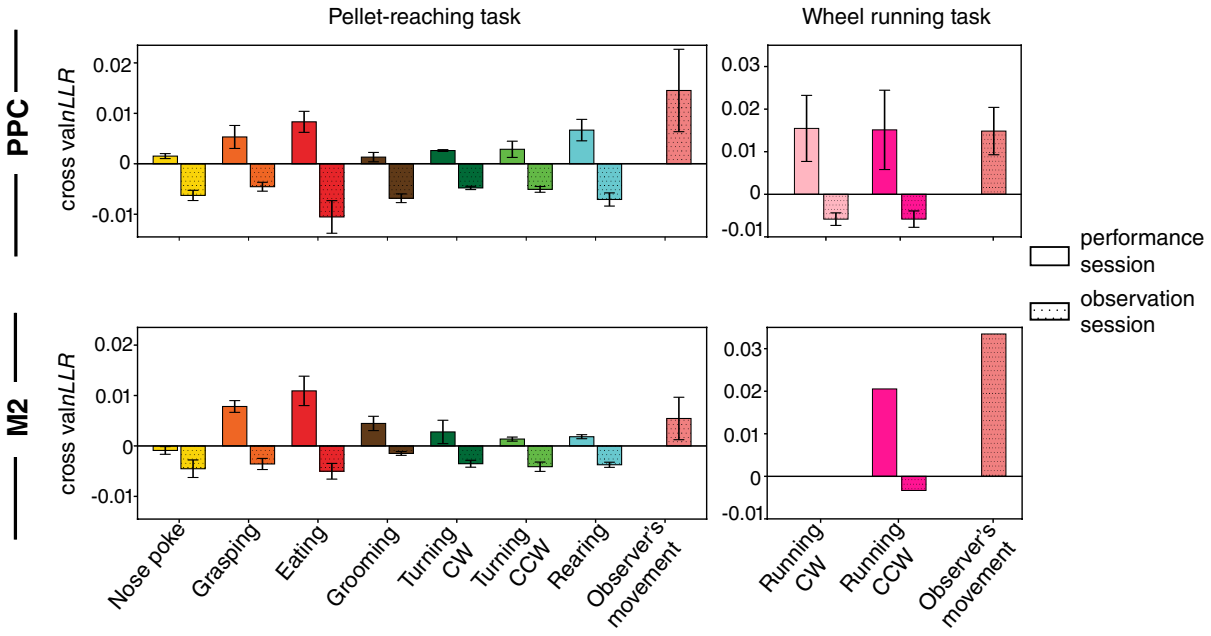
Pellet-reaching task
Wheel running task
PPC
M2
cross valnLLR
0.02
0.01
0
-0.01
0.03
performance session
observation session
Nose poke
Grasping
Eating
Grooming
Turning CW
Turning CCW
Rearing
Observer's movement
Running CW
Running CCW

Figure 5

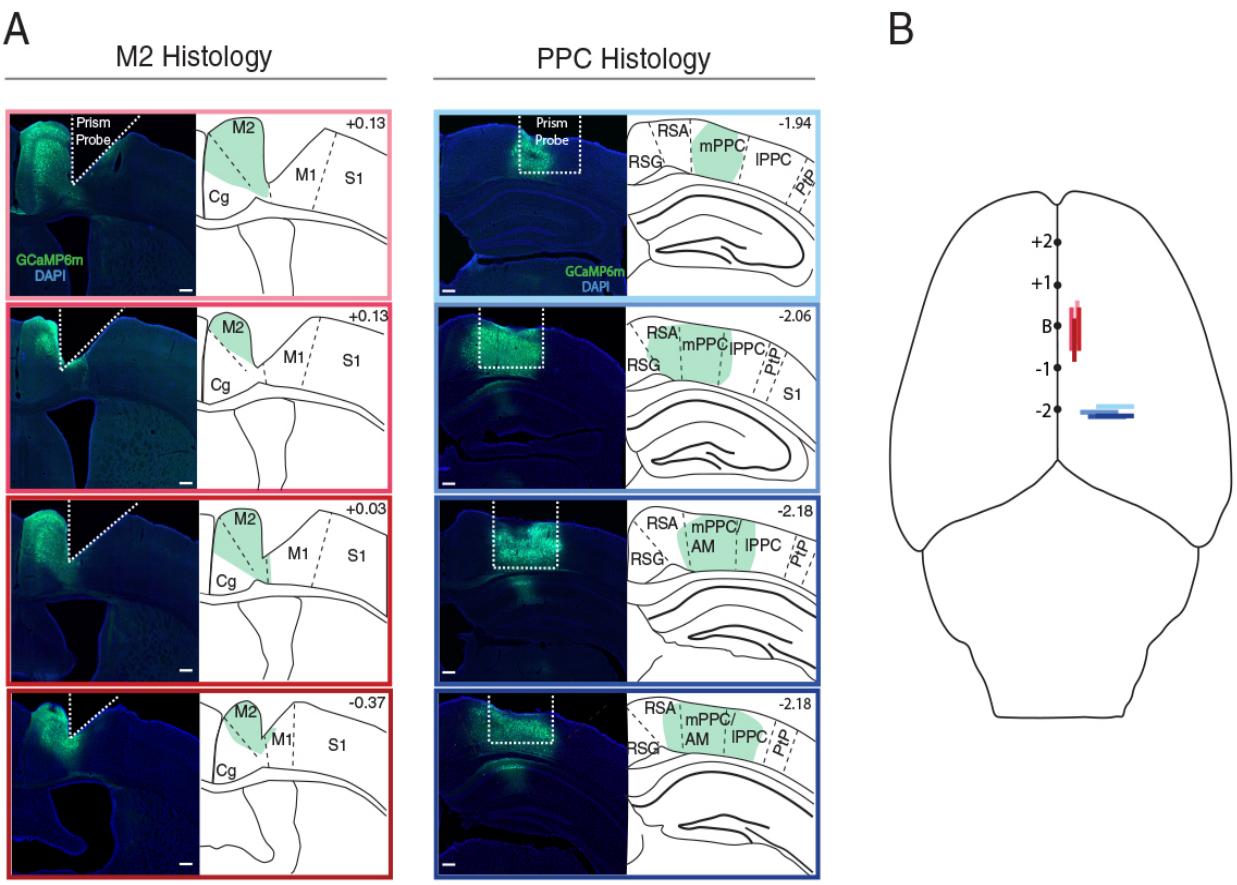
A
M2 Histology
PPC Histology
B
Prism
Probe
GCaMP6m
DAPI
M2
M1
S1
Cg
+0.13
+0.13
+0.03
-0.37
RSA
RSG
mPPC
lPPC
PtP
-1.94
-2.06
mPPC/
AM
-2.18
-2.18
+2
+1
B
-1
-2

Figure S1

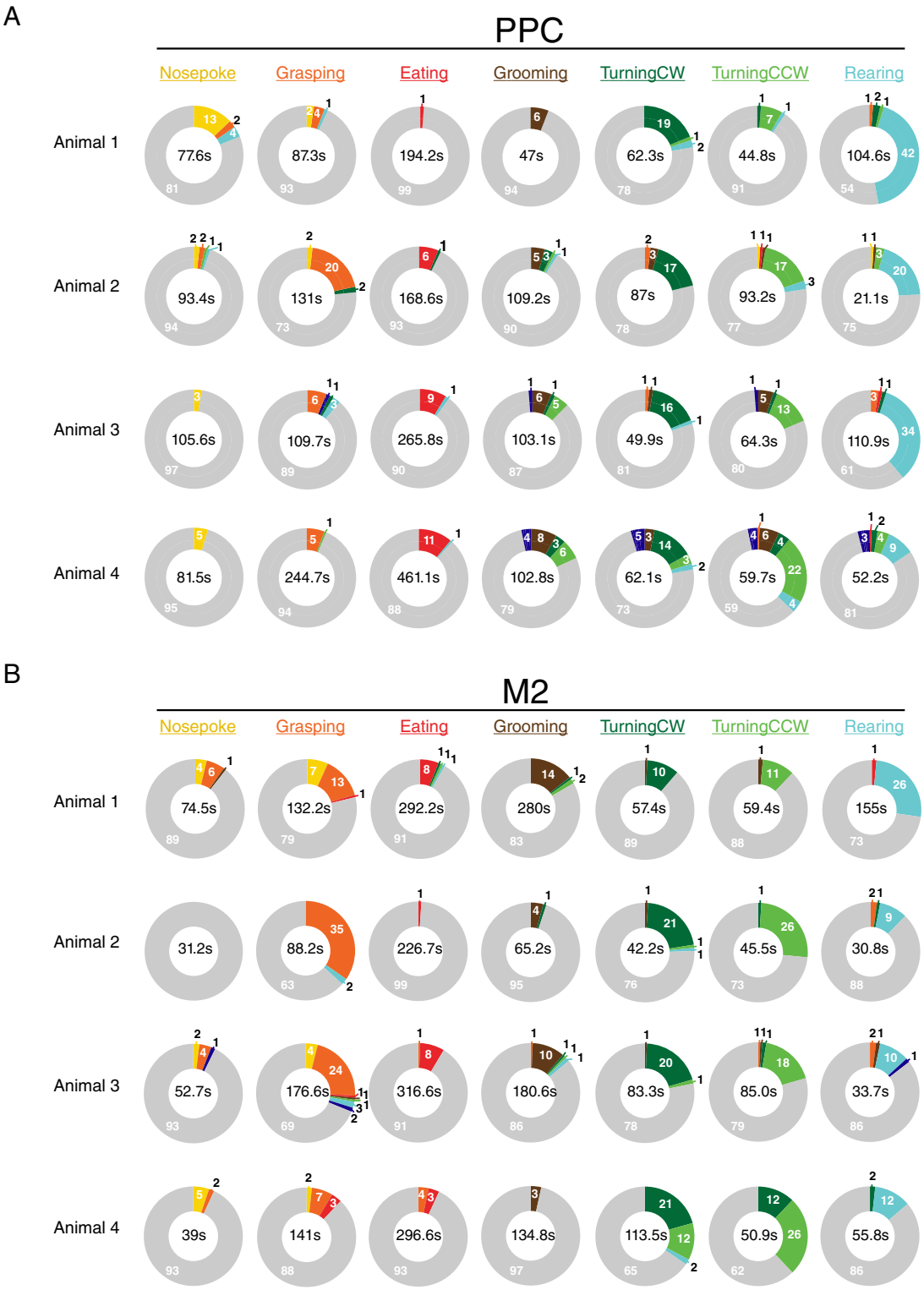
A
PPC
Nosepoke
Grasping
Eating
Grooming
TurningCW
TurningCCW
Rearing
Animal 1
77.6s
87.3s
194.2s
47s
62.3s
44.8s
104.6s
Animal 2
93.4s
131s
168.6s
109.2s
87s
93.2s
21.1s
Animal 3
105.6s
109.7s
265.8s
103.1s
49.9s
64.3s
110.9s
Animal 4
81.5s
244.7s
461.1s
102.8s
62.1s
59.7s
52.2s
B
M2
Nosepoke
Grasping
Eating
Grooming
TurningCW
TurningCCW
Rearing
Animal 1
74.5s
132.2s
292.2s
280s
57.4s
59.4s
155s
Animal 2
31.2s
88.2s
226.7s
65.2s
42.2s
45.5s
30.8s
Animal 3
52.7s
176.6s
316.6s
180.6s
83.3s
85.0s
33.7s
Animal 4
39s
141s
296.6s
134.8s
113.5s
50.9s
55.8s

Figure S2

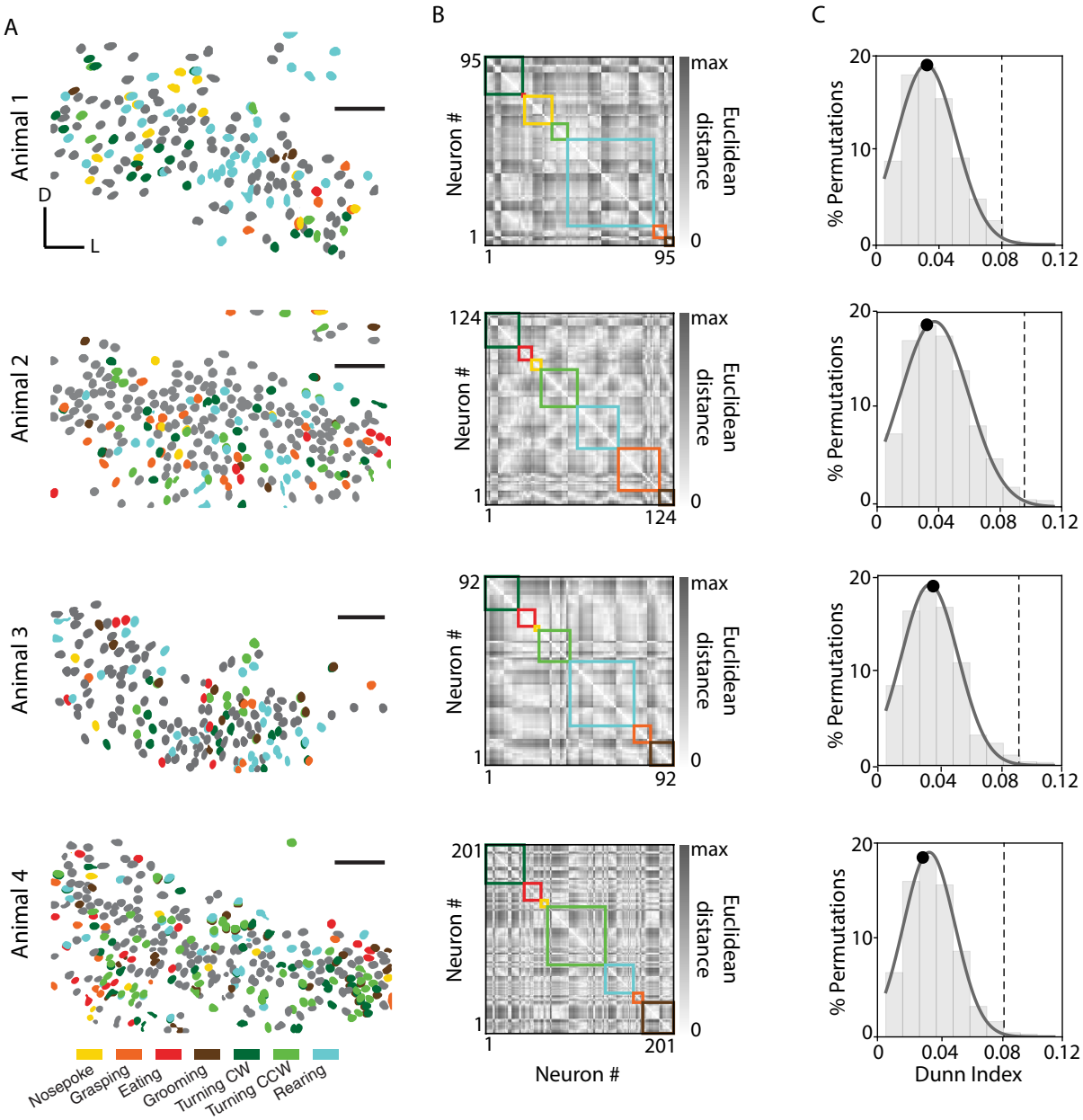
A
B
C
Animal 1
Animal 2
Animal 3
Animal 4
D
L
Neuron #
Euclidean distance
max
0
95
124
92
201
% Permutations
0.04
0.08
0.12
20
10
Dunn Index
Nosepoke
Grasping
Eating
Grooming
Turning CW
Turning CCW
Rearing

Figure S3

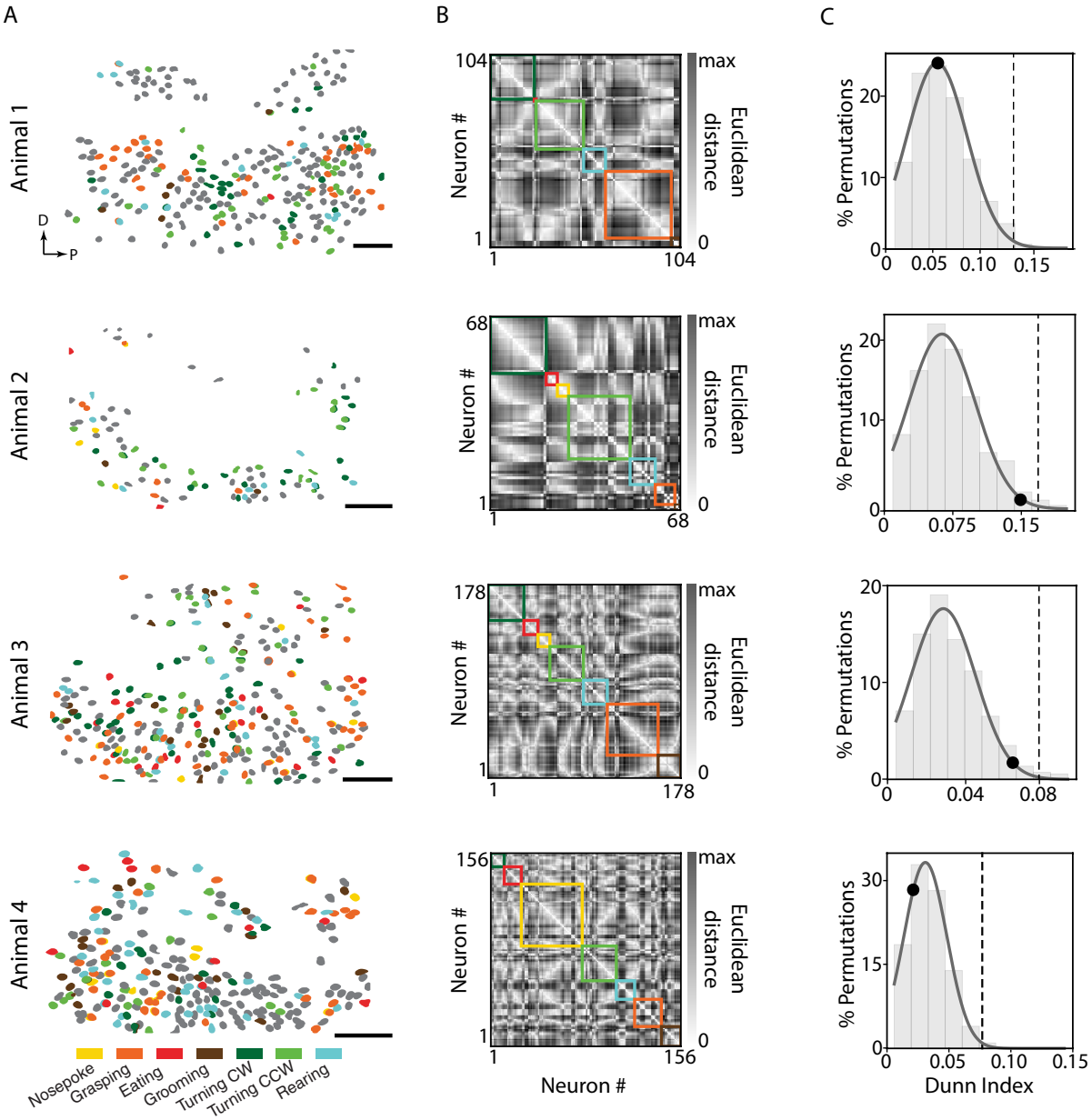
A
B
C
Animal 1
Animal 2
Animal 3
Animal 4
D
P
Neuron #
Euclidean distance
max
0
104
68
178
156
1
% Permutations
Dunn Index
0.05
0.10
0.15
0.075
0.04
0.08
20
10
30
15
Nosepoke
Grasping
Eating
Grooming
Turning CW
Turning CCW
Rearing

Figure S4

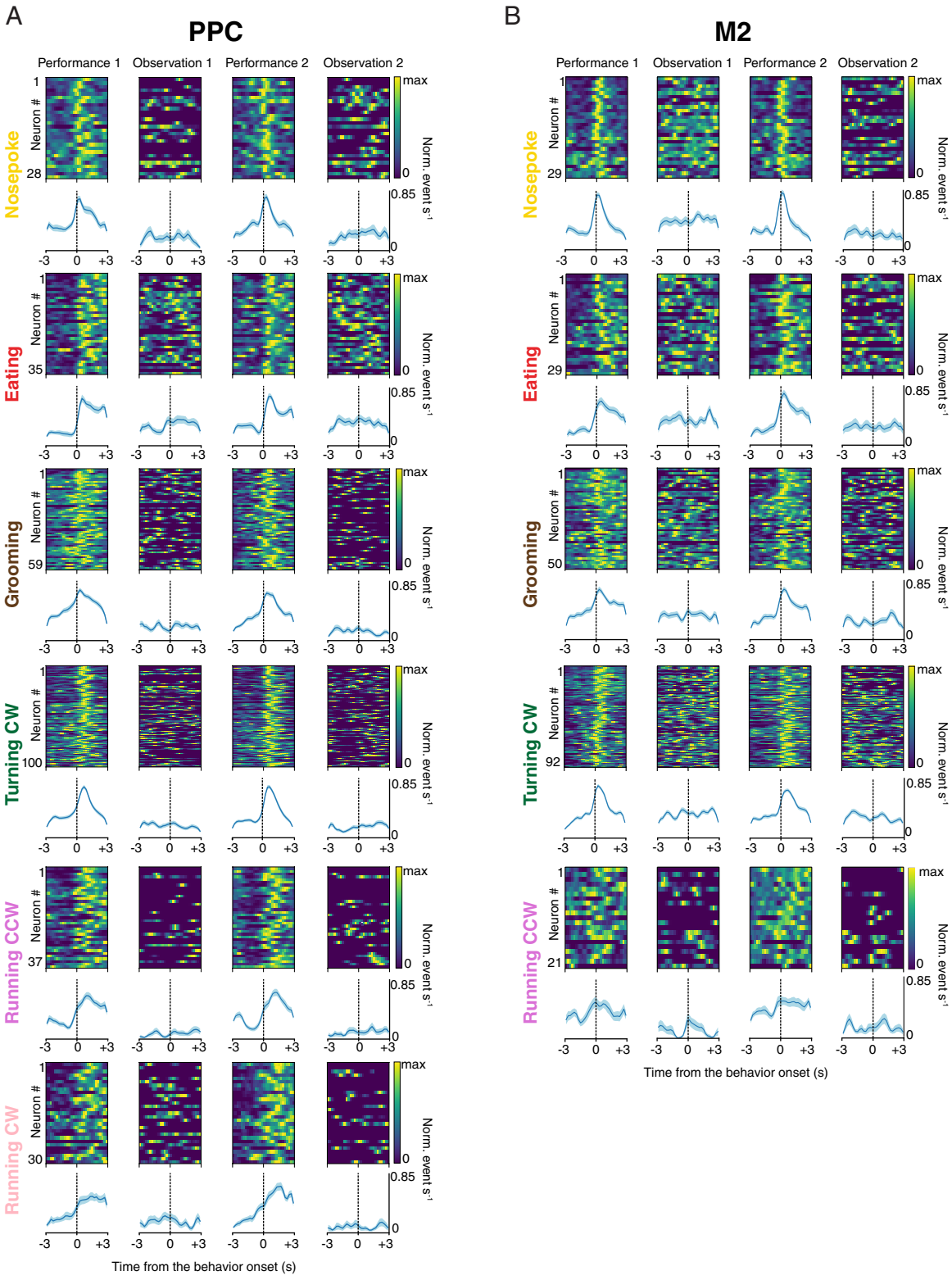
A
PPC
B
M2
Performance 1
Observation 1
Performance 2
Observation 2
Nosepoke
Eating
Grooming
Turning CW
Running CCW
Running CW
Neuron #
max
Norm. event s-1
0.85
-3
0
+3
Time from the behavior onset (s)

Figure S5

A

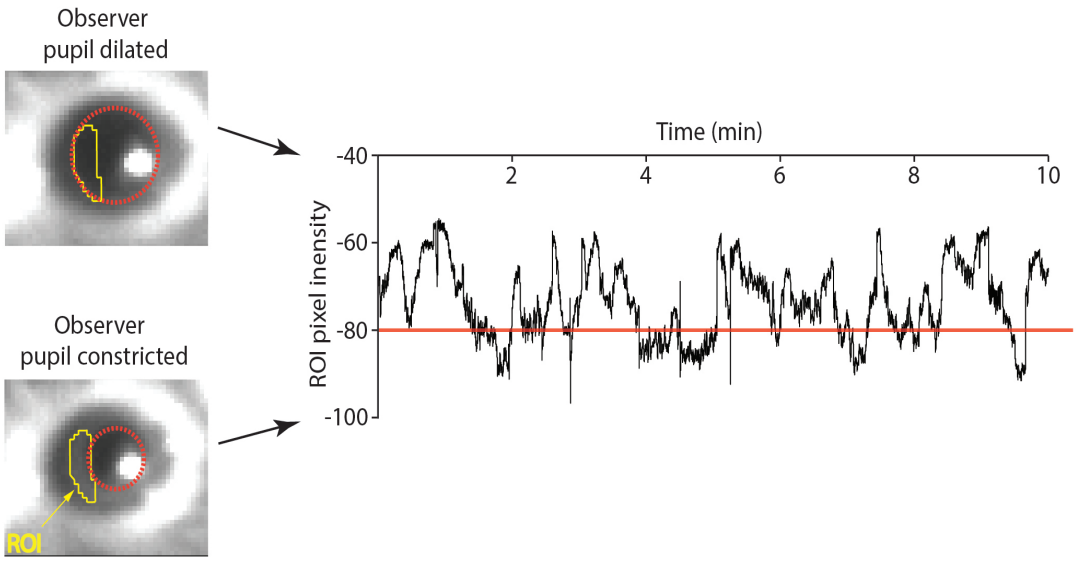

B

M2

		# cells	performance	observation	matched
Whole Session	Animal 1	264	98 (37.1%)	4 (1.5%)	1 (0.4%)
	Animal 2	99	58 (58.6%)	1 (1.0%)	0
	Animal 3	249	151 (60.6%)	4 (1.6%)	2 (0.8%)
	Total	612	307 (50.2%)	9 (1.5%)	3 (0.5%)

		# cells	performance	observation	matched
Excluding pupil constriction	Animal 1	264	98 (37.1%)	4 (1.5%)	0
	Animal 2	99	58 (58.6%)	0	0
	Animal 3	249	151 (60.6%)	4 (1.6%)	1 (0.4%)
	Total	612	307 (50.2%)	8 (1.3%)	1 (0.2%)

Figure S6

Table S1. Summary of performance and observation tuning in PPC and M2

PPC

		# cells	performance	observation	matched
Pellet Reaching	Animal 1	177	85 (48%)	1 (0.6%)	0
	Animal 2	268	111 (41.4%)	4 (1.5%)	0
	Animal 3	179	80 (44.7%)	3 (1.7%)	1 (0.6%)
	Animal 4	297	154 (51.9%)	7 (2.4%)	2 (0.7%)
	Total	921	430 (46.7%)	15 (1.6%)	3 (0.3%)

		# cells	performance	observation	matched
Wheel-Running	Animal 1	149	20 (25.5%)	0	0
	Animal 2	337	37 (10.9%)	1 (0.3%)	0
	Animal 3	238	10 (4.5%)	2 (0.8%)	0
	Total	724	67 (9.3%)	3 (0.4%)	0

M2

		# cells	performance	observation	matched
Pellet Reaching	Animal 1	264	98 (37.1%)	4 (1.5%)	1 (0.4%)
	Animal 2	99	58 (58.6%)	1(1.0%)	0
	Animal 3	249	151 (60.6%)	4 (1.6%)	2 (0.8%)
	Animal 4	240	132 (55%)	4 (1.7%)	0
	Total	852	439 (51.5%)	13 (1.5%)	3 (0.4%)

		# cells	performance	observation	matched
Wheel-Running	Animal 1	216	21 (9.7%)	1 (0.5%)	0
	Total	216	21 (9.7%)	1 (0.5%)	0

ISBN 978-82-326-4292-2 (printed version)
ISBN 978-82-326-4293-9 (electronic version)
ISSN 1503-8181

Doctoral Thesis
Karoline Hovde

Doctoral theses at NTNU, 2019:348

Karoline Hovde

Parieto-frontal architecture, connectivity and behavioral representations in rodents

NTNU
Norwegian University of
Science and Technology
Faculty of Medicine and Health Sciences
Kavli Institute for Systems Neuroscience/
Centre for Neural Computation

NTNU
Norwegian University of
Science and Technology

Doctoral theses at NTNU, 2019:348

NTNU

NTNU
Norwegian University of
Science and Technology